Chair of Petroleum Geology

Master's Thesis

Perlitic textures in silica-rich rocks: Re-evaluation of volcanological and glass technical models and their relevance for petroleum geology

Verena Meier, BSc

January 2022

MONTANUNIVERSITÄT LEOBEN
www.unileoben.ac.at

Declaration of Originality

I, Verena Meier, confirm that the submitted thesis is original work and was written by me without further assistance. Appropriate credit has been given where reference has been made to the work of others.

The thesis was not examined before, nor has it been published. The submitted electronic version of the thesis matches the printed version.

Eidesstattliche Erklärung

Ich erkläre an Eides statt, dass ich diese Arbeit selbstständig verfasst, andere als die angegebenen Quellen und Hilfsmittel nicht benutzt, und mich auch sonst keiner unerlaubten Hilfsmittel bedient habe.

Ich erkläre, dass ich die Richtlinien des Senats der Montanuniversitaet Leoben zu „Gute wissenschaftliche Praxis“ gelesen, verstanden und befolgt habe.

Weiters erkläre ich, dass die elektronische und gedruckte Version der eingereichten wissenschaftlichen Abschlussarbeit formal und inhaltlich identisch sind.

Datum 27.01.2022

Unterschrift Verfasser/in
Verena Meier

This thesis has been written as a cooperation between

the Montanuniversitaet of Leoben, Chair of Petroleum Geology,
supervised by Assoz. Prof. Dipl.-Ing. Dr. mont. Doris Groß

and the Technical University of Freiberg, Department of Geology,
supervised by Prof. Dr. rer. nat. F. Christoph Breitkreuz.

Abstract

Perlites are volcanic glasses of exclusively rhyolitic composition that contain curved fractures around still intact cores of glass. To achieve a more detailed view into the mechanisms controlling formation of fracture networks in volcanic glass and the understanding of microstructures and textures related to perlitic fractures, this study relies on a combination of volcanological and glass technical models supported by stochastic image analysis. The research is based on methodical investigations of 35 rock samples from 24 different locations from five continents (Americas, Eurasia, and Africa) and of different geological ages to cover a broad spectrum of textural variations.

The process of perlitization creates a three-dimensional fracture network which can only be found in rocks comprising elevated H_2O contents. Related studies on rhyolitic textures are sparse and it is widely debated if perlitic fractures form in response to hydration solely or due to thermal stress before hydration. The three-dimensional geometry of the fracture network, which links perlitization to a three-dimensional (paleo)strain field, was proven by computer-tomography measurements. Further investigations on the fracture network show that perlitic cracks form secondary and are always accompanied by primary sublinear quench fractures. The prevalent relation between the two discrete fracture sets is also determined by stochastic image analysis. It was additionally found that crack propagation is further advanced in old samples and ignimbrites because of longer elapsed time spans for crack propagation and the compaction of the glass itself. Crack propagation is supported by the presence of H_2O and increases with time whereby certain samples show several generations of perlitic fractures.

Besides transmitted-light microscopy, the study includes electron microprobe- and thermal analysis techniques (DSC/TG analysis) to gain insights into fluid- and elemental compositions and mobilities. Pre-Cenozoic fully hydrated samples show no variations in fluid content between rim and core but an effect of differential depletion or enrichment can be observed, whereas younger samples with unbalanced water contents indicate incomplete hydration, which reveals a direct connection between alkali mobility and hydration of a rock.

Perlitization is widespread in rhyolitic reservoirs and the fractures frequently amount to an important fraction of the total porosity. Porosity and permeability measurements were conducted to provide an insight into pore space characteristics. It is shown that they can be either improved or deteriorated through post-volcanic, low-temperature alteration processes, especially abundant in pre-Cenozoic samples. Volcanic glasses are not only important as prolific reservoirs in the oil and gas industry, as they often provide storage capacity in geothermal reservoirs and boast various other applications. It is found that perlitic fractures can form by thermal shock at temperatures just below glass transition temperature, but crack propagation and initiation of subsequent generations of rounded cracks is most likely linked to strain which is induced by continued hydration of a volcanic glass.

Zusammenfassung

Perlite sind vulkanische Gläser mit rhyolithischer Zusammensetzung, die gekrümmte Bruchstrukturen enthalten. Um einen detaillierteren Einblick in damit verbundene Mikrostrukturen, Texturen und Mechanismen, die die Bildung von Bruchnetzwerken in vulkanischem Glas steuern, zu erhalten, stützt sich diese Studie auf eine Kombination aus vulkanologischen und glastechnischen Modellen, die durch stochastische Bildanalysen unterstützt wird. Die Forschung basiert auf methodischen Untersuchungen von 35 Gesteinsproben von 24 verschiedenen Orten (Amerika, Eurasien und Afrika) unterschiedlichen geologischen Alters, um ein breites Spektrum an Texturvariationen abzudecken.

Durch den Prozess der Perlitisierung entsteht ein charakteristisches dreidimensionales Kluftnetzwerk, das nur in Gesteinen mit erhöhten H_2O-Gehalten zu finden ist. Verwandte Studien zu rhyolithischen Texturen sind spärlich und es wird diskutiert, ob sich perlitische Brüche nur durch Hydratation oder aufgrund thermischer Belastung vor der Hydratation bilden. Die dreidimensionale Geometrie des Bruchnetzes wurde durch Computertomographie-Messungen nachgewiesen und deutet auf ein 3D-(Paläo-)Stressfeld hin. Weitere Untersuchungen am Bruchnetzwerk zeigen, dass perlitische Risse sekundär entstehen und immer von primären sublinearen Abschreckbrüchen begleitet werden. Es wurde außerdem festgestellt, dass die Rissausbreitung bei alten Proben und Ignimbriten, aufgrund längerer Zeitspannen für die Rissausbreitung und die Verdichtung des Glases selbst, weiter fortgeschritten ist. Die Rissausbreitung wird durch die Anwesenheit von H_2O unterstützt und nimmt mit der Zeit zu, wobei bestimmte Proben mehrere Generationen perlitischer Brüche aufweisen. Neben der Durchlichtmikroskopie umfasst die Studie Elektronenmikrosonden- und Thermoanalysetechniken (DSC/TG-Analyse), um Einblicke in die Zusammensetzung und Mobilität von Fluiden und Elementen zu gewinnen. Vorkänozoische vollständig hydratisierte Proben zeigen keine Schwankungen des Flüssigkeitsgehalts, jedoch kann Auslaugung bzw. Anreicherung von Alkalien entlang des Kluftnetzwerkes beobachtet werden, während jüngere Proben mit unausgeglichenem Wassergehalt eine unvollständige Hydratation anzeigen, was einen direkten Zusammenhang zwischen Alkalimobilität und Hydratation verdeutlicht.

Perlitisierung ist weit verbreitet in rhyolithischen Lagerstätten und die Brüche stellen häufig einen wichtigen Teil der Gesamtporosität dar. Porositäts- und Permeabilitätsmessungen zeigen, dass die Poreneigenschaften durch postvulkanische Umwandlungsprozesse bei niedrigen Temperaturen, insbesondere in präkänozoischen Proben, entweder verbessert oder verschlechtert werden können. Es wurde festgestellt, dass sich perlitische Brüche durch Thermoschock bei Temperaturen knapp unterhalb der Glasübergangstemperatur bilden können. Die Rissausbreitung und die Entstehung späterer Generationen von abgerundeten Brüchen ist höchstwahrscheinlich mit Dehnung verbunden, die durch die fortsetzende Hydratation des Glases induziert wird.

Acknowledgements

First and foremost, I want to express my sincere appreciation to my two supervisors, Prof. Breitkreuz and Prof. Groß, for the extraordinary support during the whole time, the motivational discussions and all the thoughts and ideas which made significant contributions to this study.

I would also like to pay my special regards to Prof. Bermejo for providing valuable insights into fracture mechanics of brittle materials and for supporting this research. Without your help the research goal of my thesis would not have been realized in this way.

I am also indebted to Prof. Ohser for the decisive help with image analysis and for providing the required software and I am grateful to Prof. Stoyan, who facilitated the stochastic approach.

The contribution of “Lamberts Glasshütte” is also truly appreciated with special thanks to Lukas Gerg for valuable technical advice.

I also wish to acknowledge the support of Prof. Aneziris, Dr. Hubálková, Dr. Gevorgyan, Sabine Gilbricht, Dr. Caspari, Pit Arnold and Sascha Schmid. I really appreciate the invaluable assistance that you all provided and your considerable contributions to this work.

The mental support and encouragement from my friends and family is whole-heartedly appreciated, and I would particularly like to thank Uwe and Jakob for all critical and precious inputs.

Table of Contents

1. Objective & introduction

Perlites are described as rhyolitic volcanic glasses which are characterized by delicate and gently curved fractures around intact cores of glass (McPhie et al., 1993). As an industrial resource material, perlite is generated after heat treatment and is used in its expanded form as a light-weight microporous product during building construction (e.g. Kaufhold et al., 2014). This thesis will especially focus on researching for the hydrous behavior of volcanic glass, its implications for perlite origins and hierarchy of fracture generation. The curved fractures in perlitized rhyolites form more or less rounded circles or ovals in 2D with diameters ranging from 0.1 mm up to almost 10 mm (Drysdale, 1991; Denton, 2010), which are macroscopically observable in several samples. Studies on hydrogen isotope compositions showed that the elevated water content in those perlitized rocks does not result from an originally water-rich magma, but is meteoric in origin instead (e.g. Ross & Smith, 1955; DeGroat-Nelson et al., 2001).

Volcanic rocks in general occupy almost a tenth of all global outcrops. These include rhyolitic rocks, which form one of the major groups of volcanic rocks (e.g. continental exposures of Schutter, 2003). The reservoir potential of rhyolites was considered to be insignificant for a long time but advanced research in volcanology and related reservoir characterization during the past two decades suggested that rhyolitic reservoirs can host significant volumes of hydrocarbons (e.g. Mao et al., 2020). In total, there are more than 300 discovered oil and gas shows in volcanic rocks worldwide, among which 169 reservoirs contain proven reserves (Zou et al., 2013). Volcanic reservoirs are not only important for the oil and gas industry, but also for various other applications such as oil and gas storage, groundwater resources, potential environmental impacts associated with waste disposal (e.g. Lenhard & Götz, 2013), and, especially, for geothermal energy production which is often bound to rhyolitic reservoirs (e.g. Saubin, 2019). Microstructures related to volcanic rocks can provide significant pore space (e.g. Mao et al., 2020); however, heterogeneity, complex pore space development and distribution, as well as the still sparse research on those microstructures, yield in difficult and high-risk reservoir quality prediction for volcanic reservoir exploration (e.g. Sruoga et al., 2004). Therefore, investigation of rhyolitic microstructures bears valuable scientific and economic implications; however, related studies so far are sparse.

Perlitic textures in general are one of the most thermodynamically unstable structures in rhyolites and become easily modified by post-emplacement processes such as alteration or further fracturing (e.g. Denton et a., 2009) which can either decrease or remarkably improve pore volume (e.g. Wang & Chen, 2015). The equilibrium between dissolution and precipitation, as well as subsequent fracturing, is strongly controlled by the ingress of freshwater and the glass-water interaction (de´Genaro et al., 2000). Hence, the formation and propagation of those fracture systems are still strongly discussed, and it is not yet clear whether the fractures form in response to hydration (e.g. Davis & McPhie, 1996) or

if they form due to thermal stress before hydration (e.g. Yamagashi & Goto, 1992) or as a combination of both processes. Previous studies found that most naturally formed surfaces of volcanic glasses had undergone hydration (e.g. Friedman & Smith, 1960) whereby water diffuses into the glass and reacts with the glass network, which results in compositional change in terms of e.g. alkali mobilities (e.g. Noble, 1967) and textural change in form of volume reduction and formation of tensile stresses (e.g. Lacy, 1966). The hydration of volcanic glasses provided the basis for the development of the obsidian hydration method (e.g. Friedman & Smith, 1960), which makes it possible to derive hydration rates and date hydration rims back into Pleistocene time (Michels, 1986). The magma-water interaction is not only of importance when it comes to fracture formation but is of significance for the eruptive environment in general, with about 85 % of all volcanic eruptions worldwide being subaqueous (White et al., 2003) and therefore strongly related to the ingress of water from various sources (Wohletz et al., 2013).

The effect of moisture and water on glass, or, rather on the fracture behavior of such brittle materials, is also intensely studied in material sciences. Subcritical crack growth is strongly promoted by moisture (Wiederhorn, 1974), occurs under applied loads and results in a decrease in strength over time (Bermejo, 2020). However, a contrary effect called swelling can be observed in cases where water penetrates the area surrounding the crack tips where it can cause the build-up of compressive stresses which result in a strengthening of the glass (e.g. Wiederhorn et al., 2011). Considering crack growth in brittle materials, a distinction between crack formation and crack propagation is warranted (e.g. Bermejo & Danzer, 2014). While the influence of environmental conditions is rather affecting crack propagation, crack formation is often linked to the thermal shock behavior of a glass, which is caused by quenching and results in temporary stresses which in turn results in brittle failure of the material (e.g. Harrer & Danzer, 2011).

To achieve a more detailed view into the mechanisms controlling formation of fracture networks in volcanic glass and the understanding of microstructures and textures related to perlitic fractures, this study draws attention to a combination of volcanological, and glass technical models supported by stochastic image analysis. The latter is concerned with the analysis of image data, in this case thin section images, which enables a classification and quantification of random structures (e.g. Chiu et al., 2013). Detailed analysis of these textures and the results of the thesis may be beneficial for future exploration concerning potential rhyolitic reservoir characterization and help ascertain further volcanic reservoir predictions in analogue basinal settings.

1.1. Definitions

Due to the fact that the term “perlite” and related terms have historically been used in different ways and to describe distinctly different features, it is inevitable to specify some fundamental terms, which will be used in the thesis.

1.1.1. Perlite

Perlite is a term used in this thesis to describe a volcanic glass of silicic composition, which is characterized by its typical perlitic, sub-spherical fractures. Thus, the term is not used in the material science nomenclature of industrial perlite. In almost all cases, naturally occurring perlites show a higher water content than the original glass; however, conversely, not every hydrous volcanic glass is ultimately perlitized, i.e. shows perlitic textures (e.g. Yamagashi & Goto, 1992).

1.1.2. Perlitization

Perlitization delineates the formation and general prevalence of perlitic cracks and is not directly linked to the process of hydration. As alluded to earlier, this process also has no relation to any form of heat-treatment, which is used for the expansion of perlite for industrial reasons (e.g. Kaufhold et al., 2014).

1.1.3. Pitchstone

This term is used to characterize a highly hydrated volcanic glass which in addition to frequent partial mineralization may often contain perlitic fracture networks. Pitchstones differ from perlites only by higher water contents (e.g. Friedman et al., 1966).

1.1.4. Perlitic cracks, fractures, and beads

The observed arcuate, gently curved cracks, which are a characteristic feature of perlites, are named perlitic cracks in the further course of this study. The terms “crack”, “fracture”, and “beat” describe the same phenomenon and are used synonymously. As a collective term for these perlite-related features, the expression “perlitic textures” is used.

2. State-of-the art knowledge

This chapter gives an overview about what is already known in the fields of volcanology, petroleum geology, and material sciences. Various aspects which concern perlitic fracturing are explained to clarify important information necessary for further discussion and evaluation of obtained results.

2.1. Volcanology

2.1.1. Historic background

The term “perlite” was mentioned for the first time by Francois Sulpice Beudant in his records of “Voyage mineralogique et géologique en Hongrie” in 1822. It was introduced as a translation to the German word “Perlstein” and used to describe a glassy rock exhibiting a particular structure (Beudant, 1822). Allport (1877) was one of the first authors who described the curved cracks in further detail and who suggested a concept on the formation of perlitic structures. It has already been discussed in the late 19th century on whether the term can only be used for the glassy rock or also for the globules and cracks in rhyolites, which are characteristic for the structure (Grenville, 1895). Regrettably, the usage of terms related to perlites and perlitic textures has not been clearly specified in usage down to the present day and the term “perlite” itself is not used synonymously by different authors. Therefore, it was deemed necessary to clearly predefine essential terms in advance to avoid potential misunderstandings (chapter 1.1.).

2.1.2. Perlitic textures in lava and pyroclastic rocks

Coherent, glassy silicic lava is often characterized by the presence of continuous perlitic textures. However, it has been observed that perlitic textures are not compulsorily limited to lava but can also be found in strongly welded pyroclastic rocks like ignimbrites. Pumice and shards in those rocks are compressed and form a dense glass, which is a suitable precondition for perlitic cracks to propagate (e.g. Gifkins et al., 2005).

Marshall (1935) proposed the name “ignimbrite” for the first time, where he defines ignimbrites as rocks of acidic composition, deposited from volcanic eruption clouds or air-fall deposits of intensely heated fragments of volcanic magma. Specifically, a pyroclastic density current originates from one of three mechanisms: 1) fountain-like collapses of an eruption column, 2) hot avalanches derived from lava domes or 3) laterally inclined blasts. However, it is impossible to investigate processes within pyroclastic density currents; therefore, inferences are drawn from associated deposits. According to lithology and sedimentary structures, deposits of pyroclastic density flows are subdivided into ignimbrites, pyroclastic surge deposits and block-and-ash flow deposits. It was suggested by Branney & Kokelaar (1992), that massive ignimbrite layers aggrade progressively from the base upwards, with sedimentary processes being independent of overriding parts of the current, a notion which is

supported by evidence from fabric studies, variations in lithofacies and welding characteristics, as well as the presence of compositional zonation within a flow-unit. Ignimbrites are characterized by a poorly sorted mixture of pumice and lithic lapilli within a matrix of vesicle-wall-type vitric shards and crystal fragments. They are typically ash-rich and can either be loose and uncompacted or partly to entirely indurated and show thickness variations from a few centimeters to many hundreds of meters (Branney & Kokelaar, 2002).

In addition, ignimbrites feature a large variability of different structures from a mainly massive non-stratified appearance to particle fabrics and soft-state deformation structures. A very common feature that can be observed in several ignimbrites are so called “fiamme”, which are glassy deformation textures with a lens- or flame-shaped appearance, that occur in welded pyroclastic deposits resulting from plastic deformation, flattening, and sintering of hot glassy clasts (Smith, 1960a). The two main factors influencing the texture are temperature and load, i.e. the thickness of the cooling unit. In general, fiamme form above the glass transition temperature (T_g), whereby T_g is dependent on the cooling rate on the one side and the volatiles content on the other side, which implies that higher amounts of volatiles as well as low cooling rates lead to a decrease in T_g (Gottsmann et al., 2002). Considering a cooling body, there is a non-welded, pectinate zone with vapour-phase crystallization on the top, followed by a welded eutaxitic zone and an even stronger compacted and welded parataxitic zone, surrounding a flow-banded zone of extreme attenuation in the core of the cooling unit. Within the welded zone, it is observed that the volatile content within the fiamme is higher than in the surrounding matrix, which leads to higher T_g in the matrix and a decrease in T_g in the fiamme, respectively (McArthur et al., 1998).

The fiamme show a large variability of internal textures and are not necessarily restricted to welded pyroclastic deposits (Gifkins et al., 2005). However, they often show a texture of sustained vesicles, creating a linear appearance with a grey to brownish color, which results from hematite dust (Fig. 1). The creation of the elongated texture can form either in-situ through welding compaction or already in the vent, shortly below the level of fragmentation, due to the shearing process, that results from different ascending velocities within the rising mass. The latter causes a linear structure within the fiamme, whereas the matrix can be relatively uncompacted, as compaction is not the driving mechanism in that case.

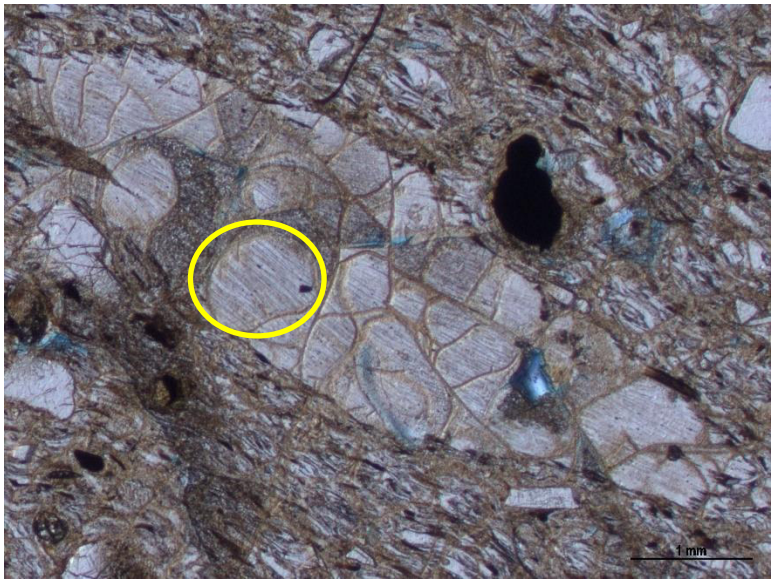

Fig. 1: Thin section of an ignimbrite with perlitized fiamme which shows lineated traces of hematite dust (e.g. indicated in area within the yellow circle); sample SS 16782.

2.1.3. Alteration and mineralization

Induced by the fracturing process, fluids can enter the rock and move along the fracture network causing the alteration of the glassy rhyolite. This alteration is accompanied by minerals which nucleate along the cracks and grow into the glass. The glass between the cracks might get replaced and the fractures themselves get preserved by thin infilling layers, which are mostly consisting of phyllosilicates and opaque minerals (Allen, 1988).

According to the classification scheme introduced by Allen (1988), perlitic textures can be subdivided into classical circular perlite and banded perlite with each group in turn being divided into three sub-categories: original texture, false siliceous shards, and false phyllosilicate shards (Fig. 2). The shard-like textures develop from classical perlite when the continuity of perlitic fracture networks gets obscured by quartz phyllosilicate alteration, creating isolated shard segments. These shards can then be preserved according to their alteration either as siliceous altered segments between several fractures or as phyllosilicate-altered section of the perlitic cracks themselves, whereby the original network system shape determines the shape of the shards (Allen, 1988).

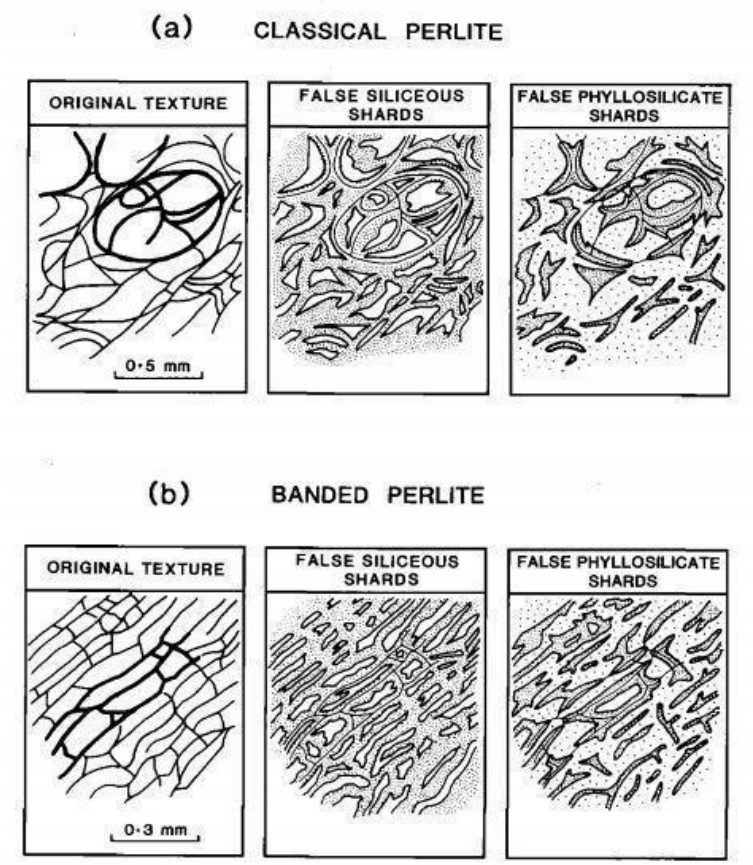

Fig. 2: Classification of perlites into (a) classical perlites, and (b) banded perlites (according to Allen, 1988).

2.1.4. Microlites

Microlites and trichites are characteristic features that can be observed in silicic glassy volcanic rocks and were first described in two milestone papers from Iddings (1899) and Zirkel (1986). Microlites are minute crystals visible only under the microscope and trichites represent a subgroup of microlites which are a common feature in obsidian, characterized by their distinct optical appearance (Webster, 1933). Moreover, they can be separated according to their appearance into slender prism microlites, showing a parallel distribution imposed during emplacement, and trichite loops, spirals, and helices without systematic arrangement. The most common type of microlites and trichites are pyroxenes. Sanidine-type microlites are rarely observed in obsidians and biotite is generally rare in glassy rocks. Amphibolites are scarce in fresh and only slightly hydrothermally altered glass. Magnetite is prevalent in many glassy rocks and forms strains of magnetite dust. Magnetite is an early crystallization product as it is the locus for the development of pyroxene and amphibolite microlites in many samples. However, in densely welded glasses it mostly develops on the welding contact and represents a late product in a rock´s cooling history (Ross, 1962). The consideration of microlites for studies on perlite textures can be useful as the differences in habit and time of formation of the microlites indicate a difference in the formation environment (Ross, 1962).

2.1.5. Formation models

Besides the discussion of related terms and changing definitions, an even more ambivalent debate on how perlitic fractures form has been going on for many years of research. Three different major formation models have developed, yet. Until now, no agreement has been found. Notably, Tab. 1 lists findings and suggestions from authors who dealt with this issue for more than 140 years, whereby a separation into opposing schools of thoughts emerged and is consequently indicated by different colors:

- perlitic fracturing due to hydration (Tab. 1, blue)
- perlitic fracturing as a result of thermal stress (Tab. 1, white)
- perlitic fracturing as a combination of hydration and thermal stress/strain (Tab. 1, grey)

From a retrospective consideration of the applied methods, it gets evident that thin section as well as XRF analysis mostly led to the conclusion that perlitic fracturing happens due to thermal impacts, whereas the hydration model is often based on laboratory hydration tests accompanied with calculated models and physical justifications. All formation models and corresponding constraints are explained in the next chapters and will be discussed in several other chapters throughout this work.

Tab. 1: Formation models of perlitic textures; blue: fracturing due to hydration; white: fracturing as a result of thermal strain/stress; grey: unclear or mixture of both models

REFERENCES	APPLIED METHODS	RESULTS
Allport, 1877		– the spheroids are not formed by the superposition of successive laminae and are no concretions but are merely portions of homogeneous glass partially separated from the general mass by the formation of a number of small, curved planes of fracture – the fractures are caused by strain produced during contraction of brittle glass – perlitic spheroids must have formed subsequently to solidification
Ross & Smith, 1955; Ross, 1962	– determination of refraction index – determination of volatiles by weighing and heating	– all perlites form from obsidian through secondary hydration after emplacement of the obsidian – volume change due to hydration of a surface layer causes strained surfaces – refraction indices show that water of hydration in perlite has been added to original glass – water in obsidian is pristine, derived from the parent magma; water of perlite is the result of a later episode
Marshall, 1961	– examination of thin sections with a petrographic microscope – filar- and stage micrometers pressure-bomb experiments	– perlitic structures develop due to strain formed during the rapid cooling of silica melts – some volcanic glasses are probably transformed by heat alone – perlitic structure form essentially at the same time at which the rock forms – perlites continue to pick up more water with time under certain conditions – no more than a few tenths of 1% of water in perlites is magmatic but of secondary origin
Friedman et al., 1966	– determination of hydration rates	– hydration results in a stress that is great enough to form perlitic crack at the interface between hydrated and un-hydrated glass – pitchstones formed due to hydration under elevated water pressure
Lacy, 1966		– the formation of perlite textures is characteristic of low temperature hydration of rapidly chilled glass – perlitic fractures form as water diffuses into the glass causing a change in structure which results in volume reduction and tensile stresses, which are released during perlitic fracturing – 400°C is a too high temperature to produce characteristic features of low temperature hydration and the formation of perlite
Allen, 1988		– perlitic fractures develop after emplacement of volcanic rocks as a result of the expansion of the glass during hydration and associated release of residual stress incurred during cooling – subsequently extensive volumes may be altered by fluids moving along the fracture network

Drysdale, 1991		– low (down to ambient) temperature hydration by meteoric water or under subaqueous conditions of obsidians & rapidly chilled glasses produce perlitic textures – hydration at elevated temperatures prevents perlitic cracking
Yamagashi & Goto, 1992	– XRF analysis – thin section analysis	– obsidian glass is changed into perlite by fracturing due to thermal stress arising from quenching and shear stresses related to flowage before hydration – perlitic fractures form primarily in response to strain derived from rapid cooling and external water was later absorbed by the glass – the rhyolite is not necessarily hydrated
Davis & McPhie, 1996	– petrographic thin section analysis – electron microprobe analyses	– fracture sets form in response to contraction during quenching & allow access of external water to the interior of the dyke – perlite forms as a result of low-temperature hydration of rapidly chilled glass as the fractures release strain imposed by a volume change on the uptake of water but probably depends on both cooling and exposure to external water – rapid cooling alone does not directly result in classical perlitic fracturing – fractured glass is hydrated, containing higher amounts of meteoric water whereas the cores retain pristine magmatic water contents – perlitic fracture sets develop after substantial heat loss between 100-200°C – textural consequences of glass hydration depend on the rate of cooling and the temperature at which hydration begins
Willson et al., 1999	– FTIR	– perlite cracks have developed from hydration and consequent expansion of the glass – the margins of these fractures increase the surface area to which water molecules can weakly bond
Denton et al., 2009	– thin section analysis – sieving and eye-estimation – DSC, TG, mass spectrometry – X-ray diffraction	– perlitized obsidian is water rich due to diffusion of meteoric water and not a water-rich original magma – perlitization is driven by water ingress – unresolved whether water diffusion results in cracks or crack formation facilitates water diffusion – hydrating water in perlites is concentrated in altered zones directly adjacent to cracks
Denton et al., 2012	– field studies – thin section characterization – volatile analysis by thermogravimetry	– major fractures form due to cooling contraction – water travels along these fractures & diffuses into the glass through fracture-glass interface leading to perlitic fracture formation – perlitization occurs mainly at temperatures just below T_g, additional perlitization at ambient temperatures if times-scales are long enough

2.1.6. Hydration of volcanic glass and related stress/strain conditions

Previous studies on high-water-content volcanic glasses (e.g. Ross & Smith, 1955; Friedman & Smith, 1960) show that naturally formed surfaces of glass had undergone hydration in most cases. During the process of hydration, water diffuses into the glass and reacts with the glass network. Hydration produces hydroxyl groups, which bond to silica atoms and form silanol groups, interstitial OH groups, and hydrogen bonds (Lacy, 1966). The formation of two hydroxyl groups provides an efficient mechanism for breaking strong Si-O-Si bridges and sufficient cross-links can be broken to orient silica tetrahedra (Marshall, 1961). The resulting change in structure leads to a volume reduction, i.e. a shrinkage, and the formation of tensile stresses (e.g. Lacy, 1966). A slow imbibition of surface water into the glass stretches its structure and forms further hydrogen bonds (Lacy, 1966). To break Si-O-Si bondings, diffusion of entire water molecules is required (Marshall, 1961).

Based on the hydration of volcanic glasses, the obsidian hydration method was developed. It is about a chronometric technique, which is widely used for the dating, classification, and identification of obsidian artifacts from cultural prehistory (Michels, 1986). The worldwide distribution of obsidian artifacts makes it one of the most relevant dating methods for archeologic applications. The method is based on the assumption that ancient cultures exposed fresh surfaces on artifacts, which subsequently began to extract atmospheric- or ground water, resulting in the gradual formation of hydration rims. The hydrated layers in obsidian and other silica-rich glasses, formed by the absorption of water on the surface, show different densities and optical properties compared to the original glass. Due to a diffusion-controlled process, these hydrated layers grew slowly over time and a relationship between the thickness of the hydrated layer and the age can be derived from the law of diffusion (Friedman & Smith, 1960). There are outstanding examples of hydration rates, e.g. for some Hawaiian glass, which hydrates at more than 300 μm^2 /1000 years, while diffusion rates in other examples are so slow that they provide the possibility to date back into Pleistocene times (Michels, 1986). A non-chronological application is the thermal history reconstruction simply based on the hydration layer thickness (Friedman & Obradovich, 1981).

The approach of considering hydration rates is substantial for evaluating the significance of hydration for the formation of perlite as it can be used to prove if the rate of hydration of obsidian is fast enough to induce perlitic fracturing (e.g. Friedman & Smith, 1960). However, there are considerable discrepancies in different investigations and calculations of diffusion rates (Tab. 2).

Tab. 2: Calculated diffusion rates as a function of temperature.

REFERENCE	DIFFUSION RATE [μm^2/1000 YEARS]	TEMPERATURE	IMPLEMENTATION / COMMENT
Friedman & Smith, 1960	0.4	average in arctic regions at ambient temperatures	study on hydration rims on samples
	11	average in tropical Equator regions at ambient temperatures	
Marshall, 1961	$1.4*10^6$	330°C	1 atm H_2O pressure, 2,550 hrs of sample treatment, neglect original water content
	0.00001	20°C	calculated
Friedman et al., 1966	$1*10^4$	100°C	1 atm H_2O pressure, 4 years of sample treatment, consider original water content in glass
	5	20°C	calculated
Denton et al., 2012	$1.7\text{-}2.5*10^{11}$	850-400°C	calculated from cooling rates measured by geospeedometry

The hydration rates examined by different studies show an increase in velocity, i.e. diffusion rate, with increasing temperature (Tab. 2). This implies that the diffusion of water is fastest right after emplacement of a magmatic body and due to the presence of water, e.g. an ingress of meltwater, the partial pressure of water enhances (Denton et al., 2012). Nevertheless, it has to be considered that on the one hand water can drain away or vaporize very quickly, causing a rapid decrease in pressure, but on the other hand hydration rates rapidly decrease by more than two powers of ten during cooling of 100°C and gradually slow down during further cooling to ambient temperature (e.g. Marshall, 1961). Moreover, it has to be taken into account for average diffusion rates of specific geographic regions, that the temperature is rather an estimate at which hydration proceeds at the calculated rate for the case that the temperature is maintained constant. Therefore, the effective hydration temperature in nature is not only dependent on the maximum temperature but also on the time of maintaining the high temperatures (Friedman et al., 1966). As it is unlikely to have sustained temperatures over a long period, the calculation of the hydration velocity for natural situations is highly sensitive to errors, especially when it comes to volcanic events, which are always linked to rapid changes in temperature and a complex cooling history.

To examine if the rate of hydration is sufficient for perlitic cracks to form, obsidian artifacts were analyzed, and it was stated by Friedman & Smith (1960) that the diffusion rate is not only dependent on temperature but also on the water content of the glass, as the diffusion of water into the glass causes a concentration gradient from the surface inward. They proposed that hydration rates are slowest in arctic and highest in tropical regions. For perlitic samples they concluded that it would take

40.000 years for a 20 µm thick hydrated surface to form on obsidian at 22 °C and after that, cracks would form at the interface between hydrated and non-hydrated glass due to the resulting stress. This implies, that an obsidian would be fully replaced by perlite in 200.000 years if the greatest distance between the cracks is 0.2 mm (Friedman & Smith, 1960). Marshall (1961) calculated the diffusion rate based on the assumption that it is independent on the glass's original water concentration. From the significantly lower hydration rate he inferred that perlitic fracturing must be the result of thermal strain and that the higher water content in perlite - compared to obsidian - derives from post-volcanic adsorption of water in the fractures.

Furthermore, Drysdale (1991) and Lacy (1966) suggested that the release of tensile stresses and the formation of hydrogen bonds over the course of the hydration process results in volumetric shrinkage as the origin of perlitic cracks. Ross & Smith (1955) also recognized the volume change due to hydration causing a strained obsidian surface and concluded that perlites form after the emplacement of obsidian following secondary hydration.

Several investigations on water samples extracted from obsidian specimen and enclosing perlite have been done in previous years (e.g. Ross & Smith, 1955; Davis & McPhie, 1996). Isotopic composition or rather analysis of deuterium contents showed that water from perlites is of meteoric origin. Moreover, isotopy showed that the water present in the samples fits to the area where the samples were collected. In contrast, this relationship cannot be established in analyzed water from obsidian samples, which consequently is attributed to a magmatic origin (e.g. DeGroat-Nelson et al., 2001). However, the findings on the origin of the water in perlites and obsidian samples apply to both models as meteoric water can enter the rock during hydration but also during thermal shock reactions in ambient water; hence, it cannot be used to eliminate one assumption but rather confirms both models.

From all investigations conducted to-date it can be generally concluded that obsidian glass is able to absorb meteoric water and that most perlites retain meteoric water. However, the questions whether the long-term process of hydration of the obsidian surface is accountable for the ingress of meteoric water into the glass triggering perlitic fracture formation, or, alternatively, if the water entered during cooling or post-volcanic hydrothermal alterations, remain unanswered and will be discussed i.a. in this thesis.

2.1.7. Cooling of volcanic glass and related stress/strain conditions

The cooling process of brittle materials generally induces stress. The magnitude is believed by several authors (e.g. Marshall, 1961) to be strong enough to shatter glass. Volcanic glass generally forms when a magma cools rapidly and viscosity increases until the point where the rate of crystal growth is insignificant. It is believed that if subsequent cooling is also fast, the associated strain which develops in the glass is high enough to splinter the glass even at very low temperatures whereby parts of the strain get consumed by shattering (Marshall, 1961). This thermal stress associated with cooling contraction, is commonly known to form sublinear fractures or joints dubbed quench fractures (e.g. Yamagashi & Dimroth, 1985). The remaining glass may subsequently be fractured by arcuate perlitic cracks, which surround intact cores of glass (Ross & Smith, 1955). It was also suggested by Cas & Wright (1987) that an obsidian glass can form perlitic fractures in a hot lava during cooling even before the process of hydration due to thermal stress. The water which is responsible for the elevated water contents in perlites and pitchstones can enter at any time subsequently to the fracturing process from groundwater supply, the atmosphere (e.g. Marshall, 1961) or any other external sources (e.g. Wohletz et al., 2013), as the primary formed network of quench fractures allows access of external water into the interior of the cooling body (Davis & McPhie, 1996). It was found that subsequent heating to no more than 100° C can already produce a thin devitrified layer (Marshall, 1961).

Generally, the cooling process is not uniform throughout a heat-venting volcanic body, i.e. a lava or pyroclastic flow. The two most important factors regulating cooling are the eruption temperature (T_0) and thickness of the lava flow deposit. A realistic temperature for a rhyolite flow is T_0= 850 °C with an estimation of a flow thickness at time of eruption and emplacement of approximately 90 m. By determining these values, Stevenson et al. (2001) suggested that the lava flow emplacement time can be calculated by first computing the average flow velocity and then integrating from the emplacement temperature T_0 to the final temperature T_g. This yields in an average flow velocity of 10^{-4} m s^{-1} with a minimum emplacement time of 1.5 years and a maximum emplacement time of 6 years. Calculations show that a thick lava flow takes approximately 4 years for the upper 10 m to cool below the glass transition temperature, i.e. the temperature threshold of brittle-ductile transition. Indeed, the interior of a magmatic flow can remain ductile for up to 15-20 years after emplacement (Stevenson et al., 2001). For the case example of a 90 m-thick rhyolitic flow, cooling from emplacement temperature to a temperature of 500 °C in the interior of the body takes 50 years (Fig. 3; Stevenson et al., 2001). This assessment implies that it takes a lava flow on average 50 years to reach a temperature decrease of 350 °C in its core, which in turn supports the argument that it would take approximately 120 years to cool the core of this cooling unit down to ambient temperatures, if cooling is assumed to follow a constant linear behavior (Stevenson et al., 2001). However, it is very likely that this value underestimates the real time required for cooling, because the basement cannot take up the same

amount of heat anymore as it has already been heated up in the course of the time (Fig. 3). The discussion on cooling rates might be significant for the development of perlitic fractures due to the fact that on the one hand it is still unclear in which temperature range the fractures form, and, on the other hand, because hydration and thermal shock both are dependent on temperature in one way or another.

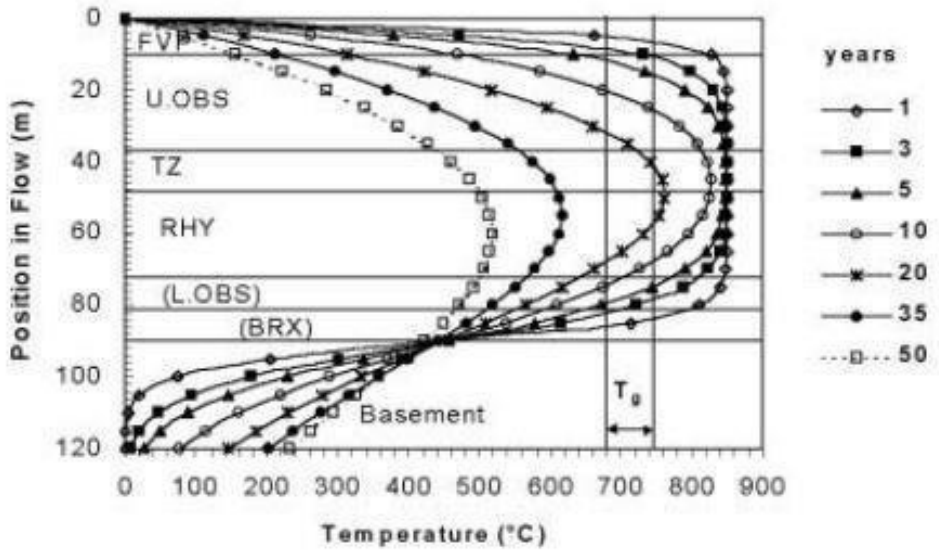

Fig. 3: Temperature profiles for a lava flow at time steps of 1 to 50 years, derived by numerical modeling with an eruption temperature of T_0= 850 °C. Thickness of the flow is 90 m. Horizontal solid lines mark textural zones observed in the lava flow (FVP= Finely Vesicular Pumice, U.OBS= Upper Obsidian, TZ= Transition Zone, RHY= Crystalline Rhyolite, L.OBS= Lower Obsidian, BRX= Breccia); vertical lines mark the range of the glass transition temperature, T_g (Stevenson et al., 2001).

2.1.8. Eruption environment indications

Characteristics of volcanic eruption products are not only controlled by the magma properties themselves but also by the environment of the eruption. The two different eruption media, i.e. water and air, cause differences in several properties (e.g. density, viscosity, etc.) and lead to the special characteristics controlling magma-water interactions. Therefore, proper recognition of these characteristics can provide useful information for identifying the eruption environment (Xian et al., 2018).

The interaction between meteoric or connate water and lava is described as hydrovolcanism and this term includes subaqueous eruptions as well as subaerial eruptions associated with water (Xian et al., 2018). The term also comprises all dynamic processes that determine behavior and character of eruption products and deposits (Wohletz et al., 2013). White et al. (2003) found that subaqueous eruptions account for 85 % of volcanic eruptions worldwide whereby water can arrive from various surface and subsurface sources, such as marine, lacustrine, fluvial, glacial, rain, connate or ground

water (Wohletz et al., 2013). The magma-water interaction significant for perlitic fracturing will be discussed in several chapters of this thesis, as it leads to variations in eruption processes and volcanic products and therefore has a strong impact on pore- and fracture characteristics (White et al., 2003). Hydrovolcanism in general is distinctive in several aspects. The two main indications of formerly eruptive environments are (1) “normal” sediment (i.e. clastic or chemical) which become eventually covered by volcanic deposits, and (2) peculiar intra-glass-structures, like perlitic textures and quench fractures. These characteristics of a volcanic rock succession can in turn be used to determine type and process of eruption (for instance, hyaloclastic) and thus pinpoint environmental conditions of a particular eruptive event recorded in the rock record (Xian et al., 2018).

Microtextures in particular provide important information on magma properties and the eruption process(es). For instance, it was found for certain perlitic textures from subaqueous eruptions, that they link to hydrovolcanism, i.e. a magma-water interaction, with an eruptive close to the final place of deposition. In such cases, the perlitic fractures are either related to a lava flowing into a water-bearing environment or a magma that intrudes in a colder environment. In both cases, the occurrence of perlitic textures indicates the depositional environment or the emplacement environment (Shan et al., 2007). The sublinear fractures, which are also discussed in this thesis, result from cooling and contraction, and are also caused by the interaction between a hot melt and cool water or hydrated deposits (Cas & Wright, 1987). Quenching in general can occur in underwater volcanic eruptions, or, when a lava or pyroclastic flow enters a subaquatic setting, or, when the melt intrudes unconsolidated, yet hydrated sediment. These various case examples nonetheless demonstrate the strong correlation between water and the occurrence of quench fractures (Xian et al., 2018).

The cementation type also gives strong hints on the eruption environment. Increasing water depth, for instance, is related to higher hydrostatic pressures which result in non-magmatic cementation. A further aspect for the eruption environment is given by the oxidation index, i.e. the ratio of Fe_2O_3 to FeO. If this ratio exceeds 1.5 it indicates a strongly oxidizing environment whereas a value smaller than unity implies a reducing environment. Furthermore, the oxidation index is also related to the rock´s SiO_2 content and it correlates positively with higher acidity and elapsed weathering time (Qiu, 1985). Considering other sediments which encase volcanic units, information of the environment at the beginning and end of the eruption can be directly inferred. This means, that the entire core and outcrop data can be used to reconstruct the volcanic depositional environment (Xian et al., 2018).

2.1.9. Glass transition temperatures and devitrification in silica-rich rocks

Silica-rich melts belong to the group of glass forming substances. Such substances are characterized by two distinct reference temperatures, which are the melting temperature T_m and the glass transition temperature T_g (Sakka & Mackenzie, 1970). The melting point is of no special relevance for research into perlites, due to the fact that perlitic fracturing corresponds to brittle deformation after the

supercooled liquid has reached the glass state at temperatures below T_g (Fig. 4). T_g separates the liquid (relaxed) from the glassy (unrelaxed) state (Giordano et al., 2008) and correlates to the temperature at which annealing of the glass starts. T_g is also used in material sciences for characterizing amorphous materials (Sakka & Mackenzie, 1970).

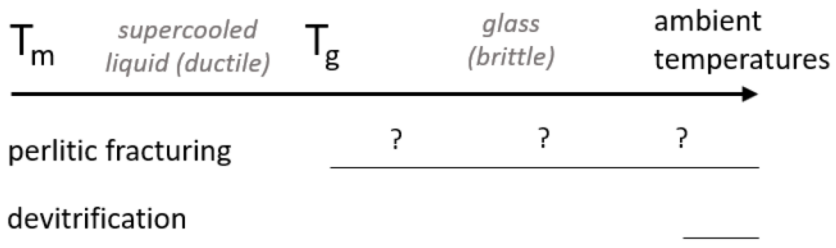

Fig. 4: Timing of perlitic fracture formation and devitrification in relation to the melting temperature T_m and the glass transition temperature T_g (modified after McArthur et al., 1998).

Although the exact temperature or temperature range of perlitic fracture formation is not known, Davis & McPhie (1996) suggest that perlitic fractures form after substantial heat loss at temperatures between 100-200°C. In contrast, Denton et al. (2012) stated that most significant perlitization occurs at temperatures just below T_g and additional perlitization occurs at ambient temperatures if timescales prove long enough.

The cooling rate from eruption temperatures to T_g and below is controlled by various factors like melt composition, fluid and volatile content, initial temperature, latent heat, thermal conductivity, and the thickness of the cooling body (Giordano et al., 2008; Breitkreuz et al., 2021). T_g strongly decreases when water contents increase with the largest decrease registered within the first 5 mol.% of H_2O (Giordano et al., 2008). Different authors calculated values for T_g for rhyolites of only slightly different melt composition (Tab. 3) but with different water contents. These temperatures set the upper limit for the temperature range in which perlitic fracturing may happen.

Tab. 3: Calculated values for glass transition temperatures for rhyolites with different melt compositions (modified after Giordano et al., 2008).

T_g, °C	H_2O, %	REFERENCE
763.85	0	Goto et al., 2005
465.85	3	Goto et al., 2005
496.85	2	Streck & Grundner, 1995

As a thermodynamically unstable material, glass becomes crystalline under a variety of conditions and with time. The term devitrification describes the hydrothermal or thermal in-situ deconstruction of a glass with negligible loss of material. Leaching of certain constituents and in-situ crystallization of the remainder are intermediate effects of chemical weathering and hydrothermal alteration (Marshall, 1961). Several experiments and observations (e.g. Hauser & Reynolds, 1939; Norton, 1941) showed

that volcanic glasses get devitrified in the presence of water at temperatures slightly above boiling point. The rates of devitrification (Tab. 4) are significantly higher than the diffusion rates of water, whereby the depth of devitrification is strongly dependent on the age of the flow (Marshall, 1961).

Tab. 4: Time required for devitrification as a function of temperature (modified after Marshall, 1961).

TEMPERATURE	TIME
400 °C	at least a few thousand years
300 °C	at least a million years
ambient temperatures (~20 °C)	4-5 µm in 100 million years

2.2. Petroleum geology

2.2.1. Volcanic hydrocarbon reservoirs worldwide

Volcanic reservoirs are assigned to the group of unconventional reservoirs and have been discovered in various hydrocarbon-bearing basins worldwide (Mao et al., 2020). The reservoir potential of volcanic rock units is not only of importance for the oil & gas industry but also for various other branches of subsurface analysis, such as groundwater resources, oil or gas storage, geothermal reservoirs and potential environmental impacts associated with waste disposal (Lenhard & Götz, 2011). Due to their high heterogeneity and complex pore system, volcanic reservoirs have been considered as poor targets for exploration for a long time (e.g. Manville et al., 2009). Nevertheless, advanced understanding of volcanology and related reservoir characteristics during the past two decades showed that they are a valuable hydrocarbon source (e.g. Sun et al., 2018).

Volcanic reservoirs can be found in various locations around the world (Fig. 5), mostly on convergent margin and rift basin settings (Lenhard & Götz, 2011).

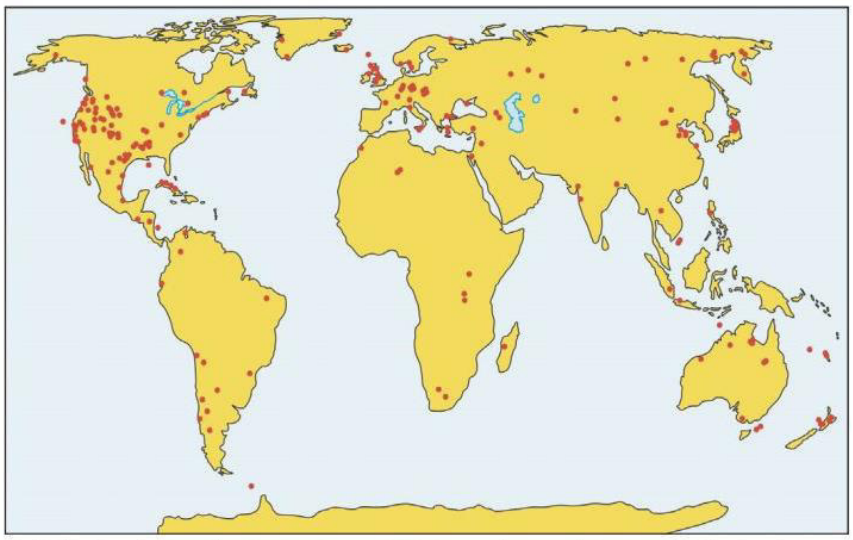

Fig. 5: Distribution of oil and gas shows in volcanic rocks worldwide (Zou et al., 2008).

The San Joaquin Basin in Northern California was the first spot for the discovery of a volcanic gas reservoir in 1887 (e.g. Gries et al, 1997). Nowadays, volcanic hydrocarbon reservoirs can be found on five continents (Fig. 5) with a significant number of important reservoirs in China, Argentina, and Japan (e.g. Sun et al., 2018). In total, more than 300 discoveries of oil and gas shows and reservoirs in volcanic rocks have been made so far, among which a number of 169 reservoirs contain proven reserves (Zou et al., 2013). However, due to the heterogeneity, complex pore space development and distribution, and the still relatively sparse research in microstructures, reservoir quality prediction is still difficult thus posing a high risk for volcanic reservoir exploration (e.g. Wang & Chen, 2015).

2.2.2. Rhyolitic reservoirs

Volcanic rocks in general occupy approximately 8 % of global outcrop exposures of which rhyolites constitute a major part with about 20 % on a global scale (e.g. Schutter, 2003). A lot of research on rhyolitic hydrocarbon reservoirs throughout the last few years proved that they can provide a prolific source of hydrocarbons (e.g. Sun et al., 2019; Lenhard & Götz, 2011) and, as a consequence, a considerable number of reservoirs worldwide has been discovered and developed (e.g. Schutter, 2003). To foster exploration in rhyolitic hydrocarbon reservoirs, it is especially important to understand their microstructures which in turn is necessary to understand the related porosity as well as storage and transport processes related to fluids. Pre-, syn- and post-volcanic processes determine the formation of these microstructures (Mao et al., 2020).

The most favorable targets considering rhyolitic hydrocarbon exploration are phenocryst-rich rhyolitic lava, spherulitic rhyolites, and perlitic lava. Rhyolitic reservoirs can either be fragmental and glassy pyroclastic deposits or non-fragmental, partly glassy, and partly devitrified lavas. Typically, they are strongly anisotropic (VTI = vertical transverse isotropy), showing variable textures, which leads to complex pore systems (e.g. Wang & Chen, 2015).

Geothermal reservoirs in rhyolitic rocks

Besides several geothermal fields within basaltic and andesitic rocks (e.g. in Mexico, Arellano et al., 2005), rhyolites also play a key role for geothermal reservoirs. For geothermal energy production, fluid flow characteristics are very important, especially for related storage and transport processes. The processes which are related to the motion of fluids are strongly influenced by the microstructures of the rocks and therefore, a good understanding of those rock textures is inevitable (Saubin et al., 2019). A key area for geothermal energy production is Iceland. Although magmatic activity there is mostly basaltic in composition, partial melting and fractional crystallization generates rhyolitic magma at central volcanoes (e.g. Jónasson, 1994). One example is the Krafla volcano, where supercritically heated fluids are stored at the margins of these rhyolitic intrusions and can then be used for energy extraction (Saubin et al., 2019). Porous rock successions favor the circulation of hot fluids which in turn

favor thermal alteration and further fracturing. It was observed by von Aulock et al. (2013), that it is very common that perlitic fracture networks develop in such glassy intrusion margins. They promote on the one hand significant ingress of water and on the other hand permeability is strongly increased due to the high fracture density. The latter enables a better circulation of high-enthalpy fluids, which is the perfect condition for a geothermal resource (e.g. Mordensky et al., 2018a). The fracture network is also strongly related to heat transfer, which is, among others, controlled by the thickness of the intrusion (Annen, 2017). However, originally weak, porous, and high-permeable rocks are more susceptible for mineral precipitation and compaction, which decreases the porosity and reduces permeabilities by >1 order of magnitude (Saubin et al., 2019). Another location for geothermal energy production in Iceland consists of welded ignimbrites, which have been densely compacted into glass and highly fractured. This increase in fracture density causes a weakening of the rock; however, the intense fracturing also creates a high permeability which is advantageous for hydrothermal fluid circulations (Saubin et al., 2019).

2.2.3. Porosity and permeability in volcanic rocks

Porosity in volcanic rocks is strongly dependent on both, lithology, and sequence of eruption processes. The petrophysical characteristics, i.e. porosity and permeability, provide important information for reservoir characterizations. They can be substantially modified during several processes of cooling and post-cooling stages. It was shown by Sruoga et al. (2004) that non-welded ignimbrites and quench-fractured glasses show the highest porosity and permeability values. Glass dissolution leads to an enlargement of sublinear quench fractures and perlitic cracks which results in open spaces that are heterogeneously distributed in the matrix. It was also observed, that even in cases of significant glass alteration, primary features such as quench fractures and perlitic cracks are preserved. Quenched obsidian glasses showed excellent porosity (up to 37.6 %) and permeability values (up to 762 mD) whereas ignimbrites have porosities between 17-30 % and low permeabilities less than 0.1 mD (Sruoga et al., 2004). According to Sruoga et al. (2004) five types of porosities can be distinguished in volcanic rocks:

- quenching-related porosity in dense glass
- ubiquitous glass dissolution-related porosity
- intershard porosity in non- to poorly welded ignimbrites
- secondary porosity generated by tectonic deformation
- intergranular porosity in epiclastic breccia

The origin of primary porosity in volcanic reservoirs can be vesicles and gas pipes, inter- and intra-grain pores, interflow laminar voids and cooling fractures whereby each of them can coexist with each other.

Secondary porosity is created by faults and joint fractures, pores resulting from dissolution or alteration, and pores formed by hydrothermal brecciation (Wang & Chen, 2020).

In general, volcanic reservoir pores can roughly be classified into micropores, small pores with pore diameters of 0.01-0.1 mm, medium pores, and large pores with diameters larger than 1 mm. In most cases of volcanic reservoirs, small pores are the most common (e.g. Sun et al., 2018). It was also shown that high-quality petrophysical parameters, i.e. high porosity and permeability, decrease with burial depth (Wang & Chen, 2015).

Porosity and permeability controls

Whereas a lava rapidly cools right upon emplacement, ignimbrites show a prolonged cooling history because of their extraordinary heat retention capacity (Sruoga et al., 2004). However, it is questionable if this founding is true when comparing ignimbrites and lavas of the exact same composition. According to Sruoga et al. (2004), the processes which occur during the volcanic phases are subdivided into two main stages, which are the pre-emplacement and the post-emplacement stage (Tab. 5). The pre-emplacement consists of vesiculation and fragmentation whereby vesiculation is the most important control on primary porosity and permeability. Especially in the vent, sufficient pore space for releasing gas is created in ignimbrites. The post-emplacement stage is divided into a cooling- and a post-cooling history. The most important influence on primary porosity of pyroclastic rocks during the cooling history is welding. However, due to the disconnected pore systems in those rocks, primary porosity is relatively low even in non-welded rocks but gets reduced further by progressive welding and vapor phase crystallization, whereas primary permeability is generally low. During the cooling history, one of the most advantageous processes for creating pore space is quench fragmentation which results from magma-water interaction. This process leads to a well-connected pore system and associated perlitization further improves permeability. The interaction with fluids also leads to dissolution and alteration of glasses. Porosity and permeability are increased by dissolution while alteration only improves the porosity of a rock when mica and clay aggregates replace the coherent glass. However, generally porosity is reduced by high amounts of clay, which occupies free pore space. Another example of a cooling history process that enhances petrophysical parameters is auto-brecciation. A negative effect on porosity and permeability in the post-cooling stage is mineral precipitation, since formerly open pore space can get partially to totally occluded or even become sealed (Sruoga et al., 2004). The ingress of freshwater and the glass-water interaction is strongly controlling the equilibrium between dissolution and precipitation (de´Genaro et al., 2000). Processes during the post-cooling history, which can enhance porosity and permeability, are hydrothermal alteration and the formation of tectonic fractures, which can create hydraulic fracture networks (Sruoga et al., 2004).

Tab. 5: Processes of porosity increase or decrease in SiO_2-rich volcanics during volcanic stages after Sruoga et al., 2004.

STAGE	PROCESS	
Pre-emplacement	vesiculation fragmentation	
Post-emplacement	cooling history	welding devitrification feldspar alteration silicification vapour-phase crystallization quench fragmentation and perlitic fracturing glass alteration
	post-cooling history	hydrothermal alteration weathering tectonic deformation

Perlitic fracture formation in this model (Tab. 5) is assigned to cooling history processes, indicating crack development during cooling of a lava or pyroclastic sequence. This is in contrast to assumptions from other authors (e.g. Lacy 1966) who associated perlitic fracturing with post-cooling history processes, suggesting hydration at temperatures much below the glass transition temperature to be the underlying formation mechanism. This issue will be discussed in detail in subsequent chapters of the thesis.

Porosity in rhyolitic lavas and ignimbrites - general

Considering their petrophysical characteristics, heterogeneity and a complex microstructure typically denote rhyolitic rocks. However, they are porous in many cases and hence may provide significant pore space for representing moderate to good reservoirs. Porosity in phenocryst-rich rhyolites is provided in form of cleavages, cavitational and shear fractures, embayment and intracrystalline sieve pores. Significant pore space in spherulitic rhyolites is found in radiating micropores and interspherulite pores. In perlitic lavas, perlitic fractures make up the major pore space. For all types of microstructures within rhyolites, pore-size distributions are dominated by small pores <15 µm, whereby small and large pores (>300 µm) contribute the most to the total volume (Mao et al., 2020). The primary porosity in rhyolites may reach values of up to 25-30 %, which can even get increased by 3 – 5 % by dissolution (Sun et al., 2018). Conversely, low-grade metamorphic processes such as mineral overgrowth or carbonate mineral cementation can reduce the pore space by up to 20 % (Sun et al., 2018).

Compared to other non-volcanic reservoir rocks like sandstone, lava and ignimbrites in general show a relatively slow decrease in porosity with burial depth, and pore space can be well preserved in rocks which have a quartz-poor groundmass as they are solidified by cooling. In many cases (e.g. in the Songliao Basin, China), lava and ignimbrites represent the best reservoir rocks below a certain burial

depth as their porosities and permeabilities significantly exceed those of rocks from non-volcanic sequences, which suffered more intense compaction and cementation at equal depths and/or temperatures (Wang & Chen, 2015). However, for silica-rich rocks with significant amounts of quartz it has to be considered that this behavior changes at depths where temperatures higher than 300 °C are reached as the point of ductile deformation of quartz is between 300 – 350 °C (Sibson, 1977).

Porosity in rhyolitic lavas and ignimbrites with perlitic fractures

Perlitic cracks are commonly found in many rhyolites and proved to provide good reservoir space in many cases. The pore space in perlitized rocks is created by the apertures of perlitic fractures. A case study on perlitic lavas showed effective porosities between 2.9 and 31.9 % with mean and median porosities of 10.9 and 9.3 %, respectively, and moderate permeabilities which vary from 0.002 up to 213.80 mD (Mao et al., 2020). The results for permeabilities contrast with the finding from Sruoga et al. (2004) who suggested elevated permeabilities in perlitic fractured rocks of up to 762 mD. For ignimbrites, values from 0.002 – 164 mD were found (Sruoga, et al., 2004), which matches with permeabilities reported by Mao et al. (2020).

In general, perlitic textures belong to the most unstable structures which can be found in rhyolites. They get easily modified by several post-emplacement processes, especially by alteration or further fracturing (e.g. Denton et al., 2009), which can remarkably improve the secondary porosity. However, pore space can also get significantly reduced by mineral precipitation along the fractures (e.g. Sruoga et al., 2004).

2.2.4. Overburden pressure effect

Elastic moduli increase with burial depth, however, the Young´s modulus of lava and welded ignimbrites is less influenced by overburden pressure than for sedimentary rocks, which show a strong increase of the Young´s modulus with depth. It was observed that below depths of approximately 3000 m, petrophysical parameters of sedimentary rocks decrease with further depth whereas they stay mostly unchanged in volcanic rocks and as a matter of fact, both porosity and permeability are generally greater in volcanic successions than in sedimentary rocks below depths of 3000 m (Wang & Chen, 2015). Nevertheless, the effect of ductile quartz-deformation at temperatures higher than 300 °C has to be considered (Sibson, 1977). Other pyroclastic rocks, such as tuffs, show a behavior similar to sandstones, since both consist of clasts and matrix, but tuffs are generally of poorer reservoir quality due to dense compaction and related cementation (Wang & Chen, 2015).

Porosity preservation is strongly aided by resistance to overburden pressure, which depends on rock type (Fig. 6). Shallow samples (upper line) show higher porosities than deep samples (lower line) whereby the differences increase from lava over ignimbrite to pyroclastics. Pyroclastics show the

highest change, whereas lava changes least in reservoir parameters from shallow to deep, a result of the lava's groundmass preservation of primary porosity (Wang & Chen, 2015).

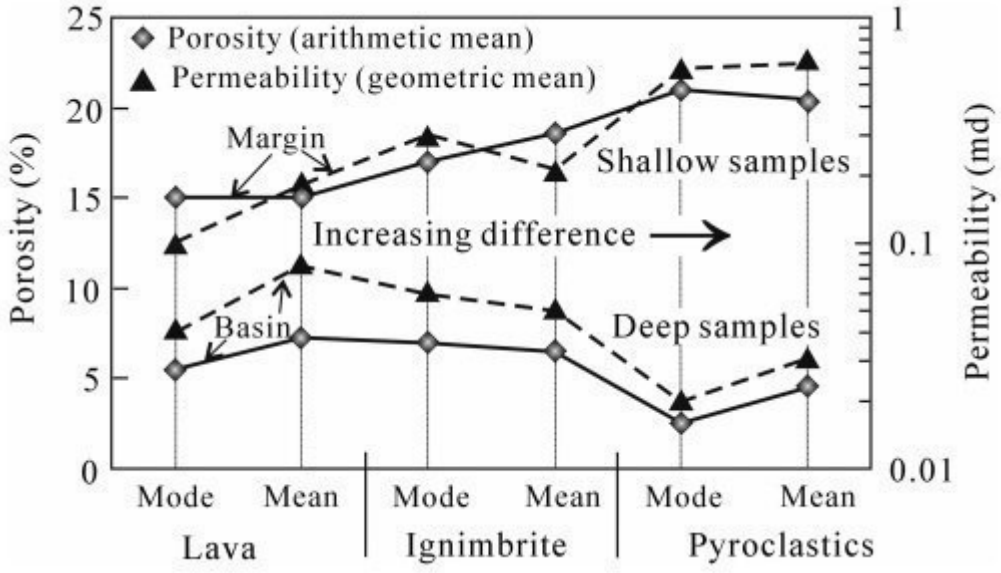

Fig. 6: Influence of overburden pressure on different volcanic rocks (Wang & Chen, 2015).

2.2.5. Eruption environment influence on volcanic reservoirs

For exploring high-quality reservoirs, the prediction of volcanic reservoirs is of special importance. The influence of water has been mostly ignored in the characterization of volcanic reservoirs due to the assumption, that subaerial and subaqueous eruptions are similar. However, it has been shown that the eruption environment has significant impact on reservoir quality (e.g. Dong et al., 2012) as the difference between the two eruption media (water vs. air) influences the products of an eruption process (Xian et al., 2018). Considering primary pores such as vesicles, intergranular pores, or primary fractures, an increasing water depth may inhibit the exsolution of volatile components, which results in a decrease in porosity. Vesicle development, for instance, can get retarded by high hydraulic pressures in subaqueous environments aggravating volatiles escape. Therefore, a subaerial environment is more favorable for vesicle formation which in turn facilitates ease of hydrocarbon migration there (Run et al., 1996). Magma-water interaction also proves a key parameter when it comes to quenching and the development of related structures like quenching fractures and perlitic cracks, which are promoted by condensation and contraction (Xian et al., 2008). A case study on two depressions with the same rock constituents within the same basin showed that the reservoir quality is strongly dependent on the volcanic eruption environment: One depression consists of rocks from a subaerial eruption without any water involved, whereas the rocks from the other depression originated from a subaqueous eruption. The difference in porosity between the two is approximately 7 % where the higher porosity is achieved in rocks from the subaerial eruption (Zou et al., 2013; Xian et al., 2008). Further, magma-water interactions and quenching are strongly related to the eruptive

vent and water depths. A deep vent therefore shows elevated hydrostatic pressures which may suppress the exsolution of volatiles (Xian et al., 2018). However, magma-water interactions in shallow water are generally favorable as the number and connectivity of matrix pores and fractures get increased (Xian et al., 2018).

Secondary porosity and especially pore space, which results from dissolution or devitrification, is also influenced by the impact of the eruption environment on primary porosity. For instance, the formation of primary pores and fractures may get improved by an eruption in shallow water. This can increase matrix pore space, which may in turn create space for early cement growth and enable late fluid activity, which favors the formation of secondary dissolved pores (Mathisen & Mcpherson, 1991).

2.3. Material sciences

Due to certain outstanding properties like high-temperature stability, resistance against corrosion and oxidation, optical, thermal, and electrical characteristics, and their inherent brittleness, ceramic and glass are widely used as structural components and machine parts in many industrial and technical applications. The resistance against tensile stress implies potential limitations for brittle materials and is strongly affected by two factors, which are fracture toughness and the sensitivity of their strength to the presence of defects. The material property “fracture toughness” describes the resistance of a material to crack propagation (Bermejo & Danzer, 2014). The occurrence of cracks is of special importance in material sciences when it comes to brittle materials, since the propagation of those cracks in most cases leads to unexpected and catastrophic failure of a component (Bermejo & Danzer, 2014). Therefore, fracture mechanics play an important role in this field, and a lot of research related to fracturing of those materials has been done to learn more about fractures and the strength of brittle materials in order to be able to better foresee or rather avoid the occurrence of cracks (e.g. Bermejo, 2020).

Material science distinguishes between crack formation and crack propagation when talking about fractures in brittle materials since these two parameters cannot be described synonymously. This consideration might also be helpful to get a better and more complex understanding for perlitic fracturing, since a fracture process in most cases is not terminated right after the crack formation but proceeds over time during the process of crack propagation.

2.3.1. Crack formation

Inherent brittleness is related to the relatively immobile dislocations and the absence of plasticity during the fracture process (e.g. Davidge, 1979). In general, critical fractures originate from random occurrences of microstructural defects, which at first act as stress concentrators that allow the initiation of cracks and subsequently, they may extend and result in fractures. Crack formation is

strongly related to the inherent strength and the fracture toughness of the material, and both are influenced by the texture of the material (Bermejo & Danzer, 2014).

2.3.2. Crack propagation

Generally, brittle fracturing is controlled by the extension of small flaws or defects. For describing the behavior of fractures in brittle materials, assuming a linear elastic material behavior, the Griffith-Irwin energy balance criterion (Eq. 1) is used, which states that a crack will propagate normal to the crack plane under uniform applied tensile loading, if a certain combination of applied stress σ and crack length a reaches a critical value (Griffith, 1920). E' is the modulus of elasticity, E, for the plane stress and $E/(1-\nu^2)$ for the plane strain conditions, ν is the Poisson´s ratio, Γ_c is the absorbed or consumed energy per unit area of crack advance and Y is a dimensionless constant depending on crack configuration, geometry, and loading situation:

Eq. 1: Griffith-Irwin energy balance criterion

$$\sigma(\pi a)^{1/2} = \frac{1}{Y}(E'\Gamma_c)^{1/2}$$

According to Griffith´s criterion, fracture toughness scales with strength and it is inversely proportional to the square root of the critical crack size. This is called size effect and implies that at a given stress level, an increasing crack size lowers the strength and fracture toughness of the material (Griffith, 1920). It is difficult to reach high values of yield strength in brittle materials like glasses and ceramics; therefore, energy dissipation due to plastic flow is mostly impossible. As a consequence, the energy which is required for crack propagation is consumed in new fracture surface formation and the propagation of such cracks then leads to failure of the material (Bermejo & Danzer, 2014).

The resistance to crack propagation can be described by fracture toughness, which is a material property measured normal to the direction of applied stress. Another essential parameter for crack propagation is the stress intensity factor, which characterizes the stress field near a crack tip. In general, the requirement for crack propagation is granted if the stress intensity factor at the tip of a crack equals or exceeds the material toughness (e.g. Bermejo & Danzer, 2014).

The critical defects or cracks can be very different: volume flaws acting as fracture origins can be large pores, grains, or inclusions; at the surface, contact damage and grinding scratches can serve as typical fracture origins. The measured stress at the fracture is therefore strongly dependent on the critical defect size and in return, the strength of a brittle material also depends on the size of the largest or most critical defect (Danzer, 2006). Due to the fact that the strength of silica glass is strongly controlled by the presence of cracks in the glass surface, a removal of cracks or rather making the glass completely free of cracks would enhance its yield strength significantly (Wiederhorn et al., 2011).

2.3.3. Influence of environmental conditions on brittle materials

Another important influence on crack propagation are environmental conditions such as humidity and temperature, and two essential related mechanisms are subcritical crack growth (e.g. Bermejo, 2020) and the swelling effect (Wiederhorn et al., 2011). Environmental conditions, especially humidity, are naturally related to the presence of water, which has to be considered when discussing fracture mechanics. Considering environmental influences on the behavior of brittle materials is of special importance when it comes to crack formation and propagation in volcanic glasses, since volcanic events are inevitably associated with different environmental conditions, e.g. humid environments, the presence of water/fluids, and/or strongly varying temperatures. Since perlitic fracturing is strongly related to hydration or rather an ingress of water, the effect of humidity and water on brittle materials will be examined in more detail from the point of material sciences within the next chapters.

Subcritical crack growth

Subcritical crack growth (SCCG) or delay fracture is a significant and, at ambient temperature, probably the most important fracturing mechanism for brittle materials. It enables stable crack growth under an applied load and results in a strength decrease over time, which inadvertently reduces a material´s load bearing capability (Bermejo, 2020). SCCG is strongly promoted by elevated temperatures and moisture contents (Wiederhorn, 1974). In geoscientific and material sciences publications, many different mechanisms for delayed fracturing are discussed, which include thermally assisted breaking of bonds at crack tips (Schoeck, 1990), stress enhanced corrosion (Wiederhorn, 1974), hydrolysis of silica bonds (Wiederhorn et al., 2011), the diffusion of water within the crack (Wakabayashi & Tomozawa, 1989), etc. However, a direct chemical attack of the environment on the crack tips, for instance from the presence of acids, proved to have the strongest support in silicate glass (e.g. Michalske & Freiman, 1983). Strength measurements related to subcritical crack growth behavior were tested in different environments and showed that the highest strength values can be reached in a quasi-inert environment. Strength values in oil are similar for low stress rates. At intermediate stress intensities, the crack growth rate is dependent on the diffusion rate of water molecules delivered to the crack tip. In general, SCCG of a glass immersed in oil changes in different environments and is also affected by temperature. A material which is immersed in water yields 50 % lower strength values. This implies that the crack growth rate in water is more than two orders larger than in ambient air (Bermejo, 2020).

Effect of water on the strength and toughness of silica glass

As discussed earlier, water exerts a detrimental effect on the strength of silica glass and proves to be the key accelerant for slow crack propagation (Wiederhorn, 1967); however, there has been no universal agreement on the causes of this effect. The assumption of water molecules breaking Si-O-Si

bonds at the crack tips into silanol groups is the most common and widespread underlying lynchpin for water acting as a weakening agent and is called “stress corrosion” (Michalske & Freiman, 1983). In the course of research on SCCG it was unanimously agreed upon that a glass breaks more rapidly under load when water is present due to stress-enhanced interaction between water and glass. In general, the diffusion of water into silica glass is described by a diffusion-reaction process in material scientific work on brittle materials (e.g. Doremus, 1995), where water molecules react with Si-O bonds to form -SiOH groups, a technical finding which is consistent with findings on hydration in volcanic glass by the volcanology community (e.g. Marshall 1961) that generally identify water as the main driver for stress corrosion. However, it has been shown that in some cases the strength of silica glass increased when soaked in water (e.g. Ito & Tomozawa, 1982). A possible explanation lies in the closer examination of the crack tips and how they control the crack growth. It is suggested by Wiederhorn et al. (2011) that this strengthening effect occurs due to the penetration of water into the area that surrounds the crack tip and the adjacent crack walls, which then causes compressive stress at the crack walls which in turn leads to negative stress intensity factors at the crack tips (Wiederhorn et al., 2011) and a swelling related to an ion exchange (Langford et al., 1979).

By comparing soaked and freshly abraded glasses it was found that the differences in strength results from the zones of swelling around the crack tip (Wiederhorn et al., 2011). This phenomenon is called “swelling effect” and occurs in aged glass but not in freshly abraded ones, which were previously exposed to an aqueous environment. Therefore, the latter show no swelling along the fracture surface and hence no toughening (Wiederhorn et al., 2011). For hydrous glass it was found by Waurischk et al. (2020) that crack growth in vacuum occurs at larger stress intensity factors because water acts as a toughening agent, whereas at ambient air, crack growth in hydrous glass occurs at lower stress intensities compared to dry glass. Consequently, ambient water proves to be a strong weakening agent which overrides the toughening effect of dissolved water (Waurischk et al., 2020).

2.3.4. Thermal shock behavior of silica glass

Rapid heating and cooling lead to high thermal stress in glass due to its brittleness, which can ultimately result in failure of the material. This phenomenon is called “thermal shock” and plays an important role in material sciences, especially for brittle materials. Thermal shock is caused by quenching and thereby the total surface including the edges and corners is put under tensile load (Harrer & Danzer, 2011). As rapid cooling is also of great concern for lava and ignimbrites, the consideration of this aspect from the material science perspective might be gainful.

Damages or defects at the surface or edges of the material do not only influence crack growth in general but are also strongly decreasing the thermal shock resistance. Generally, cooling of a material leads to the development of thermal strain and an inhomogeneous temperature field causes localized, differential thermal expansion. Constraining this expansion can then lead to the development of

thermal stress and if this stress exceeds the strength of the glass, cracks can propagate. Failure corresponds to ΔT_c which is the critical temperature difference for a crack to propagate. This depends on the crack size as well as on the material itself, whereby ΔT is the temperature change during cooling (e.g. Danzer et al., 2010). It was further found that fractures created by thermal shock in most cases start at edges or edge defects and again, a size effect can be seen, which implies that thermal shock resistance is decreasing with the size of the specimen. To heal surface cracks and consequently increase the material´s strength, which in turn leads to enhanced thermo shock resistance, annealing of the specimen is applied (Harrer & Danzer, 2011). Thermal shock can occur due to local heating or cooling of a glass, though, cooling has the stronger effect. Further, the thermally induced stress disappears again as soon as the temperature difference has decreased to zero, i.e. thermal stresses are of a temporary nature only (Jebsen-Marwedel & Brückner, 2011).

3. Methods

3.1. Samples

This thesis is based on geometrical, optical, and geochemical investigation and examination of 35 samples from 24 different locations, which are spread over different areas of the globe (Fig. 7). Therefore, this study on perlitic textures is not restricted to a particular region but is rather based on methodical investigations on widely distributed samples from different geological periods to cover a broader spectrum of textural variations. Available samples are mostly stored in the Center for Volcanic Textures (CVT) in the Humboldt-Building (University of Freiberg, DE[1]). Samples come from different projects of previous studies or were collected during past field trips. Therefore, there is no uniform nomenclature, but sample names are inherited. Most sample designations follow the principle dd-mm-yy-nr (or d-m-y-nr) and thus provide information about the year of sample collection. A list of all samples and several additional information can be gleaned from Tab. 6.

The geologic ages of the rocks range from Ediacaran (Proterozoic) to Late Quaternary and the boundary between historic ("old") samples and geologically younger rocks for certain considerations is set at the transition from the Mesozoic to the Cenozoic. Therefore, old samples are often referred to as "pre-Cenozoic" and young samples as "Cenozoic". The rocks can be divided into silica-rich lava and ignimbrites, whereby 18 samples are from solidified lavas, 13 are from ignimbrites and 4 obsidians.

Fig. 7: Location map of investigated samples.

[1] https://tu-freiberg.de/geowsam/ausstellungen/centre-of-volcanic-textures-cvt

Tab. 6: List of all analyzed samples, sample information & methods; green: obsidian, blue: lava, orange: ignimbrite; TSA= Thin section analysis, TG= Thermo Gravimety, DSC= Differential Scanning Calorimetry (green: results inherited from previous study), EMP= Electron Micro Probe, IA= Image Analysis (contains line densities, specific crack areas, crack distances, histograms of directions; green: additional cell size calculation) Poro= Porosity with Triple Weight Method (green: additional measurement with Helium Pycnometer), Perm= Permeability, CT= Computer Tomography, TS= Thermo Shock; DA= Master thesis; BA= Bachelor thesis.

Nr.	Sample	Location	Age	Rock type	Perlite characteristics	TSA	TG/ DSC	EMP	IA	Poro	Perm	CT	TS	Literature
1	4-8-97-7	USA, Big Southern Butte, California	Neogene	Obsidian lava with microlites, large lithophysae	no perlitic fractures, pure glass	✓	✓							Spear & King, 1982
2	24-7-97-2	USA, Big Glass Mtns., NE-California	Holocene	Obsidian lava with microlites	no perlitic fractures, pure glass								✓	Fink, 1983
3	3-12-04-2	Armenia	Pleisto-cene	Obsidian lava with microlites	no perlitic fractures, pure glass								✓	Karapetian et al., 2001
4	5-11-07-3a	Argentina, west of San Antonio de los Cobres	Miocene	Apache Tears (Obsidian) in perlite (see 5-11-07-3b)	no perlitic fractures, pure glass	✓	✓							Breitkreuz et al., 2021
5	1-8-97-3b	USA, Beaver Head mountains, Rattlesnake Point, California	Quarter-nary	rhyolitic perlitic lava flow, flow-banded, spherulitic bands	very fine cracks, partially opened, evenly distributed cracks and crack size	✓			✓	✓	✓			Branney et al., 2008; Ellis et al., 2013
6	9-9-01	Italy, Eolian Islands, Vulcano, Lentia	Quarter-nary	lava, glassy, strongly vesicular, flow banded	highly porphyritic, highly porous, cracks highly deformed and not evenly distributed, hard to recognize	✓			✓	✓				De Astis et al., 2013
7	10-12-20-a,b	Greece, Milos	Late Quarter-nary	Perlitic, vesicular obsidian lava	very fine cracks, hydration rims visible under microscope	✓	✓	✓	✓	✓				Lampropoulou et al., 2020; Kaufhold et al., 2014

8	**1-8-97-1**	USA, NW side of Snake River Plain, Idaho [underneath Kilgore tuff unit]	Neogene	Rhyolitic perlitic lava with small and large spherulites, partly open	evenly distributed cracks and crack size	✓			✓					Branney et al., 2008; Ellis et al., 2013
9	**3-8-97-1**	USA, Kelly Canyon	Neogene	probably top breccia of rhyolitic lava, perlitic glass with obsidian remnants, Apache Tears	fractures visible, partly mineralization on rims, partly opened fractures	✓	✓		✓					Morgan & McIntosh, 2005
10	**5-11-07-3b**	Argentina, west of San Antonio de los Cobres	Miocene	greenish/grey perlite with flow texture marked by dark grey lines	highly perlitized, fractures evenly distributed, clay minerals on rims	✓	✓	✓	✓	✓				Breitkreuz et al., 2021; Willson et al. 1999
11	**27-6-14-1e**	Mexico, west of San Luis de Potosí, San Miguelito	Oligo-cene	silica rich lava, lithophysae-rich domain	perlitic fractures, partly altered, different generations of fractures recognizable	✓	✓		✓	✓				Torres-Hernández et al., 2006; Torres-Sánchez et al., 2019
12	**10-12-08-2a**	Armenia	Cenozoic	silica rich lava brecciated with Apache tears	very fine cracks, no alteration	✓			✓					Gevorgyan et al. 2018, 2020
13	**13-12-04-01**	Northern Chile	Cenozoic	flow-banded rhyolitic lava with large spherulites	fully devitrified, high amount of clay minerals, fractures visible with naked-eye and limited to specific areas	✓			✓	✓				
14	**Tokai 24-1**	Hungary, Tokaj Mts.	Cenozoic	perlitic glassy lava	cracks visible with naked-eye, evenly distributed, partly opened	✓			✓	✓				Zelenka et al., 2012
15	**Tokai 24-2**	Hungary, Tokaj Mts.	Cenozoic	perlitic glassy lava	cracks visible with naked-eye, evenly	✓			✓	✓				Zelenka et al., 2012

					distributed, partly opened							
16	6-4-01-1a	Germany, Saxony, Triebisch Valley, Meißen, Kleiner Königssee	Late Carboniferous	rhyolite glass („pitchstone"), spherulites and elongated perlitic cracks	fine cracks evenly distributed; alteration limited to certain areas	✓	✓		✓	✓		Breitkreuz et al., 2021; Hoffmann et al., 2013
17	C 28-01	Germany, Saxony, Triebisch valley, Garsebach	Late Carboniferous	green perlitized pitchstone	evenly distributed cracks and crack size, different generations of fractures recognizable	✓	✓		✓	✓		DA Czoßek, 2002; Hoffmann et al., 2013
18	TT-2-B-3	Germany, Meissen	Late Carboniferous	rhyolitic pitchstone lava	perlitic glass, subsequently crystallized, highly devitrified, very fine cracks, no alteration	✓			✓			BA Vorreier, 2017; Hoffmann et al. 2013
19	TT-6-B-1	Germany, Meissen	Late Carboniferous	rhyolitic pitchstone lava	perlitic glass, subsequently crystallized, highly devitrified, cracks vary in size and alteration in each zone	✓			✓			BA Vorreier, 2017; Hoffmann et al. 2013
20	TT-8-B-3	Germany, Meissen	Late Carboniferous	rhyolitic pitchstone	perlitic glass, subsequently crystallized, highly devitrified	✓			✓			BA Vorreier, 2017; Hoffmann et al. 2013
21	Ad-18	Germany, Garsebach, Meissen Volcanic rock complex	Late Carboniferous	phreatic lava breccia	phreatic breccia which developed from hot porphyritic lava; matrix is hematitic; angular obsidian fragments are fully perlitized							DA Czoßek, 2002; Hoffmann et al., 2013
22	8 Ta PS	Germany, Tautendorf, Leisnig Porphyry	Lower Permian	pitchstone, sub-volcanics	evenly distributed cracks and crack size, highly altered	✓			✓			Götze et al., 2020

23	5-12-04-3	El Salvador	Miocene-Quarter-nary	high grade, parataxitic ignimbrite, welded, glassy matrix with HTCDs	evenly distributed cracks, very fine, hardly any alteration	✓	✓	✓	✓	✓		✓		Rapprich et al., 2010
24	1-8-97-7b	USA, Idaho, Reno Point, East of Howe, Blue Creek Tuff	Neogene	Parataxitic high grade pyroclastic ignimbrite, lower vitrophyric, perlitic domain; partially spherulitic	evenly distributed crack size, perlitization limited to specific areas, cracks widely opened, high amount of smectite on cracks	✓			✓					Morgan, L.A., 1992; Branney et al., 2008; Ellis et al., 2013
25	11497	Germany, Zwickau, Schedewitz	Lower Permian	Silica Rich (SR)-type welded flow tuff, vitrophyre	uncompacted matrix, perlitization limited to fiamme	✓			✓					Repstock et al. 2019
26	11510	Germany, Hohendorf / Oelsnitz	Lower Permian	SR-type welded flow tuff, vitrophyre	perlitization mainly in fiamme but also visible in some matrix areas, mineralization on rims	✓			✓					
27	P 1500a	Germany, Beharrlichkeits-schacht, Grühna	Lower Permian	SR-type welded flow tuff, vitrophyre	perlitization in matrix and fiamme, highly altered	✓			✓					
28	SS 16782	Germany, Bürgerschacht, Zwickau	Lower Permian	SR-type welded flow tuff, vitrophyre	perlitization mainly in fiamme but also visible in some matrix areas, mineralization on rims	✓			✓					
29	26-6	Germany, Zwickau, construction site	Lower Permian	SR-type welded flow tuff, Planitz Ignimbrit from Chemnitz Basin, vitrophyre	weakly devitrified, cracks extremely small	✓			✓					MA Franziska Heuer, 2014; Repstock et al., 2019
30	RS 3636	Germany, Obermühlbach	Lower Permian	Vent system, partially vitrophyric	weakly perlitized and altered	✓			✓					Löcse et al., 2020

31	**44.20 I**	Germany, Ebersbach, drill samples	Lower Permian	Rochlitz-α Porphyr; welded ignimbrite with perlite cracks	small cracks, hard to recognize	✓			✓				Hübner et al., 2021
32	**44.20 II**	Germany, Ebersbach, drill samples	Upper Carbon.-Lower Permian	Rochlitz-α Porphyr; welded ignimbrite with perlite cracks	small cracks, hard to recognize	✓			✓				Hübner et al., 2021
33	**44.20 III**	Germany, Ebersbach, drill samples	Upper Carbon.-Lower Permian	Rochlitz-α Porphyr; welded ignimbrite with perlite cracks	relatively small cracks, evenly distributed	✓			✓				Hübner et al., 2021
34	**Fl 93**	Germany, Flechtingen-Roßlau Block	Upper Carbon.-Lower Permian	Flechtingen Ignimbrit, welded ignimbrite	perlitization limited to crystal grains and fiamme	✓			✓	✓			DA Balthazar, 2001; Geißler et al., 2008; Luthardt et al. 2020
35	**JK 20**	Africa, NE Egypt, Eastern Desert, Ras Gharib	Edia-caran	lithic-rich & crystal-rich, welded ignimbrite	preservation of fracture structure by mineralization	✓			✓				DA Zimmermann, 2010; DA Stopora, 2010; Breitkreuz et al., 2010

3.2. Sample preparation and analytic methods

3.2.1. Thin section analysis

The basis for textural investigations is transmitted-light microscopy of selected thin sections using the "Axiolab A1" microscope of the Carl Zeiss Microscopy GmbH. Pictures of thin sections are taken with the "AxioCam ERc5s" digital microscope camera, which provides precise monitoring and documentation of textures and are processed with the program "AxioVision". For this thesis, 32 thin sections are analyzed with special focus given to their textural characteristics. Most rock samples get soaked with colored epoxy resin before the preparation of the thin section, thus pore spaces are indicated as light blue areas. Based on thin section analysis, the samples get classified according to observed characteristic textural features, remarkable differences, and similarities amongst the individual thin sections. For the purpose of analyzing fracture in more detail, the open-source software "Inkscape" is used, which is a professional program for the editing of vector graphics. Using this program, the individual fracture structures can be tracked in order to obtain images, which make the fracture systems visible. This is of particular interest for a classification and to get an understanding of the fracture networks but also for stochastic geometry analysis.

3.2.2. Computer tomography (CT)

Computer tomography or CT is an x-ray-based imaging method, where multiple x-ray measurements are conducted from different angels. The signals of those measurements are then computer-processed and converted into a full 3D image of the sample. For the purpose of investigating the 3D structure of the fracture network, micro-CT imaging was applied with a standalone-mCT instrument and at a synchrotron beamline at the Department of Petroleum Engineering (Chair of Reservoir Engineering) at the Montanuniversitaet Leoben. CT uses ionizing radiation, i.e. photons which are emitted from a source and subsequently pass through the sample. An electronic detector array records a pattern of densities and creates an image of a slice. The beam rotates around the sample such that multiple x-ray projections pass through the rock (Caldemeyer & Buckwalter, 1999). Contrasts between pore space, fluid phases, and grains result in different x-ray attenuations whereby the magnification is generated by the geometry itself. The setup consists of a standalone-system from the company ProCon X-Ray and measurement parameters can be seen in Tab. 7. The commercial software XAid, which uses a unique statistical interative reconstruction module with a semi-automated workflow, is used for processing of the obtained images.

Tab. 7: Measurement parameters for micro-CT measurements.

X-ray tubes	up to 300 kV microfocus
min. focal spot	0.5 µm
Detector	up to 16 MP
Pixel sizes	0.27 µm to 200 µm
max. scanspeed	< 10 seconds per part
Axes	up to 8
Spatial Resolution	0.4 µm
Scanning time	max. 1920 number of angles 0.5 - 8 hours depending on the settings and desired quality
Detector panel	1980x1536
Maximum sample size	4x4 cm for a resolution of 20 µm

3.2.3. DSC/TG analysis

A thermal analysis technique is an experimental method, which is based on the measurement of changes in a physical or chemical property of a system as a function of increasing temperatures (Gordon, 1960). Differential Scanning Calorimetry (DSC) and Thermo Gravimetry (TG) are two of the most common thermo-analytical techniques. The simultaneous DSC/TG analysis provides the option of a direct correlation between thermal effects and weight loss. During DSC, the change of the difference in heat flow rate [mW/mg] to an analyzed sample and to a reference sample is measured while temperature is increased (Höhne et al., 2003). The thermogravimetric analysis (TG) is applied in order to determine the changes in weight [%] or rather the weight loss as a function of temperature (Coats & Redfern, 1963). Both measurement systems only operate if a temperature difference is present, which directly results in a heat flow difference. DSC/TG measurements were conducted on 6 samples, which were first pestled into a coarse-grained powder and afterwards analyzed using a "NETZSCH STA 409 PC/PG" thermoanalysis device from the Institute of Ceramics, Refractories, and Composite Materials (TU Freiberg) and evaluated with the "Proteus" software. For each analysis, an amount of 20-23 mg of crushed sample material was analyzed. At ambient air, a heating rate of 10° K/min was used in a temperature interval from 20 to 1000 °C.

3.2.4. Electron microprobe analysis (EMP)

Based on the characterization of the samples by thin section analysis with a transmitted-light microscope, three samples are selected for further investigations using an electron microprobe (EMP). This method is used to obtain further information on hydration behavior and chemical composition of certain samples. The results reported here are obtained using the JEOL-JXA-8230 electron probe microanalyzer at the Institute for Material Sciences and Material Technologies at TU Freiberg. Polished thin sections are selected based on several exclusion criteria and prerequisites: (1) little to no microlites, (2) little to no alteration, (3) clear and intact fractures with a high sphericity, and (4) an even (homogeneous) distribution of fractures throughout the whole thin section. The microprobe is used

for the analysis of main- and secondary elements. For the purpose of this thesis, it is used to assess the change in elemental composition and chemical changes in the volcanic glass from the rim or even slightly beyond to the center (core of a fracture). The microprobe detects wavelength-dispersive X-rays, which are characteristic for each measured chemical element. Weight percentages are calculated from intensities and then compared with intensities of the same element detected in a standard, i.e. calibration material, based on which it is possible to calculate atomic weights and structural formulas. During the measurement, an acceleration voltage of 15 kV, a beam current of 20 nA and an emission power of 7.1 µA are used. The chosen beam diameter for the analysis of glasses is 10 µm.

Calibration measurements on 13 standard samples were performed before the actual analysis started. The Table of standard samples and calibration results can be found in the electronic Appendix.

3.2.5. Comparison to artificially produced glasses

As it is hardly impossible to reconstruct perlitic fracture formation retrospectively, an attempt was made to find a comparable, artificially produced material with similar fracture behavior and similar textures. It turned out that curved fractures are a rare phenomenon in industrial glasses and that perlitic fracturing in general is not known in material sciences. However, an example of an artificially produced glass was found which shows comparable structures. This kind of glass is called “crackled glass“, also known as “Craquelé glass” (Fig. 8). It is not an industrial glass sensu stricto, but a mouth-blown glass which consists of silica sand, sodium carbonate, and limestone sand. The hot, clear melt, which at this point does not yet have any structures, is blown into a cylinder and is then cut open into planar sheets of glass, which are subsequently immersed in a barrel with cold water. The "crack-like" structure is thereby created by the induced temperature difference. The crackled glass is not in fact broken through but consists of its characteristic structure of surface cracks which are created by this process of quenching the hot glass with water, which at this point has a temperature of approximately 500 °C. The glass is produced and all information is provided by “Glasshütte Lamberts Waldsassen Gmbh”.

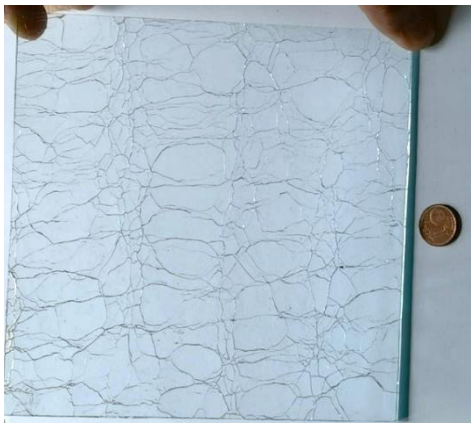

Fig. 8: Crackled glass provided by Lamberts Glashütte.

3.2.6. Thermo shock experiments

Thermo shock experiments were performed on two obsidian samples (24-7-97-2 and 3-12-04-2) at the Chair of Structural and Functional Ceramics at the Montanuniversitaet Leoben. For these experiments, the samples, which were totally fracture- and inclusion-free with only small amounts of microlites, were cut into cubes with dimensions of 4x4x8 cm. The cubes were heated for one hour in an oven at a temperature of 300 °C. Afterwards, they got immersed in a barrel of cold tap water (~15-20 °C) to achieve an artificial thermo shock effect. The samples were then dried and impregnated with an UV-fluorescing oil in order to create a better visibility of the produced cracks under UV light.

3.2.7. Stochastic geometry and image analysis

Stochastic geometry and image analysis provide methods to analyze random structures in form of image data. In many scientific fields, automatic and quantitative methods are inevitable to study such huge amounts of data. In the field of geosciences, image analysis can be a useful tool when it comes to, e.g. satellite photographs, geological maps or, as in this case, microscopic thin section images (Chiu et al., 2013).

The images are available as a pixel array, and a software then determines important features of the images and performs statistical procedures automatically (Ohser, 2018). This approach provides an additional way to classify and quantify the fracture systems in more detail, using statistical method of image analysis. For the evaluation, a subdivision was made into sublinear and rounded (perlitic) cracks, which are genetically referred to as “primary” and “secondary”, respectively. In some samples, fractures were observed which could not definitely be assigned to either of these two groups and which were therefore assigned to a third system termed “unknown”. In following chapters and for the reason of illustration, the perlitic, sublinear, and unknown fractures are depicted as green, red, and orange, respectively.

Line, fibre, and surface processes

Fibre and surface processes are quantified by stochastic models, which are concerned with the study of fibres, surfaces or fragments of surfaces that are distributed at random on a plane or in space. Considering the fracture networks as a fibre or surface process, basic characteristics of such models, i.e. intensity measures, line densities, and rose diagrams of direction can be computed. In this way, a total of 111 thin section images from all lava and ignimbrite samples (exept for fracture-free obsidians) were analyzed, which have been evaluated according to their fracture networks beforehand.

The line density L_A can be described as the mean line length per unit area. For the case of isotropic fracture structures, the specific crack area S_v can be stereologically inferred from L_A (Eq. 2). S_v in such cases represents the mean total area of all plane pieces, which intersect a unit cube (Chiu et al., 2013).

Eq. 2: Formula for calculation of specific crack area S_v from line density LA

$$S_V = \frac{4 * L_A}{\pi}$$

Rose diagrams (directional histograms capturing the distributions for each fracture system by azimuth) were also computed by the software. Results can be interpreted as a directional distribution of a randomly selected line within the line process (Chiu et al., 2013). Additionally, the specific length density of the perlitic cracks (green) depending on the distance to the primary sublinear cracks (red) were determined for 20 distance classes. The width of one distance class is 0.05 mm whereby distances between 0 and 1 mm were considered (Fig. 9).

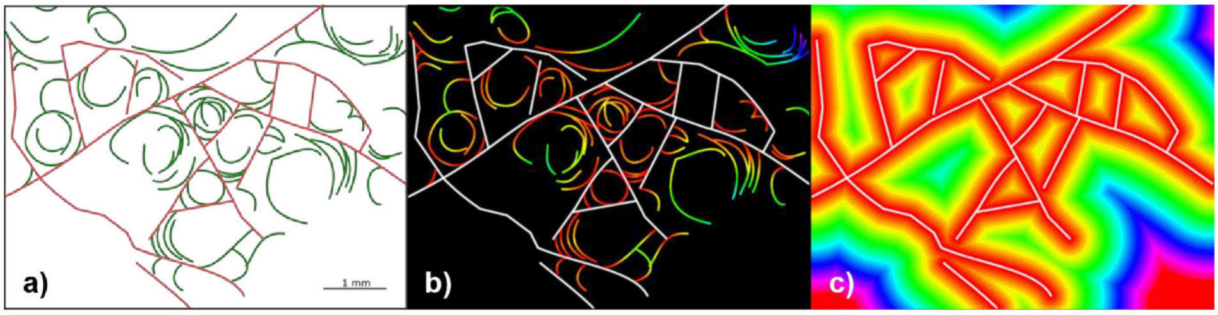

Fig. 9: a) Thin section image of sample 27-6-14-1e_2 evaluated according to the fracture systems; red: primary sublinear cracks, green: rounded perlitic cracks; b) and c) distance classes indicated by different colors.

Random tessellations and geometrical networks

A tessellation or mosaic is a geometrical pattern which divides a plane into polygons. Such pattern often occur in natural situations which could for example be crystalline structures or crack patterns and thus are well-suited to be applied on the perlitic fracture networks (Chiu et al., 2013). The analysis was carried out exemplarily for only one sample (5-12-04-3) on 10 thin section images of the same sample (5-12-04-3_1 to 5-12-04-3_10) to illustrate the method and address another possibility of characterizing the crack pattern. However, to obtain statistically reliable results of the mean cell area for one thin section, $\bar{a}$ should be estimated for at least 10 images of different areas belonging to this one certain thin section. For a number of 30 thin sections, this would require an evaluation of at least 300 thin section images, which goes beyond the scope of this thesis.

Statistics for planar tessellations can be used in order to get information on the cells by the determination of four basic parameters which are:

- the line density L_A,
- the intensity of vertices λ_0,
- the proportion ϕ of π-vertices, and
- the mean number of cells per unit area λ_2.

A π-vertex is a vertex which does not appear at a corner but at an inner point of a polygonal side (Chiu et al., 2013). L_A is estimated by using the method for planar fibre processes as described in the previous chapter. The final result is $\bar{a}$, which is defined as the mean cell area (Chiu et al., 2013).

The mean number of vertices per unit area as well as the proportion ϕ of π-vertices are calculated by estimating the number of vertices (Eq. 3). The area A(W) corresponds to the specific area of a certain thin section image, whereby W refers to the window of observation with an area A(W) (Chiu et al., 2013).

Eq. 3: Formula for calculation of mean number of vertices per unit area λ_0

$$\lambda_0 = \frac{\#\{vertices\ observed\ in\ W\}}{A(W)}$$

In the case of isotropy, the mean number of cells per unit area is computed by estimating N(W), which is the number of cells intersecting the window W, and $N_e(W)$, which describes the number of edges that intersect the boundary of W (Eq. 4). Since results have shown to be slightly overestimated due to the influences of cells at the marginal areas, the Eq. includes an edge correction. Fig. 10 shows how the individual parameters are determined, which are necessary for the calculation. The calculation of λ_2 yields an estimation of the mean cell area $\bar{a}$, which is computed by dividing the sum of cell areas by the number of cells, i.e. λ_2 (Chiu et al., 2013).

Eq. 4: Formula for calculation of mean number of cells per unit area λ_2.

$$\lambda_2 = \frac{N(W) - 1 - \frac{1}{2}N_e(W)}{A(W)}$$

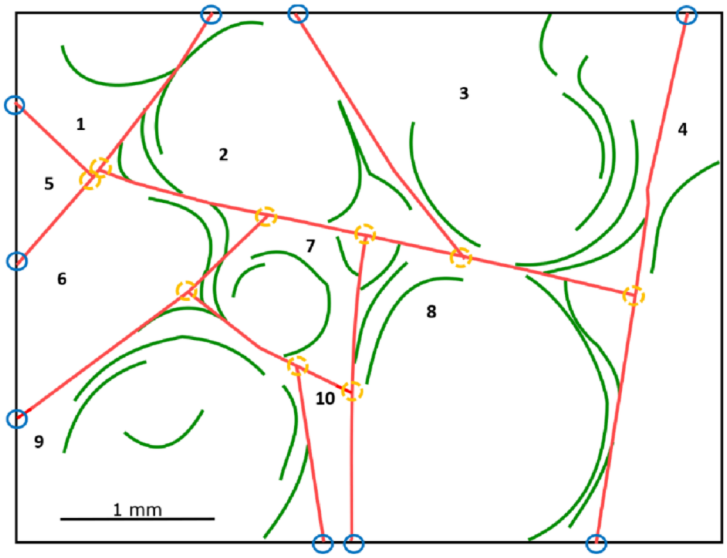

Fig. 10: Example for estimation of necessary parameters on sample 5-12-04-3_10; blue circles: N_e(W), orange circles: vertices observed in W, black numbers: N(W), black frame marks the window area A(W).

Curvature calculation

The calculation described in the following has not been done for each individual curve in each thin section but exemplarily for one individual crack to introduce a further possible analytical data reduction method. For more details according curvature estimations of analyzed samples see chapter 4.1.4. Curved cracks, such as perlitic fractures, in a planar cut can be described by a parametric curve, whereby $x(0)$ marks the starting point and $x(1)$ the end point of the curve (Fig. 11).

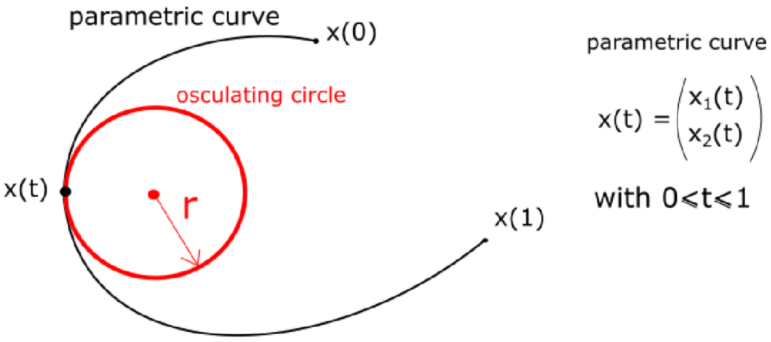

Fig. 11: Parametric curve with osculating circle with radius r.

The curvature at a certain point $x(t)$ is defined according to Eq. 5, whereby *r* defines the radius of the osculating circle.

Eq. 5: Formula for curvature at a point x(t).

$$\kappa(t) = \frac{1}{r(t)}$$

The integral of curvature along the curve can be calculated (Eq. 6), whereby γ is defined as the angle between the orthogonals of the tangents at the end points $x(0)$ and $x(1)$.

Eq. 6: Formula for calculation of integral I.

$$I = \gamma = \int_0^1 \kappa(t)dt$$

The meaning of the formula for the curvature integral is as follows: Actually, one would have to fit the circle of curvature into each point of the crack line to be able to measure the radius of curvature, to calculate the local curvature from this and to finally integrate the local curvature along the crack line. Instead, the tangents can be fitted to the ends of the crack lines and the angle γ can be determined directly, which is a more straightforward approach. For a closed curve γ is 2π, whereas γ is 0 for a straight-line segment. For every crack, which is treated as a curve, γ can be estimated and can then be expressed in terms of the portion of a full circle.

3.2.8. Porosity- & Permeability estimation

For each method, masses of the analyzed samples were measured with a "Rauch PS 360/C/2" weighing device. Each measurement was conducted three times to keep any measurement error as low as possible. For further calculations, mean values were taken. Porosities were measured in two ways: (1) using a Helium Pycnometer, and (2) using the Triple Weight Method. For permeability measurements, a Gas Permeameter was used.

Porosity measurement using the standard Triple Weight Method

The Triple Weight Method is based on Archimedes´ principle which states that "the fluid displaced by a sample can be observed either volumetrically or gravimetrically" (Schön, 2015). Therefore, it is necessary to measure the weight of the sample in three different conditions: (1) dry (m_{dry}), (2) water saturated (m_{sat}), and (3) water-saturated, immersed in water (m_{sus}). The upward buoyant force which is exerted on a rock sample immersed in a fluid - tap water in this case - is equal to the weight of the fluid which is displaced by the sample (Schön, 2015).

For this measurement, the samples do not have to be in a specific shape. However, it is necessary to dry the samples for about 8 hours beforehand, which was done in an oven at 70°C, in order to obtain the dry mass of each sample. Subsequently, the samples got emerged in water for 48 hours and as a last step, masses were measured. The mass of the fluid in the pore space and the mass of the displaced fluid were then calculated as shown in Eq. 7 and Eq. 8 (Schön, 2015).

Eq. 7: Mass of the fluid in the pore space.

$$V_{pore} * \rho_{fluid} = m_{sat} - m_{dry}$$

Eq. 8: Mass of the displaced fluid.

$$V_{bulk} * \rho_{fluid} = m_{sat} - m_{sus}$$

The porosity can then be expressed as a ratio of pore volume to bulk volume of each sample (Eq. 9). In that way, porosities of 12 samples were estimated.

Eq. 9: Calculation of the porosity φ according to the Triple Weight Method.

$$\varphi = \frac{V_{pore}}{V_{bulk}}$$

Porosity measurement using a Helium Pycnometer

A helium pycnometer uses the principle of gas expansion to measure the porosity of a rock sample. The gas expansion is described by Boyle´s law (Eq. 10) to determine the grain volume of a rock. If the mass of a sample is known, the grain density can directly be obtained (Schön, 2015).

Eq. 10: Boyle´s law for gas expansion.

$$p * V = const.$$

In the first step, the rock sample is confined in a vessel of a known volume (V1) and gets pressurized by gas (air, N_2, He) to a pressure (p1) at closed valve. A second vessel of known volume (V2) is initially evacuated. Subsequently, the valve which separates the two vessels is opened and the pressure in the two vessels equals the pressure p2 (Eq. 11).

Eq. 11: Basic equations for Helium Pycnometer measurements.

$$p1 * (V1 - Vgrain) = p2 * (V1 - Vgrain + V2) \qquad Vgrain = V1 - \frac{V2 * p2}{p1 - p2}$$

For the measurements with a Helium Pycnometer, intact core plugs of samples are required. Due to the extensive fracture network in most samples or because of inappropriate sample sizes, it was mostly impossible to generate applicable plugs. Only one useful plug could be produced and subsequently measured.

The length l and the diameter d for the core plug were measured three times and the average is used for the subsequent calculation. The output parameter of the measurement are the mean grain volume (V_{grain}) and the mean grain density (ρ_{grain}). By knowing these values, the porosity can then be calculated according to Eq. 12 (Schön, 2015).

Eq. 12: Calculation of the porosity φ with the Helium Pycnometer.

$$V = \frac{d^2}{4} * \pi * l \qquad \rho_{bulk} = \frac{m}{V} \qquad \varphi = 1 - \left(\frac{\rho_{bulk}}{\rho_{grain}}\right)$$

Permeability measurement using a Gas Permeameter

To measure the permeability of a core plug, a constant head permeameter ("Vinci Gasperm") with a Hassler cell is used. As for the Helium Pycnometer measurement, the gas permeameter also requires clean and dry plugs with planar surfaces. Due to previously stated problems in plug preparation, again the permeability for only one sample could be measured. The measurement is based on the flow of a fluid with known viscosity through the rock sample with a pressure gradient, which is based on Darcy´s law of laminar flow (Schön, 2015). To minimize the fluid-rock interaction, a dry, inert, and non-reactive gas (air, N_2, He) in a steady-state condition is used. The measurement was repeated three times and then the arithmetic average was calculated. It has to be considered that only the gas permeability has been measured without the application of the "Klinkenberg" correction. Although these results inadvertently represent slight overestimates for water, the associated error is considered negligible. The permeability is measured three times and the values obtained from the gas permeameter are

recorded by “GasPerm 2 Flows” computer software (Vs. 5.15.3). The result is again the average of the individual measurements.

4. Results

The results of thin section analysis, electron microprobe, thermoanalysis, porosity and permeability measurements, thermo shock, and stochastic image analysis are presented in the following chapter and observed perlitic characteristics and features are described.

4.1. Thin section analysis

4.1.1. Fracture network

Based on thin section analyses, a continuous fracture system can be tracked over most samples. It consists of two individual main types of fractures, which can be clearly separated from each other by their appearance, and one minor group:

- round to spherical cracks (perlitic fractures)

  The perlitic fractures could be clearly identified based on the typical rounded structure. To make them better visible and emphasize structures more clearly, these fractures were traced in a green color in the process of thin section analysis (Fig. 12). In the following chapters and images, green lines always indicate perlitic fractures.

- sublinear cracks

  The second major group of fractures consists of linear to sublinear cracks, which can often be traced continuously throughout large parts (give scale in microns) or even the whole thin section. They are indicated in red color (Fig. 12).

- Detected, yet, unidentifiable cracks

  In some thin sections, assignment to a fracture class could not be unequivocally carried out and due to their ambiguous geometric manifestation, these fractures were not assigned to one of the two major groups since they proved neither distinctly rounded nor linear. To avoid misinterpretations, they were not dedicated to one of the previous two groups but were characterized as unidentifiable cracks in orange color (Fig. 12).

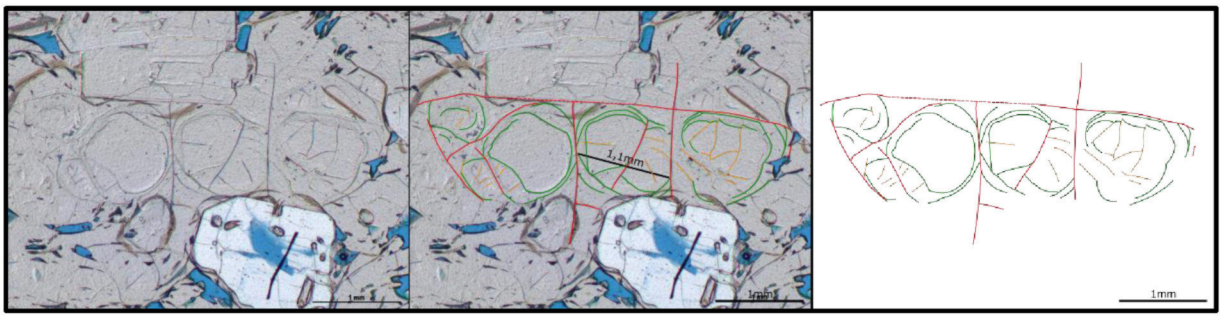

Fig. 12: Fracture system identification and evaluation; green: round to spherical cracks, red: sublinear cracks; orange: unidentifiable cracks; sample 10-12-20b.

The relative position of the two main fracture types and thus, the fracture network, show a clear pattern: sublinear fractures (red) form a mosaic-like structure or a more or less rectangular or trapezoidal cells. Within these cells, rounded perlitic cracks (green) are positioned. In most cases, these fractures are concentrated on the edges between two sublinear cracks (Fig. 13). A pattern for the unidentifiable cracks (not visible in this image) cannot be observed, i.e. they are randomly oriented. If the midpoints of each perlitic crack are seen as the center of the fracture and if they are considered with respect to their position and distance to the sublinear fractures, it is again evident that they are located close to each other, focused mainly on the marginal areas and especially on the edges of the red fractures (Fig. 14).

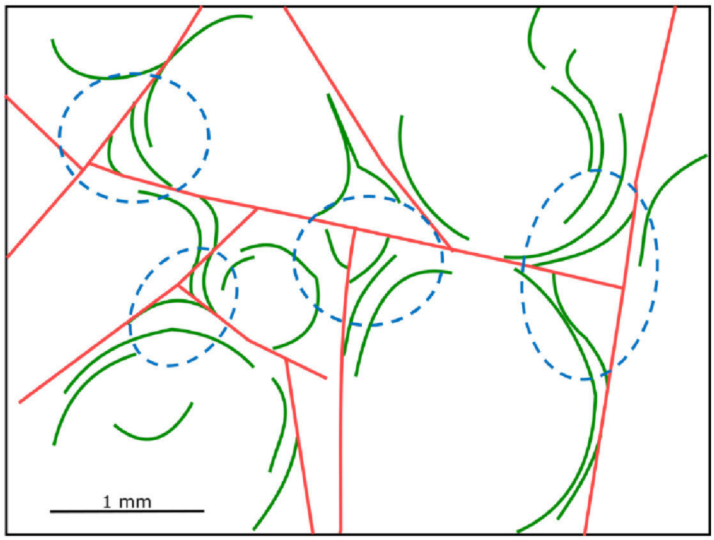

Fig. 13: Blue circles demonstrate the concentration of green fractures at the edges within each cell, which is circumscribed by red fractures; sample 5-12-04-3.

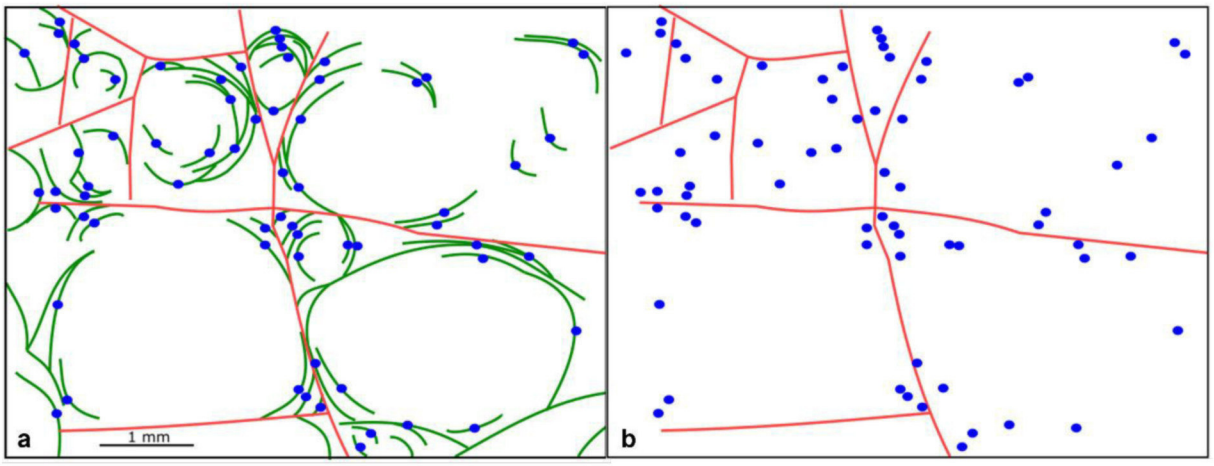

Fig. 14: a) Perlitic (green)- and sublinear (red) fractures, blue points mark the midpoints of each perlitic crack; b) perlitic fractures are hided; sample 5-12-04-3.

4.1.2. 3D-Geometry

Thin section analyses give valuable insights into characteristic textures, e.g. perlitic fractures, in a two-dimensional manner. However, it provides only limited information about the three-dimensional character of certain textural features. A similar problem is encountered at a macroscopic scale. On most of the hand samples, no matter if polished or not, cracks can only be seen on one plane. The same applies to the outcrop scale, where views are most of the time only possible from one perspective and no three-dimensional section through the formation is available. Generally, this does not state a problem for most geological investigations; however, for the case of spherical perlitic cracks the question concerning a three-dimensional character of the crack domain arises and is relevant for understanding of the prevalent paleo-stress-strain-regime.

Macroscopic 3D-investigation on fracture geometry

In order to get a three-dimensional impression of perlitic crack systems, a sample of a fully perlitized rock (5-11-07-3b) is cut along three planes perpendicular to each other. A schematic illustration demonstrates how the rock is intersected (Fig. 15).

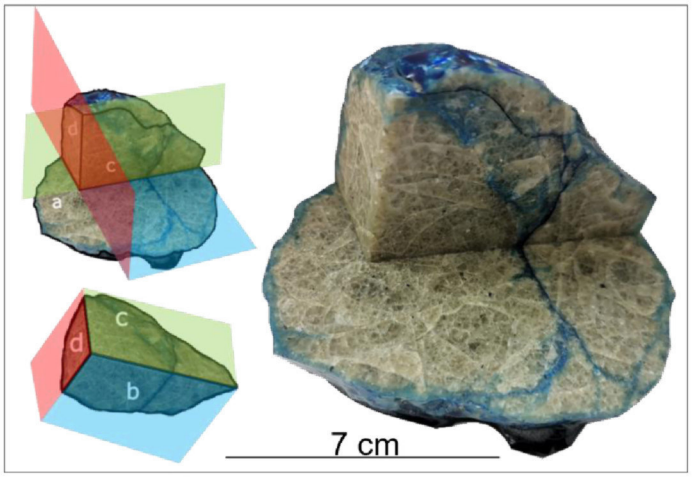

Fig. 15: Three-dimensional cut through a fully perlitized rock; sample 5-11-07-3b.

Macroscopic observations of the sectional planes do not show a preferred trend in orientation of the sublinear cracks; however, their continuations can be seen on each plane (Fig. 16). The sublinear cracks can also be traced along the edges, which gets visible on Fig. 16 (e). For the circular perlitic cracks it also becomes obvious that they show a continuation from one plane to another, e.g. a crack domain on the cutting edge in (b) can be traced on the cutting edge in (c). Examples for the three-dimensional continuations of the cracks are made evident by the dotted lines in Fig. 16. On broken edges it can be seen in detail that the fracture network is a three-dimensional phenomenon, and it is a proof for the spherical form of perlitic cracks (Fig. 16 f & g).

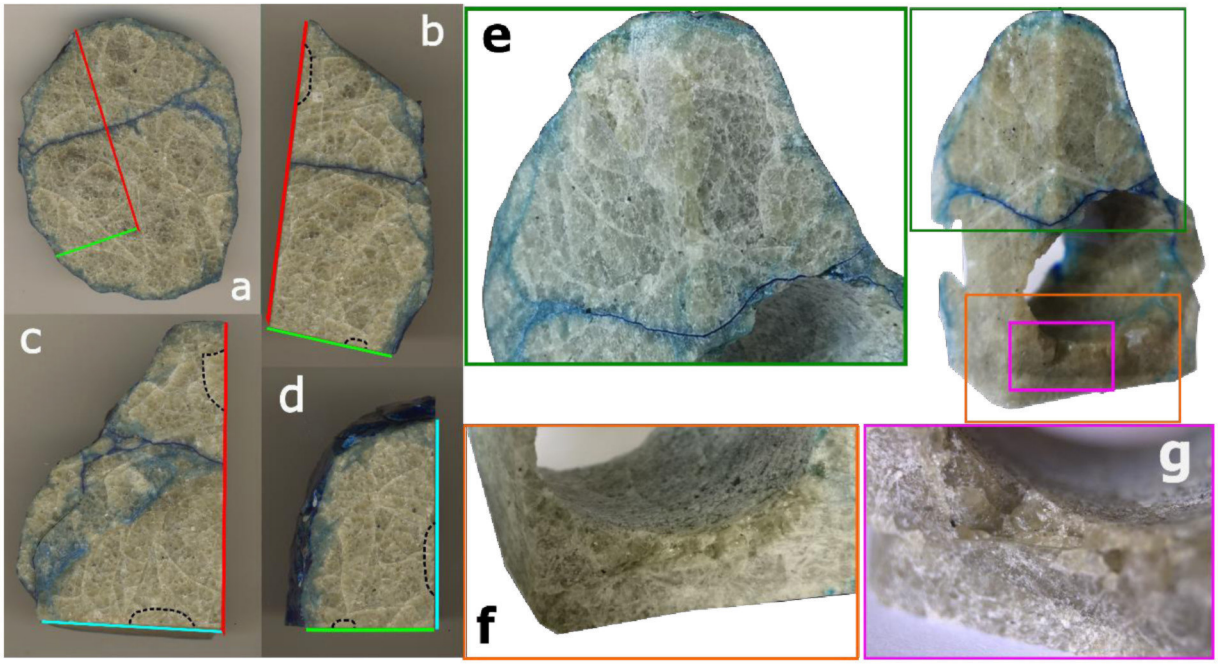

Fig. 16: Continuation of perlitic fractures on each plane, a-d: planar view on different sides of the cutted rock sample, e: view on an edge between to planes, f-g: view on edges produced by plug preparation; sample 5-11-07-3b.

Computer tomography results

Micro-CT measurements on sample 5-12-04-3 were conducted with the aim of getting additional insights into the three-dimensional geometry of the perlitic fracture network (Fig. 17). A high resolution of 9.68 µm was chosen for a sample size of approximately 2x2 mm. For this sample a stack of 1.536 image slices along a horizontal axis through the rock was conducted and a continuous fracture network of sublinear and spherical cracks can be observed (Fig. 17). This proves again that there is a connected three-dimensional fracture system which proceeds through the whole sample. Even though the analyzed sample shows a high number of perlitic and sublinear fractures, contrasts between fractures and surrounding rock were too low for producing three-dimensional images of the rocks. Generally, it turned out that CT measurements are not perfectly efficient for analyzing perlitic rocks which consist of a dense but fine fracture network without significant pore space and without fracture apertures.

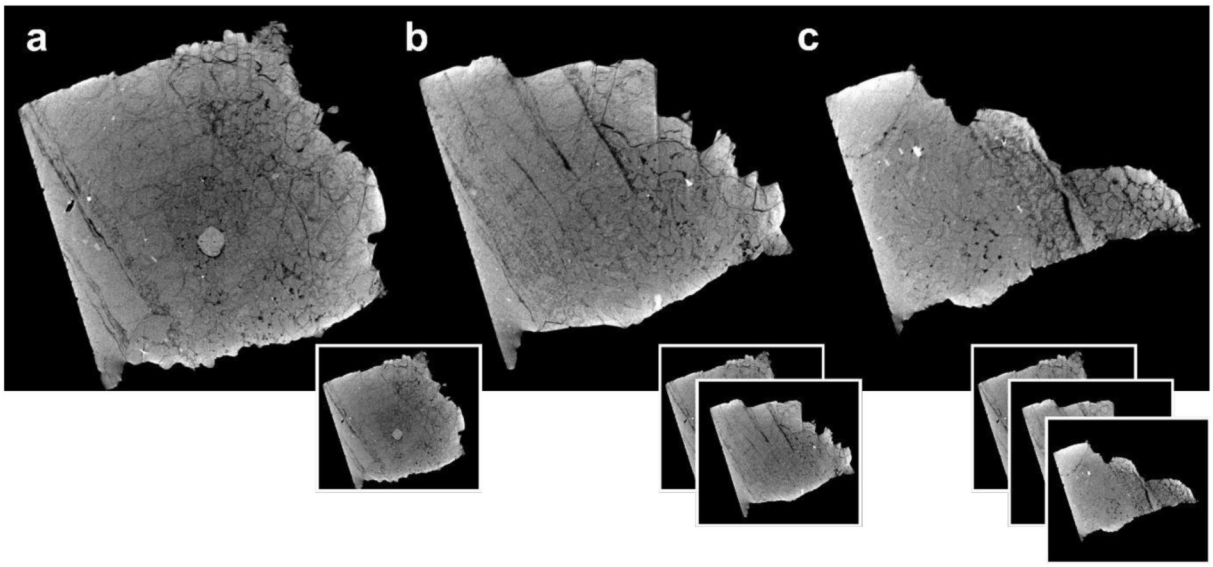

Fig. 17: CT results for sample 5-12-04-3; a), b) and c) show selected examples of image slices which cut through the rock (left to right is from bottom to top); 1944x1944 pixels; 9.68 µm resolution.

Size ratios and measuring method

In the case of perlitic fractures, a spherical texture only provides an indication of a curved shape of the cracks in a plane but gives no certainty on whether a cross-section through an actual three-dimensional sphere or ellipse is observed or not. Additionally, in the case of three-dimensional spherical bodies, the diameter of a two-dimensional circle depends on the position at which a three-dimensional sphere or ellipse is cut along a plane. Consequently, investigating a two-dimensional extract of an initially three-dimensional body gives no information on the continuation of a texture in and out of the drawing plane, which complicates obtaining a clear estimate of the average diameter of the cracks. Therefore, the "maximum particle size" principle is applied in order to find the crack with the largest diameter within one thin section, since this method provides the best estimation for the upper limit in crack size for each particular sample. For elliptically shaped cracks, the largest diameter is measured along the longitudinal (major) axis of the ellipse.

As mentioned previously, one individual spherical fracture does not necessarily have to be closed but is also considered as a perlitic crack if it only appears as the partial arc length of a circle. For that reason, measuring of diameters is not restricted to closed textures. If a particular crack is intermittent, it is not considered as a coherent crack, as there is no certainty if the two individual parts have been connected and, for instance, got separated by another fracture system or became overgrown by alteration minerals, or if the two dissociated cracks result from the propagation of two individual fractures. Therefore, diameters are only measured for cases of clearly connected fractures. Moreover, it has to be considered that each thin section represents only a small part of the whole rock and size measurements cannot be transferred directly to the whole rock sequence.

The maximum observed diameter of approximately 8 mm (Tab. 8) was too large to be pictured as a whole with the microscope but was visible and could be measured macroscopically. The smallest diameters have not been measured individually due to previously stated problems; however, fractures with a diameter of less than half of a centimeter are found. This observation is consistent with those of Drysdale (1991), where he describes the circles/ovals in 2D showing diameters ranging from 0.1 mm up to a few millimeters.

4.1.3. Perlitisation in lavas and ignimbrites

Even though the average fracture diameter of ignimbrite samples is smaller than that of rhyolitic lava (Tab. 8) due to a few very large diameters in some lava samples, a clear trend or difference cannot be seen. The average maximum fracture diameter size of analyzed lava samples is 4.1 mm and for ignimbrites it is 2.1 mm. Young (Cenozoic) samples have maximum diameters of 4 mm on average while pre-Cenozoic samples showed an average of 2.9 mm (Tab. 8).

Ignimbrite samples showed a clear tendency that perlitic crack formation is mainly focused on the welded fiamme (e.g. Fig. 18a). However, in some cases (e.g. P 1500a & 44.20 III) the fractures encroach on the matrix (Fig. 18b). The sample in Fig. 15a shows a distinctly stronger compaction of the surrounding matrix with significantly higher numbers of glassy fractions within the matrix.

Tab. 8: Maximum perlitic fracture diameters of lava and ignimbrite samples; bold: Cenozoic (younger) samples; not bold: pre-Cenozoic.

SAMPLE LAVA	DIAMETER [MM]	SAMPLE IGNIMBRITE	DIAMETER [MM]
1-8-97-1	2.1	**1-8-97-7b**	2.3
1-8-97-3b	1.8	**5-12-04-3**	4.3
3-8-97-1	5.0	11497	1.5
13-12-04-01	3.0	11510	0.9
10-12-08-2a	4.1	P 1500a	1.7
27-6-14-1e	2.8	SS 16782	1.7
10-12-20- b	1.1	RS 3636	4.8
Tokai 24-1	8.0	44.20 I	1.5
Tokai 24-2	7.0	44.20 II	2.0
8 Ta PS	1.3	44.20 III	0.7
C 28-01	5.6	Fl 93	1.9
6-4-01-1a	3.3		
TT-2-B-3	7.0		
TT-6-B-1	6.3		
TT-8-B-3	5.1		
MEAN LAVA	4.1	mean Cenozoic	4.0
MEAN IGNIMBRITE	2.1	mean pre-Cenozoic	2.9

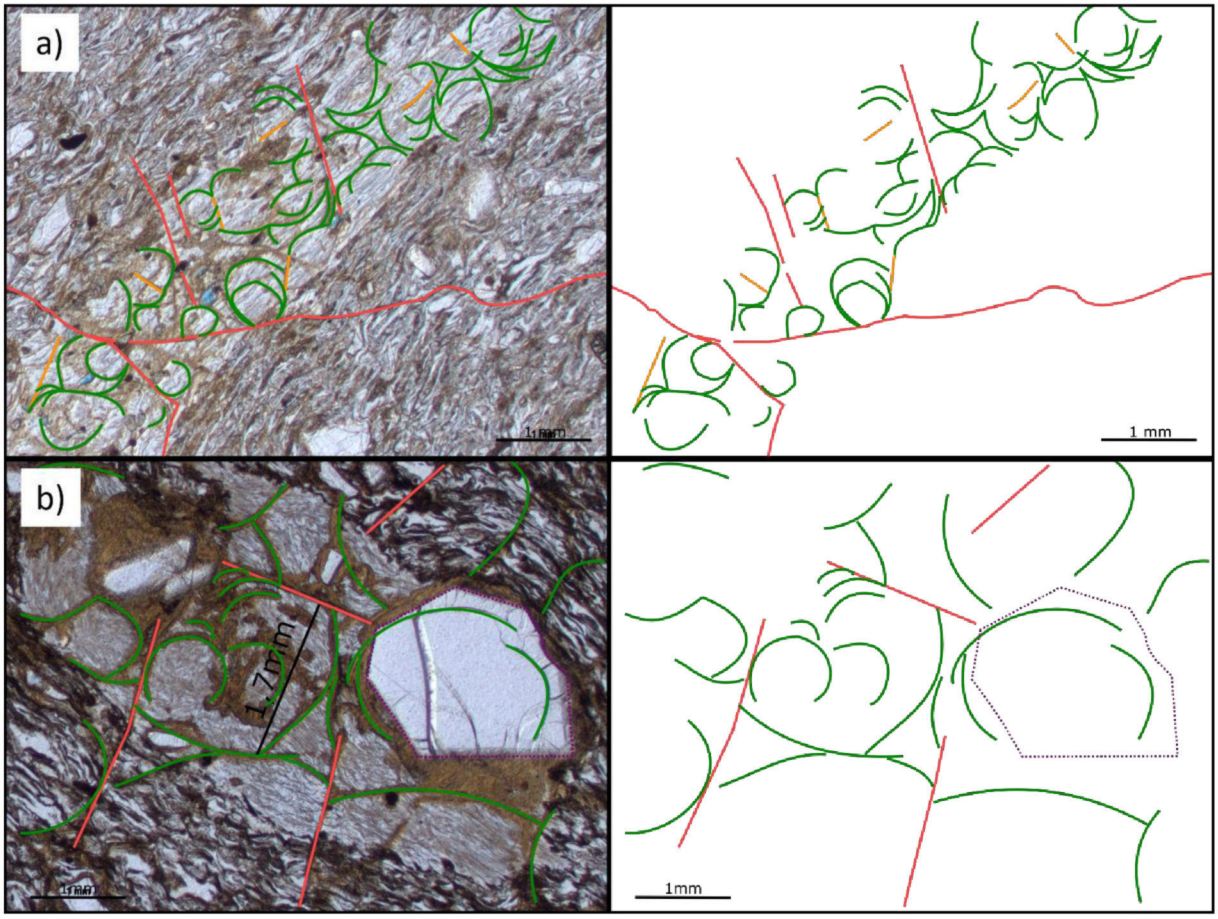

Fig. 18: Perlitization in ignimbrites; a) fracture formation limited to fiamme, sample 11510; b) fracture formation not restricted to fiamme, sample P 1500 a.

A thin section through a phreatic lava breccia was also examined (Fig. 19). The breccia developed in a hot porphyritic lava. The pinkish color of the rock´s matrix arise from a high amount of hematite. It can be seen that the angular obsidian fragments (dark color) are fully perlitized whereas there is no clear fracturing visible in the pinkish matrix. Some rocks are highly porphyritic with high amounts of microlites and phenocrysts. Those crystals are present before the crack formation and hence, cracks cannot freely propagate and are highly deformed for that reason (Fig. 20).

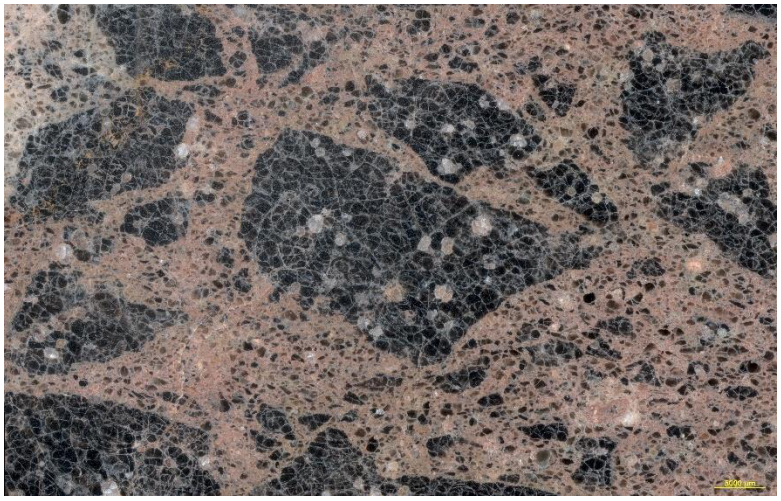

Fig. 19: Thin section of phreatic lava breccia with high degree of perlitic fractures; sample Ad-18.

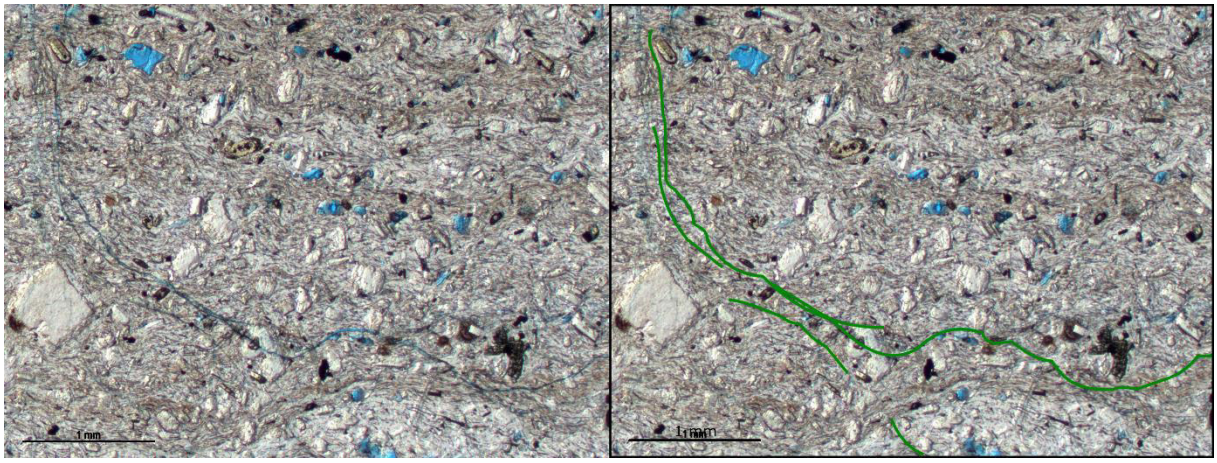

Fig. 20: Highly porphyritic lava with deformed perlitic fractures; left: uninterpreted, right: interpreted; sample 9-9-01.

4.1.4. Degree of perlitization

The degree of perlitization is linked to (1) the density of the perlitic fractures in general and in comparison to the density of the sublinear fractures, and (2) the fraction of a full circle of one crack.

For the estimation of the line densities and specific crack areas as well as of the growth to the inside of the cells, a stochastic approach for a quantitative analysis of each sample was found and is further explained and discussed in chapters *5.2.4.*, *6.5*. and *7.6.* It was not possible to find a way to calculate the fraction of each fracture of a full circle automatically, but two alternative methods are presented, which is a semi-quantitative estimation done for each thin section (Tab. 9) and a mathematical approach to calculate the curvature manually (see chapter *5.2.4. Curvature calculation*).

For the semi-quantitative estimation seen in Tab. 9, the number of perlitic fractures observed in each analyzed thin section were counted and the mean value for every sample was computed first (total

no.), secondly, the number of curves with a certain radius (subdivided into four groups) were counted manually as well and each percentage calculated. The numbers presented in Tab. 9 represent the mean value for each sample based on thin section images.

Tab. 9: Estimation of curvature; total no. = total number of perlitic cracks; left column: samples Cenozoic; right column: samples older than Cenozoic; blue: lava; orange: ignimbrites.

	CURVATURE						CURVATURE				
SAMPLES YOUNG	< 90°	< 180°	< 270°	< 360°	total no.	SAMPLES OLD	< 90°	< 180°	< 270°	< 360°	total no.
	%	%	%	%	-		%	%	%	%	-
1-8-97-3b	88	8	4	0	16	6-4-01-1a	61	25	14	0	20
10-12-20-b	56	28	12	5	37	C 28-01	33	39	22	6	29
1-8-97-1	84	11	5	0	29	TT-2-B-3	36	30	22	12	29
3-8-97-1	85	14	0	1	36	TT-6-B-1	34	34	14	17	29
5-11-07-3b	78	21	2	0	18	TT-8-B-3	25	38	24	13	34
10-12-08-2a	38	32	22	8	36	8 Ta PS	29	42	28	1	17
13-12-04-01	29	37	21	13	19	11497	31	36	26	7	23
27-6-14-1e	32	29	29	9	40	11510	31	36	22	21	28
Tokai 24-1	23	29	40	8	44	P 1500a	32	35	23	9	12
Tokai 24-2	9	43	43	6	35	SS 16782	19	47	26	7	27
5-12-04-3	65	23	10	2	45	26-6	0	50	39	10	24
1-8-97-7b	78	19	4	0	34	RS 3636	58	24	19	0	11
						44.20 I	34	31	30	5	16
						44.20 II	25	34	31	10	23
						44.20 III	26	35	26	13	26
						Fl 93	28	39	24	10	12
						JK 20	35	31	26	8	8
mean lava	45	29	18	6	28	mean young	55	22	16	4	33
mean ignimbrite	36	33	24	8	23	mean old	32	33	25	9	22

For an interpretation it has to be taken into account that the propagation of an individual perlitic crack is often impeded or limited by sublinear quench fractures which surround them, or by other obstacles in form of an incoherent matrix (e.g. in ignimbrites) or unbreakable crystal grains. Therefore, a small radius of a perlitic crack does not necessarily imply that it did not propagate farther due to too short cooling times and/or associated thinner flow thickness, but it can simply be attributed to propagation being spatially limited.

Young samples of Cenozoic age show a relatively linear trend in curvature with the highest number of fractures being smaller than a quadrant and only a small percentage of full circles. The number of perlitic fractures is generally high. Samples older than Cenozoic show a relatively even distribution; full circles are relatively rare, though, and the number of fractures is relatively high. The same behavior of young and old samples can be observed for lava and ignimbrites, respectively (Fig. 21.

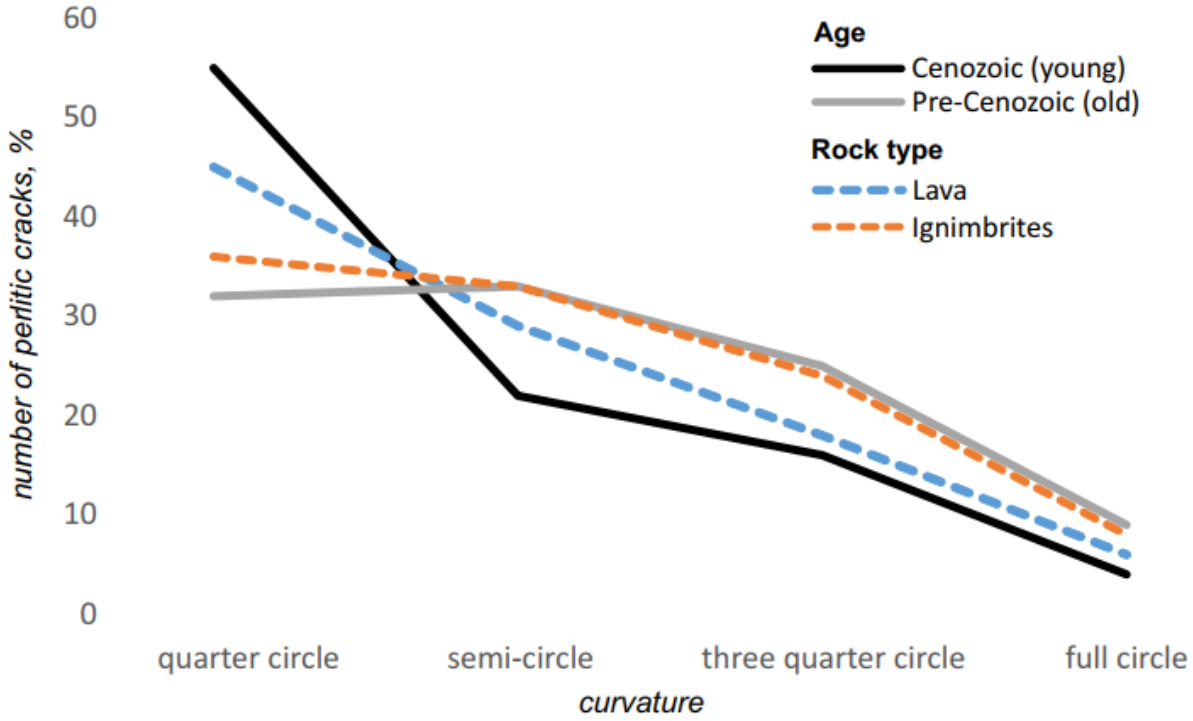

Fig. 21: Plot of number of perlitic cracks, expressed as a percentage of all visible cracks in a sample, against the degree of roundness for Cenozoic vs. pre-Cenozoic samples (solid lines), and for lavas vs. ignimbrites (dashed lines).

4.1.5. Relation between geological age and perlitic fracturing

Observations of perlitic fractures in samples of strongly varying ages made clear that these structures are not necessarily restricted to geologically young rocks but can also occur in Precambrian and Paleozoic rocks. Fig. 22 shows a sample of Ras Gharib from the Ediacaran period, where perlitic fractures can still be recognized. However, the fractures themselves are probably already closed or healed throughout the long timespan or completely overgrown by alteration minerals but outlines of the beads are still visible. Tab. 8 shows that there is no clear trend of an increase in fracture diameter with increasing geological age. Mean diameter sizes for old and young samples only differ by approximately 1 mm.

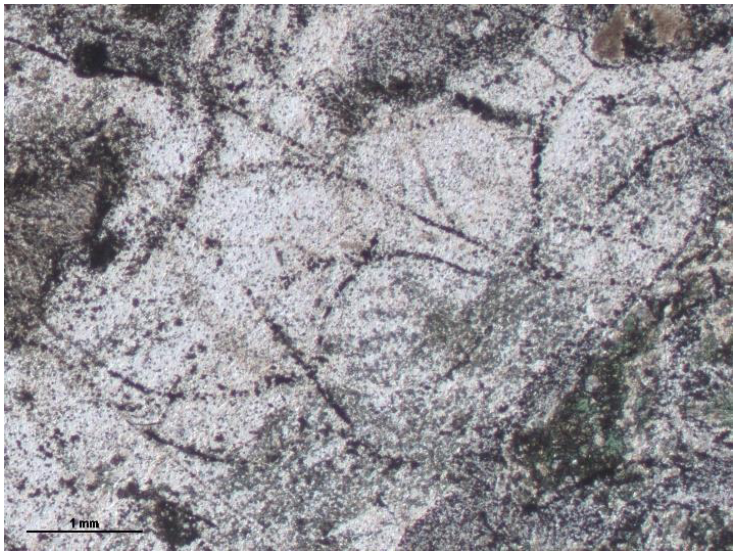

Fig. 22: Healed cracks with outlines preserved by mineral precipitation in Ediacaran sample; sample JK 20.

4.1.6. Alteration and devitrification

A high amount of the investigated samples shows mineralization and alteration features along the perlitic fracture rims (Tab. 10). Among all analyzed samples, only six show no or only minor alteration features. Generally, it was found that samples older than Cenozoic are affected more often by alteration and mineral precipitation. The same is observed for devitrification. However, devitrification in general is not a prominent feature in ignimbrites. The most common alteration minerals that can be observed are phyllosilicates, especially, clay minerals like smectites (Fig. 23b)), and metal oxide minerals such as hematite (Fig. 23a)).

Tab. 10: Alteration of lava and ignimbrite samples; bold: Cenozoic (and younger) samples.

LAVAS	ALTERATION, MINERAL PRECIPITATION, DEVITRIFICATION FEATURES
1-8-97-1	hardly no alteration
9-9-01	hardly no alteration
10-12-20-b	hardly no alteration
1-8-97-3b	hardly no alteration
3-8-97-1	mineralization on cracks
13-12-04-01	fully devitrified
10-12-08-2a	in some areas no alteration, in some areas phyllosilicates along fractures
27-6-14-1e	in parts highly altered; some healed fractures preserved by minerals; traces of hematite
Tokai 24-1	hardly no alteration
Tokai 24-2	hardly no alteration
8 Ta PS	high amount of clay minerals along the cracks (probably smectite), strongly altered
TT-2-B-3	fully devitrified, no alteration
TT-6-B-1	fully devitrified
TT-8-B-3	fully devitrified
5-11-07-3b	clay minerals on cracks (prob. illite/smectite)
IGNIMBRITES	**ALTERATION, MINERAL PRECIPITATION, DEVITRIFICATION FEATURES**
1-8-97-7b	microcrystalline devitrification in dark areas; phyllosilicates on fracture surfaces (maybe smectite)
5-12-04-3	in most areas no alteration, in some places phyllosilicates along the cracks
11497	phyllosilicates along cracks in fiamme
11510	phyllosilicates along cracks in fiamme; alteration limited to fractured areas
P 1500a	high amount of phyllosilicates along cracks in fiamme
SS 16782	phyllosilicates along cracks in fiamme
RS 3636	highly altered/mineralized (probably clay minerals)
44.20 I	highly altered, almost undevitrified
44.20 II	highly altered, almost undevitrified
44.20 III	highly altered, almost undevitrified
Fl 93	strongly devitrified; large parts overgrown by minerals
26-6	weakly devitrified, high amount of phyllosilicates along fracture rims
JK 20	cracks at most areas fully healed but shapes are preserved by minerals

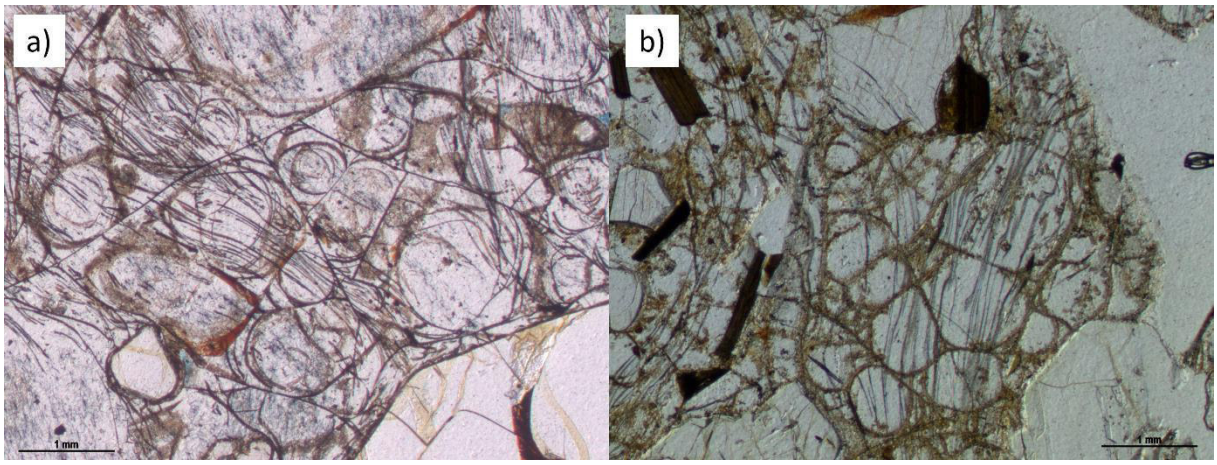

Fig. 23: Alteration in perlitized rocks; a) traces/lineations of hematite, sample 5-11-07-3b; b) smectite along fracture rims (brownish) and traces of hematite (grey), sample 8 Ta PS.

Mineral precipitation very often occupies free pore space and especially for pre-Cenozoic samples, both lava and ignimbrites; it is observed that the minerals grow from the rims further inside the core of a fracture. However, dissolution of the glass can increase the aperture of the fractures and hence, lead to an increase in pore space and significantly improve porosities (Fig. 24). This effect is also observed for both lava (e.g. 1-8-97-1) and ignimbrites (e.g. 44.20 II).

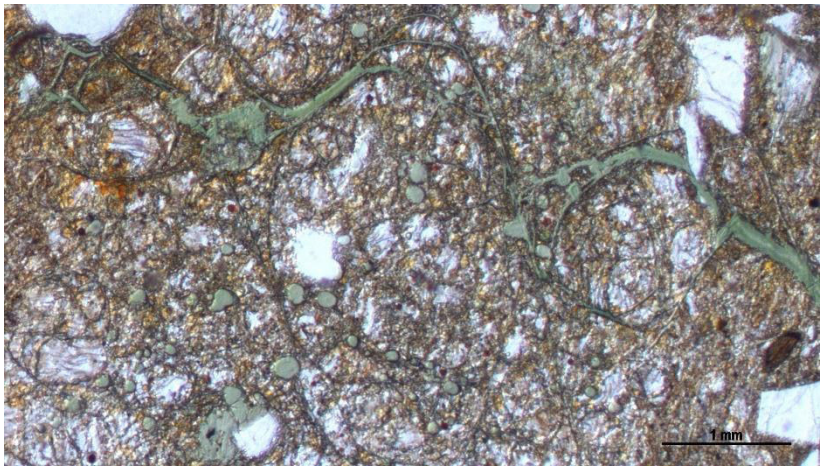

Fig. 24: Increased pore space along apertures of perlitic fractures (greenish areas), sample 44.20 II.

Fig. 25a represents a classical perlite according to the classification of Allen (1988). Banded perlites are less common than classical perlites and most likely develop in rhyolitic rocks with a flow fabric (Allen, 1988). Fig. 25b shows an example of a banded perlite with significant alteration. In some lava and ignimbrite samples of both Cenozoic and pre-Cenozoic age it can be observed that alteration is not homogeneously distributed along all perlitic fracture rims (Fig. 26).

Especially lava samples of ages older than Neogene are at least partially devitrified (Fig. 27). Devitrification is generally not very abundant in ignimbrites. Irregular zones of crystallization along the cracks are characteristic for devitrification in perlites (Marshall, 1961) and can often be observed as speckled birefringent zones under crossed nicols. It was already observed by Marshall (1961) that surfaces along larger cracks are often considerably devitrified and more deeply altered, which is consistent with observations made during this study.

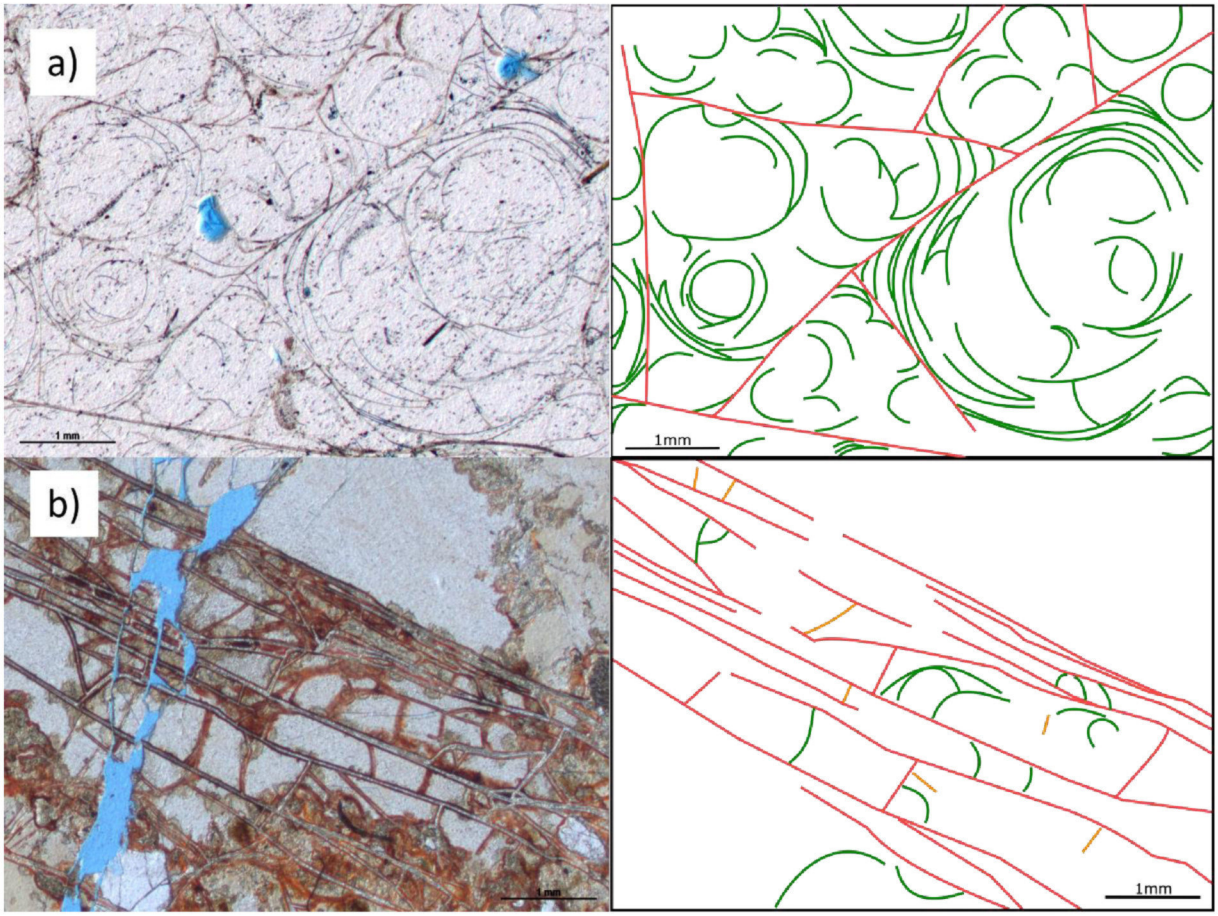

Fig. 25: a) classical perlite, sample 5-12-04-3; b) banded perlite with high amount of alteration minerals (oxides) along the fracture rims, sample RS 3636.

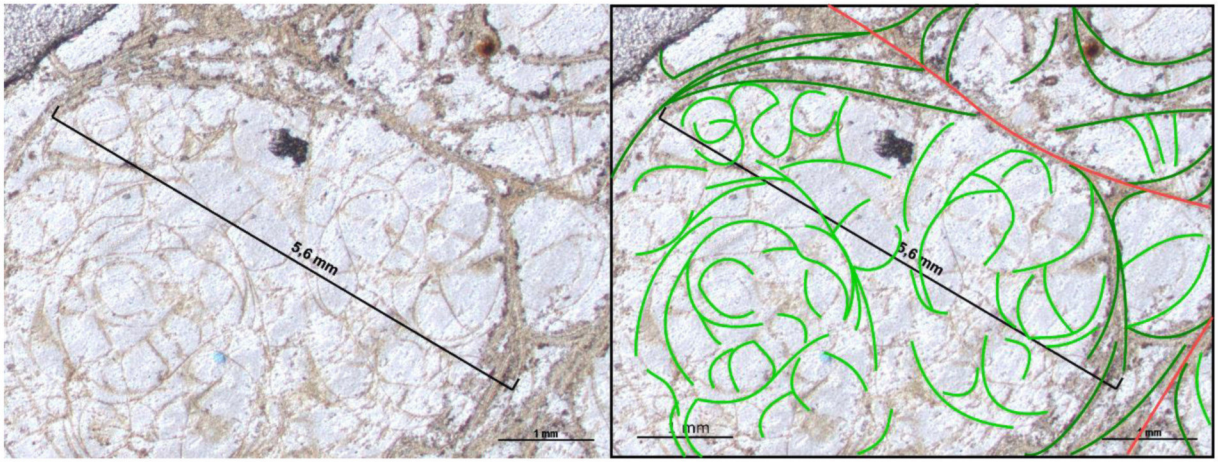

Fig. 26: Different generations of perlitic fractures with changing degree in alteration; dark green: first generation of rounded fractures with high amount of alteration minerals; light green: later generation of rounded fractures with less alteration; sample C 28-01.

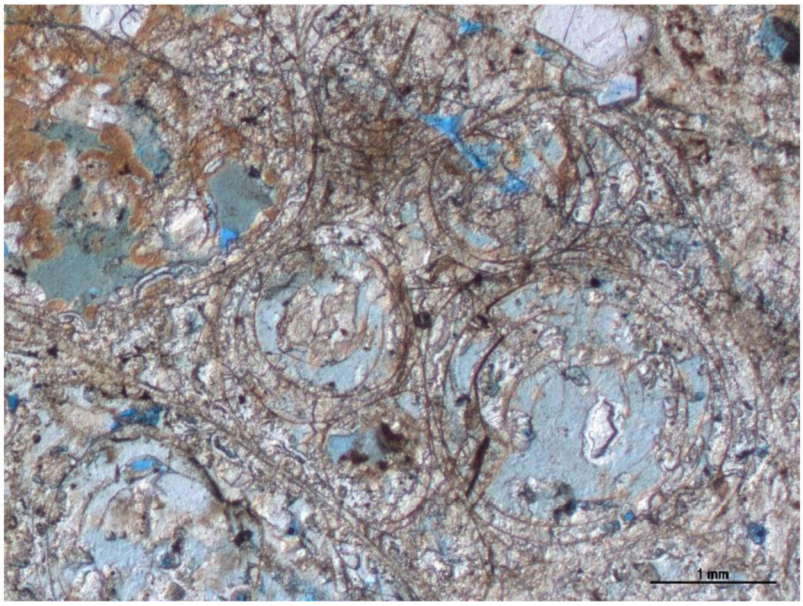

Fig. 27: Devitrified sample, blue color indicates pore space (dyed epoxy resin); sample TT-2-B-3.

4.1.7. Perlitic fractures in crystal grains

In several lava samples it can be seen that perlitic fractures occur within crystals grains (Fig. 28a). Ignimbrites mostly do not contain large crystals and therefore, the effect is not very dominant in analyzed thin sections of ignimbrites. In some other lava samples, the fractures concentrate on the areas around the crystalls but do not encroach from the matrix into the grain (Fig. 28b).

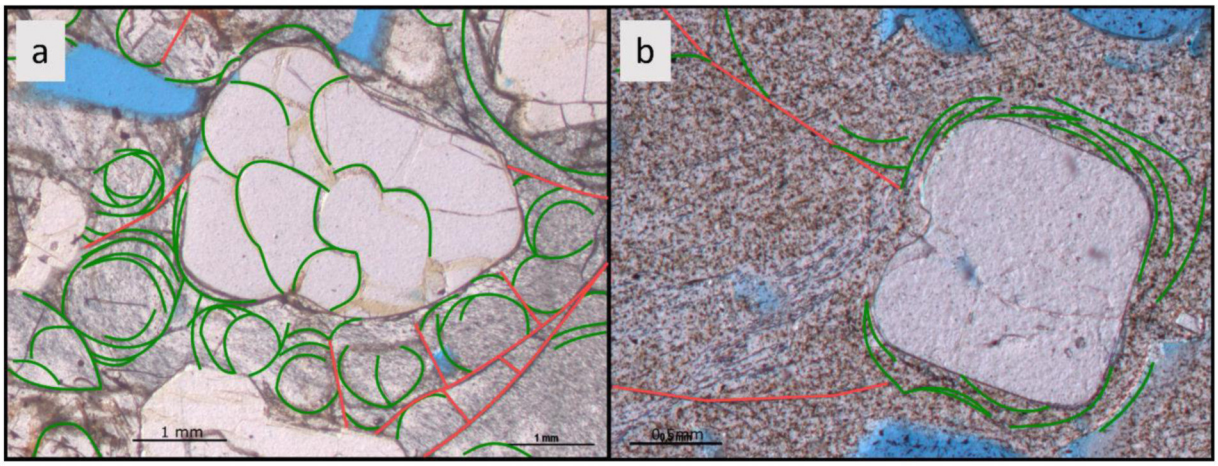

Fig. 28: a) Perlitic fractures intersecting crystal grain; sample 27-6-14-1e; b) Perlitic fractures concentrated around a crystal grain; sample 1-8-97-3b.

4.1.8. Microlites

Microlites cannot be observed in every investigated sample but are prominent in certain thin sections, especially in glassy lava samples but also occasionally in glass shards in ignimbrites (e.g. Fig. 29). The observation of perlitic textures in general is aggravated by the presence of microlites. Sample 1-8-97-1 shows a simultaneous appearance of both, parallel arranged pyroxene microlites and loopy trichites.

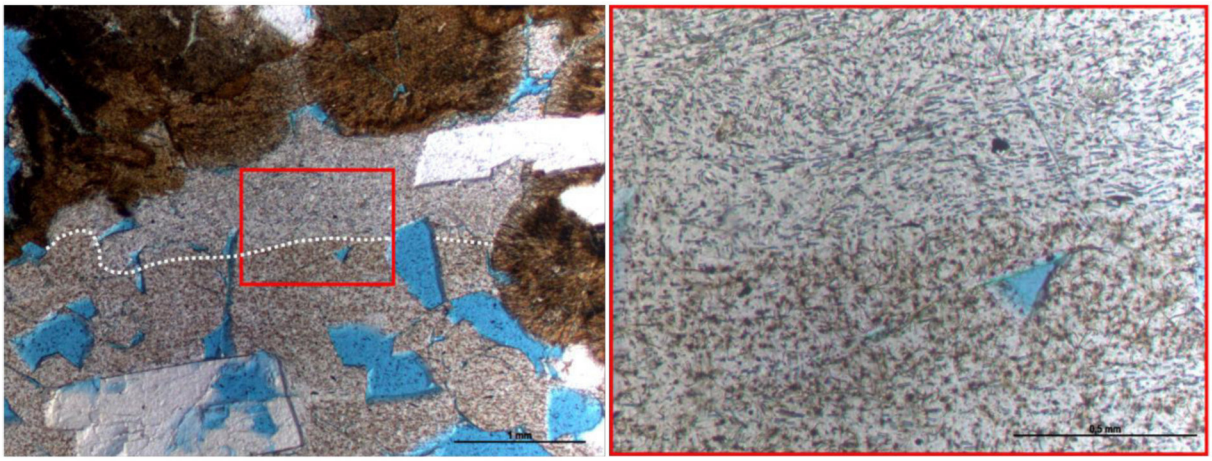

Fig. 29: Brighter area shows parallelly arranged microlites; darker area shows high amount of brownish loopy trichites; sample 1-8-97-1.

4.2. DSC/TG Analysis

The combined results of each TG and DSC analysis obtained on one obsidian, five perlites and two pitchstones specimen are shown in Fig. 30 and Fig. 31. Single curves for each of the eight analyzed samples are in the electronic Appendix.

A quantification of mass loss during heating can be obtained directly from the TG curves. Mass losses range between 0.23 to 7.68 wt.% for all examined samples on a dry basis (ambient air). Each mass loss curve shows a characteristic sigmoidal shape, and the slope of the curve gives an indication of the mass loss rate. These losses can either be caused by oxidation or the release of fluids and volatiles. To confirm that water is the only species which is released during heating and that there are no chemical alterations during thermal analysis, special treatment of the samples would have been necessary beforehand.

The weight loss of the perlite samples is relatively constant during heating up to 300 °C and subsequently starts to decrease until a temperature of about 600 °C is reached. From that point on, the weight loss is again relatively constant and only some tenth of the mass may be retained by further heating up to 1000 °C. The average weight loss for the analyzed perlites is 3.99 wt.%. Compared to that, the pitchstones show no constant course at the beginning and have an inflection point of the sigmoidally shaped curves slightly below the perlitic sample curves at approximately 250 °C. The most significant weight loss however is between 100 and 600 °C. The average weight loss is distinctly higher with 7.42 wt.%. Additionally, one obsidian sample without perlitic textures was analyzed, which shows

a weight loss of 0.23 wt.%. In a previous study, the Apache's Tear from Argentina (5-11-07-3a) was analyzed and showed a similar weight loss of 0.27 wt.% (Weißmantel, 2018).

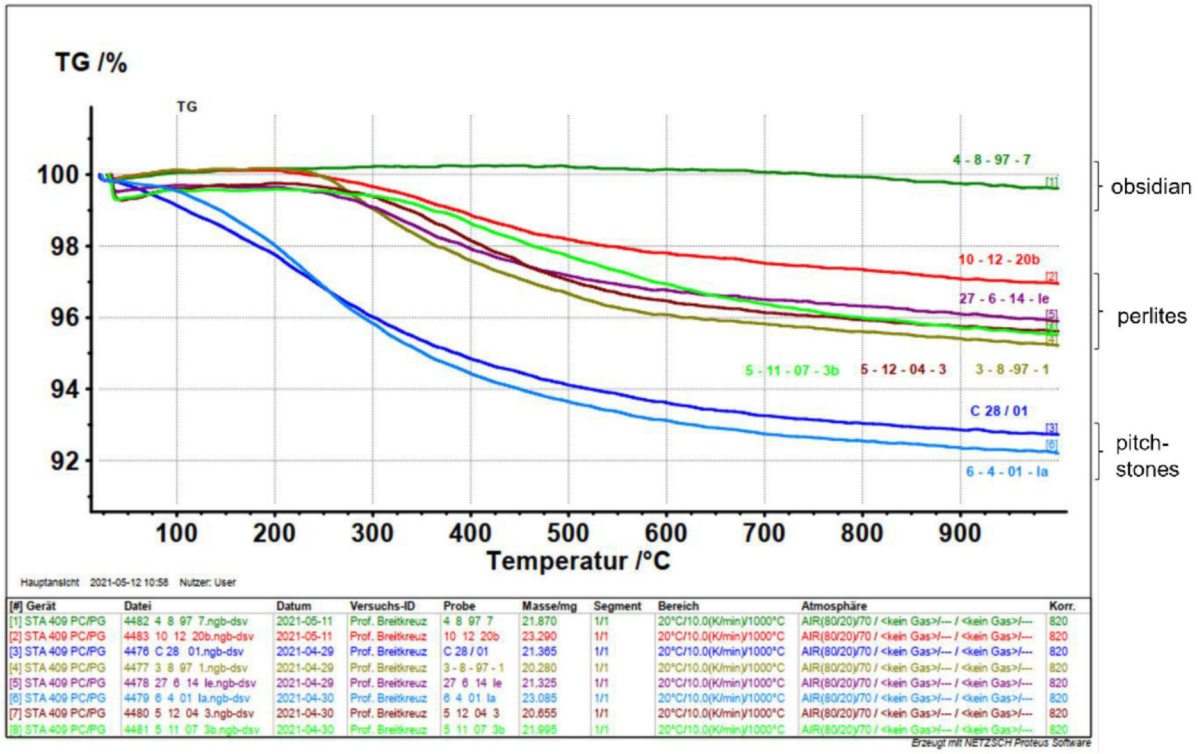

[#] Gerät	Datei	Datum	Versuchs-ID	Probe	Masse/mg	Segment	Bereich	Atmosphäre	Korr.
[1] STA 409 PC/PG	4482 4 8 97 7.ngb-dsv	2021-05-11	Prof. Breitkreuz	4 8 97 7	21.870	1/1	20°C/10.0(K/min)/1000°C	AIR(80/20)/70 / <kein Gas>/--- / <kein Gas>/---	820
[2] STA 409 PC/PG	4483 10 12 20b.ngb-dsv	2021-05-11	Prof. Breitkreuz	10 12 20b	23.290	1/1	20°C/10.0(K/min)/1000°C	AIR(80/20)/70 / <kein Gas>/--- / <kein Gas>/---	820
[3] STA 409 PC/PG	4476 C 28 01.ngb-dsv	2021-04-29	Prof. Breitkreuz	C 28 / 01	21.365	1/1	20°C/10.0(K/min)/1000°C	AIR(80/20)/70 / <kein Gas>/--- / <kein Gas>/---	820
[4] STA 409 PC/PG	4477 3 8 97 1.ngb-dsv	2021-04-29	Prof. Breitkreuz	3 - 8 - 97 - 1	20.280	1/1	20°C/10.0(K/min)/1000°C	AIR(80/20)/70 / <kein Gas>/--- / <kein Gas>/---	820
[5] STA 409 PC/PG	4478 27 6 14 Ie.ngb-dsv	2021-04-29	Prof. Breitkreuz	27 6 14 Ie	21.325	1/1	20°C/10.0(K/min)/1000°C	AIR(80/20)/70 / <kein Gas>/--- / <kein Gas>/---	820
[6] STA 409 PC/PG	4479 6 4 01 Ia.ngb-dsv	2021-04-30	Prof. Breitkreuz	6 4 01 Ia	23.085	1/1	20°C/10.0(K/min)/1000°C	AIR(80/20)/70 / <kein Gas>/--- / <kein Gas>/---	820
[7] STA 409 PC/PG	4480 5 12 04 3.ngb-dsv	2021-04-30	Prof. Breitkreuz	5 12 04 3	20.655	1/1	20°C/10.0(K/min)/1000°C	AIR(80/20)/70 / <kein Gas>/--- / <kein Gas>/---	820
[8] STA 409 PC/PG	4481 5 11 07 3b.ngb-dsv	2021-04-30	Prof. Breitkreuz	5 11 07 3b	21.995	1/1	20°C/10.0(K/min)/1000°C	AIR(80/20)/70 / <kein Gas>/--- / <kein Gas>/---	820

Fig. 30: Thermo Gravimetry results for analysed rock samples.

DSC curves show no remarkable difference between pitchstones and perlites. The change in heat flow is constant at the beginning of the heating process and starts to increase slightly above 200 °C. The DSC curves show a distinct wide and single peak at approximately 500 °C and heat flow changes are constantly decreasing during further heating. However, one obsidian (4-8-97-7) shows a slightly retarded peak at 600 °C and a less significant decline of the hyperbola after reaching the peak.

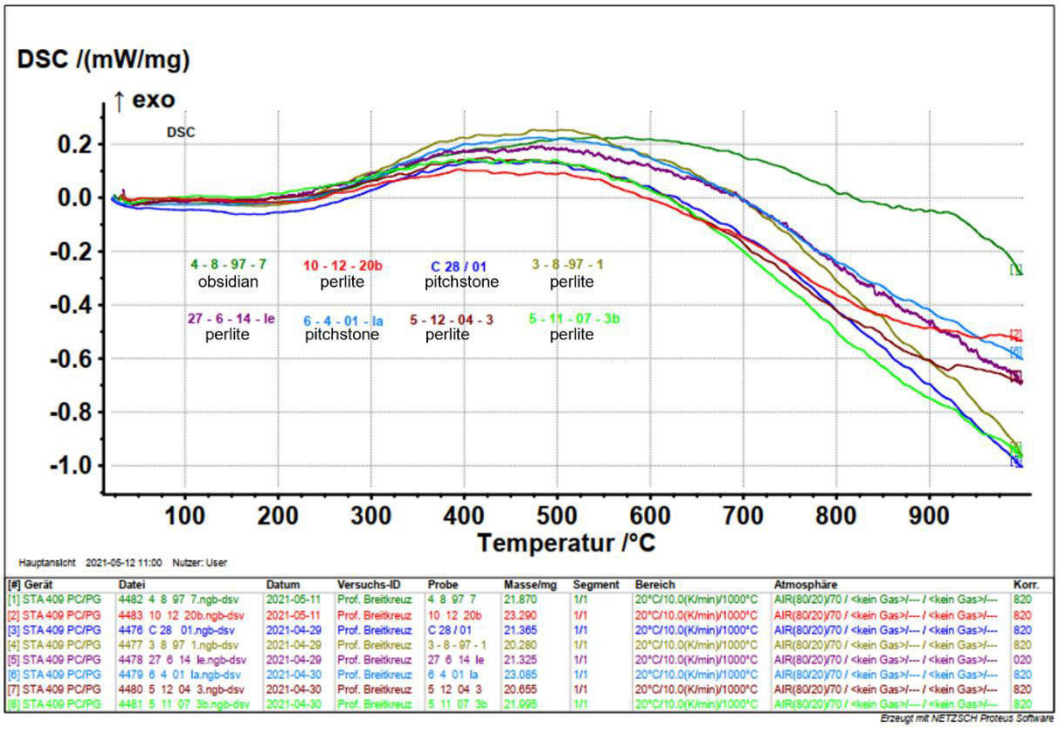

Fig. 31: Differential Scanning Calorimetry results for analyzed rock samples.

4.3. EMP Analysis

4.3.1. Procedure and sample selection

Electron microprobe analysis has been conducted on samples 5-12-04-3, 5-11-07-3b and 10-12-20b. The amount of measurement points and profiles can be seen in Tab. 11. As a starting point of each profile, a position outside the first visible crack was chosen and is referred to as “rim”. The profiles proceed from the rim to the center of a cell which is surrounded by sublinear fractures, referred to as “core”, and each profile contains four to ten measurement points. To demonstrate the positioning of the profiles, some exemplary profiles along the cracks can be seen in Fig. 32. The entire profiles for each thin section are provided in the attachment.

Tab. 11: Sample list of Electron Microprobe Analysis with number of measurement points and profiles. Samples are sorted from oldest to youngest.

SAMPLE	ORIGIN	MEASUREMENT POINTS	PROFILES	AGE	ROCK TYPE
5-11-07-3b	Argentina	82	12	Miocene	lava
5-12-04-3	El Salvador	102	18	Miocene-Quarternary	ignimbrite
10-12-20b	Milos	94	14	Late Quarternary	lava
	Total	278	44		

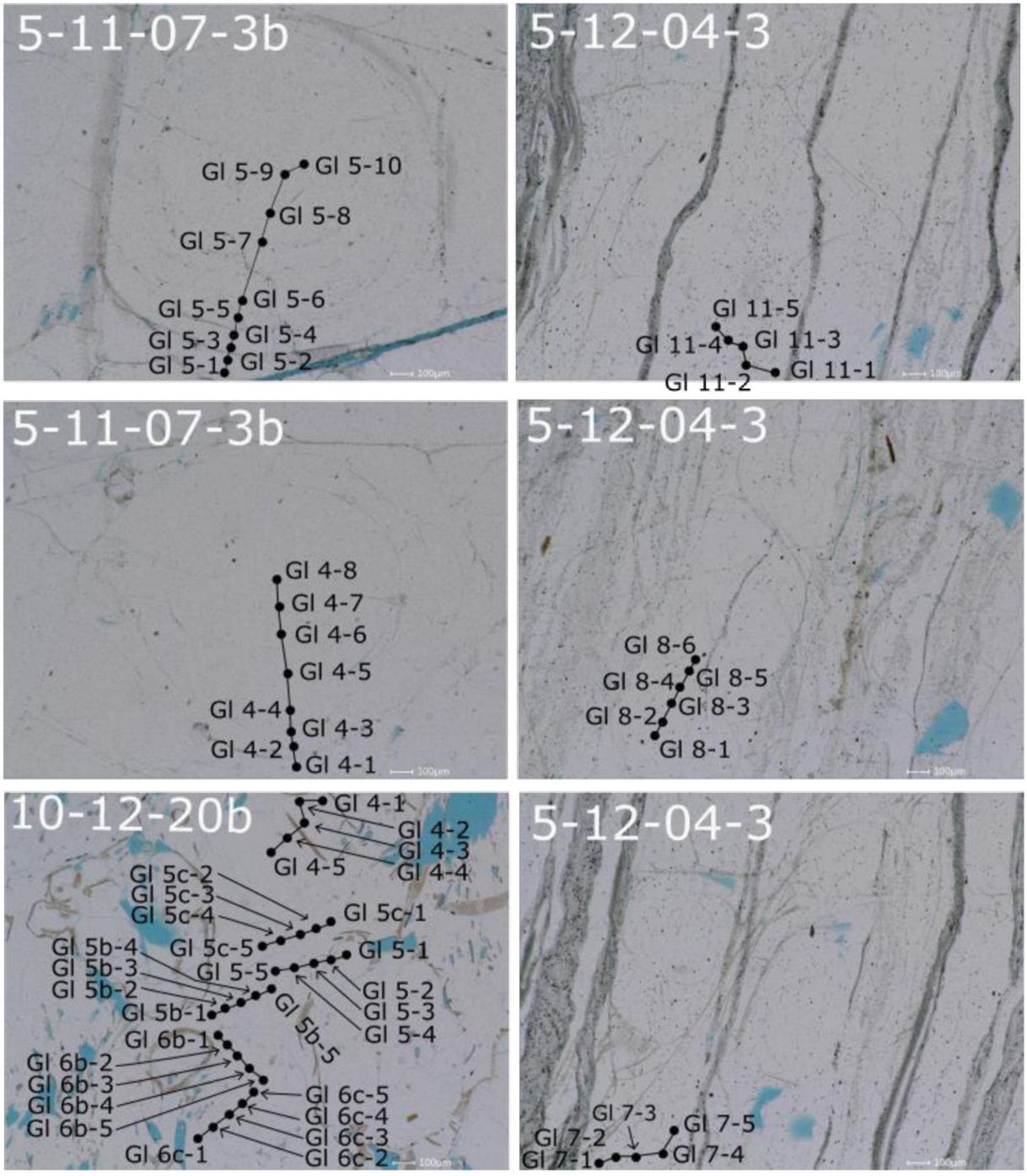

Fig. 32: Close-up images of certain measurement profiles.

The main target of microprobe analysis was to get a more detailed view into silica contents and alkali mobilities and into the amount of volatiles and fluids. The latter cannot be measured directly but can be calculated by subtracting the sum (total) of all elemental compounds, i.e. the water-free oxide composition, from 100, which correlates to the overall composition of 100%. This calculated number is afterwards referred to as either “100-Total” or “fluid/volatile content”. It has to be considered that this number is also not equivalent to the pure H_2O content, which would have required additional measurements. Other fluids, e.g. F^- or Cl^- might also be present and thus, be included in this computed number. For a study on primary fluid and volatile contents, the analysis of silicate-melt inclusions is

common. They form at high pressures and are enclosed in incompressible phenocrysts and hence may retain volatiles which would normally dissolve during degassing (Lowenstern, 1995). However, contrasts in viscosity and density between volatile-rich phases and the enclosing silica melt reinforce the separation between the two and the residual magma is assumed to be relatively depleted in volatiles (Davidson & Kamenetsky, 2007). Therefore, it can be expected that water represents the largest share of the calculated "100-Total".

4.3.2. EMP measurement results

SnO_2, MgO, TiO_2, Cr_2O_3, Cl, MnO and NiO contents are neglected in all three samples with amounts less than 0.13 wt.%. The same is applied for iron- and calcium oxide with an average of 0.59 and 0.57 wt.%, respectively. However, slight variations in CaO and MgO contents were observed for the El Salvador (5-12-04-3) sample when comparing contents on the rim and in the core. The average content of aluminum oxide is 12.32 wt.%. For a rough classification of the volcanic rocks, the sum of the alkali contents (Na_2O+K_2O) is plotted against the silica content (SiO_2) in a total-alkali-silica (TAS) diagram. All samples are rhyolitic with mean silica contents between 68.94 to 73.96 wt.%, whereby the Argentinian sample (5-11-07-3b) partly plots on the transition to dacites (Fig. 33).

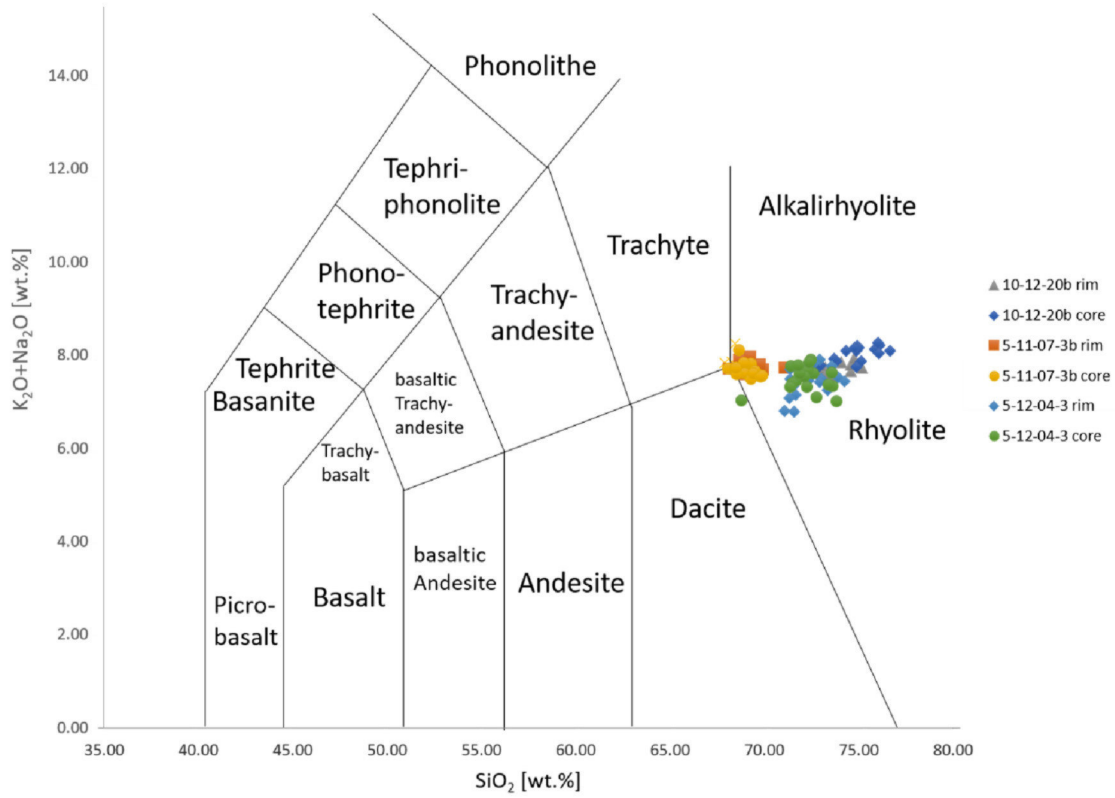

Fig. 33: TAS-Diagram of analyzed samples.

The spread in variations of alkali content with silica content is relatively low. In general, K_2O contents are significantly higher than Na_2O contents for all analyzed samples.

K_2O and Na_2O contents were plotted against silica contents and again there is no apparent trend for Argentina (5-11-07-3b) and El Salvador (5-12-04-3) with even distributions of potassium and sodium in rim and core and slight variations in K_2O and Na_2O of up to 2 wt.%. These variations are significantly smaller for Milos (10-12-20b), though, the spread in silica content is significantly larger with a higher SiO_2 content in general (Fig. 34).

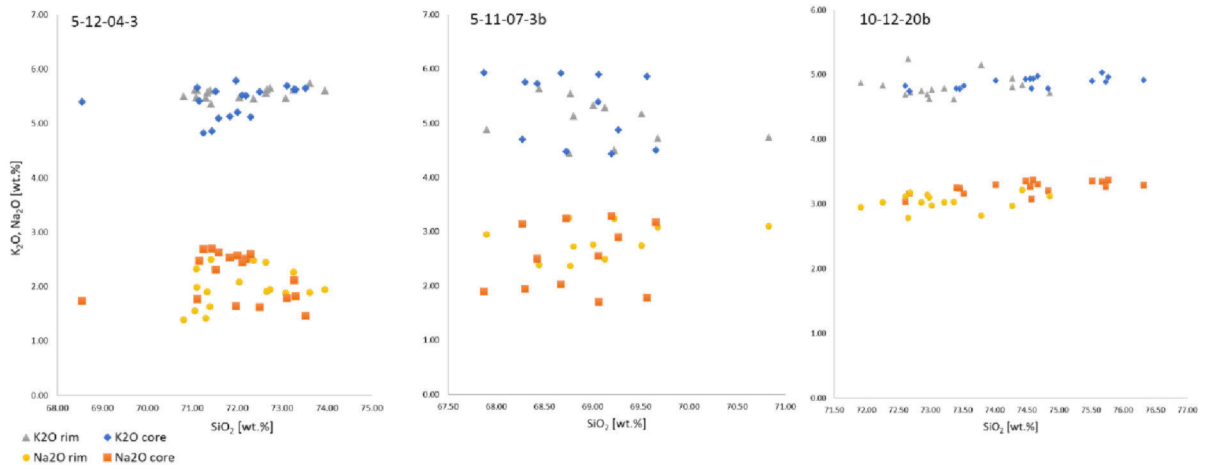

Fig. 34: K_2O and Na_2O contents plotted against silica contents.

Alkali contents were also plotted against "100-Total", and the exact same behavior as in Fig. 34can be observed, which shows that there are no significant variations in neither silica contents nor "100-Total" contents for El Salvador (5-12-04-3) and Argentina (5-11-073b) but stronger variations in alkali contents, whereas Milos (10-12-20b) represents the opposite situation for alkali-, fluid/volatile- and silica contents.

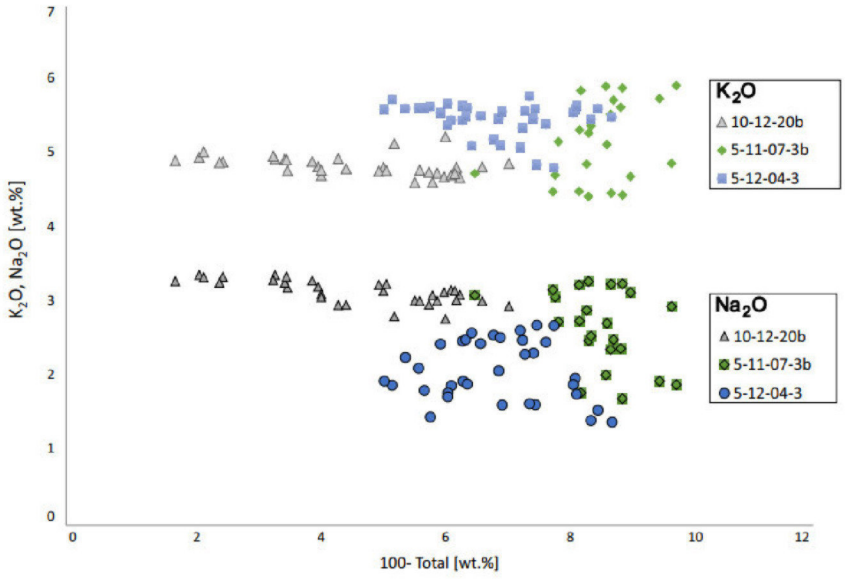

Fig. 35: K_2O and Na_2O contents plotted against volatile/fluid contents.

Considering the variations in “100-Total” along the profiles there is no general trend observable (Fig. 36). For El Salvador (5-12-04-3) and Argentina (5-11-07-3b), spreads in “100-total” are larger at the rim than closer to the core, but there is no general tendency of an increase or decrease from rim to core. Variability in general is the smalles for Argentina (5-11-07-3b). For the sample from Milos (10-12-20b), the spread at the rim is not larger, but there is an overall trend of slightly decreasing “100-Total” contents towards the center.

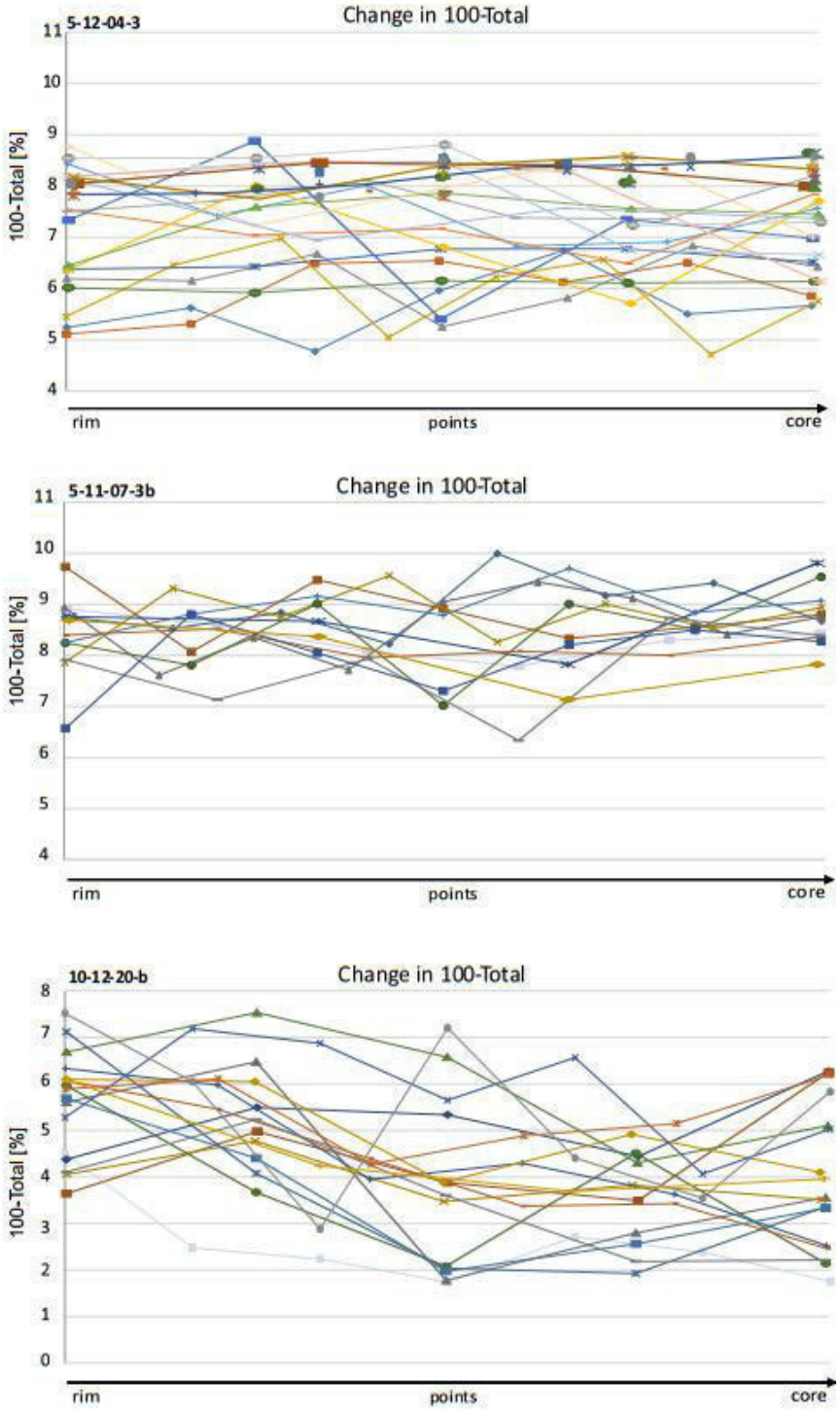

Fig. 36: Change of 100-Total contents along each profile proceeding from the rim (edge) towards the center of a cell (core).

Plots of K_2O against Na_2O contents for El Salvador (5-12-04-3) and Argentina (5-11-07-3b) show inversely proportional potassium and sodium contents, which means that potassium decreases with an increase in sodium for both rim and core (negative regression line; Fig. 37). The same situation can be observed for measurement points at the rim of the sample from Milos (10-12-20b). However, there is a reverse trend for measurement points at the cores, which show a proportional behavior, i.e. an increase in sodium with increasing potassium contents. The contents of both alkalis are lower at higher contents of fluids/volatiles and get higher when fluid/volatile contents get lower.

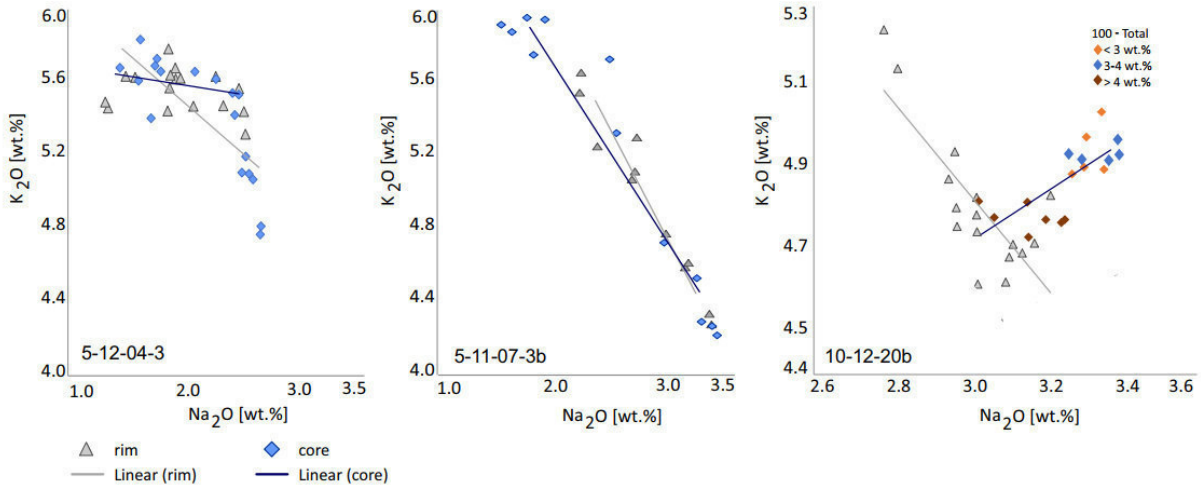

Fig. 37: K_2O plotted against Na_2O contents.

For an easier and condensed visualization of variations in alkali- and "100-Total" contents between rim and core, boxplot diagrams for each sample were compiled, which support previous observations (Fig. 38). Variations in sodium and potassium are the smallest for Milos (10-12-20b) whereas the spread in "100-Total" is the largest with most significant fluctuations in the core. For Argentina (5-11-07-3b) and El Salvador (5-12-04-3), variations in alkali contents are larger in the cores, while fluid/volatile content (100-Total) variations are smaller in the core. Considering absolute values, the boxplots show that there is no significant trend concerning an increase or decrease from rim to core in both, alkali and "100-Total" contents for Argentina (5-11-07-3b) and El Salvador (5-12-04-3), but again, the decrease in fluid/volatile contents from higher values in the rims to lower values towards the core with stronger fluctuations gets obvious for the Milos sample (10-12-20b).

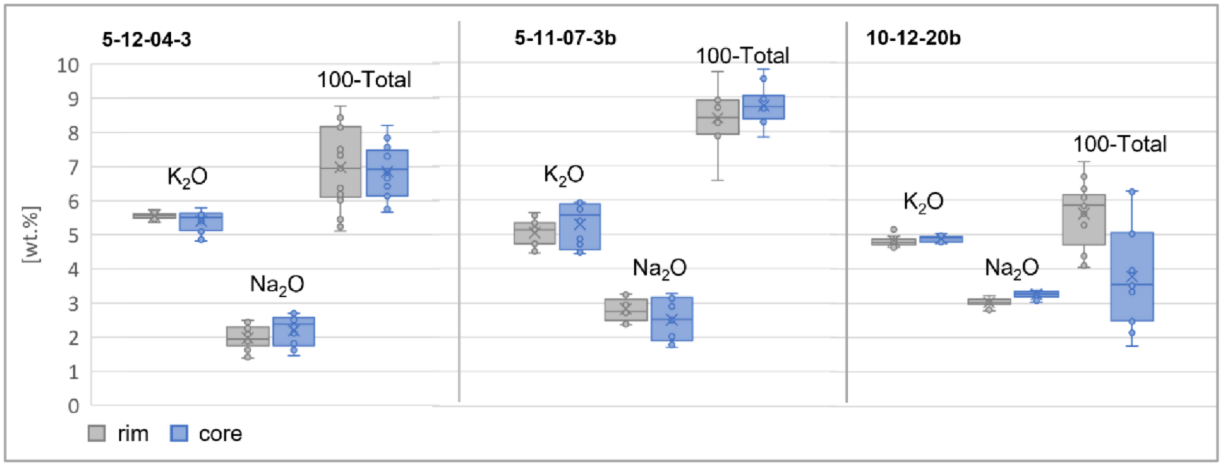

Fig. 38: Boxplots for variations in K_2O, Na_2O, and "100-Total" contents for rim (grey) and core (blue) for each analyzed sample; lowest point excluding any outliers= minimum of the data set, highest point excluding any outliers= maximum of the data set, box is drawn from Q1 (first or 25th quartile) to Q3 (third or 75th quartile) with a horizontal line drawn in the middle to denote the median (50th quartile, middle value of the data set), all other observed points are plotted as outliers (Dekking, 2005).

4.4. Fluid/Volatile contents

No measurements which directly measure the total pure H_2O content have been conducted. However, fluid/volatile contents could be acquired by thermoanalysis and computed from electron microprobe measurements. Summarized results can be seen in Tab. 12. For EMP measurements, mean values for each thin section are used.

Tab. 12: Fluid/Volatile contents measured with Thermo Gravimetry (TG) and calculated from Electron Microprobe Analysis (EMP)

SAMPLE	ROCK TYPE		AGE	WEIGHT LOSS TG [wt.%]	"100-TOTAL" EMP [wt.%]
4-8-97-7	obsidian	lava		0.23	
5-11-07-3a	obsidian	lava	Cenozoic	0.27	
10-12-20b	perlite	lava	Cenozoic	3.05	4.49
5-12-04-3	perlite	ignimbrite	Cenozoic	4.14	7.03
3-8-97-1	perlite	lava	Cenozoic	4.95	
27-6-14	perlite	lava	Cenozoic	3.75	
5-11-07-3b	perlite	lava	Cenozoic	4.06	8.57
6-4-01-1a	pitchstone	lava	pre-Cenozoic	7.68	
C 28-01	pitchstone	lava	pre-Cenozoic	7.15	

The obsidian glass analyzed in this study shows a weight loss of 0.23 wt.%, which fits to expected results for obsidians, typically comprising water contents below 2 wt.% (e.g. Angelopoulos et al., 2020). Previous studies suggested water contents between 2 and 5 wt.% for perlites and exceeding 5 wt.% for pitchstones (e.g. Le Maitre et al., 2002). Results from thermogravimetric analysis correlate very well to those predicted H_2O contents for the obsidians, perlites and pitchstones. Therefore, it is

assumed, that these results reflect the pure water content relatively well. Calculated results from microprobe analysis are slightly above the expected values (Tab. 12).

From all conducted analysis on fluid contents, it is evident that each sample of perlites shows elevated water contents with pitchstones containing even higher amounts of water. Therefore, every analyzed sample which shows perlitic fractures has also got hydrated at one point or during a protracted time span of its history.

4.5. Crackled glass

Further investigations of the fracture behavior of the crackled glass show that the fracture network is constructed in the same way as it is observed in perlitized volcanic glass (Fig. 39). A set of sublinear quench fractures with interjacent spherical fractures can be clearly recognized.

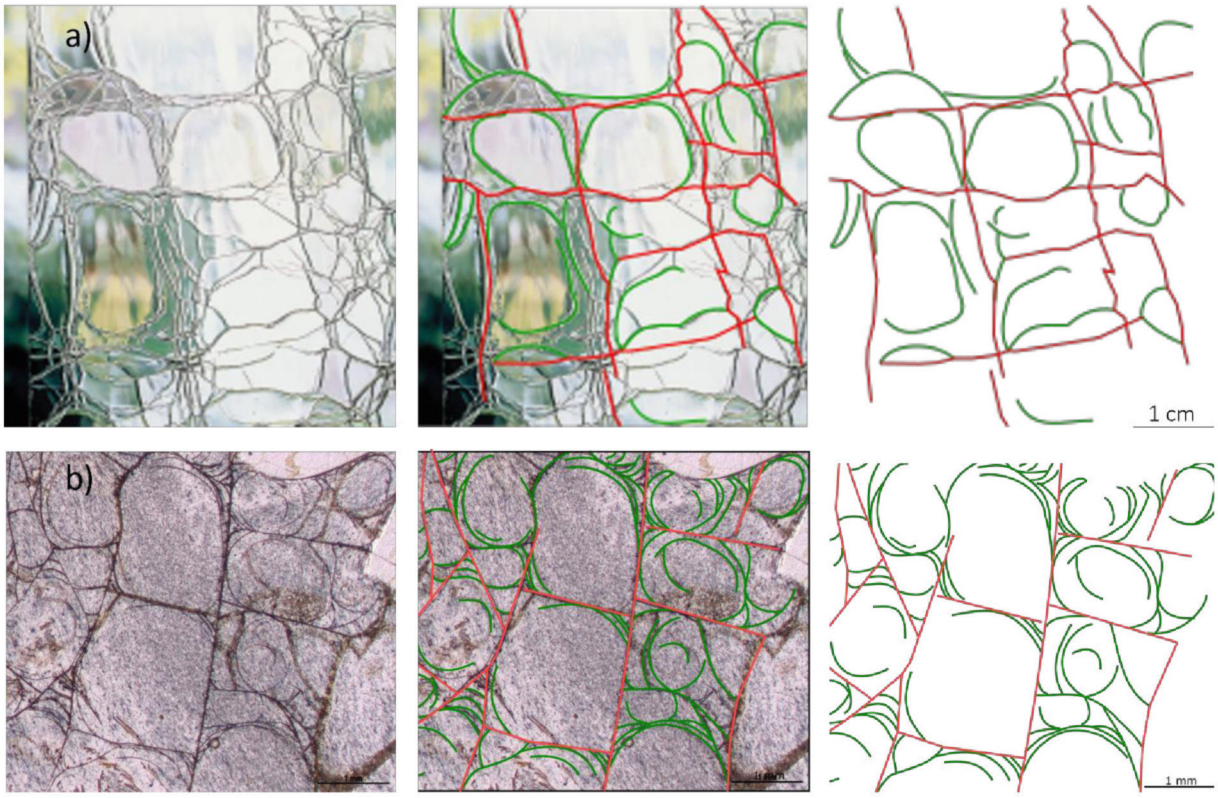

Fig. 39: Comparison of fracture network in artificially produced glass vs. volcanic glass; a) artificially produced crackled glass; b) thin section; sample 27-6-14-1e.

4.6. Thermo shock experiments

Thermo shock on pure obisidan samples (27-7-97-2 & 3-12-04-2) at ΔT= ~ 280 °C resulted in a coherent fracture network, which gets well visible under UV light (Fig. 40a & b) but is also visible under normal light on un-polished sides of the cubes (Fig. 40c & d).

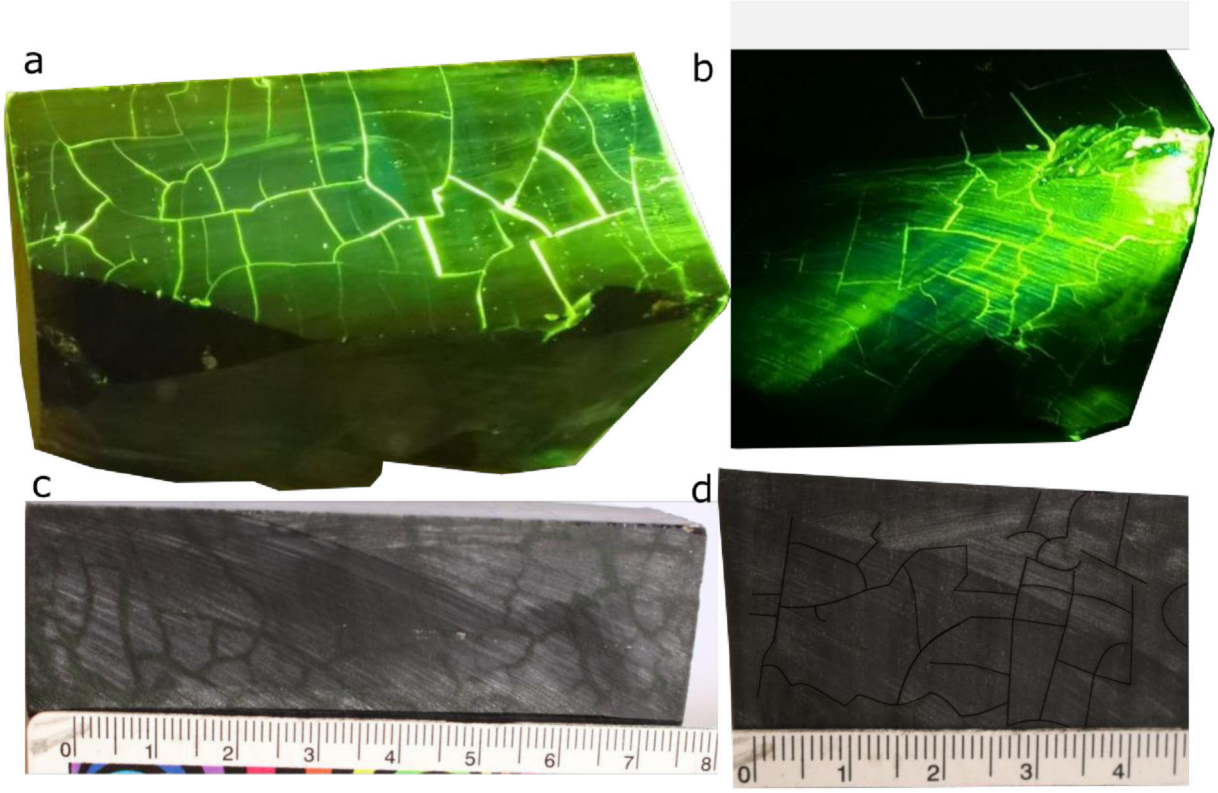

Fig. 40: Fractures after thermal shock, a) & b) under UV light, c) & d) under daylight after drying (for better visibility fractures were traced with black color in d)); sample 27-7-97-2 (a & c) & 3-12-04-2 (b & d).

The cracks can be traced along edges of the cubes, which implies that the thermal shock produced a three-dimensional fracture network (Fig. 41a & b). The network consists primarily of sublinear fractures (Fig. 41d, red), which stand perpendicular on top of each other. Besides, minor numbers of curved fractures can be observed, which occur especially in between cells formed by the sublinear cracks or originate from terminations of them (Fig. 41d, green).

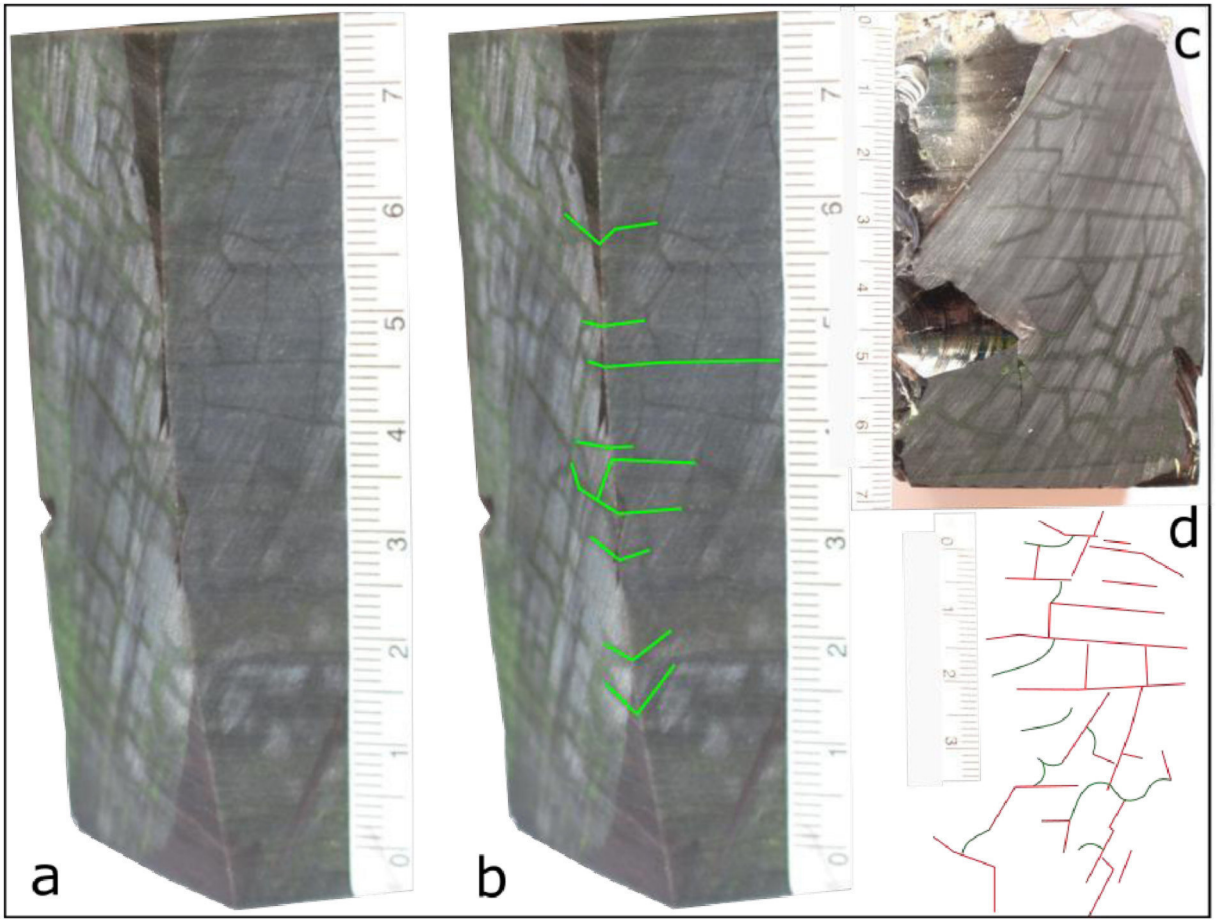

Fig. 41: a) & b) Fractures produced by thermal shock can be traced along the edges; sample 3-12-04-2; c) & d) fracture network consisting of sublinear and linear cracks; sample 27-7-97-2.

4.7. Stochastic geometry and image analysis

4.7.1. Line, fibre, and surface processes

On average, three to four images per thin section were analyzed and for each, the following parameters were calculated by the software:

- Line densities: $L_{A,p}$ (primary), $L_{A,s}$(secondary), $L_{A,u}$ (unknown, if available), and $L_{A,t}$ (total)
- histogram of directions for primary, secondary, and unknown (if available)
- specific length of green depending on distance to red cracks

As already mentioned (chapter 3.2.7.), a subdivision was made into sublinear and rounded (perlitic) cracks, genetically referred to as “primary” and “secondary”, respectively. From the line densities, the specific crack area S_V was calculated as well as the proportion of each color system of the total. As a next step, the weighted average of each of these parameters was determined for all images belonging to the same thin section in order to obtain the mean values for each individual thin section (for results see electronic appendix). The minimum, maximum, and mean line densities as well as the specific crack

areas S_v for the red sublinear, the green perlitic and the orange unassignable cracks can be seen in Tab. 13.

Tab. 13: line densities L_A, specific crack areas S_V, and proportions of line densities for primary (p), secondary (s), unknown (u), and total (t); * marks edited values.

	$L_{A,p}$	$L_{A,s}$	$L_{A,u}$	$L_{A,t}$	$S_{v,p}$	$S_{v,s}$	$S_{v,u}$	$S_{v,t}$	$\frac{L_{A,p}}{L_{A,t}}$	$\frac{L_{A,s}}{L_{A,t}}$	$\frac{L_{A,u}}{L_{A,t}}$
	mm^{-1}	mm^{-1}	mm^{-1}	mm^{-1}	mm^{-1}	mm^{-1}	mm^{-1}	mm^{-1}	-	-	-
min	0.00	0.38	0.00	0.62	0.00	0.48	0.00	0.79	0.00	0.36	0.00
max	1.14	2.61	0.37	3.30	1.45	3.32	0.47	4.20	0.63	1.00	0.14
mean	0.48	1.47	0.03	1.93	0.61	1.87	0.00	2.46	0.24	0.76	0.02
min*	0.05	0.38	0.02	0.62	0.06	0.48	0.03	0.79	0.06	0.36	0.01
max*	1.14	2.61	0.37	3.30	1.45	3.32	0.47	4.20	0.63	0.94	0.14
mean*	0.49	1.47	0.10	1.93	0.63	1.87	0.12	2.46	0.25	0.75	0.05

In some images, no primary and unidentifiable cracks were recognizable; hence, the upper part of the Table represents the original results before eliminating samples without data and the lower part (marked with *) shows the results after deleting those zero-values. As there are only very few samples where the red sublinear cracks are missing, results are almost unchanged after editing, whereas the opposite is true for the unknown fractures.

Considering the original results, the red cracks make up approximately a quarter of the total line densities whereas the curved (green) cracks occupies three-fourths (Tab. 13). Due to the fact that orange cracks make up an extremely slight percentage with a mean proportion of 2 % from the total, they are ignored during further evaluations and discussions. It would be expected that the computed result of $L_{A\,tot}$, which corresponds to $L_{A,p+s+u}$ equals the sum of $L_{A,p} + L_{A,s} + L_{A,u}$; however, there are slight deviations which arise from the fact that red, green, and orange partially touch or even overlap.

In general, the specific crack area of the rounded (green) fractures is about three times as high as of the sublinear (red) ones. A plot of red vs. green line densities shows a directly proportional relation (Fig. 42). The coefficient of determination R^2 is 0.189. The value is very close to 0, which means that there is no significant relationship between the two variables. However, a clear trend can be observed and a higher correlation could be achieved if outliers were neglected.

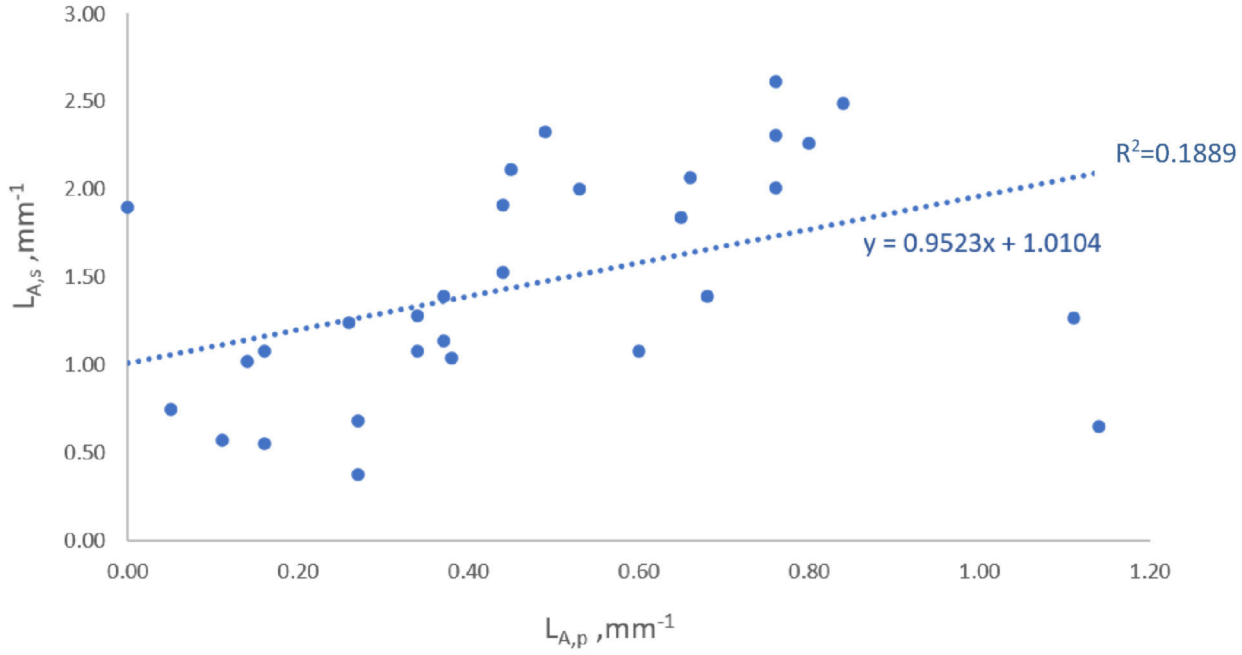

Fig. 42: Plot of $L_{A\ red}$ against $L_{A\ green}$

Plots of the specific length of green cracks in dependence on distance to red cracks show a similar trend in most cases (Fig. 43). First there is a rise in the curve from a distance of 0 mm up to a maximum at distances between 0.05 and 0.10 mm. Then the curve drops sharply and continues to decrease asymptotically until a distance of 1 mm is reached. In some cases, no peak of the curve is visible but yet, a decrease from 0 to 1 mm distance can be observed for nearly every sample.

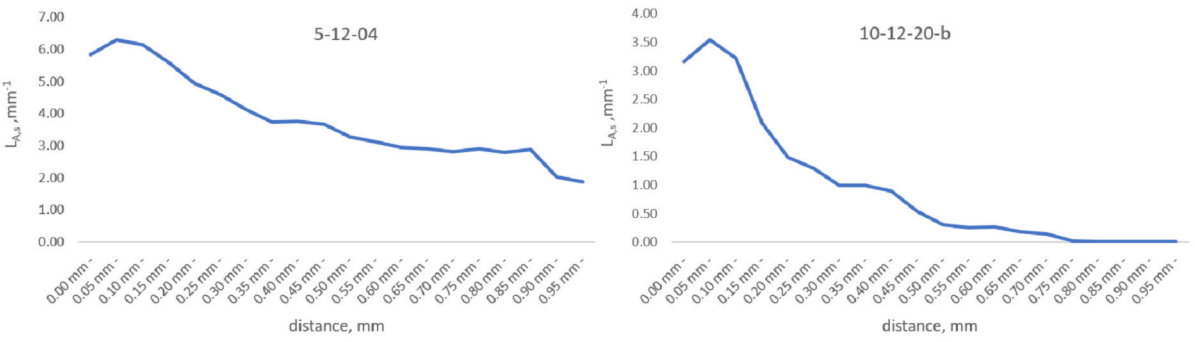

Fig. 43: Specific length density of green depending on distance to red cracks for two samples 5-12-04-3 and 10-12-20-b.

Line densities for perlitic cracks were plotted against microprobe-, thermoanalysis-, and porosity results (Fig. 44). There is no trend recognizable for both fluid- and alkali contents whereas porosities are decreasing with increasing line density.

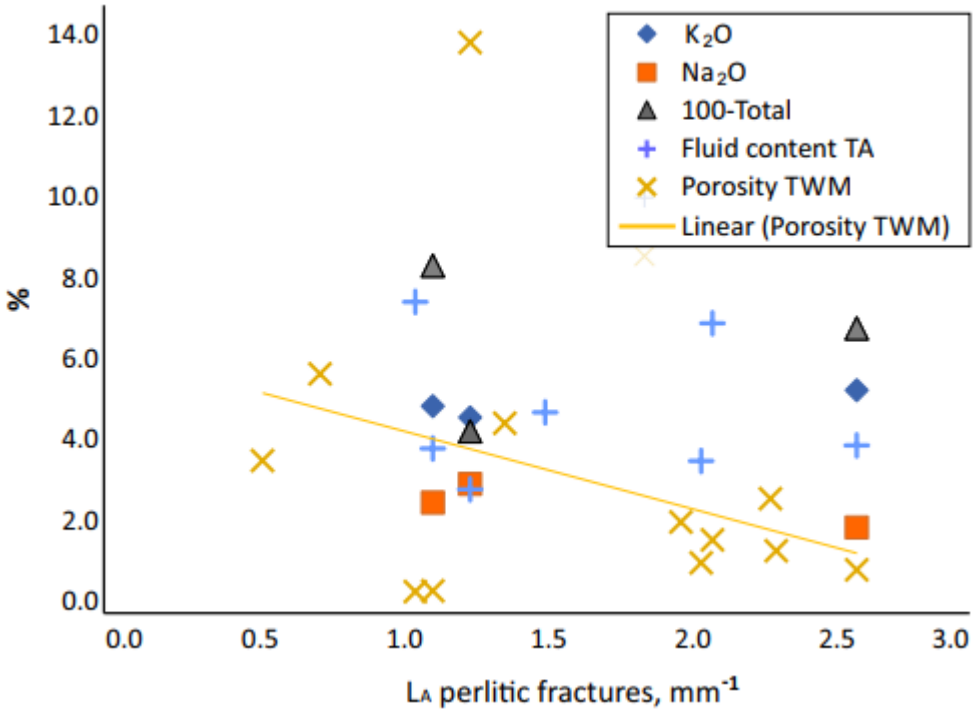

Fig. 44: Plot of line densities of perlitic fractures against K_2O, Na_2O, 100-Total (obtained from microprobe analysis), fluid contents (obtained from thermo gravimetry) and porosity (obtained from TWM).

4.7.2. Random tessellations and geometrical networks

The results of estimating the mean number of vertices per unit area λ_0, the mean number of cells per unit area λ_2, and the mean cell area $\bar{a}$ for ten sections within one thin section can be seen in Tab. 14 (for complete results see appendix). The calculations yield a total mean cell area of 6.21 mm^2 for the whole sample 5-12-04-3.

Tab. 14: Estimated values for λ_0, λ_2, and $\bar{a}$.

SAMPLE	λ_0 mm^{-2}	λ_2 mm^{-2}	$\bar{a}$ mm^2
5-12-04-3_1	0.26	0.13	7.68
5-12-04-3_3	0.16	0.08	12.29
5-12-04-3_4	0.16	0.08	12.29
5-12-04-3_5	0.26	0.16	6.26
5-12-04-3_6	0.58	0.29	3.48
5-12-04-3_7	0.64	0.29	3.48
5-12-04-3_8	1.02	0.54	1.84
5-12-04-3_9	0.32	0.13	7.82
5-12-04-3_10	0.58	0.29	3.48
5-12-04-3_11	0.58	0.29	3.48

4.7.3. Curvature calculation

The curvature estimation is demonstrated on one perlitic fracture (Fig. 45). Tangent lines were fitted to both ends of the crack lines in the two points $x(0)$ and $x(1)$. Then the angle between the radii to each point is measured to obtain the curvature of the crack.

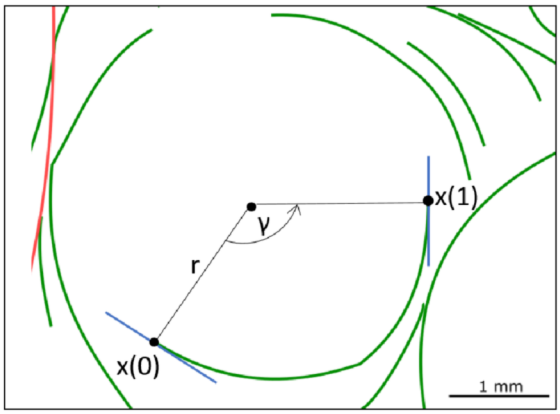

Fig. 45: Illustration of a curvature x(t); blue: tangents at the start and end point of the curve.

The integral can be calculated as following:

$$\gamma = \int_0^1 \kappa(t)dt = \int_0^1 \frac{1}{r(t)}dt$$

As explained above, the angle γ can now be determined directly from the graphical solution. For the illustrated case (Fig. 45), γ=125°. This result can now be expressed as the fraction of a full circle (γ=2π), yielding a percentage value of 34.72 %. According to the classification that was introducted in chapter 4.1.4. (Tab. 9) this value is < 90°, which means that the analyzed section of a perlitic fracture falls into the category “quarter circle or smaller” when describing the fracture in terms of fractions of a full circle.

4.8. Porosity & Permeability

4.8.1. Microscopic observations

In several analyzed thin sections of both lava and ignimbrites, an aperture of perlitic fractures is observed (e.g. Fig. 46). A semi-quantitative measure of some fractures showed an aperture with a width of up to 0.1 µm.

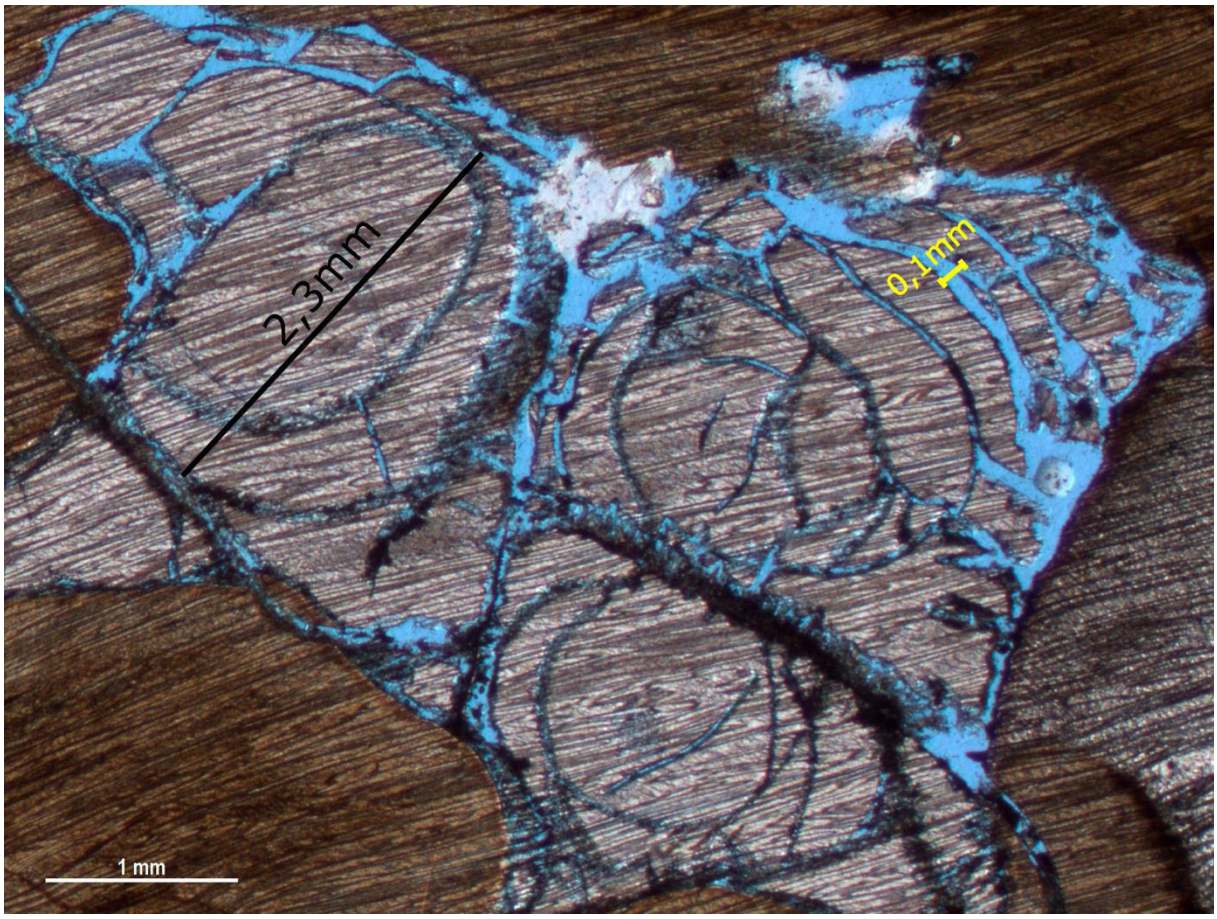

Fig. 46: Crack porosity caused by dissolution; blue epoxy resin identifies open pore space; sample 1-8-97-7b.

4.8.2. Porosity and permeability measurements

Due to previously stated problems in core plug preparation (see chapter 4.2.6.), the helium pycnometer and gas permeameter could only be used on one particular, untreated sample (1-8-97-3b). Additionally, porosities could not be measured for the remaining samples as most of them are impregnated with epoxy resin, which occludes free pore space, and, hence, result in zero porosity and permeability. For those reasons, estimates of porosity and permeability are not key aspects of this thesis, but help delineate the characteristic dynamic range of reservoir property values.

The Triple Weight Method is not dependent on the sample´s shape but the error increases with the sample size. With this method, the effective pore space is measured. Thus, both He-porosity and

porosity obtained from the Triple Weight Method measure the effective porosity of a sample. Varying results for effective porosity can be expected due to distinctly different shape, macroscopically observable porosity, and the general appearance (e.g. very dense rock vs. brittle samples) of the analyzed samples. Effective porosities range from 0.52 to 14.08 % (Tab. 15). The only successful permeability measurement yielded a value of 1.817 mD.

Porosities are generally higher in undevitrified lava samples without significant mineral precipitation (e.g. 10-12-20b) with a range between 5 to almost 15 %. A strong decrease in porosity down to values between 1.5 – 3 % can be observed for lava samples with alteration features (e.g. 27-6-14-1e) and for devitrified rocks (13-12-04-1). Pre-Cenozoic lava samples (C 28-01 & 6-4-01-1a) contain the least pore space with porosities of 0.5 to 1.8 %. Only two ignimbrites were analyzed with generally low porosities between 1.1 to 3.8 %. Due to a limited amount of glass shards consisting of perlitic cracks and a crack-free matrix in ignimbrites, it is difficult to draw general conclusions on pore space behavior in analyzed samples.

Tab. 15: Porosity and Permeability results; blue: lava, orange: ignimbrite; bold: Cenozoic, not bold: pre-Cenozoic; TWM= Tripple Weight Method; He Pycn.= Helium Pycnometer.

SAMPLE	POROSITY, %		PERMEABILITY,	SAMPLE
	TWM	HE PYCN.	mD	CHARACTERISTICS
1-8-97-3b	4.69	7.76	1.817	mostly no min. precip.
9-9-01	5.90			highly porphyritic, no min. precip.
10-12-20b	14.08			no mineral precipitation, highly perlitized
13-12-04-1	1.54			fully devitrified, not fully perlitized
27-6-14-1e	1.24			partly strong min. precip.
Tokai 24-1	2.82			mostly no min. precip., not fully perlitized
Tokai 24-1	2.24			mostly no min. precip., not fully perlitized
C 28-01	1.81			partly strong min. precip., partly second generation of less alteration
6-4-01-1a	0.52			strong min. precip., cracks healed in some areas
5-12-04-3	1.06			in most areas no alteration, partly phyllosilicates along the cracks
Fl 93	3.76			perlitization limited to fiamme, strongly devitrified, min. precip.

5. Discussion

Previously stated results of thin section analysis, DSC and TG measurements, electron microprobe analysis, stochastic image analysis, porosity and permeability estimations, thermo shock experiments, and conclusions drawn from comparison with artificially produced glass are discussed within the next chapters. The discussion is separated into different aspects according to diverse problems covered in this thesis. The focus is on geometric aspects, particularly the three-dimensional geometry and the perlitic fracture network, textural characteristics, also with respect to reservoir space, fluid contents and chemical compositions/changes in perlitic rocks. As a last, different crack formation- and propagation mechanisms and processes are discussed.

5.1. Geometric aspects

5.1.1. 3D-Geometry

A fully perlitized sample was used for the investigation of the three-dimensional geometry of perlitic fracture domains (Fig. 15). Additionally, CT measurements were conducted on the same sample (5-11-07-3b) and on a second sample (5-12-04-3) to analyse the 3D fracture network.

The investigation of the intersected rock sample and CT results illustrate that perlitic fractures are a three-dimensional phenomenon of spherical to ellipsoid shape, which in turn underscores that a three-dimensional (paleo)stress or strain regime must prevail for the cracks to develop. Consequently, perlitic fracturing is not an effect which only occurs in one plane of a solidified lava or ignimbrite but is influenced by a three-dimensional stress or strain field.

5.1.2. Fracture systems

Thin section analysis made already clear that perlitic fractures are generally positioned within cells, which are formed by sublinear fractures, yet they never intersect them. With respect to establishing a chronological order, this hierarchical behavior is clear evidence that sublinear cracks form the primary generation of fracture types in the network, whereas the perlitic fractures are secondary.

The comparison of red and green line densities, estimated by image analysis, shows a clear trend of increasing green crack densities with an increasing number of red cracks. Therefore, it can be concluded that their formation is in a direct relationship to one another, and the more sublinear cracks are originally present the more likely it is to have a higher number of perlitic cracks.

Even though it is expected that the perlitic cracks originate from the sublinear primary cracks, the calculation of the specific crack areas emphasizes the prevalence of the perlitic compared to the sublinear fractures with average line densities and specific areas three times as high (mean line density of perlitic fractures: 1.47 mm^{-1} and of sublinear fractures: 0.48 mm^{-1}; mean specific area of perlitic

fractures: 1.87 mm^{-1} and of sublinear fractures: 0.61 mm^{-1}). The primary cracks, however, are more continuous while the perlitic cracks seem to propagate from the outside to the inner side of the cells.

These assumptions are also highlighted by the estimation of the specific length densities of the perlitic cracks in dependence on distance to the red cracks. The high number of perlitic fractures which lie in a distance-range from 0 to 0.2 mm, with a continuous decrease in line densities towards the cores of the cells, support the suggestion that the green cracks have their origin close to the primary sublinear cracks and then proceed to certain degrees to the cell centers. For samples which show line densities of 0 mm^{-1}, i.e. no fractures from a certain distance from the sublinear fractures towards the core of a cell, it can be said that the growth of the perlitic cracks probably terminated after a given time. The peak around 0.05 mm shows that it is more likely to find the first perlitic crack "shell" not directly touching or overlapping the primary cracks but within a short distance.

Davis & McPhie (1996) already recognized the presence of different fracture types related to the occurrence of perlitic fractures on one rhyolite dyke. They suggested that the rapid cooling led to contraction and the formation of long fractures, which are perpendicular to the dyke walls at temperatures already below T_g (Fig. 47 I a). Further cooling resulted in a second set of quench fractures which they called cross fractures (Fig. 47 I b) and finally, the hydration of this rapidly chilled glass yielded in the formation of the perlitic fractures within the two other sets of quench fractures (Fig. 47 I c).

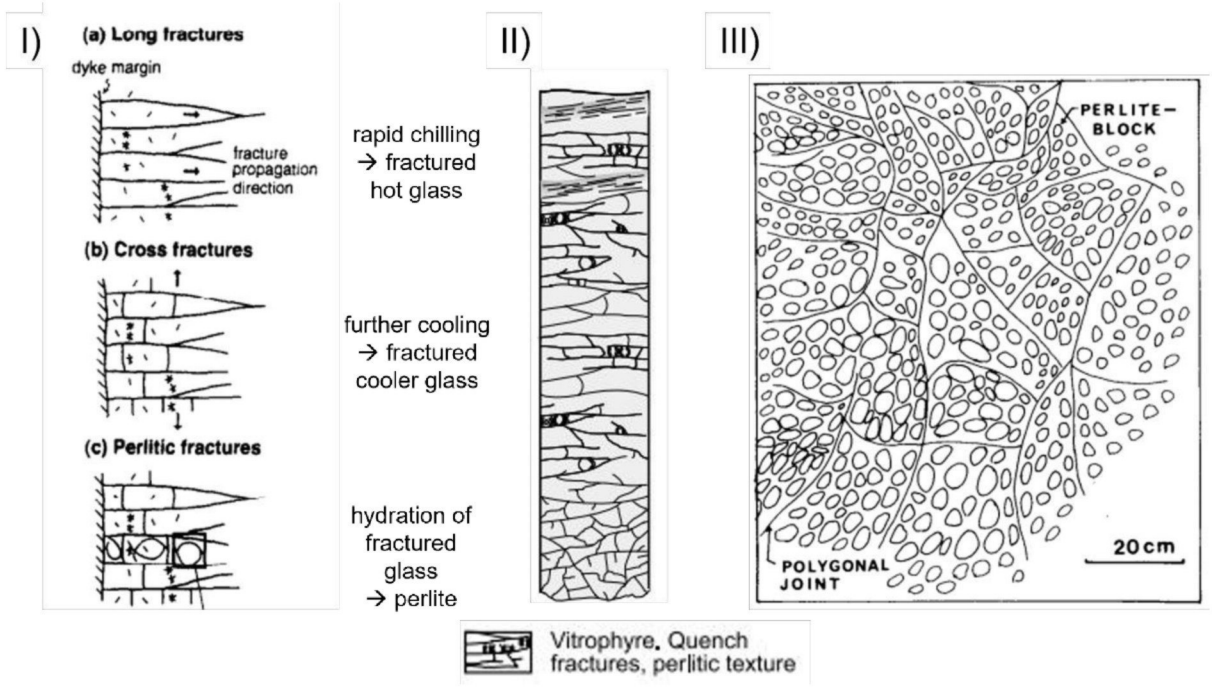

Fig. 47: I) Textural evolution for a rhyolite dyke after Davis & McPhie (1996); II) orientation of perlitic fracture network in an oriented core after Sruoga et al (2004); III) unoriented joints with perlitic fractures after Yamagashi & Goto (1992).

Those long and cross fractures observed by Davis & McPhie (1996) correspond to our sublinear fractures and form the same cells as described in previous chapters (see 4.1.). However, a difference between long and cross fractures as well as the preferred fracture propagation direction could not be observed in all examined samples. Two possible explanations or reasons might be (1) the small-scale thin section observations, which prevented to see the "big picture" of the fracture network, and (2) the unavailable original coordinate system of the hand samples, which makes it simply impossible to determine a fracture propagation direction. Nevertheless, the observations of Davis & McPhie (1996) on preferred directions are consistent with those described by Sruoga et al. (2004), who illustrated the same fracture propagation direction (Fig. 47 II). The suggestion concerning the two generations of linear quench fractures in turn is consistent with the findings from Yamagashi & Goto (1992), who assumed first and second order contraction to be the reason for columnar and polygonal joints, respectively. However, they pictured the quenching fractures on a macroscopic scale (Fig. 47 III) without any preferred propagation direction. Therefore, it cannot be said for sure that they always propagate in a special relation to the dyke margin, but it cannot be excluded that they do so in some cases. The same also applies for the two-generation model of the sublinear cracks. Fig. 48 shows a thin section of one analyzed sample which illustrates a possible quench fracturing in two steps: 1. long fractures and 2. cross fractures.

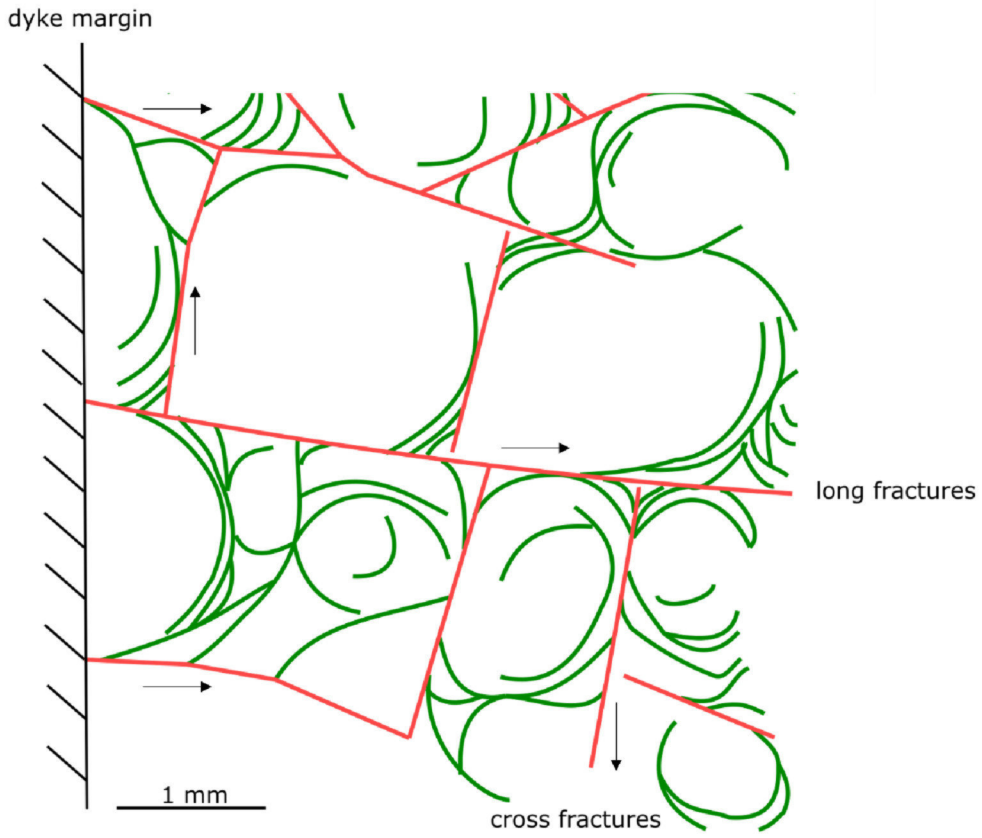

Fig. 48: Two potential sets of quench fractures (1. long fractures, 2. cross fractures) with perlitic fractures enclosed; possible (assumed) position of dyke margin is indicated; arrows indicate the direction of long- & cross fractures; sample 27-6-14-1e.

However, the findings on the origin of the sublinear fractures are consistent, i.e. quenching is timed directly after emplacement of a cooling unit. Thermo shock experiments proved that a rapid change in temperature results in the observed cell-like arrangement of those sublinear quench fractures (see also chapter 5.6.1.). Different authors described them as quenching-, polygonal- or columnar fractures or joints (e.g. Denton et al., 2012).

On a larger scale it was also found during field observations, that the fracture morphology and spacing change with their position in a lava, which is very likely related to changes in cooling rate inwards from the margin of a cooling body. According to Denton et al. (2012), an increasing spacing between the columnar joints from the margin to the core reflects a decrease in cooling rates.

The relative position of the analyzed thin section samples within the cooling body is unknown, but it is likely that samples, which show increased spacing between the sublinear fractures, were positioned more inwards and therefore experienced lower cooling rates. However, fracture spacing is probably not only dependent on the position within the cooling body, but also on the rock properties itself and the rock´s reaction to changes in temperature. Therefore, spacings cannot be compared directly between different samples. For a useful evaluation, various samples from the same lava or ignimbrite at different positions from margin to core would need to be analyzed.

It is obvious from various thin section images and is proven by image analysis (calculation of distances of rounded to sublinear fractures; see chapter 4.7.) that perlitic fractures are mostly concentrated on the edges between two sublinear cracks. Edges in general always represent points of lowest strength and in material sciences they are referred to as tension- or stress peaks. Therefore, it makes sense that those points of weakness depict the origin for the propagation of a further generation of fractures, i.e. the perlitic fractures.

Thin section analysis showed that there are no perlitic fractures in samples which are free from quench fractures, which already led to the assumption that these two fracture systems (sublinear and rounded) are connected. This finding was supported by the results of microprobe analyses (see chapter 4.3. and 5.4.): Observed fluid- and alkali mobilities or rather changing contents of alkalis and fluids from the rim (close to the cell edges formed by sublinear fractures) to the core of a perlitic crack (i.e. the core of a cell) demonstrated that the two fractures systems are in correspondence and form an effective fracture network which is substantial for considerations regarding hydrocarbon storage and geothermal energy production (see chapter 5.8.). Statistical image analysis on primary and secondary fracture densities provided further evidence for the relation between the two and showed a direct proportional relationship, which means that the number of perlitic fractures rises with increasing quench fractures (see chapter. 4.7. and 5.5.).

The unidentifiable cracks are most likely either quench fractures or perlitic cracks which are not fully developed or could not propagate and can therefore not be clearly identified. Moreover, they are only recognizable in a small number of analyzed samples and were not considered as meaningful in terms of any interpretations and therefore ignored in the following chapters.

Closer statistical evaluations of rose diagrams were considered as unnecessary and caused some problems due to several reasons: First, samples were not taken oriented, which precludes predictions of absolute directions. Second, as discussed in previous chapters and as can be seen in Fig. 5, the round fractures are mostly concentrated at the edges of each cell; hence, considering distributions of directions for each individual cell would be meaningful to quantify this statement in a mathematical sense. However, due to the fact that the red fractures are not consistently orientated within one thin section and roses of directions were computed for one thin section as a whole, results do not reflect the expected outcome.

5.2. Textural characteristics and pore space prediction

5.2.1. Differences between perlitization in lavas and ignimbrites

The main reason for the different degrees of perlitization within ignimbrites lies in the varying extent of compaction. Certain samples (e.g. 11497 & 11510) show significant linear textures within the fiamme, whereas the matrix remained less compacted. This implies that the characteristic elongated fabric already originated in the vent due to shearing processes and not due to in-situ welding compaction. As a result, the mechanical difference between the coherent, tighter fiamme and the less compacted matrix provides a physical border for the cracks to propagate from the fiamme into the matrix.

The high degree of welding within the matrix as well as the texture of the matrix, which is parallel to the lineation within the fiamme, indicates that the texture develops in-situ through welding compaction. Consequently, the physical difference between fiamme and matrix is relatively small, and the cracks can also spread in the matrix (e.g. 44.20 I). In some cases, the fiamme contain volatiles, which makes them softer compared to the melt shard matrix. The observation of the propagation of perlitic cracks within ignimbrites gives an indication of the degree of matrix compaction and consequently of the position within a cooling unit in terms of welded or non-welded, eutaxitic or parataxitic zone (Allen, 1988).

It was stated by Allen (1988), that a continuous perlitic texture is characteristic for a coherent glassy lava and not for pyroclasts. However, this suggestion cannot be generally supported by the findings of the investigations, as continuous perlitic textures can also be found in several ignimbrite samples (e.g. 44.20 I & P 1500a) as described in previous chapters.

The fractures in the fiammes, however, do not encroach upon the uncompacted matrix of the rock (e.g. 11510). The edges of the obsidian clasts in the investigated lava breccia (Ad-18) serve the same purpose as the sublinear fractures and as the edges of the fiamme: They depict a boundary for the propagation of the perlitic fractures. In the special case of the breccia, the fracture network gives evidence that brecciation must have happened before perlitic fracturing. Consequently, a perlitic fracture formation during a still hot stage of the lava, in which brecciation happened, can be excluded.

5.2.2. Size ratios and degree of perlitization

Diameters of perlitic fractures are measured and are examined regarding age and rock type (i.e. lava or ignimbrite). There is no trend visible in the change of bead diameters with geologic age which indicates that the age of the rock has no influence on diameter size. Consequently, it is very likely that diameter sizes of perlitic fractures are rather dependent on intrinsic rock parameters than on age. The calculation of average diameter sizes for lava and ignimbrites shows a higher value for lava samples, which could imply that glassy lava is more suited for a larger expansion of the cracks. However, it has to be considered that development of longer cracks in ignimbrites is opportunity-limited, since cracks here are mostly limited to fiamme, which often occupy less space and would thus prohibit or limit a further expansion. Moreover, diameters are strongly varying among both lava and ignimbrite samples and the mean value is perhaps not a suitable representation.

Log-normal distributions have been determined for perlitic bead diameters by Denton et al. (2012): It was proven for the first time that the distributions are similar to particle size distributions of clastic and fluvial sediments as well as vesicle size distributions. It was also found that size range covers several orders of magnitude from small to large cracks and the tail towards higher values in diameter suggests that there is a high probability to find fractures with diameters which are too large to be observed under the microscope but are visible in the field. This observation might probably be true due to the fact that some investigated samples of this thesis, show bead sizes that are too large to be measured under the microscope (e.g. Tokai 1 & 2, 5-11-07-3b). Therefore, it cannot be excluded that there might be cases where fractures are even larger than common thin section sizes. However, there is no example among the analyzed rock samples where fractures of that magnitude could have been observed so far.

The basic idea behind considering curvatures of the perlitic cracks was to draw conclusions about the propagation of the fractures. Despite the fact that those results are based on a manual estimation and that the estimation in turn is influenced by several factors as described in chapter 4.1.4, different trends when comparing samples older than Cenozoic and young samples of Cenozoic age and also when comparing lava and ignimbrites could be observed (Fig. 21). Old samples and ignimbrites show a more even distribution between strongly (i.e. full circle) and slightly rounded (i.e. quarter circle)

fractures whereas younger samples and lavas show a strong decrease from slightly to strongly rounded cracks (Fig. 21). Based on the assumption that curvatures reflect the propagation of the cracks, those results would approve the established theory, that cracks in old samples had more time for propagation and thus, show a higher amount of strongly rounded fractures compared to the more recent samples. Interestingly, ignimbrites behave the same as old samples when compared to lavas. This effect is probably related to the condition and compaction of the glass itself.

Notably, the mean number of perlitic fractures is significantly higher in fresh samples than in old rocks. This is very likely caused by the more abundant alteration and mineral precipitation in older samples, which might heal or close fractures or overgrow them.
When comparing lava and ignimbrite samples, the latter also shows lower numbers which is simply caused by the limited space for fracturing in ignimbrites as perlitization is mostly concentrated in fiammes.

Another effect which could influence the degree of perlitization was stated by Denton et al. (2012). He recognized a decrease in perlitization with distance from the lobe margin. This effect cannot directly be related to the distance from an external source of water, but it is not excluded to play a role. However, as mentioned in a previous chapter (5.1.2.), the spacing between the major sublinear quench fractures is increasing towards the core of a cooling body. This effect is accompanied by the decreasing perlitization (Denton et al., 2012). Consequently, it can be suggested that the higher rate of cooling in the marginal areas of a cooling unit causes an increased strain, which on the one hand facilitates quench fracturing and on the other hand leads to a higher degree of perlitization or rather favors abundance of perlitic fracture propagation.

5.2.3. Alteration, devitrification, and crack preservation

Nearly all preserved volcanic glasses are of Neogene age or even younger, which was also stated by Marshall (1961) before. This study included 31 samples which show perlitic fractures and 11 of them can be assigned to this age group. Other samples which were investigated are significantly older with ages up to Ediacaran times, some of which fully devitrified. However, outlines of perlitic cracks could be observed even in these samples, which indicates on the one hand the glassy origin of the samples and on the other hand the ability of perlitic fractures to persist despite devitrification.

Hydration or rather entry of external water prompted by the formation of the crack system in many cases causes an alteration which involves associated mineralization during low-grade metamorphism. In many investigated samples where alteration features were visible, the growth of the alteration minerals (e.g. illites and smectites) starts at the fracture rims and proceed to grow into the glass to certain extents. Subsequently, the glass between the crack domains gets replaced. Generally, it can be observed that alteration, mineralization, and devitrification are most abundant in samples older than

Cenozoic. Therefore, those features can be useful indications on a rough estimation of the approximate age of a dislocated sample of the rock.

Once the minerals started to grow, it is unlikely that they vanish or dissolve during later times. After long geological time spans, the fractures themselves however may no longer be visible or heal but the alteration minerals which nucleated along the fractures stay in place. Therefore, alteration which occurs along a fracture rim is a very useful facies indicator to get evidence that a rock was formerly a glass, i.e. a lava or an ignimbrite.
This in turn provide an indication about temperature regimes as the cracks must have formed at temperatures higher than the formation temperature of the overgrowing minerals.

In several samples, changes in the degree of alteration from outer fractures with larger diameters and a high degree of alteration minerals to inner fractures with smaller diameters and significantly less mineral precipitation leads to the assumption that the inner domain of perlitic fractures represent a second generation of rounded fractures which formed during later times and therefore show less alteration.

5.2.4. Reservoir space in perlitized rocks

Analytical measurements of the effective porosities of several rocks with the Triple Weight Method and the Helium Pycnometer exhibited a relatively wide range of values from 0.5 to 14.1 %, that reflect the nature of the complex pore space history of volcanic rocks. In all analyzed rhyolitic samples, the most significant pore space for suitable reservoir porosity was created by the apertures of perlitic fractures in certain samples: As expected, in cases without any observed mineral precipitation, the pore space was found to be the largest. In addition, alteration in form of dissolution is favored in that fraction of the pore volume created by uncemented (i.e. open) fracture apertures. However, other post-emplacement processes and features, such as the growth of spherulites or devitrification, might also significantly change pore space properties of the rocks.

Helium in general is capable of invading smaller pores than water due to its smaller atomic radius. Therefore, helium-derived porosities score slightly higher than porosities obtained from the Triple Weight Method, which is conducted with water (Semel & Lados, 2006). This was also observed for samples 1-8-97-3b, which was analyzed in both ways (Triple Weight Method & Helium Pycnometry; see Tab. 15).
Porosity results for lava samples support the assumption that rocks which lack significant alteration (especially mineral precipitation) and which are undevitrified show elevated porosities up to 14 % (e.g. 10-12-20b) whereas samples with prominent mineral precipitation show significantly lower porosities down to 1.2 % (27-6-14-1e). However, it has to be considered that sample 10-12-20b contains notable amounts of magmatic vesicles, which is also increasing the pore space to a certain amount. The lowest

porosities (down to 0.5 %) were observed for old (pre-Cenozoic) and highly altered samples (e.g. C 28-01). Porosities in analyzed ignimbrites are difficult to interpret since perlitization in ignimbrites is limited to strongly compacted and glassy sections. However, the results or rather the strong variations in porosities show that pore space prediction in such rocks is very risky and complex and simple microscopic observations are not enough, as thin sections portray only a small section of the actual pore space and do not provide sufficient overview of overall pore connectivity.

The measured permeability plots in the expected range of permeabilities measured in previous studies (e.g. Sruoga et al., 2004; Mao et al., 2020). However, higher values are known for some rhyolitic quench fractured glasses (Sruoga et al., 2004). In general, image analysis on the fracture systems of perlitic rocks showed that perlitic fracture densities are especially high in Cenozoic rocks and it was found that there is a direct relation between quench fractures and perlitic cracks. Therefore, it is assumed that young rocks with insignificant alteration on the one hand show good porosities and on the other hand contain a well-connected fracture network which provides good permeabilities. This assumption is supported by field studies on rhyolite intrusions in Iceland (e.g. Krafla geothermal field), where connected perlitic fracture networks proved to be of beneficial influence on geothermal energy production (Saubin et al., 2019).

It would have been expected to obtain a direct proportional relation between line densities of the fractures and measured porosities, which would mean that the pore space increases with increasing line densities. However, the opposite was found for the analyzed samples: Porosities are slightly decreasing with increasing line densities of perlitic fractures (Fig. 44). There are several possible reasons: (1) porosities are way more influenced by alteration than by the number or density of fractures itself, (2) there is no link between pore space and the density of fractures but porosity is solely controlled by the aperture of the fractures, and (3) a too small number of samples were analyzed to see a more clear and distinct trend. In general, however, it can be said that porosities can not be directly associated with crack densities of a rock sample.

Generally, to be able to draw more sophisticated conclusions on pore systems in rhyolites, also regarding geological age and rock type, a higher number of analyzed samples would have been required and at best, core plugs of each sample would have been produced for better comparability.

5.2.5. Connection of perlitization with crystall grains and microlites

Fractures intersecting crystal grains can give information on either relative timing of fracture- and crystal formation or on the hardness of a crystal. In those cases where fractures clearly crosscut or intersect a crystal it is clear that the crystal had to be in place before perlitic fracturing occurred. On the other hand, information can be obtained about the fracture resistivity or rather fracture toughness of the crystal. Those grains which are surrounded - but not intersected - by perlitic cracks are probably

due to a high fracture toughness, which could be related to a high crystal hardness or a tougher matrix surrounding the grain. To get more information about the relation between perlitic fractures and the mentioned characteristics of different crystals, further observations on mineralogy would be necessary but were not within the scope of this research.

The parallel orientation of pyroxene microlites is a general characteristic of prismatic pyroxenes which develops by movement during the emplacement of a lava. This indicates that the microlites itself formed before the actual emplacement. However, it has been observed by Iddings (1899), that all volcanic phenomena which did not undergo modification subsequent to explosive eruptions do not show microlites. Therefore, quickly chilled glass of explosive eruptions without post-eruptive modifications is microlite-free. This implies that there are no microlites present in the magma at the time of eruption but formed in the time between eruption and emplacement.
The complex shaped trichites most likely formed after deposition, collapse and welding since their fragile character would get disrupted, fragmented, and dispersed by any movements during the emplacement of the magma. Considering these two separate formation periods it is a high possibility that they mark a change in the environment of formation and two distinct stages in the cooling history of the glass. The two major factors for the formation of trichites are a decrease in temperature triggering an increase in viscosity. Their spiral forms often show a symmetry which most likely displays some systematic crystal structure anomaly (Ross, 1962; e.g. 1-8-97-1, Fig. 29).

5.3. Fluid/volatile contents

It has already been stated that water in perlites is not of magmatic origin but entered the glass later at more ambient temperatures below T_g (e.g. Ross, 1962) and can be present in the glass structure in various forms like H^+, H_2O, OH^-, etc. (Bagdassarov et al., 1999). Re-heating the samples shows that the water, which was gained by the perlites and pitchstones below T_g, degasses at temperatures lower than T_g between 300°C and 500-550°C. It has been observed that dehydration rate peak temperature decreases with an increase in water content of a rhyolitic glass. This implies a massive release of water at temperatures well below T_g (Bagdassarov et al., 1999). The transformation of glass is a process which takes place over a wide temperature range and is dependent on a variety of parameters (e.g. atmosphere, heating- and cooling rate, etc.). To determine glass transition temperatures, dilatometry is more commonly used in material sciences. A simple comparison between DSC/TG and dilatometry results shows that heat transport conditions are strongly varying and conditions for geological processes are even more different. Therefore, measurement results from DSC/TG can only be used for a relative comparison of the materials but interpreting them in relation to geological processes requires additional knowledge.

However, there are no significant peaks in DSC during the temperature range of massive weight loss, i.e. no reaction such as a combustion of organic matter is expected to contribute to the weight loss. Therefore, the significant losses of mass can be either due to the degassing of water or gases which are heavier than air and were trapped in closed pores of the rock. In order to differentiate, further measurements with, e.g. a mass spectrometer would have been necessary. However, as shown in Tab. 12 (chapter 5.4), weight loss values are a good representation of water contents, which would be expected for the analyzed rocks, and which were measured during several previous studies on water contents in obsidians, perlites, and pitchstones.

The mass loss of rhyolites at very low temperatures below 150°C has been observed during other studies as well and can be related to the release of superficially bound molecular water (e.g. Thomas et al., 2015). This phenomenon however cannot be observed for the pitchstones.

It has also been shown by Bagdassarov et al. (1999), that peak temperatures of water loss are a function of water content and cooling rate. The higher the water content the lower is the water loss temperature and the same applies to fast cooling rates. The correlation between the water content and the cooling rate can be approved by the comparison of weight loss in perlites vs. pitchstones. The pitchstones, showing significantly higher losses, start degassing earlier and show the maximum slope of the weight loss curve at lower temperatures.

Nevertheless, there are several other mechanisms which can also contribute to the release of water from perlites such as dewatering and decomposition of clay minerals or the release of water absorbed on microcrack surfaces (Bagdassarov et al., 1999). An examination of the influence of these factors was not designated for this study and will not be discussed further.

The calculations of fluid/volatile contents by subtracting the total water-free oxide composition obtained from electron microprobe measurements from a total composition of 100% are distinctly higher than thermo-analytical results and probably overestimate the total amount of fluids and volatiles in the glass. It could be a probable reason that microprobe measurements are not very suitable for the determination of fluid and volatile contents in glasses, which could cause a systematic over- or underestimation of measurement results. However, for the purpose of this research, a systematic shift in measurements results is not problematic since it is not affecting the overall observation of alkali mobilities and the relation or ratio between alkali, silica, and fluid/volatile contents.

Thermoanalysis and research on the fluid content in perlitic fractured glass in general provided clear insights, that (1) weight loss obtained from thermo gravimetry (TG) is a good representation of the pure water content in rhyolitic glasses, (2) all examined samples which show perlitic fractures contain elevated water contents, therefore, rocks which show perlitic textures have very likely been subject to

the ingress of water, and (3) the presence of perlitic fractures in a rock sample is an indicator for a high-water content rock, though it is no proof that hydration gives rise to fracture formation since hydration can very likely happen any time after perlitic fracturing. However, no perlitic textures could be observed in any volcanic glass with water contents typical for obsidians, i.e. lower than 2 wt.%. This implies, that the presence of water is most likely inevitable for perlite fracture formation.

Plotting line densities against fluid contents from both microprobe- and thermalanalysis showed no distinct trend (Fig. 44). This implies that there is no direct correlation between the density of the perlitic fractures and the water contents of the rock. If it is assumed that a certain percentage of the water measured with TG is stored in the apartures of the fractures, it would have been expected to see a trend of increasing fluid contents with increasing line densities of the cracks; though, this is not supported by these results. Therefore, the number or rather the density of the fractures is not directly linked to fluid contents.

5.4. Chemical compositions and alkali mobility

Values of SiO_2, TiO_2, Al_2O_3, FeO_3, CaO, MgO, Cl, SnO_2, Cr_2O_3 can be used for computing the average glass composition and Na_2O and K_2O are measured to compute the alkali composition for the glass samples. All these values can be used to calculate the water-free oxide composition for each glass. Considering these chemical compositions of the measured samples, it appears that the magmatic composition was nearly the same for all rhyolite extrusions, which can also be seen in the TAS diagram (Fig. 33). Most of the slight compositional variations are probably either due to chemical mobility of certain elements or limitations of the analytical techniques used for the investigation of glass samples. The largest variations in elemental compositions can be observed in alkali contents, which is very likely a result of such alkali mobility. Duffield & Dalrymple (1990) observed, that Na_2O contents are higher in undevitrified samples, consistent with Na losses during devitrification. For the thesis only undevitrified samples were chosen, which excludes this as a major factor of influence. However, it was reported by Noble (1967) and Bacon et al. (1981), that both Na_2O and K_2O contents change during hydration of silicic volcanic glass, which means that alkali mobility is strongly connected to the hydration of the rock.

Plots of Na_2O and K_2O against silica- and volatile/fluid contents (Fig. 34 & Fig. 35) show only slight fluctuations in alkali composition for samples from El Salvador (5-12-04-3) and Argentina (5-11-07-3b). Volatile/fluid contents are relatively high and show stronger variations at the rims, thus, no general decrease towards the cores is recognizable. This implies that the samples are evenly hydrated without any visible gradient in alkali mobility. Volatile/fluid compositions show a trend of higher contents at the rims for the sample from Milos, compared to the core and are strongly fluctuating in both rims and cores with generally lower water contents compared to El Salvador (5-12-04-3) and Argentina (5-11-

07-3b) samples. The same strong fluctuations can be observed in Na_2O and K_2O contents, which leads to the assumption that hydration is not completed, and alkali mobility is still possible. These correlations and results give proof to the assumption that the mobility of alkalis is strongly connected to the hydration of glass. It is likely that there has also been such alkali mobility in the El Salvador and Argentina samples when hydration was still ongoing but terminated when the samples were evenly and entirely hydrated from the rims to the cores.

To get a closer look on the mobility and movement of alkalis, plots of Na_2O against K_2O are compiled (Fig. 37). For Argentina and El Salvador similar trends can be observed, illustrating a negative slope for both rim and core, which means that they are inversely proportional. This shows that Na_2O is decreasing while K_2O contents increase and vice versa, which can be described as an effect of differential depletion or enrichment, respectively (e.g. Thure et al., 1985). The same behavior can be seen for measurements at the crack rims of the Milos sample; however, at the core the trend is reversed, showing a positive slope of the regression line, i.e. a proportional change in Na_2O with K_2O. If water contents are additionally considered, it can be observed that both Na_2O and K_2O contents decrease with an increase in fluid/volatile contents. This phenomenon can be described as a diluting effect due to an increase in fluid contents towards the cores of the fractures and gives further evidence for the incomplete and uncompleted hydration (Fig. 49). The sublinear cracks which surround the perlitic cracks are interconnected and therefore enable an exchange of fluids and volatiles, which could cause described changes in elemental compositions and related mobilities of alkalis along the interjacent spherical cracks, which are often isolated and proceed concentrically and hence, do not admit an effective water exchange. This results in the observed variations from rim to core showing a gradient in mobility from the outer side to the inner side of the cracks.

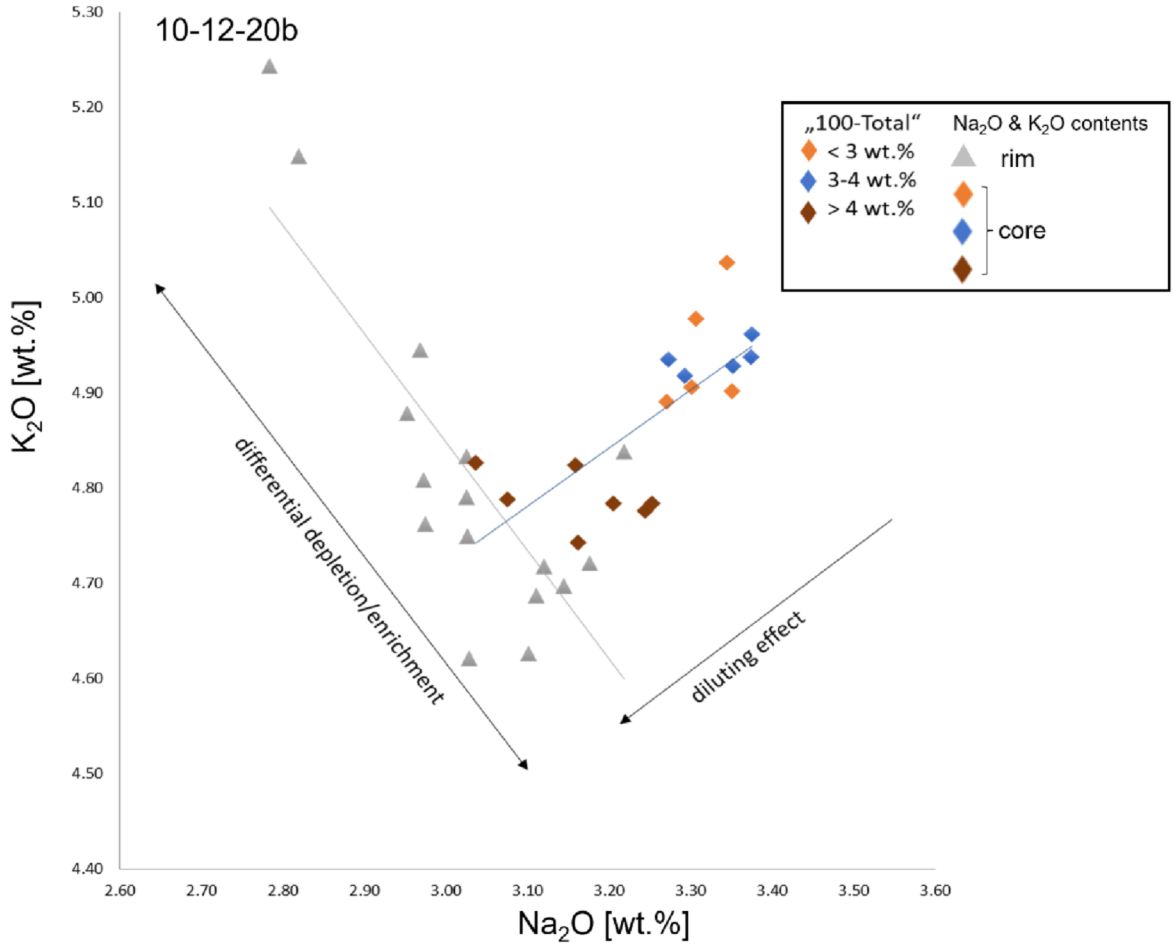

Fig. 49: K_2O plotted against Na_2O contents for Milos (10-12-20b) with observed trends in alkali mobility.

Differences in calcium and magnesium contents probably result from inherent slightly different compositions of the individual rocks. The variations between rim and core can again be caused by the impact of water after emplacement as Ca and Mg values are often related to the presence of water and varying water chemistries. The rims are stronger influenced by water and the longer the hydration process proceeds, the more balanced are the values.

Similar to fluid contents (see chapter. 5.3.), there is also no correlation between the density of perlitic fractures and alkali contents of analyzed rocks (Fig. 44).

5.5. Crack formation

It became evident by analyzing various thin sections and the fracture network in more detail that perlitic fractures are the result of a shrinkage process. However, such shrinkage of a glass can either be caused by a quench reaction or rather by the thermal shock behavior or by the hydration of the glass as the release of tensile stresses and the formation of hydrogen bonds results in shrinking and subsequent crack growth.

The rounded fractures originate either at edges between two primary quench fractures or at pores or

inclusions in the rock. Both represent zones of weaknesses and decreased fracture toughness, and it is known from material sciences that random occurrences of microstructural defects often act as stress concentrators and subsequently as crack initiators (e.g. Bermejo & Danzer, 2014).

It is also known that already existing cracks, in that case a primary generation of fractures, decreases the inherent strength of a material which promotes secondary crack growth. According to size-effects, the larger the cracks and the larger the component, the higher is the probability of failure of the material, i.e. the probability of crack formation.

5.5.1. Cooling process, thermal shock, and swelling effect

The influence of cooling on a hot rhyolitic body is dependent on various parameters such as the thickness of the cooling unit and time of cooling, which in turn is influencing the degree of perlitization. It is unquestioned that the sublinear fractures form due to rapid cooling of the lava or pyroclastic flow. This observation was made during several previous studies (e.g. Davis & McPhie, 1996; see also chapter 5.1.2.) and was proved by thermo shock experiments on obsidian samples: Artificially generated thermal shock events resulted in a fracture network consisting primarily of sublinear fractures, which are arranged similarly to the sublinear fractures in analyzed rocks (e.g. 27-6-14-1e; Fig. 50). Thermo shock also led to two sets of sublinear fractures: long (indicated by red arrows) and cross fractures (indicated by yellow arrows). This, however, proves that the two generations of sublinear fractures can be caused simultaneously and do not necessarily result from to time-separated steps of cooling as assumed in previous studies (e.g. Davis & McPhie, 1996; see also chapter 5.1.2.).

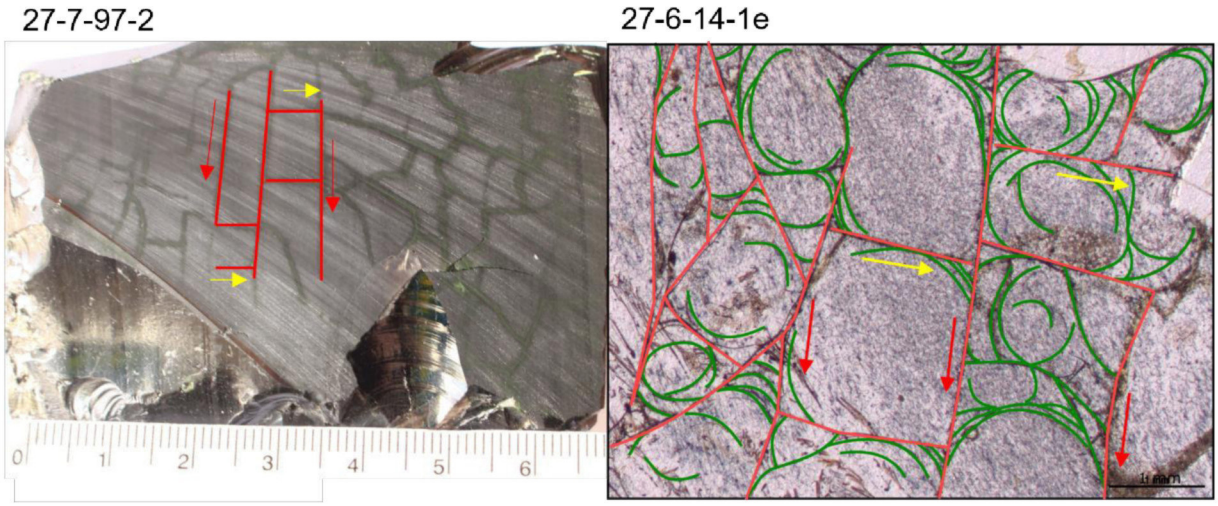

Fig. 50: Sublinear fracture systems produced by thermo shock in obsidian samples (27-7-97-2, left) and in a rhyolitic lava sample (27-6-14-1e, right). Red arrows: long fractures, yellow arrows: cross fractures.

For the formation of the perlitic fractures, there are two discussable theories: formation of the fractures by a thermo shock process or fracture formation by swelling of the glass. Comparing various

analyzed volcanic glasses with artificially produced silica-rich glasses show that it is possible to produce a perlitic fracture network simply by rapid cooling of the glass from approximately 500 °C to 20 °C. The glass is unhydrated before immersing it in cold water which in turn implies that thermal stress before hydration is capable of causing such fracture systems. It is assumed that this effect only works for rapidly chilled glass. Slow cooling alone would probably cause internal stress but would not result in crack formation. Moreover, from what is known from the production of such artificially produced crackled glasses, the observed structures can only be generated at temperatures just below the glass transition temperature T_g. This leads to the assumption, that perlitic fracture formation caused by a thermal shock reaction is only possible at temperatures close to T_g and subsequent fracturing on a temperature path to ambient temperatures is very likely not caused by a thermo shock process as discussed in chapter 5.6.2. Self-executed thermo shock experiments on obsidians yielded only minor numbers of perlitic fractures (see chapter 4.6.). There are several possible reasons for this observation. It is possible that the chosen temperature difference ΔT is too small to result in significant perlitic fracturing: ΔT in the thermal shock experiment was ~280 °C whereas ΔT for the production of crackled glass with significant perlitic fractures was ~480 °C. Another reason can be that perlitic fracture network formation in artificially produced crackled glass happened at temperatures closer to expected glass transition temperatures in volcanic glasses (e.g. Goto et al., 2005). If it is assumed that perlitic fracturing is linked to temperatures close to T_g, a heating temperature of 300 °C for thermal shock experiments was probably too low to cause significant amounts of perlitic fractures. Moreover, experiments were only conducted on two obsidian samples of similar composition; for more meaningful results it would be necessary to analyze a higher number of different samples under different temperature conditions. However, there is a small number of rounded fractures observable in the obsidian samples after thermal shock treatment (Fig. 41), which again implies that it is possible to produce curved fractures by thermo shock events.

It was also observed by Denton et al. (2010) that the degree of perlitization is dependent on the distance from the margin towards the center of a cooling body. The significant temperature differences between margin and core, in turn, leads to a larger temperature difference during thermal shock reactions which probably decreases the thermal shock induced stress towards the inner core of the cooling body. This observation was also made for obsidian samples after thermo shock treatment: Fracture density or rather the distance between fractures decreases from the edges of the samples towards the inner areas.

The second theory is based on the swelling of glass and is considering stress fields in the cooling glasses more precisely. Generally, the process of fracture formation or rather fracture initiation is always linked to a stress relieve (Wiederhorn et al., 2011). The presence of tensile stresses is a prerequisite for crack formation. It is possible, that most stress is released during the primary process of quench

fracture formation, which would imply that the stress field, especially in close proximity to the primary fractures, is degraded which stands in contrast to the theory of subsequent perlitic fracture formation close to the primary cracks. One explanation is provided by the swelling effect (e.g. Wiederhorn et al., 2011): If the primary fractures allow an ingress of water, a subsequent swelling effect could introduce compressive stresses which then cause radial stresses which in turn result in the generation of a second fracture set. However, the process of swelling probably demands more time to result in fracture formation, which stands in contrast to the fractures created by the thermal shock reaction in the crackled glass, where the immersion in water produces the described perlitic fracture network within a few seconds. These considerations, however, are only based on what is known from material sciences and theoretical assumptions and were not tested on rock samples investigated for this study.

5.5.2. Hydration

There is not yet any proof that hydration alone enables perlitic fracture formation. There are studies on how hydration rates vary over time and temperature range and also model calculations which show that the hydration-induced stress is high enough to shatter a glass.However, there were no hydration tests performed in which a similar perlitic fracture network was generated artificially so far. However, the hydration of rocks after emplacement is definitely an issue, as every perlitized rock sample shows elevated water contents whereby the water is not magmatic but meteoric in origin and therefore had to have entered the rock after emplacement (e.g. Ross & Smith, 1955). For that reason, it is undisputed that hydration or rather the ingress of water is directly related to or rather accompanies perlitization. Nevertheless, it is highly unlikely that hydration alone can cause perlitic fractures, especially at very low temperatures down to ambient temperatures, where hydration rates are remarkably low.

The thickness of a cooling body also has to be considered when discussing the influence of hydration (e.g. Denton et al., 2012). It is very likely that the marginal areas of a cooling rhyolitic body get hydrated faster and more evenly. Dependent on the fracture network and the state of hydration, the hydration of the rock proceeds towards the core of the cooling unit. However, since hydration rates and activation energies are significantly higher in hot rocks (e.g. Angelopolous et al., 2020), it is expected that perlitic fractures caused by hydration are most abundant at the very beginning when the body has not yet started to cool down significantly or in the cores of a flow. The latter notion however stands in contrast with the observed decrease in perlitization inwards a cooling body, which was also proven by thermal shock experiments.

5.6. Crack propagation

Two very important findings give evidence that the cracks propagate over time: (1) the degree of perlitization in terms of increasing degree of roundness of the fractures in old samples, and (2) the observation of further generations of rounded fractures with different degrees of alteration. However,

as mentioned previously, thermal shock is only relevant at elevated temperatures close to T_g but crack growth might proceed over time and at ambient temperatures. Therefore, the propagation of the cracks is very likely linked to hydration of the glass and is in turn influenced by the effects of moisture and water on the glass (e.g. Waurischk et al., 2020). From observations on subcritical crack growth (e.g. Bermejo, 2020) it is already established that the presence of water facilitates fracture growth which supports the assumption of slow fracture propagation over time. The swelling effect (e.g. Wiederhorn et al., 2011) however is time-dependent, and it is possible that there might be an increase in toughening of the glass over time, which in contrast to the other stated theories might prevent the glass from further fracturing.

6. Conclusions

Crack formation and propagation

Microscopic observations on perlitic textures show that sublinear fractures, the edges of obsidian clasts in lava breccia, and the edges of fiamme in ignimbrites depict a boundary for the propagation of the rounded perlitic fractures. These observations permit insights on relative timing of fracture formation: The perlitic fractures form subsequently to primary fractures, which are related to quenching immediately after emplacement of a magmatic cooling unit, i.e. lavas or ignimbrites. Thermal shock reactions were found to be the major mechanism for the formation of quench fractures, demonstrated with experiments on heretofore fracture-free obsidian samples. Formation of perlitic cracks is restricted to glass that experienced thermo shock induced sublinear cracks.

Statistical analyses investigating the degree of fracture roundness show that there is (1) a more similar distribution between slightly and strongly rounded fractures in pre-Cenozoic samples and ignimbrites; (2) yet, in Cenozoic lavas a decrease in the number of slightly to strongly rounded fractures is observable. Based on these findings, crack propagation is further advanced in old samples and ignimbrites because of longer time spans elapsed for cracks to propagate and the compaction of the glass itself. Due to higher amounts of alteration minerals on fracture rims in older samples, which can heal, close, or overgrow fractures, the average number of uncemented fractures in general is lower compared to younger samples. Ignimbrites also show a limited number of fractures resulting from limited space for fracture growth, as cracks do not encroach into the matrix, if it is uncompacted compared to the fractured glass clasts.

Likewise, samples which are free from primary quench fractures do not contain perlitic fractures which proves the conditional relation between both. This is also supported by the direct proportional relation between primary (sublinear) and secondary (perlitic) fractures. Moreover, thermoanalysis and studying of fluid contents shows that there are no perlitic fractures in rocks which are not hydrated, i.e. do not contain elevated water contents. This finding implies that the presence of water is necessary for perlitic fracture formation. However, not every rock which contains higher water contents necessarily features perlitic fractures. From these observations it is concluded that (1) it is more likely that crack formation facilitates the diffusion of water rather than vice versa and (2) perlitized rocks have been subject to the ingress of external water, which is meteoric and not magmatic in origin.

Previous research on brittle materials shows that crack formation and crack propagation must be viewed separately from each other. A direct comparison to industrial crackled glass illustrates that a similar fracture network as observed for magmatic rocks can be produced in artificial glass by inducing thermal shock reactions at a threshold just below the glass transition temperature Tg. The same effect

cannot be achieved at temperatures closer to ambient temperature and is therefore limited in time and temperature range.

It could be demonstrated for volcanic glasses that perlitic fractures propagate over time and that further (younger) generations of rounded fractures can form at later stages, probably at lower temperatures or at ambient temperature. Hydration is considered as a major mechanism for both crack propagation and later generations of fractures, as it can happen at any time after emplacement of a cooling unit and after the formation of first fracture generation. From what is known from fracture analysis in material sciences, propagation of cracks is enhanced under the presence of moisture or water. Therefore, areas of humid climate may be favorable for perlitic fracture formation; hence, perlitization could give potential paleoclimate implications. However, hydration rates are decreasing over time with a decrease in temperature.
In general, it is inferred from all these findings, that it is possible to cause rounded perlitic fractures by thermal shock processes while crack propagation is very likely linked to strain which is induced by continued hydration of a volcanic glass.

Textural and geometric features

Intense fracture network composed of perlitic cracks represents a spherical to ellipsoid three-dimensional geometry that is proven by computer tomography and macroscopic observations on crosscuts through fully perlitized rock samples. Perlitic fractures are always positioned within cells of sublinear quench fractures and are often concentrated on the edges between two intersecting sublinear cracks, which act as special points of increased weakness, or, by definition, sites of rather low fracture toughness, that act as seed points for perlitic fracture development. Hence, the origin of perlitization can be genetically linked to a three-dimensional (paleo)strain field.

Statistical analysis of line densities of sublinear and perlitic fractures reveals a direct relation between the two, namely, a proportional increase in perlitic fractures with rising numbers of quench fractures. This finding is furthermore supported by estimating the specific length densities of perlitic cracks in dependence on distance to quench fractures, which proves that the rounded cracks originate in close proximity to the primary sublinear cracks and then crack formation proceeds to the center of the cells. Another indication for the connectivity of the perlitic fracture system are observed alkali- and fluid-mobilities from the edges of a fracture cell towards the core of a perlitic crack.

Geochemical observations and reservoir characteristics

Post-emplacement or post-cooling processes, such as alteration, mineralization, and devitrification are most abundant in pre-Cenozoic samples and can therefore provide independent and relative estimates of the age of rock samples. Minerals which precipitated and grew along fracture rims (and which can potentially grow even further from the rim toward the center of a fracture over time and thereby heal

the fractures) were found to remain in their in-situ position. For that reason, mineral precipitation can provide additional useful indications on whether a by now devitrified rock was glassy in origin, as perlitic crack formation is limited to glassy material. This provides a useful assessment which provides information on changes in temperature regime (i.e. cooling temperature vs. metamorphic grade of mineral overgrowth).

Even though chemical compositions are very similar for most rhyolitic extrusions and remain unchanged between individual rock samples analyzed in this study, it is observed that both alkali and fluid contents show variations between cores and rims of perlitic fractures. Older, fully hydrated samples show no variations in fluid content between rim and core but exhibit a decrease in sodium ions with increasing potassium content from rim to core as an effect of differential depletion or enrichment. In contrast, younger samples with unbalanced water contents from rim to core indicate incomplete hydration of the sample. In these special cases, both sodium and potassium contents decrease with increasing fluid contents toward the center, caused by a dilution effect. These findings prove a direct connection between alkali mobility and hydration of a rock.

Reservoir properties are also strongly related to post-emplacement features because the apertures of perlitic fractures improve by mineral dissolution, which incrementally increases potential reservoir volume. Conversely, mineral precipitation can occlude free fracture pore space and hence, reservoir properties deteriorate with geological time. Porosities of analyzed samples vary strongly from values of 0.5 to over 14 %. High porosity measurements show that microstructures related to rhyolitic rocks can provide significant pore space. On the other, a variety of factors apart from geological age (e.g. formation of spherulites, the abundance and distribution of alteration minerals, the presence of several fracture generations, etc.) must be considered for reservoir quality evaluation. Strongly connected fracture networks and high fracture densities, which can be found in several perlitized rocks, can significantly improve permeabilities, and, consequently, facilitate fluid circulation. However, the unstable nature of perlitic textures and heterogeneities in the complex pore space of volcanic rocks are critical factors affecting reservoir quality prediction and further scientific research in this field is required.

7. References

Allen, R.L. (1988). False Pyroclastic Textures in Altered Silicic Lavas, with Implications for Volcanic-Associated Mineralization. Economic Geology, Vol. 83, p.1426-1446.

Allport, S. (1877). On certain Ancient Devitrified Pitchstones and Perlites from the Lower Silurian District of Shropshire. Quar. Journal of Geol. Soc. 1877, Vol. 33, p.449-460.

Angelopoulos, P.M., Manic, N., Tsakiridis, P., Taxiarchou, M., Jankovic, B. (2020). Dehydration of rhyolite: activation energy, water speciation and morphological investigation. Journ. of Therm. Anal. and Calorimetry, 142, p.395-407.

Annen, C. (2017). Factors affecting the thickness of thermal aureoles. Front. Earth Sci. 5.

Arellano, V.M., Torres, M.A., Barragán, R.M. (2005). Thermodynamic evolution of the Los Azufres, Mexico, geothermal reservoir from 1982 to 2002. Geothermics 34, p.592-616.

Bacon, C.R., Macdonald, R., Smith, R.L., Baedecker, P.A. (1981). Pleistocene high-silica rhyolites of the Coso volcanic field, Inyo Country, California. J. Geophys. Res. 86: 10223-10241.

Bagdassarov, N., Ritter, F., Yanev, Y. (1999). Kinetics of perlite glasses degassing: TG and DSC analysis. Glastech. Ber. Glass Sci. Technol. 72, No. 9, p.277-290.

Balthasar, M. (2001). Geochemische Untersuchungen an Ignimbriten der Flechtigngen-Roßlauer-Scholle. Unveröff. Diplomarbeit, TU Bergakademie Freiberg.

Bermejo, R., Danzer, R. (2014). Mechanical Characterization of Ceramics: Designing with Brittle Materials. Elsevier, Comprehensive Hard Material, Vol. 2, p.285-295.

Bermejo, R. (2020). Subcritical Crack Growth: Modeling of the v-K Curve in Different Environments. Encyclopedia of Materials: Technical Ceramics and Glasses doi:10.1016/B978-0-12-803581-8.12119-8, p.1-7.

Beudant, F.S. (1822). Voyage mineralogique et geologique en Hongrie pendant l´annee 1818. Tome second, p.329.

Breitkreuz, C., Eliwa, H., Khalaf, I., El Gameel, K., Bühler, B., Sergeev, S., Larionov, A., Murata, M. (2010). Neoproterozoic SHRIMP U–Pb zircon ages of silica-rich Dokhan Volcanics in the North Eastern Desert, Egypt. Precambrian Research, 182 (3), p.163-174.

Breitkreuz, C., Götze, J., Weißmantel, A. (2021). Mineralogical and geochemical investigation of megaspherulites from Argentina, Germany, and the USA. Bulletin of Volcanology, 83, 14, p.1-24.

Branney, M.J., Bonnichsen, B, Andrews, G.D.M., Ellis, B., Barry, T.L., McCurry, M. (2007). Snake River (SR)-type volcanism at the Yellowstone hotspot track: distinctive products from unsusual, high-temperature silicic super-eruptions. Bulletin of Volcanology, 70, p.293-314.

Branney, M.J., Kokelaar, P. (1992). A reappraisal of ignimbrite emplacement: progressive aggradation and changes from particulate to non-particulate flow during emplacement of high-grade ignimbrite. Bulletin of Volcanology, 54, p.504-520.

Branney, M.J., Kokelaar, P. (2002). Pyroclastic Density Currents and the Sedimentation of Ignimbrites. Geological Society Memoir No. 27, p.1-4.

Caldemeyer, K.S., Buckwalter, K.A. (1999). The basic principles of computed tomography and magnetic resonance imaging. Journal of American Academy of Dermatology, vol. 41, 5, p.768-771.

Cas, R.A.F., Wright, J.V. (1987). Volcanic successions, modern and ancient: A geological approach to processes, products, and succession. London: Unwin Hyman.

Cerling, T.E., Brown, F.H., Bowman, J.R. (1985). Low-Temperature alteration of volcanic glass: hydration, Na, K, ^{18}O and Ar mobility. Chemical Geology (Isotope Geoscience Section) 52, p.281-293.

Chiu, S.N., Stoyan, D., Kendall, W.S., Mecke, J. (2013). Stochastic Geometry and its Application, 3rd Edition. John Wiley & Sons, Ltd, p.1-403.

Coats, A.W., Redfern, J.P. (1963). Thermogravimetric Analysis: A Review. Analyst, 88 (1053), p.906-924.

Czoßek, J. (2002). Vulkanologisch-petrographische Untersuchungen des Vulkanitkomplexes von Dobritz/Garsebach im Triebischtal/Meißen. Unveröff. Diplomarbeit, TU Bergakademie Freiberg.

Danzer, R. (2006). Some notes on the correlation between fracture and defect Statistics: is the Weibull statistics valid for very small specimens? Journal of the European Ceramic Society, 26, p.3043–3049.

Danzer, R., Lube, T., Supancic, P., Damani, R. (2010). Fracture of Ceramics. Adv. Eng. Mat., 10, p.275-298.

Davidge, R. W. (1979). Mechanical behaviour of ceramics. Cambridge: Cambridge University Press.

Davidson, P., Kamenetsky, V.S. (2007). Primary aqueous fluids in rhyolitic magmas: Melt inclusion evidence for pre- and post-trapping exsolution. Chemical Geology, v.237, issues 3-4, p.372-383.

Davis, B.K., McPhie, J. (1996). Spherulites, quench fractures and relict perlite in a Late Devonian rhyolite dyke, Queensland, Australia. Journal of Volc. and Geoth. Res. 71, p.1-11.

De Astis, G., Lucchi, F., La Volpe, L., Tranne, C.A., Frezzotti, M.L., Peccerillo, A. (2013). Geology, volcanic history and petrology of Vulcano (central Aeolian archipelago). Geological Society, London, Memoirs, 37, p.281-349.

de'Genaro, M., Capelletti, P., Langella, A., Perrotta, A., Scarpati, C. (2000). Genesis of zeolites in the Neapolitan Yellowstone Tuff: Geological, volcanological and mineralogical evidence. Contrib. Mineral. Petrol. 106, p.124-128.

DeGroat-Nelson, P.J., Cameron, B.I., Fink, J.H., Holloway, J.R. (2001). Hydrogen isotope analysis of rehydrated silicic lavas: implications for eruption mechanisms. Earth and Planetary Science Letters 185, p.331-341.

Dekking, F.M. (2005). A Modern Itroduction to Probability and Statistics. Springer. ISBN 1-85233-896-2, p.234-238.

Denton, J., Tuffen, H., Gilbert, J., Odling, N. (2009). The hydration and alteration of perlite and rhyolite. Journal of the Geological Society 166 (5), p.895–904.

Denton, J.S., Tuffen, H., Gilber, J.S. (2012). Variations in hydration within perlitized rhyolitic lavas-evidence from Torfajökull, Iceland. Journal of Volcanology and Geoth. Res. 223-224, p.64-73.

Dong, G.D., Zhang, Q., Zhu, X.M., Xian, B.Z., Zhu, S.F., Niu, H.P., Chen, Q.Y. (2012). Current status and problems of volcanic reservoir study: An example from the lower Permian volcanic rocks in Ke–Xia area of Junggar Basin. Oil & Gas Geology 33 (04), p.511–519 (in Chinese with English Abstract).

Doremus, R.H. (1995). Diffusion of Water in Silica Glass. J. Mater. Res., 10 [9], p.2379-2389.

Drysdale, D.J. (1991). Perlitic texture and other fracture patterns produced by hydration of glassy rocks. Department of Geology, University of Queensland Papers 12 (3), p.278–285.

Duffield, W.A., Dalrymple, G.B. (1990). The Taylor Creek Rhyolite of New Mexico: a rapidly emplaced field of lava domes and flows. Bull. Volconol. 52, p.457-487.

Ellis, B.S., Szymanowski, D., Wotzlaw, J.F., Schmitt, A.K., Bindeman, I.N., Troch, J., Harris, C., Bachmann, O., Guillong, M. (2017). Post-caldera Volcanism at the Heise Volcanic Field: Implications for Petrogenetic Models. Journ. of Petrology, Vol. 58, No. 1, p.115-136.

Fink, J.H. (1983). Structure and emplacement of a rhyolitic obsidian flow: Little Glass Mountain, Medicine Lake Highland, northern California. Geological Society of America Bulletin, 94(3), p.362-380.

Friedman, I., Smith, R.L. (1960). A new dating method using obsidian: Part I, the development of the method. Am Antiq 25, p.476-493.

Friedman, I., Obradovich, J. (1981). Obsidian hydration dating of volcanic events. Q Res 16, p.37-47.

Friedman, I., Smith, R.L., Long, W.D. (1966). Hydration of natural glass and formation of perlite. Geological Society of American Bulletin 77, p.323-328.

Geißler, M., Breitkreuz, C., Kiersnowski, H. (2008). Late Paleozoic volcanism in the central part of the Southern Permian Basin (NE Germany, W Poland): facies distribution and volcano-topographic hiati. Int. Journal of Earth Sci. 97, p.973-989.

Gifkins, C.C., Allen, R.L., McPhie, J. (2005). Apparent welding textures in altered pumice-rich rocks. Journal of Vol. and Geoth. Res., 142, p.29-47.

Giordano, D., Russell, J.K., Dingwell, D.B. (2008). Viscosity of magmatic liquids: A model. Earth and Planetary Science Letters 271, p.123-134.

Gordon, S. (1960). Encyclopedia of Science And Technology. McGraw-Hill Book Co. Inc. New York, Toronto and London, p.556.

Gottsmann, J., Giordano, D., Dingwell, D.B. (2002). Predicting shear viscosity during volcanic processes at the glass transition: a calorimetric calibration. Earth Planet Sci Lett 198, p.417–427.

Goto, A., Taniguchi, H., Kitakaze, A. (2005). Viscosity measurements of hydrous rhyolitic melts using the fiber elongation method. Bull. Volcanol. 67, p.590–596.

Götze, J., Möckel, R., Breitkreuz, C., Georgie, U., Klein, A. (2020). Zur Mineralogie von Vulkaniten und Lithophysen im Bereich des unterpermischen Leisniger Porphyrs (Nordwestsächsisches Becken). Veröffentlichungen Museum für Naturkunde Chemnitz, 43, p.5-44.

Grenville, A.J. Cole (1895). Perlites. Nature, No. 1365, Vol. 53, p.175.

Gries, R.R., Clayton, J.L., Leonard, C. (1997). Geology, thermal maturation, and source rock geochemistry in a volcanic covered basin; San Juan Sag, south–central Colorado. AAPG Bulletin 81, p.1133–1160.

Griffith, A. A. (1920). The phenomenon of rupture and flow in solids. Philosophical Transactions of the Royal Society of London, A221, p.163–198.

Harrer, W., Danzer, R. (2011). Thermal Shock Behavior of Si_3N_4-Specimens – Influence of Annealing and Edges. In Varner, J.R. & Wigthman, M. (eds.), Fractography of Glasses and Ceramics VI, Ceramic Transactions, Vol. 230, Florida, p.245-254.

Hauser, E.A., Reynolds, H.H. (1939). Alteration of glasses to montmorillonite. Am. Mineralogist, v.24, p.590-597.

Heuer, F. (2014). Geometric modelling of the Lower Permian Planitz-Formation; volcanosedimentary facies analysis and mineral chemistry of the related Rochlitz-Ignimbrite in Zwickau (SW-Saxony). Unveröff. Diplomarbeit, TU Bergakademie Freiberg.

Hoffmann, U., Breitkreuz, C., Breiter, K., Sergeev, S., Stanek, K., Tichomirowa, M. (2012). Carboniferous-Permian Volcanic evolution in Central Europe – U/Pb ages of volcanic rocks in Saxony (Germany) and northern Bohemia (Czech Republic). Int J Earth Sci., 102, p.73-99.

Höhne, G.W.H., Hemminger, W.F., Flammersheim, H.-J. (2003). Differential Scanning Calorimetry. 2nd rev. and enl. ed. p. cm. Springer, Berlin, ISBN 978-3-624-05593-5, p.1-2.

Hübner, M., Breitkreuz, C., Repstock, A., Schulz, B., Pietranik, A., Lapp, M., Heuer, F. (2021). Evolution of the Lower Permian Rochlitz volcanic system, Eastern Germany: Reconstruction of an intra-continental supereruption.- Int. J. Earth Sci, accepted.

Iddings, J.W. (1899). Geology of the Yellowstone National Park. U.S. Geol. Survey Mon., 32. Pt.2, sec. 1, chap. 10, p.356-430.

Ito, S., Tomozawa, M. (1982). Crack Blunting of High-Silica Glass. J. Am. Ceram. Soc., 65 [8], p.368-371.

Jebsen-Marwedel, H., Brückner, R. (2011). Glastechnische Fabrikationsfehler. „Pathologische“ Ausnahmezustände des Werkstoffes Glas und ihre Behebung. Eine Brücke zwischen Wissenschaft, Technologie und Praxis. 4. Auflage. Springer Verlag Berlin Heidelberg.

Jónasson, K. (1994). Rhyolite volcanism in the Krafla central volcano, north-east Iceland. Bull. Volcanol. 56 (6–7), p.516–528.

Karapetian, S.G., Jrbashian, R.T., Mnatsakanian, A.Kh. (2001). Late collision rhyolitic volanism in the north-eastern part of the Armenian Highland. Jornal of Volc. and Geoth. Res., 112, p.189-220.

Kaufhold, S., Reese, A., Schwiebacher, W., Dohrmann, R., Grathoff, G.H., Warr, L.N., Halisch, M., Müller, C., Schwarz-Schampera, U., Ufer, K. (2014). Porosity and distribution of water in perlite from the island of Milos, Greece. SpringerPlus, 3/1/58, p.1-10.

Lampropoulou, P., Laskaris, N., Petrounias, P., Giannokopoulou, P., Rogkala, A., Kalampounias, A.G., Tsigrou, P., Katagas, C.G., Iliopoulos, I. (2020). Petrogeochemical approaches to the characterization of obsidian derived from Nychia area (Milos Island, Greece) using combined methods. Microchemical Journal 156: 104843, p.1-11.

Langford, W. A., Davis, K., Lamarche, P., Laursen, T., Groleau, R., and Doremus, R. H. (1979). Hydration of soda-lime glass. J. Non Cryst. Solids 33, p.249–266.

Le Maitre, R., Streickeisen, A., Zanettin, B., Le Bas, M., Bonin, B., Bateman, P. (2002). Igneous rocks: a classification and glossary of terms: recommendations of the international union of geological sciences subcommission on the systematics of igneous rocks. 2nd et. Cambride: Cambridge University Press.

Lenhard, N., Götz, A.E. (2011). Volcanic settings and their reservoir potential: An outcrop analog suty on the Miocene Tepoztlán Formation, Central Mexico. Journ. of Vol. and Geoth. Res. 204, p.66-75.

Lowenstern, J.B. (1995). Applications of silicate-melt inclusions to the study of magmatic volatiles. In: J.F.H. Thompson (ed). Magmas, Fluids and Ore Deposits. Min. Ass. of Canada Short Course, v.23, p.71-99.

Löcse, F., Rötzler, J., Härtel, B., Linnemann, U., Schneider, G., Rößler, R. (2020). Geology, geochemistry and LA-ICP-MS U-Pb ages of late Palaeozoic eruption centres at the NW margin of the Erzgebirge (Saxony) – The Obermühlbach volcano. Z.Dt.Ges.Geowiss. (J. Appl. Reg. Geol.), 171 (4), p.443-480.

Manville, V., Németh, K., Kano, K. (2009). Source to sink: a review of three decades of progress in the understanding of volcaniclastic processes, deposits, and hazards. Sed. Geol. 220, p.136–161.

Mao, A., Zheng, H., Xiaomeng, S. (2020). Microstructure Investigation of Oil-Bearing Rhylites: A Case Study from the Hailar Basin, NE China. Minerals, 10, 699, p.1-18.

Marshall, P. (1935). Acid rocks of Taupo-Rotorua volcanic district: Royal Soc. New Zealand Trans., v.64, no. 3, p.1-10.

Marshall, R. (1961). Devitrification of natural glass. Geol.Soc. of American Bull., 72, p.1493-1520.

Mathisen, M.E., Mcpherson, J.G. (1991). Volcaniclastic deposits: Implications for hydrocarbon exploration. In Sedimentation in volcanic settings. Society of Economic Paleontologists and Mineralogists Special Publication, ed. G.A. Smith and R.V. Fisher, p.27–36.

McPhie, J., Doyle, M., Allen, R. (1993). Volcanic textures. A guide to the interpretation of textures in volcanic rocks. Centre of Ore Deposit and Exploration Studies.

Michalske, T.A., Freiman, S.W. (1983). A molecular mechanism for stress corrosion in vitreous silica. Journal of the american ceramic society 66, p.284–288.

Michels, J.W. (1986). Obsidian hydration dating. Endeavour, New Series, Vol.10, No.2, p.97-100.

Mordensky, S.P., Villeneuve, M.C., Kennedy, B.M., Heap, M.J., Gravley, D.M., Farquharson, J.I., Reuschlé, T. (2018). Physical and mechanical property relationships of a shallow intrusion and volcanic host rock, Pinnacle Ridge, Mt. Ruapehu, New Zealand. J. Volcanol. Geotherm. Res. 359, p.1–20.

Morgan, L.A. (1992). Stratigraphic relations and paleomagnetic and geochemical correlations of ignimbrites of the Heise volcanic field, eastern Snake River Plain, eastern Idaho and western Wyoming. Geol. Soc. of America, 179, p.215-226.

Morgan, L., McIntosh, W.C. (2005). Timing and development of the Heise volcanic field, Snake River, Plain, Idaho, western USA. GSA Bulletin, v.117, no. 3/4, p.288-306

Noble, D.C. (1967). Sodium, potassium and ferrous iron contents of some secondarily hydrated natural silicic glasses. Am. Min. 52, p.280-286.

Norton, F.H. (1941). Hydrothermal formation of clay minerals in the laboratory. Part II: Am. Mineralogist, v.26, p.1-17.

Ohser, J. (2018). Angewandte Bildverarbeitung und Bildanalyse. Methoden, Konzepte und Algorithmen in der Optotechnik, optischen Messtechnik und industriellen Qualitätskontrolle. Carl Hanser Verlag München, p.1-275.

Qiu, J.X. (1985). The adjustments of Fe_2O_3 and FeO in volcanic rocks. Geological Science and Technology Information 4 (2), p.32–39.

Repstock, A., Heuer, F., Im, J., Hübner, M., Schulz, B., Breitkreuz, C., Gilbricht, S., Fischer, F., Lapp, M. (2019). A Late Paleozoic Snaker River-type ignimbrite (Planitz vitrophyre) in the Chemnitz Basin, Germany: Textural and compositional evidence for complex magma evolution in an intraplate setting. Journal of Vol. and Geoth. Res. 369, p.35-49

Rapprich, V., Erban, V., Fárová, K., Kopacková, V., Bellon, H., Hernández, W. (2010). Volcanic history of the Conchagua Peninsula (eastern El Salvador). Journal of Geosciences, 55, p.95-112.

Ross, C.S., Smith, R.L. (1955). Water and other volatiles in volcanic glasses. American Mineralogist (1955) 40 (11-12), p..1071-1089.

Ross, C.S. (1962). Microlites in glassy volcanic rocks. The American Mineralogist, Vol. 47, p.723-740.

Run, C.D., Yu, H.L., Yu, F.Q., Wang, D.F. (1996). Pores development and reservoir properties of volcanic rocks in Jianghan basin. Journal of Jianghan Petroleum Institute 18 (2), p.1–6 (in Chinese with English Abstract).

Sakka, S., Mackenzie, J.D. (1970). Relation between apparent glass transition temperature and liquidus temperature for inorganic glasses. Journal of non-crystalline solids 6, p.145-162.

Saubin, E., Kennedy, B., Tuffen, H., Villeneuve, M., Davidson, J., Burchardt, S. (2019). Comparative field study of shallow rhyolite intrusions in Iceland: Emplacement mechanisms and impact on country rocks. J. Volcanol. Geotherm. Res., 388, p.1-18.

Schoeck, G. (1990). Thermally activated crack propagation in brittle materials. International Journal of Fracture 44, p. 1-44.

Schön J.H. (2015). Physical Properties of Rocks. 2 ed.; Elsevier B.V.: Amsterdam, The Netherlands, p.2-497.

Schutter, S.R. (2003). Occurrences of hydrocarbons in and around igneous rocks. In: Petford, N. & McCaffrey, K.J.W. (2003). Hydrocarbons in Crystalline Rocks. Geological Society, London, Spec. Pub., 214, p.35-68.

Semel, F.J., Lados, D.A. (2006). Porosity analysis of PM materials by helium pycnometry. Powder Metallurgy, vol. 49, issue 2, p.173-182.

Shan, X.L., Liu, Q.D., Ren, L.J., Zhao, Y.T. (2007). Geological characteristics and genesis of perlite in the lower cretaceous Yingcheng formation in the Santai area of the Songliao Basin. Journal of Jilin University-Earth Science Edition 37 (6), p.1146–1151.

Sibson, R.H. (1977). Fault rocks and fault mechanisms. J. Geol. Soc. London 133, p.191-214.

Smith, R.L. (1960). Ash flows. Bulletin of the Geological Society of America 71, p.795 – 842.

Spear, D. B. and King, J. S. (1982). The geology of Big Southern Butte, Idaho, in Bonnichsen, Bill, and Breckenridge, R. M., editors, Cenozoic geology of Idaho: Idaho Bureau of Mines and Geology Bulletin 26, p.395-403.

Sruoga, P., Rubinstein, N., Hinterwimmer, G. (2004). Porosity and permeability in volcanic rocks: a case study on the Serie Tobífera, South Patagonia, Argentina. Journ. of Volc. and Geoth. Res. 132, p.31-43.

Stevenson, R.J., Dingwell, D.B., Bagdassarov, N.S., Manley, C.R. (2001). Measurement and implication of “effective” viscosity for rhyolite flow emplacement. Bull. Volc. 63, p.227-237.

Stopora, K. (2010). Petrology of the Neoproterozoic Greenshist Metamorphic Intermediate Abu Hammad Metavolcanic Succession (Gharib Segment, North Eastern Dessert, Egypt). Unveröff. Diplomarbeit, TU Bergakademie Freiberg.

Streck, M.J., Grunder, A.L. (1995). Crystallization and welding variations in a widespread ignimbrite sheet; the Rattlesnake Tuff, eastern Oregon, USA. Bull. Volcanol. 57, p.151–169.

Sun, H., Zhong, D., Zhan, W. (2018). Reservoir characteristics in the Cretaceous volcanic rocks of Songliao Basin, China: A case of dynamics and evolution of the volcano-porosity and diagenesis. Energy Exploration & Exploitation, 0(0), p.1-19.

Thomas, P.S., Heide, K., Földvari, M. (2015). Water and hydrogen release from perlites and opal: a study with a directly couped evolved gas analyzing system (DEGAS). J. Therm. Anal. Calorim., 120 (1), p.95-101.

Thure, E.C., Brown, F.H., Bowman, J.R. (1985). Low-Temperature alteration of volcanic glass: Hydration, Na, Ka, 18O and Ar Mobility. Chemical Geology (Isotope Geoscience Section), 52, p.281-293.

Torres-Hernández, J.R., Labarthe-Hernández, G., Aguillón-Robles, A., Gómez-Anguiano, M., Mata-Segura, J.L. (2006). The pyroclastic dikes of the Cenozoic San Luis Potosí volcanic field:

Implications on the emplacement of Panalillo ignimbrite. Geofísica Internatical, Vol.45, 4, p.243-253.

Torres-Sánchez, D., Verma, S.K., Verma, S.P., Velasco-Tapia, F., Torres-Hernández, J.R. (2019). Petrogenetic and tectonic implications of Oligocene – Miocene volcanic rocks from the Sierra de San Miguelito complex, central Mexico. Journal of South Am. Earth Sciences 95, 102311, p.1-15.

von Aulock, F.W., Kennedy, B.M., Maksimenko, A., Wadsworth, F.B., Lavallée, Y. (2017). Outgassing from open and closed magma foams. Front. Earth Sci. 5.

Vorreier, C.P. (2017). Textural and XRD Analysis of megaspherulites from the Late Carboniferous Meissen Lava Complex. Unveröff. Bachelorarbeit, TU Bergakademie Freiberg.

Wakabayashi, H., Tomozawa, M. (1989). Diffusion of Water into Silica Glass at Low Temperature. J. Am. Ceram. Soc., 72 [10], p.1850-1855.

Wang, P., Chen, S. (2015). Cretaceous volcanic reservoirs and their exploration in the Songliao Basin, northeast China. Am. Assoc. Pet. Geol. Bull., 99, p.499–523.

Waurischk, T., Müller, R., Reinsch, S., Kiefer, P., Deubener, J., Balzer, R., Behrens, H., (2020). Crack Growth in Hydrous Soda-Lime Silicate Glass. Front. Mater. 7:66. doi: 10.3389/ fmats.2020.00066, p.1-9.

Webster´s New International Dictionary (1933). G. & C. Merriam Co. Springfield, Mass.

White, J.D.L., Smellie, J.L., Clague, D.A. (2003). Introduction: A deductive outline and topical overview of subaqueous explosive volcanism. Geophysical Monograph 140, p.1–23.

Wiederhorn, S.M. (1974). Subcritical crack growth in ceramics. In: Bradt, R.C., Hasselman, D.P.H., Lange, F.F. (Eds.), Fracture Mechanics of Ceramics. New York: Plenum.

Wiederhorn, S.M., Fett, T., Rizzi, G., Fünfschilling, S., Hoffmann, M.J., Guin, J.-P., (2011). Effect of Water Penetration on the Strength and Toughness of Silica Glass. J. Am. Ceram. Soc., DOI: 10.1111/ j.1551- 2916. 2011.04530.x94, p.196-203.

Willson, J.J., Goddard, P., Couch, S., Viramonte, J.G. (1999). Characterisation of the Quiron rhyolite of El Quevar volcanic complex, Salta. XIV Congreso Geológico Argentino, Actas II, p.222-224.

Wohletz, K., Zimanowski, B., Büttner, R. (2013). Magma-water interactions. In Modeling volcanic processes: The physics and mathematics of volcanism, ed. S. A. Fagents, T.K.P. Gregg, and R.M.C. Lopes, Cambridge University Press, p.230–257.

Xian, B.Z., He, Y.X., Niu, H.P., Wang, J.H., Liu, J.P., Wang, Z. (2018). Identification of hydrovolcanism and its significance for hydrocarbon reservoir assessment: A review. Journal of Palaeogeography 7:11, p.1-17.

Yamagashi, H., Goto, Y. (1992). Cooling Joints of Subaqueous Rhyolite Lavas at Kuroiwa, Yakumo, Southern Hokkaido, Japan. Bull. Volc. Soc. Jap., 37, 4, p.205-207.

Zelenka, T., Gyarmati, P., Kiss, J. (2012). Paleovolcanic reconstruction in the Tokaj Mountains. Central European Geology, Vol.55, 1, p.49-83.

Zhang, Y., Behrens, H. (2000). H_2O diffusion in rhyolitic melts and glasses. Chemical Geology 169, p.243-262.

Zimmermann, J. (2010). Facies analysis of the Neoproterozoic "Wadi Abu Hammad Ignimbritic-Sedimentary-Succession" and its basement within the Ras Gharib Segment; North Eastern Desert, Egypt. Unveröff. Diplomarbeit, TU Bergakademie Freiberg.

Zirkel, F. (1876). Microscopic petrography. U.S. Geol. Explor. 40th Parallel 6, p.11-12

Zou, C.N., Zhao, W.Z., Jia, C.Z., Zhu, R.K., Zhang, G.Y., Zhao, X., Yuan, X.J. (2008). Formation and distribution of volcanic hydrocarbon reservoirs in sedimentary basins of China. Petroleum Exploration and Development 35 (3), p.257–271.

Zou, C., Zhang, G., Zhu, R., Yuan, X., Zhao, X., Hou, L., Wen, B., Xiaozhi, W. (2013). Exploration History and Features of Volcanic Reservoirs. Volcanic Reservoirs in Petroleum Exploration, Chapter 1, p.1-10.

8. List of Appendices

8.1. Thin section analysis

8.1.1. Whole rock samples

8.1.2. Thin section images

8.2. CT images

8.3. Thermal analysis

8.4. EMP measurements

8.4.1. Thin section scans with profiles for EMP measurements

8.4.2. Results & calibration

8.5. Stochastic image analysis

8.6. Porosity & Permeability measurements

8.1. Thin section analysis

8.1.1. Whole rock samples

1-8-97-1

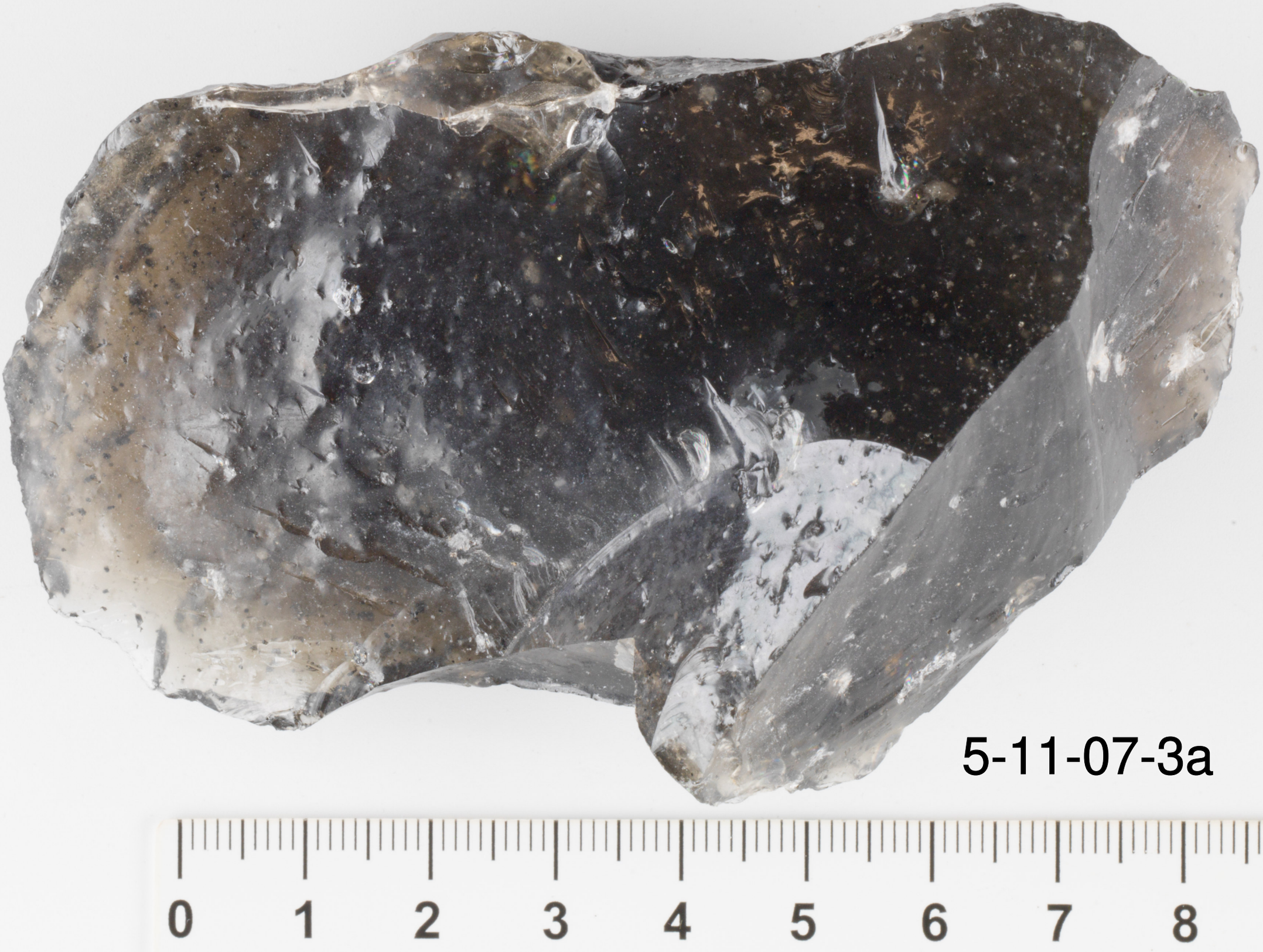
5-11-07-3a
0 1 2 3 4 5 6 7 8


9-9-01
0 1 2 3 4 5 6 7 8 9
cm

10-12-20 b

13-12-04-01

Tokai 24

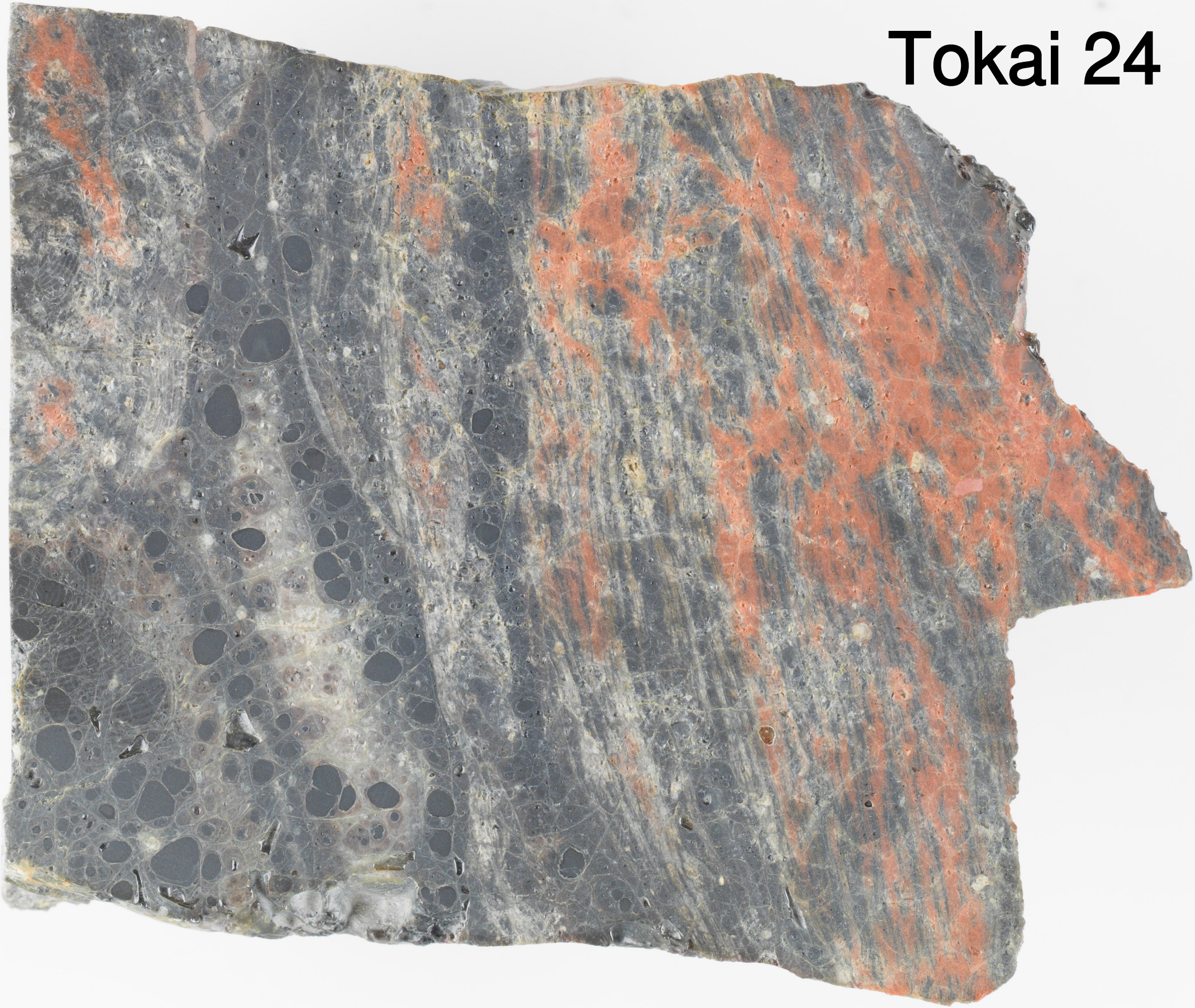

obsidian without cracks


0 1 2 3 4 5 6 7 8 9
cm
JK 20

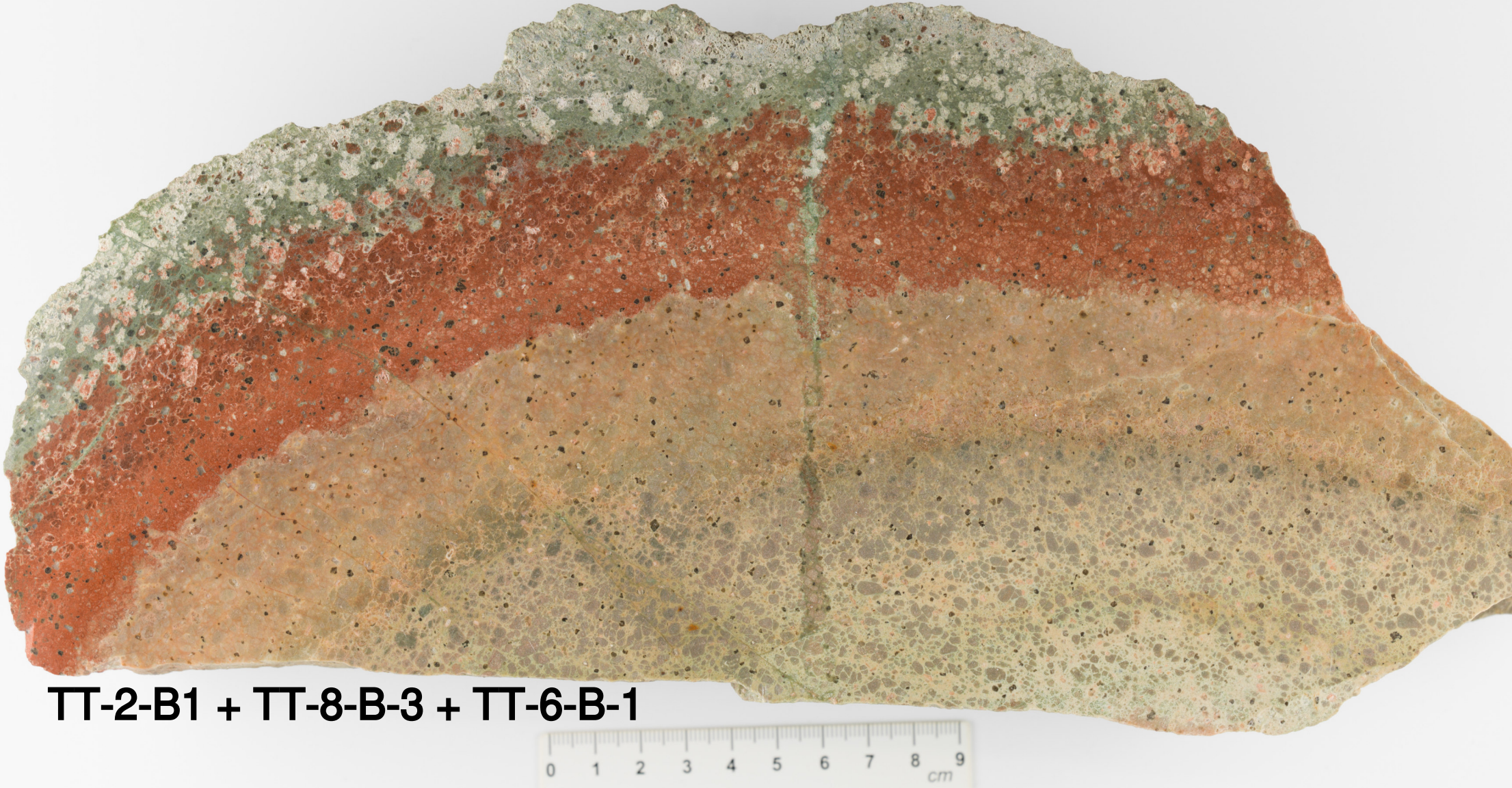
TT-2-B1 + TT-8-B-3 + TT-6-B-1
0 1 2 3 4 5 6 7 8 9
cm

8.1.2. Thin section images

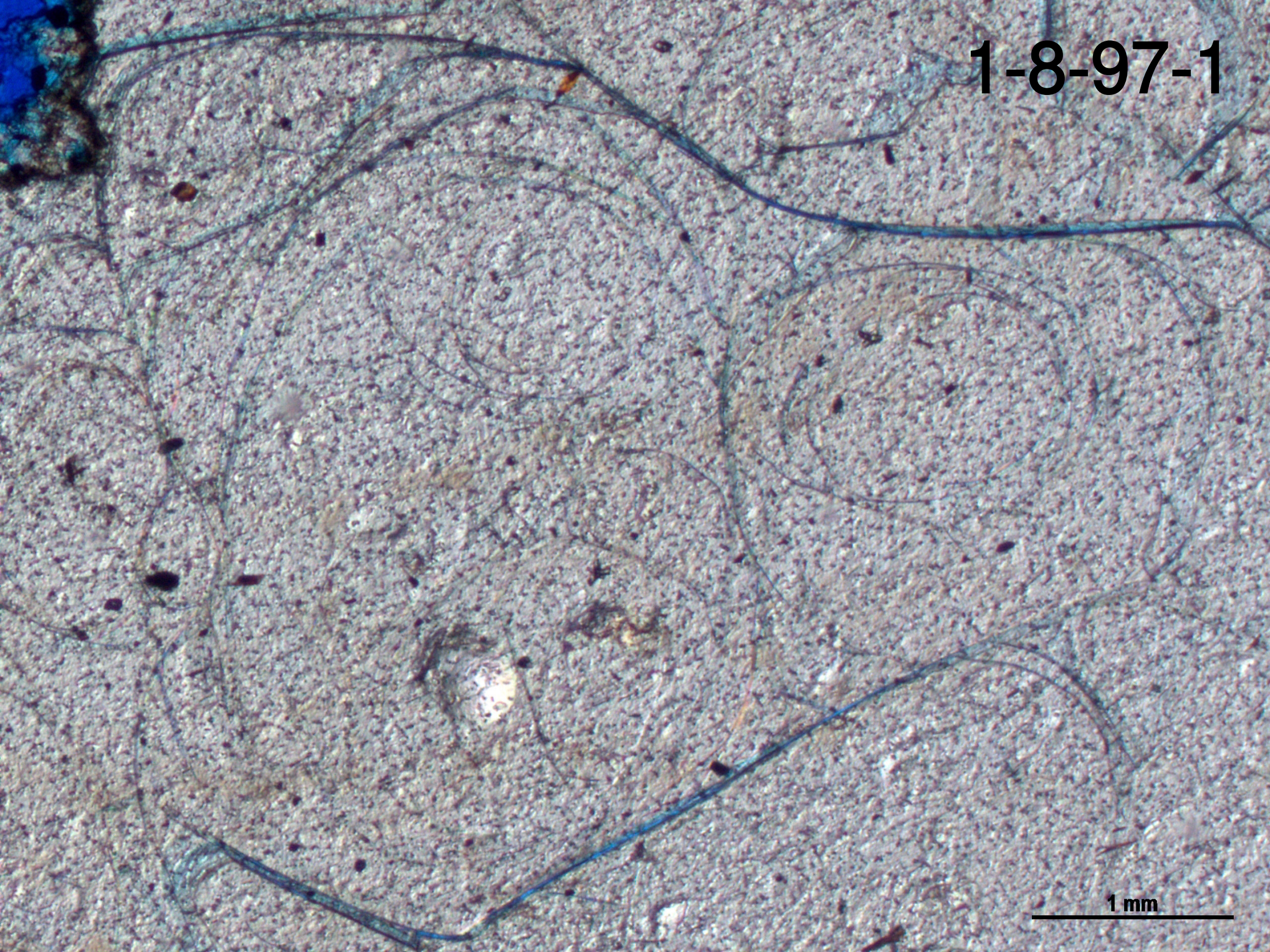
1-8-97-1
1 mm

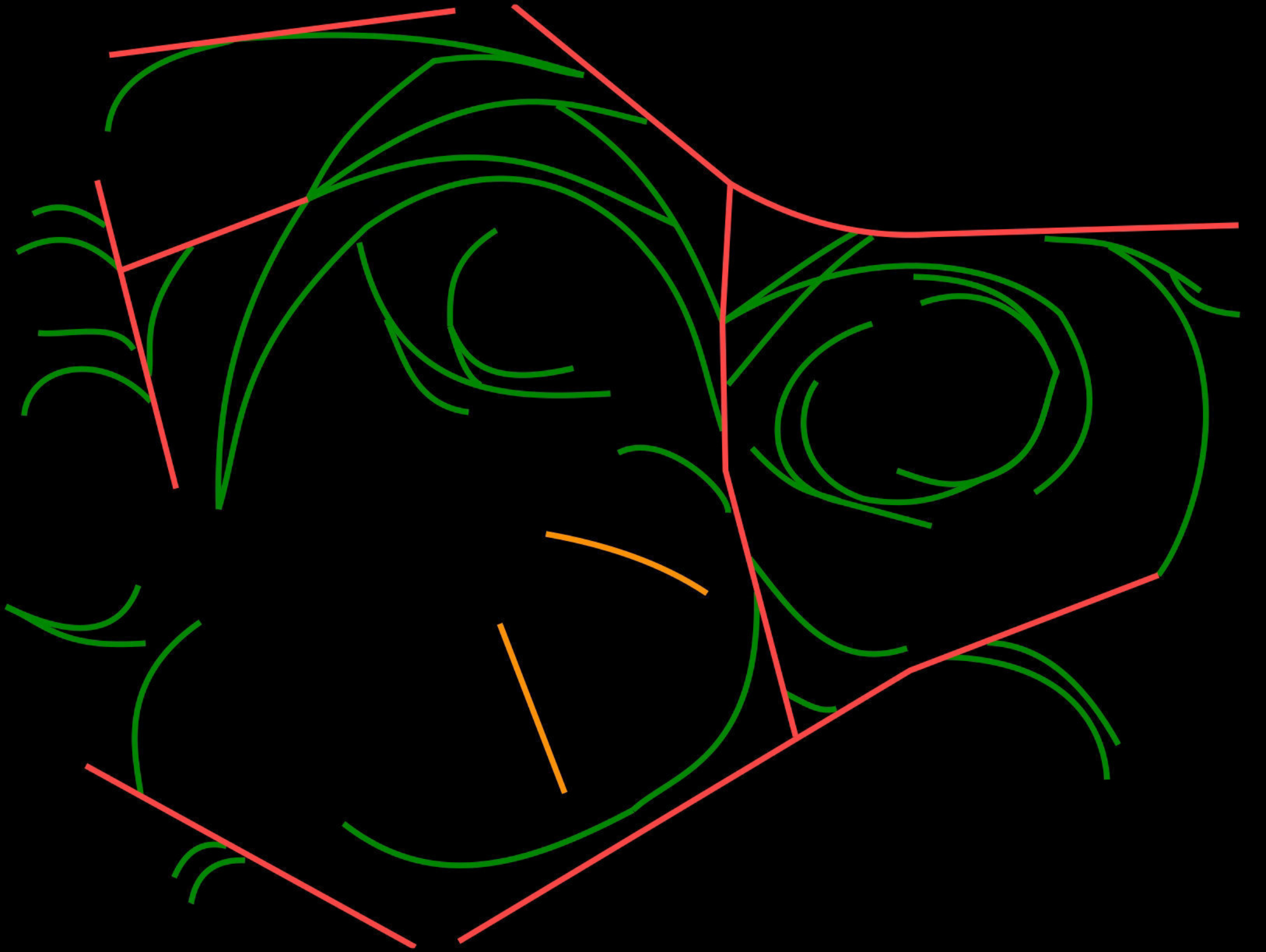

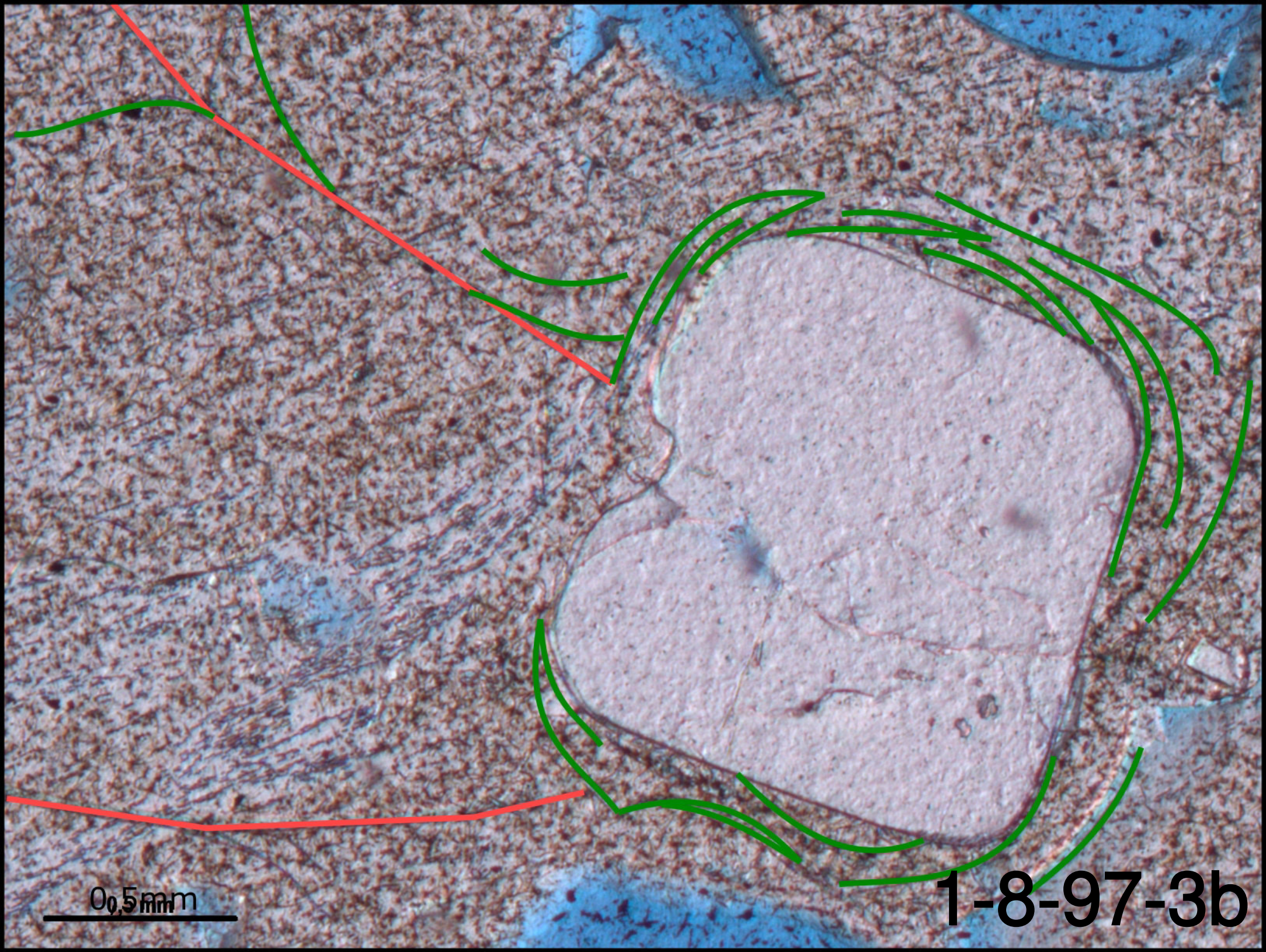
0,5mm
1-8-97-3b

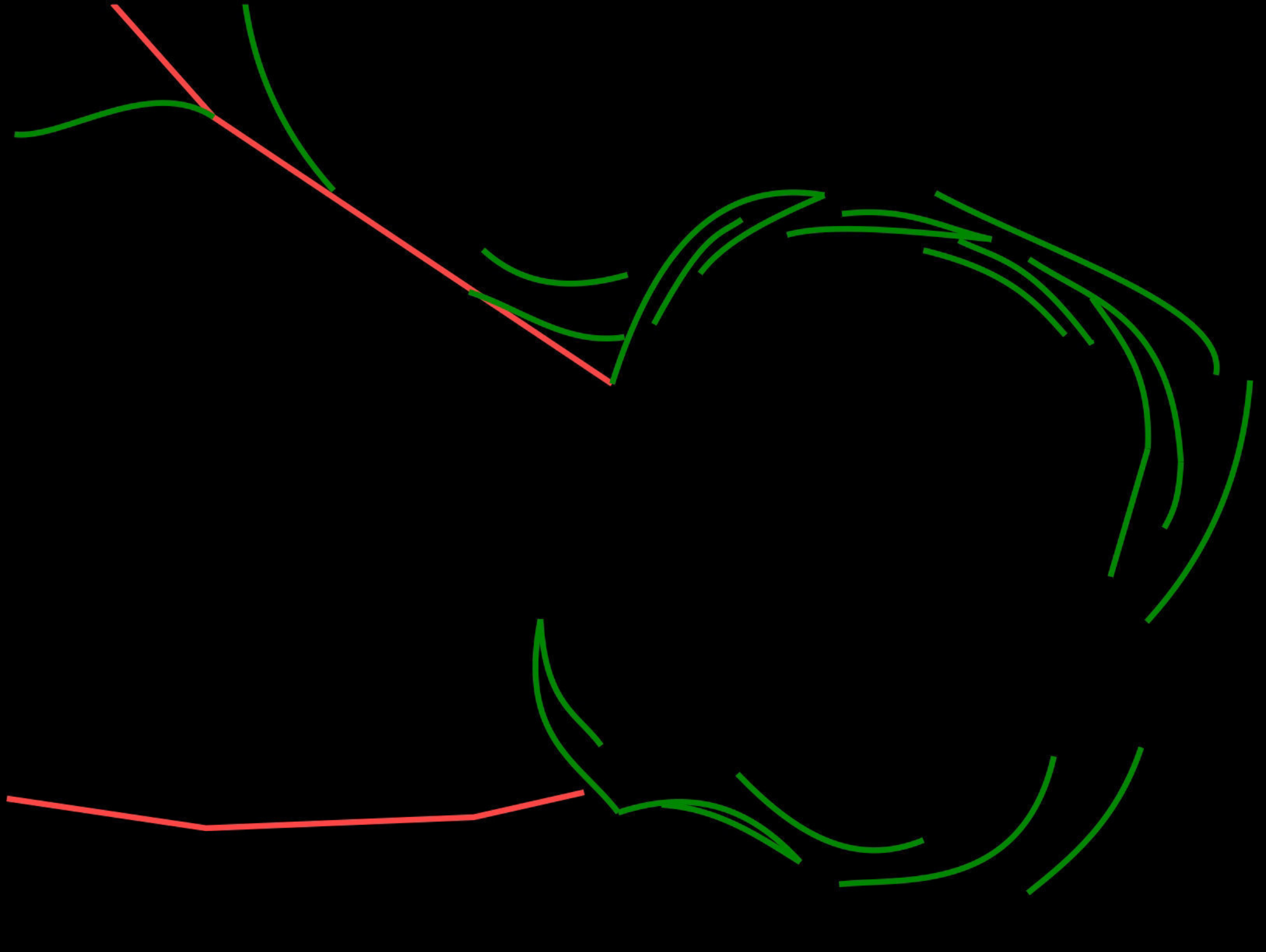

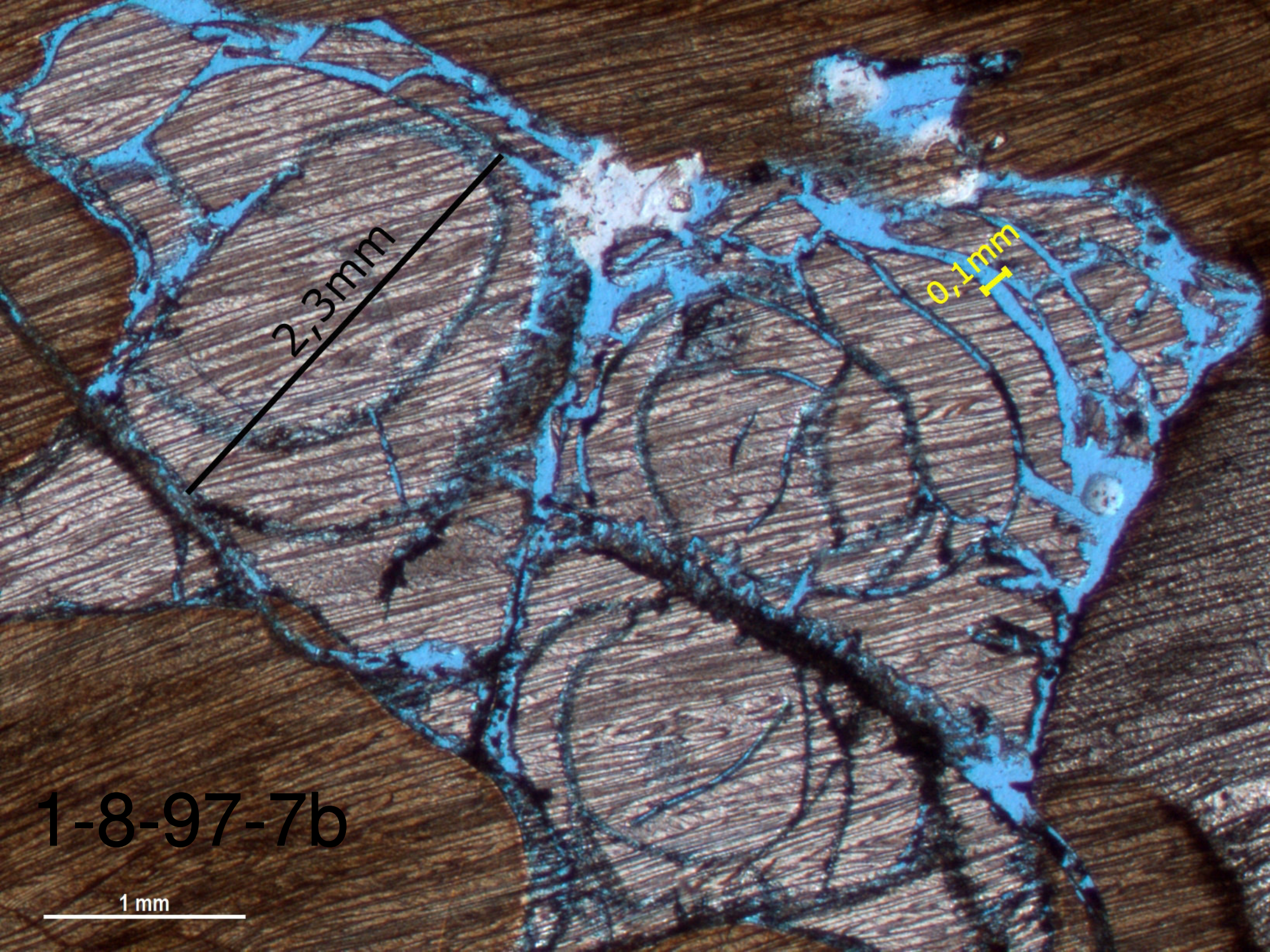
2,3mm
0,1mm
1-8-97-7b
1 mm

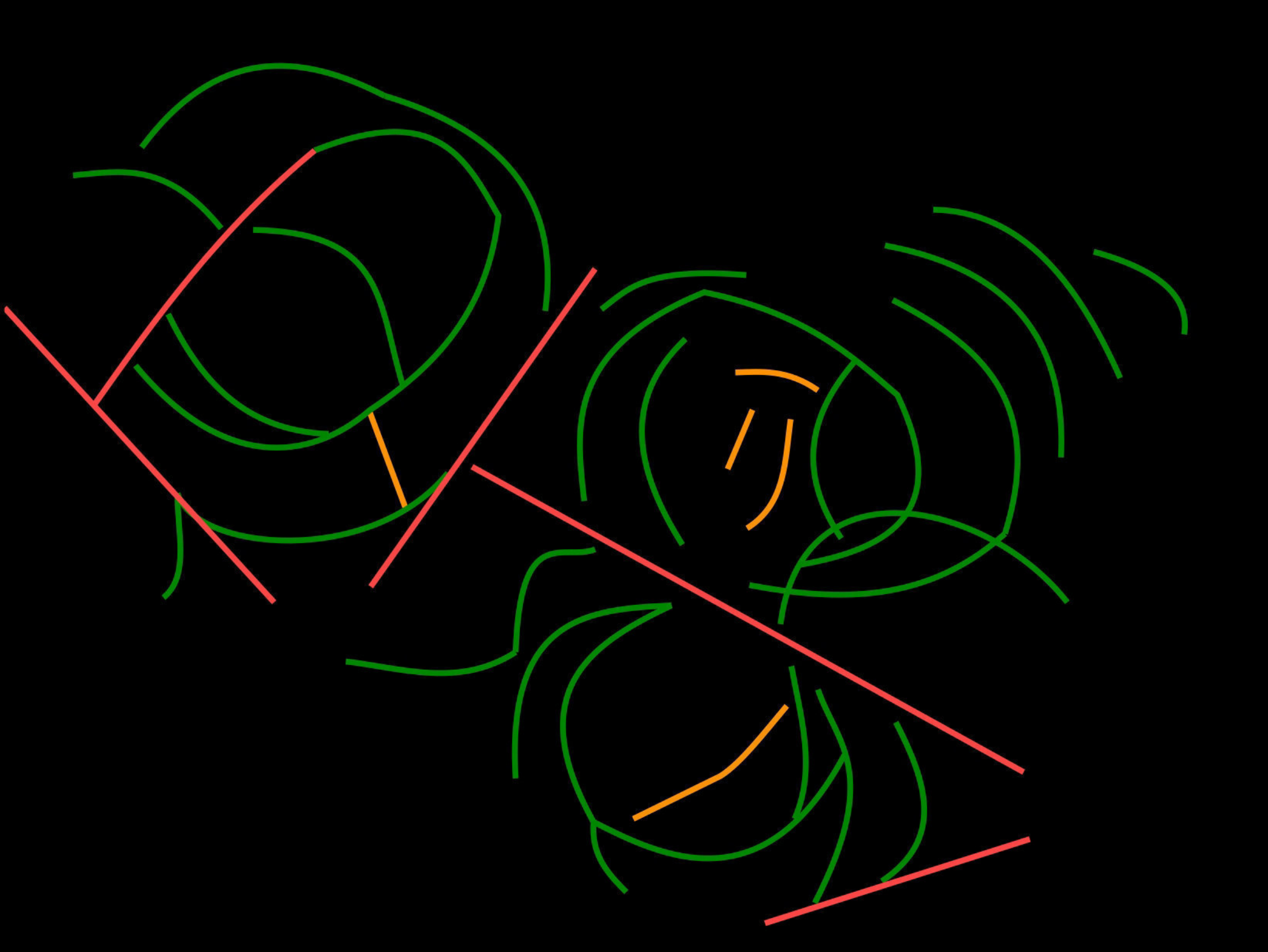

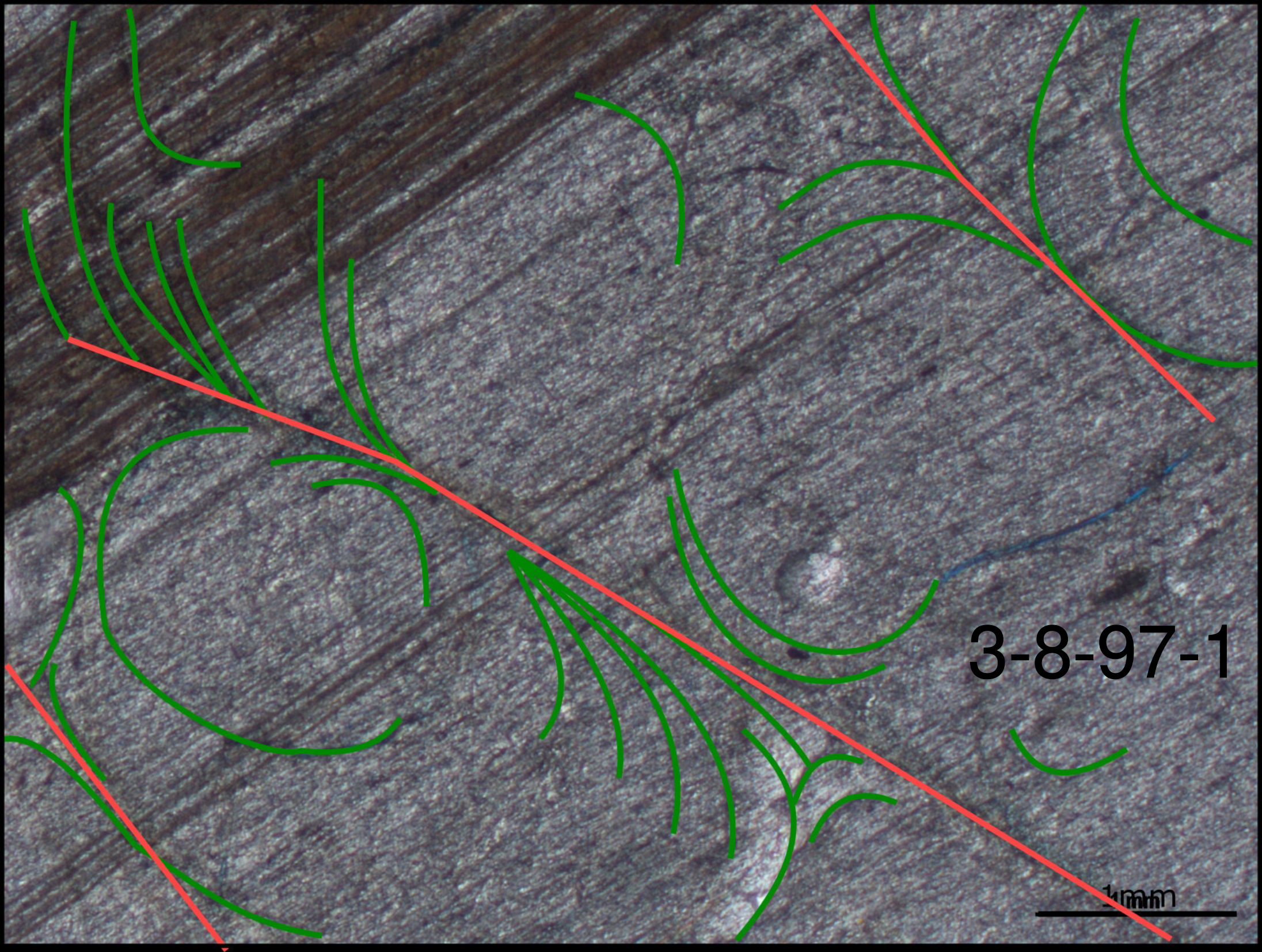
3-8-97-1
1mm

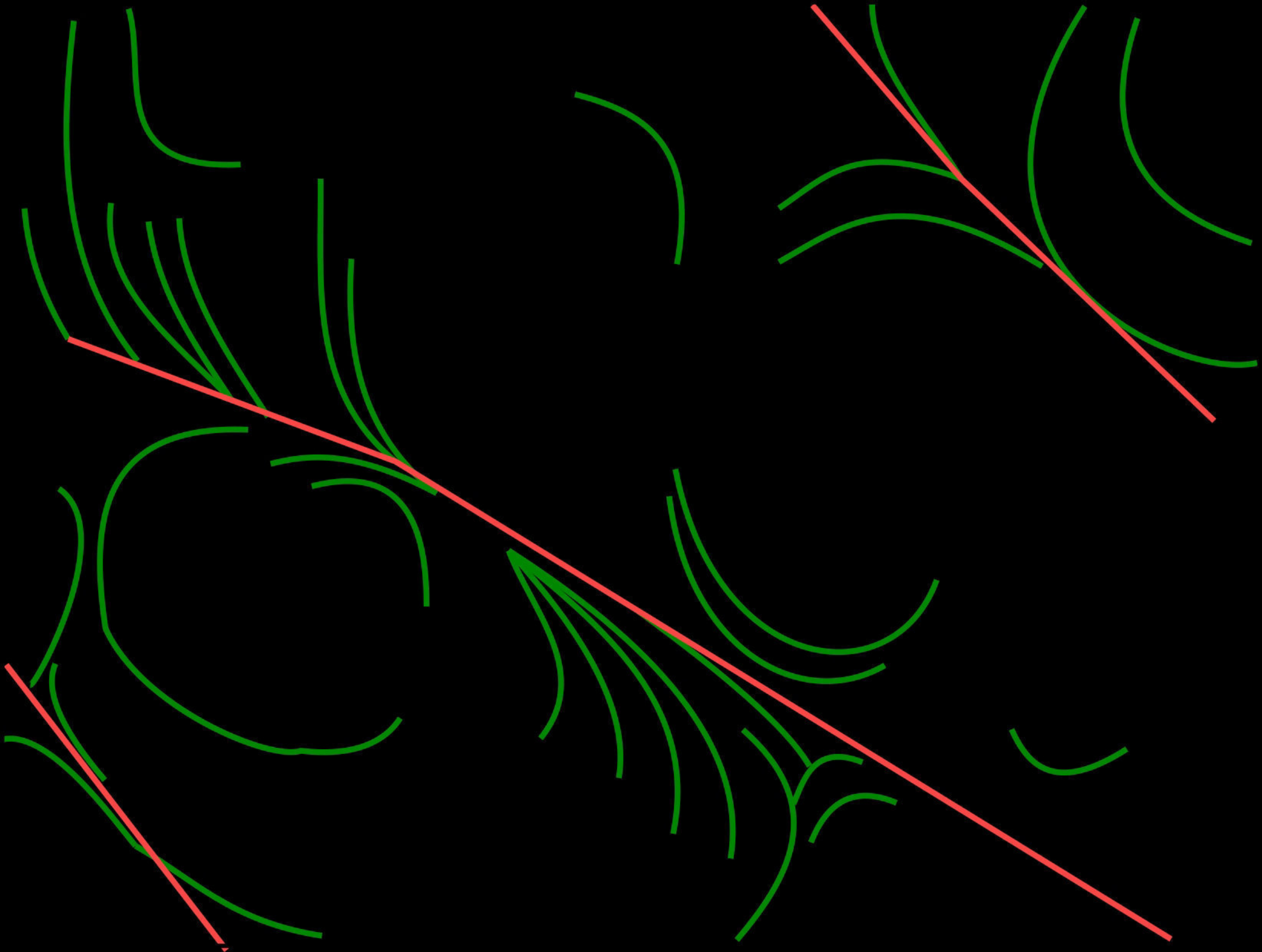

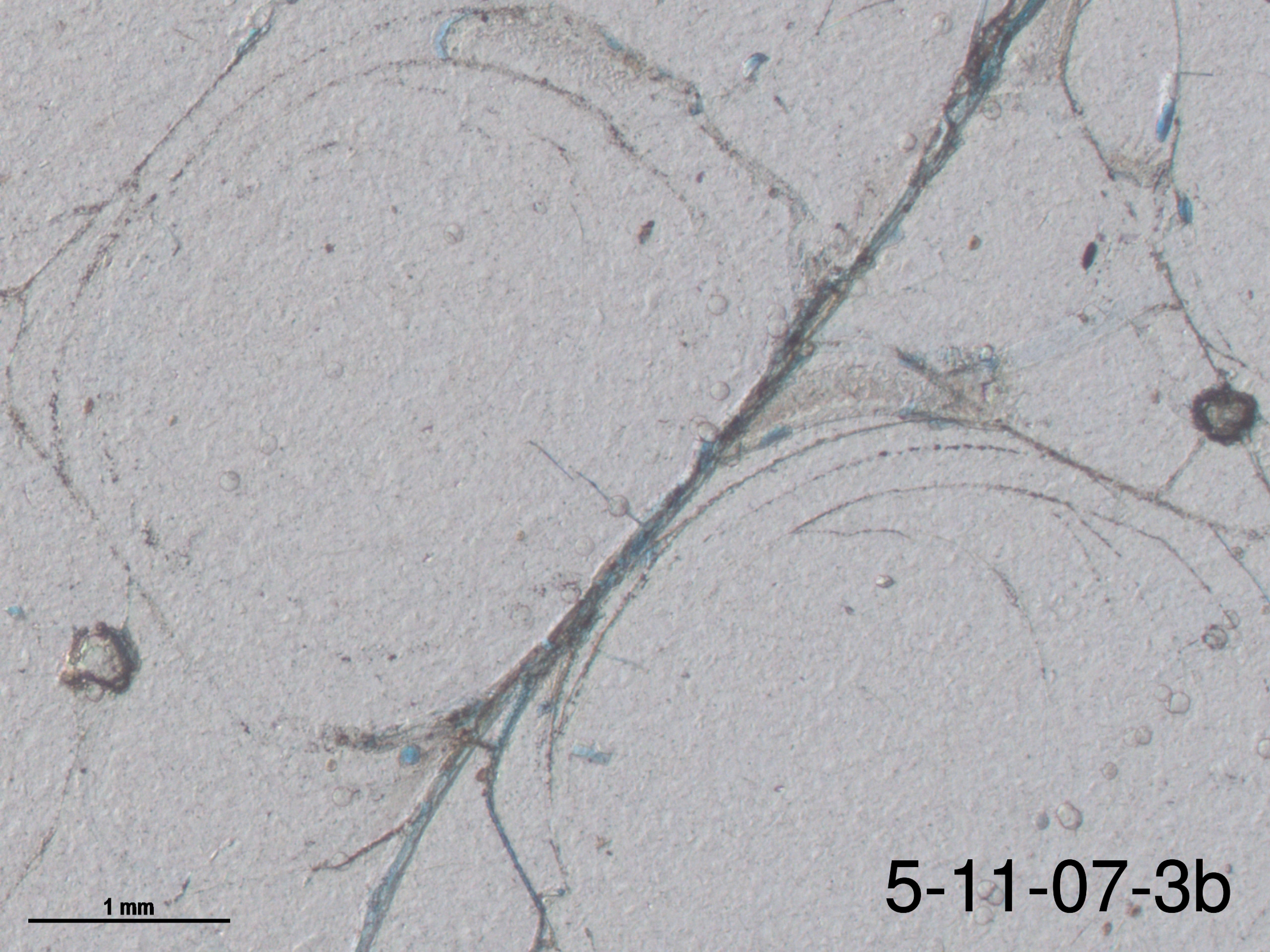
1 mm
5-11-07-3b

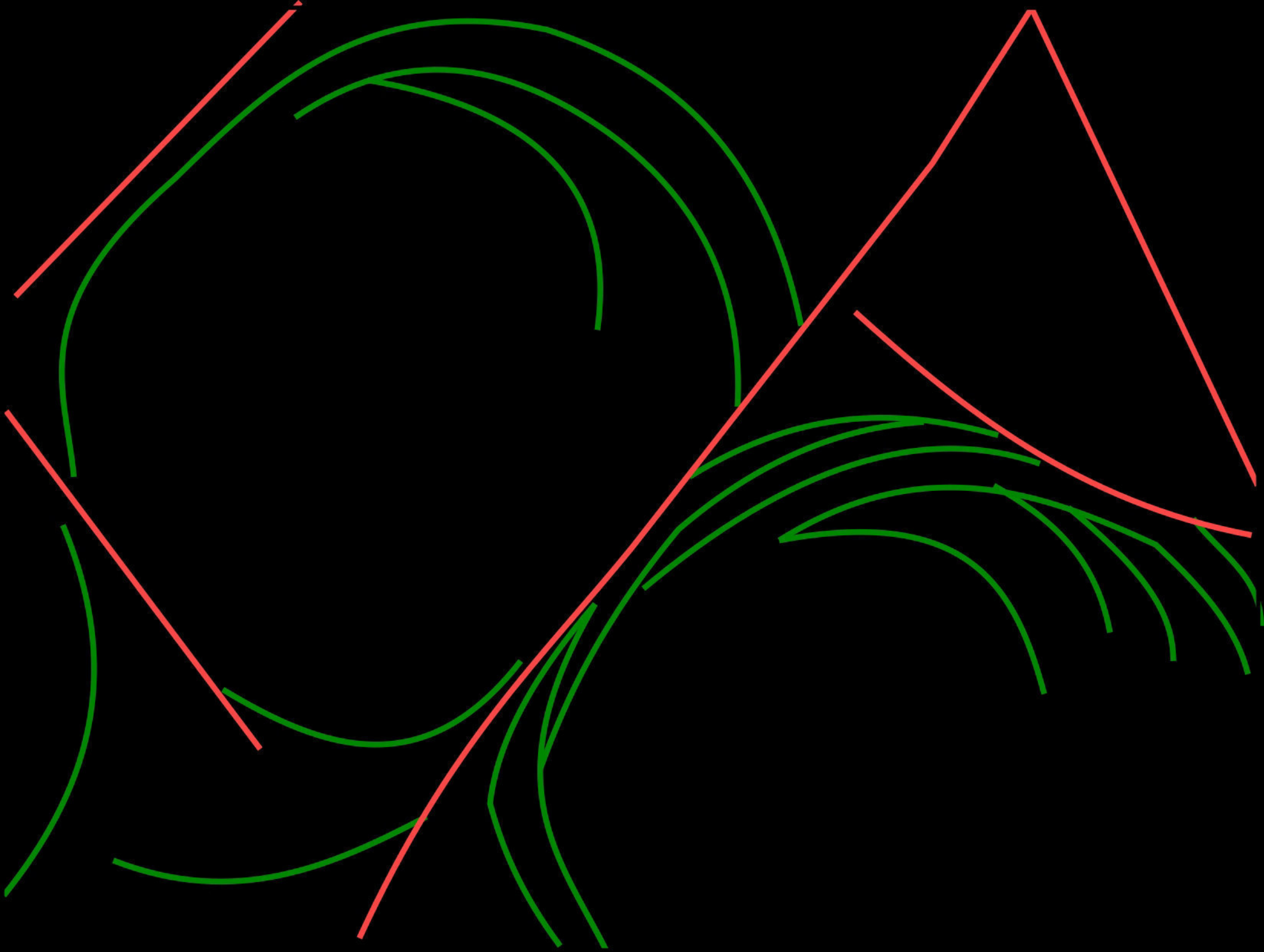

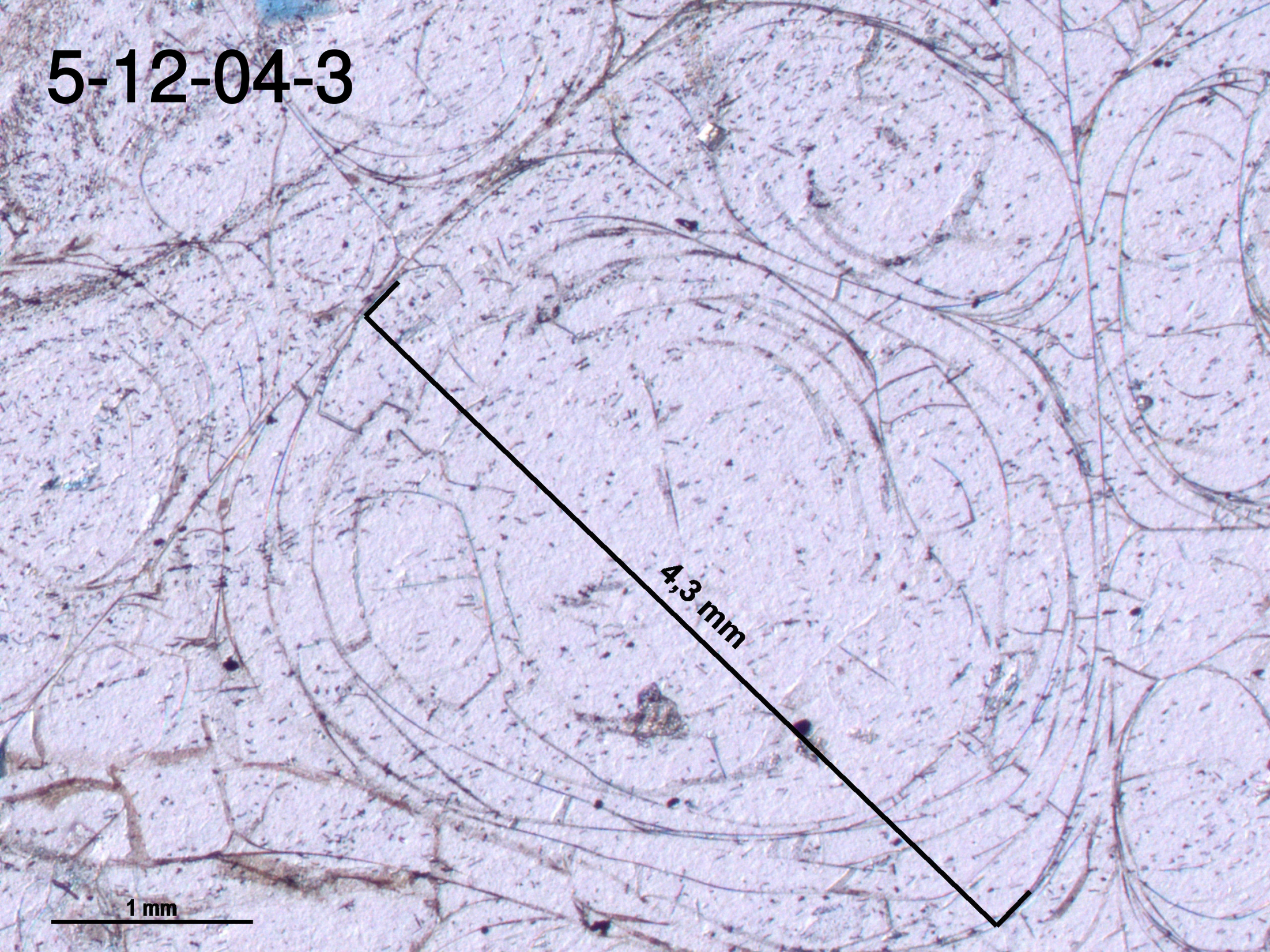
5-12-04-3
4,3 mm
1 mm

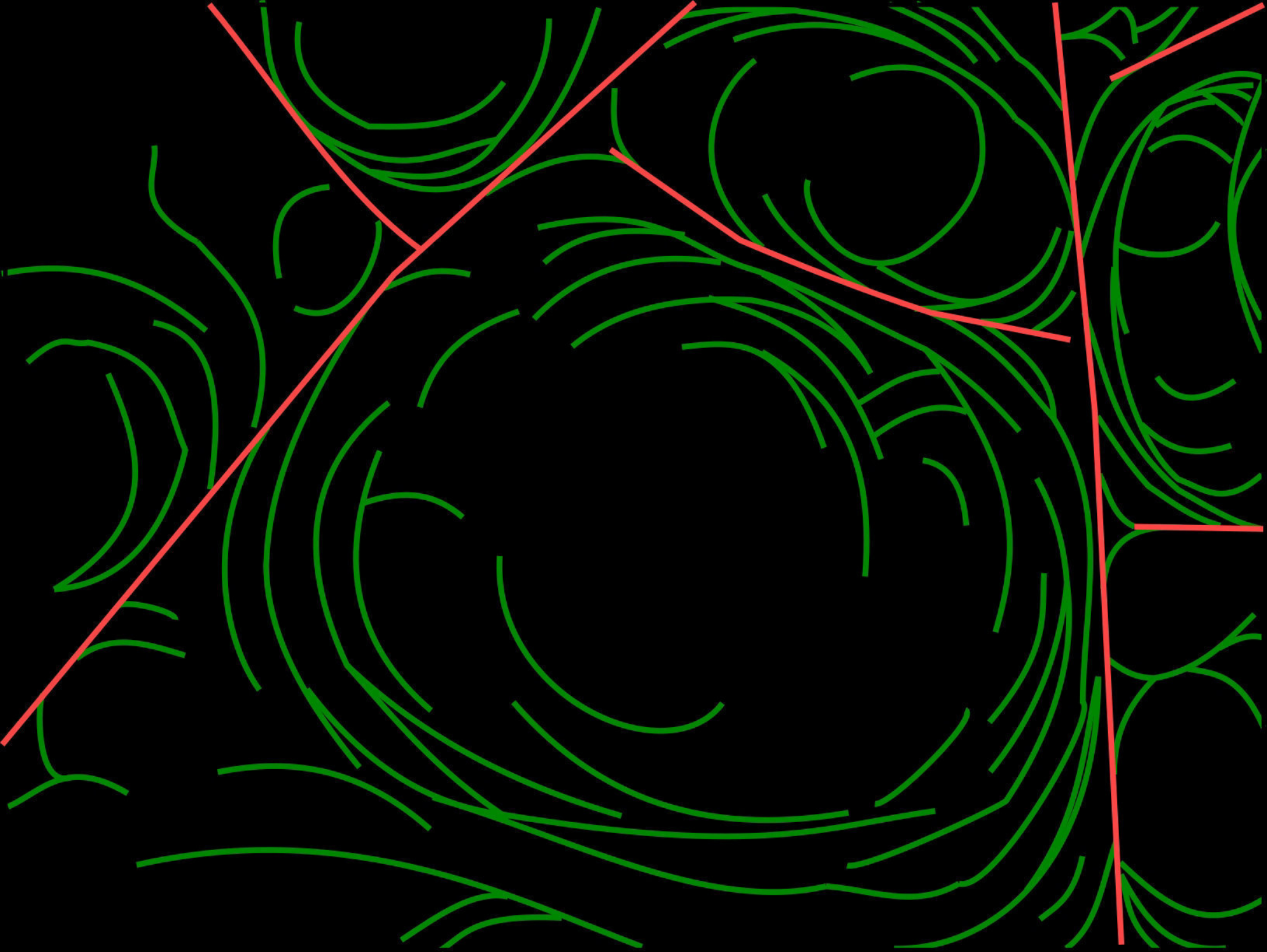

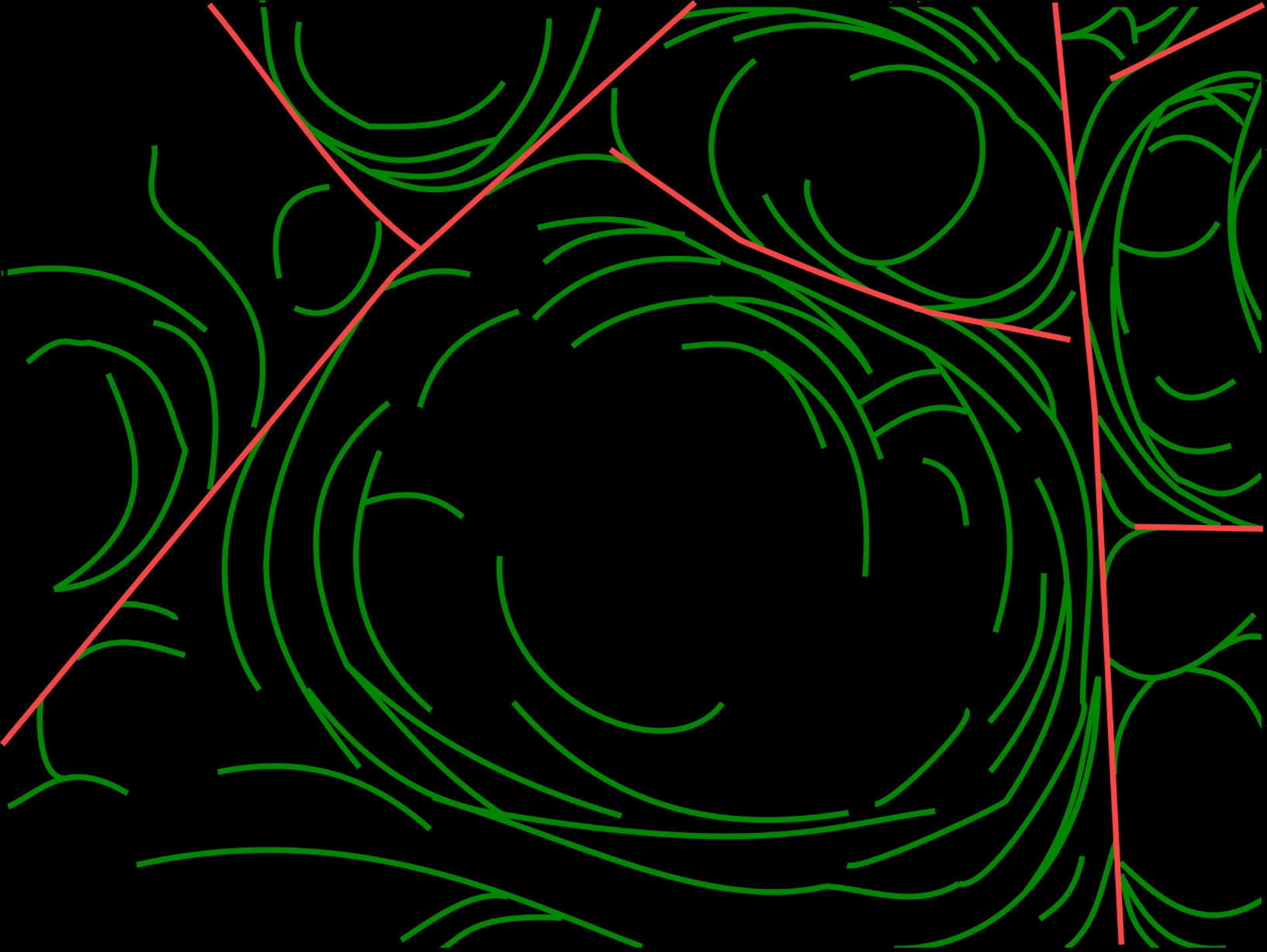

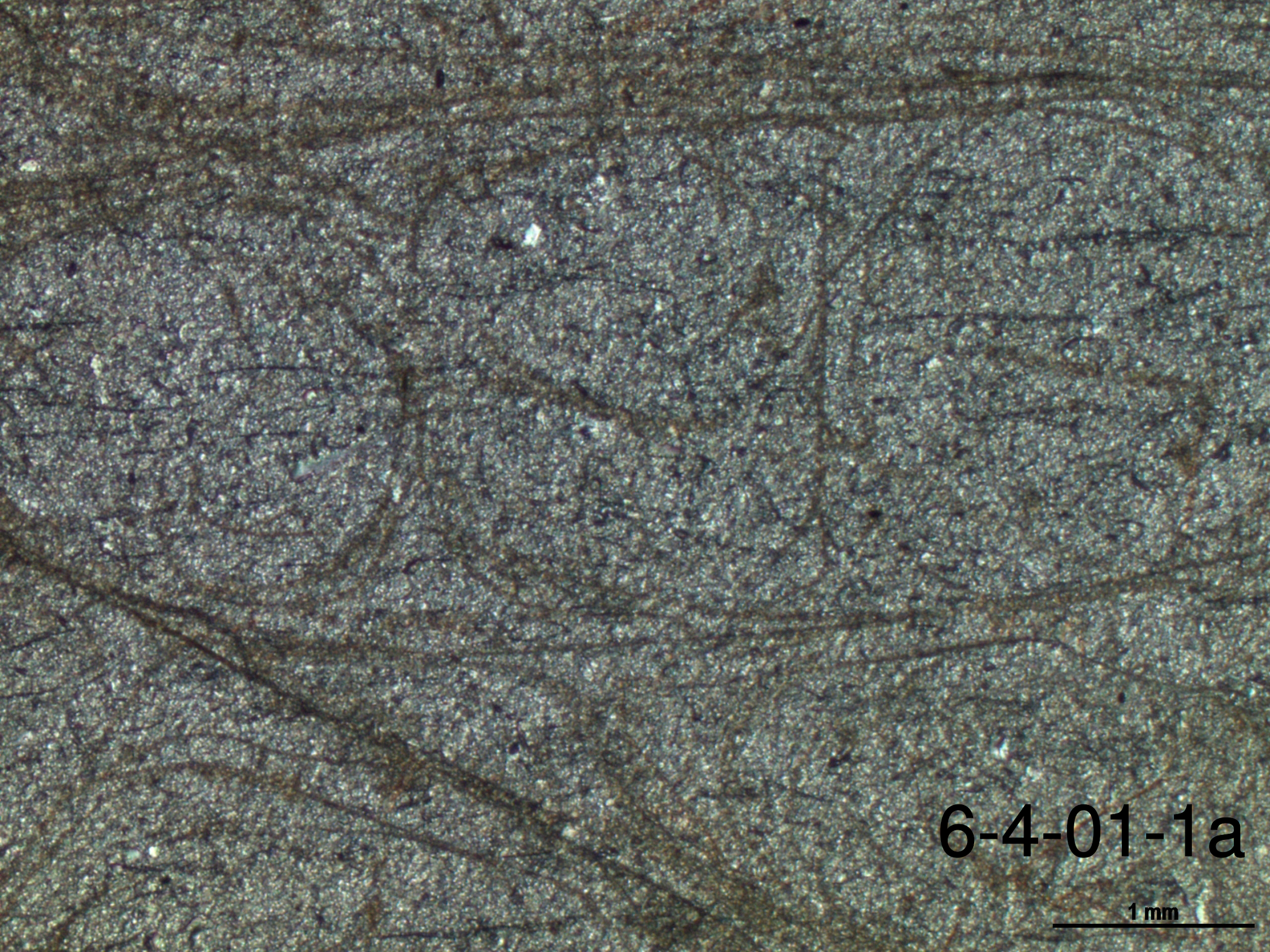
6-4-01-1a
1 mm

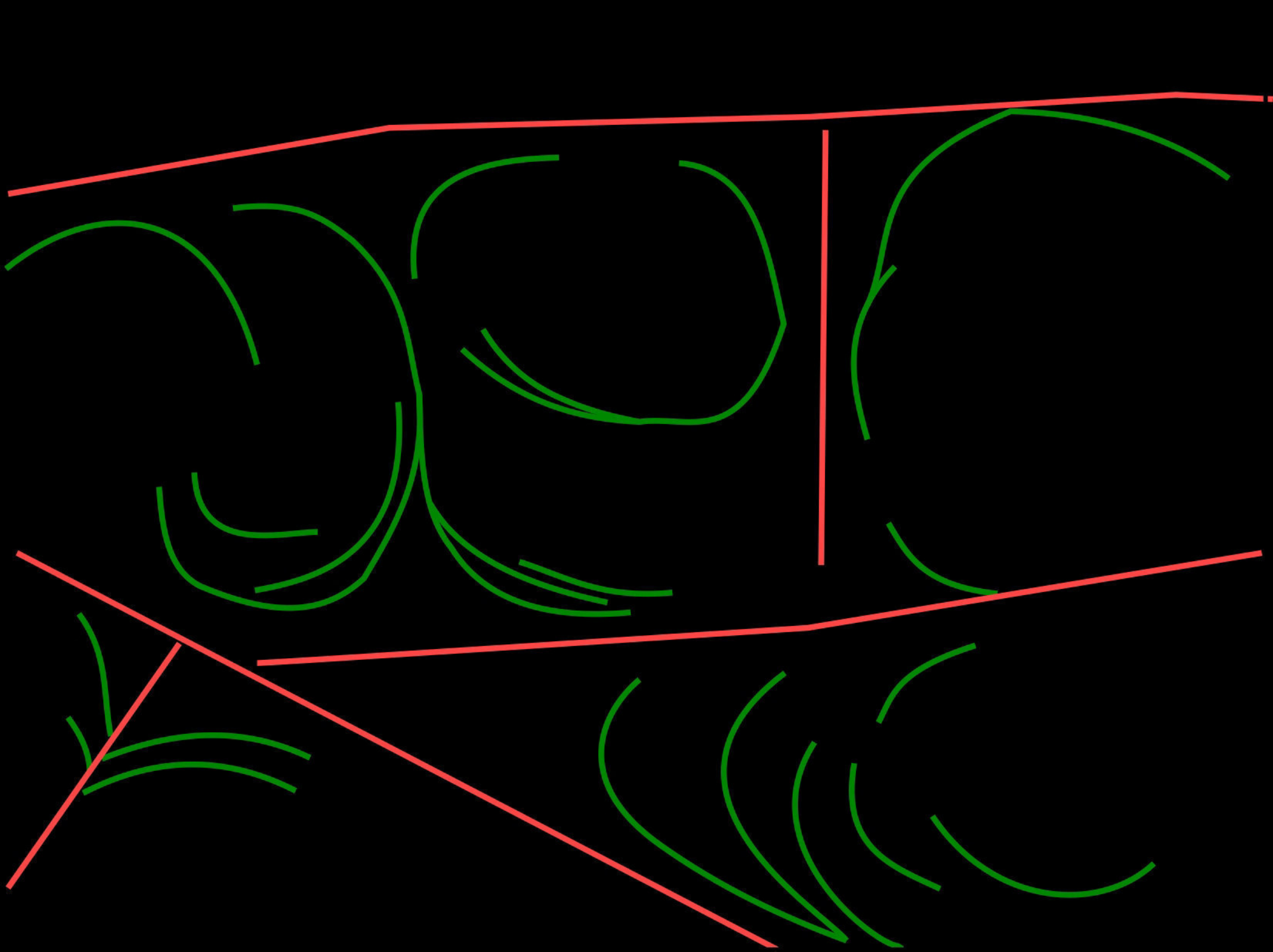

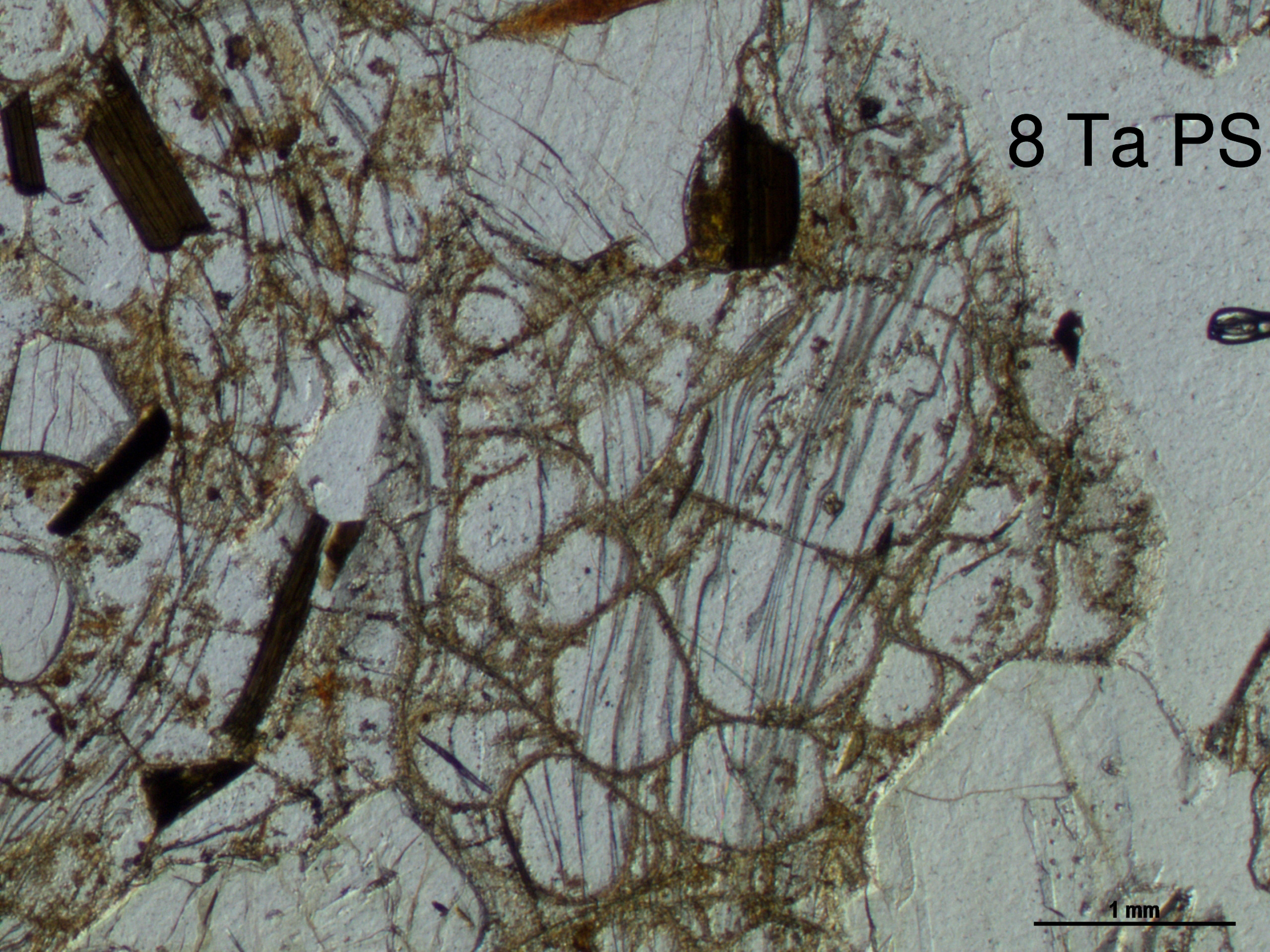
8 Ta PS
1 mm

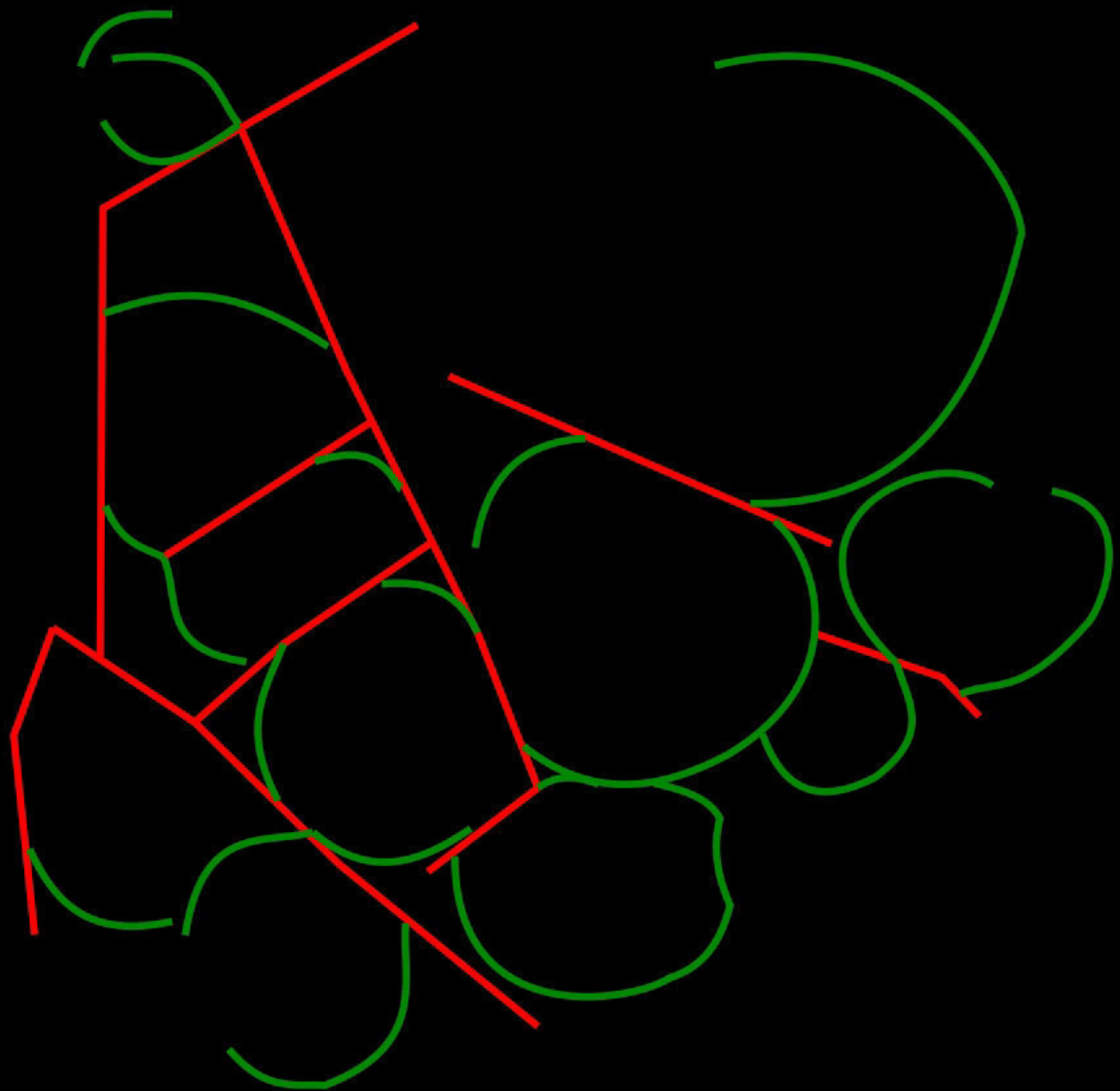

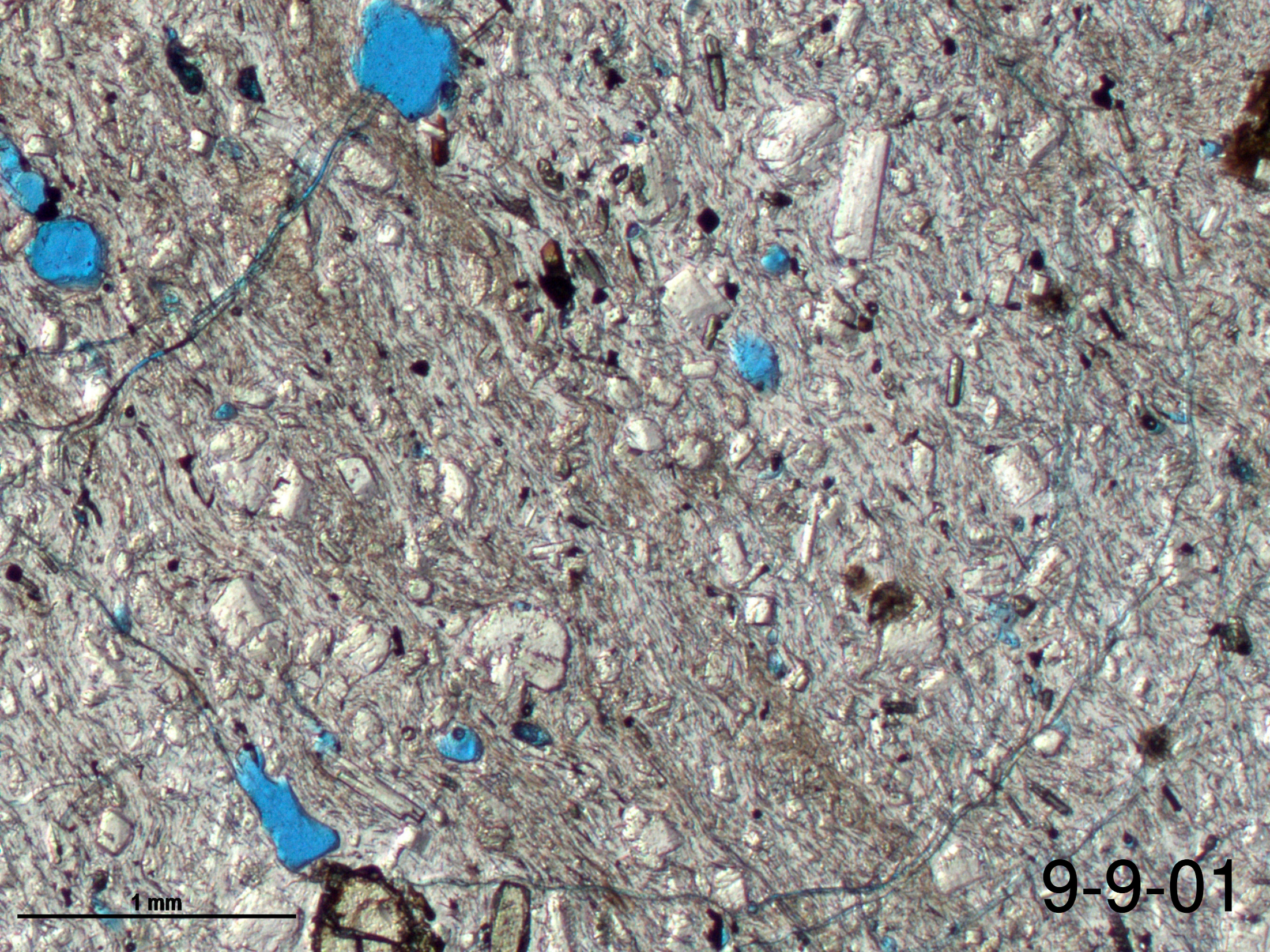
1 mm
9-9-01

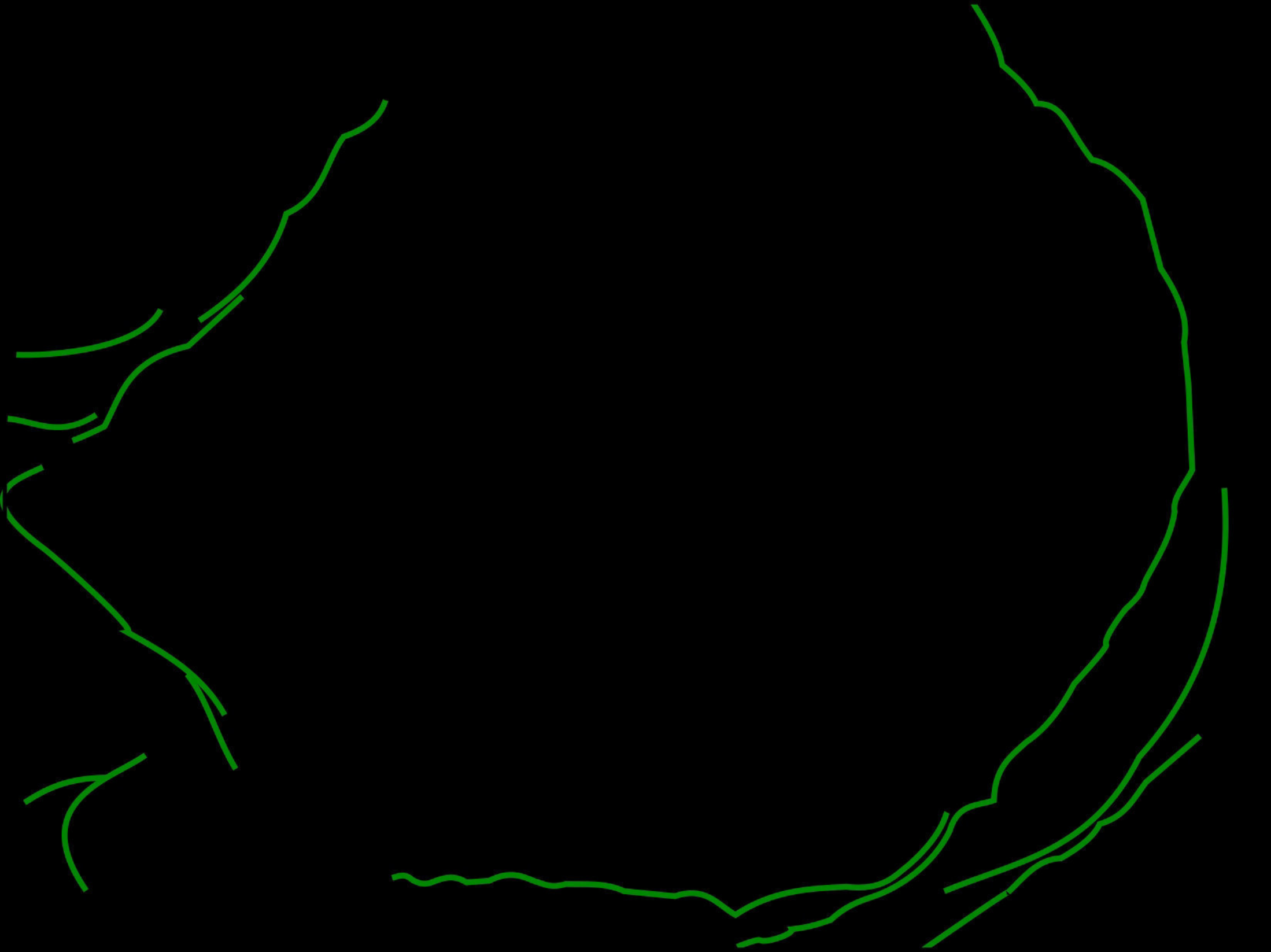

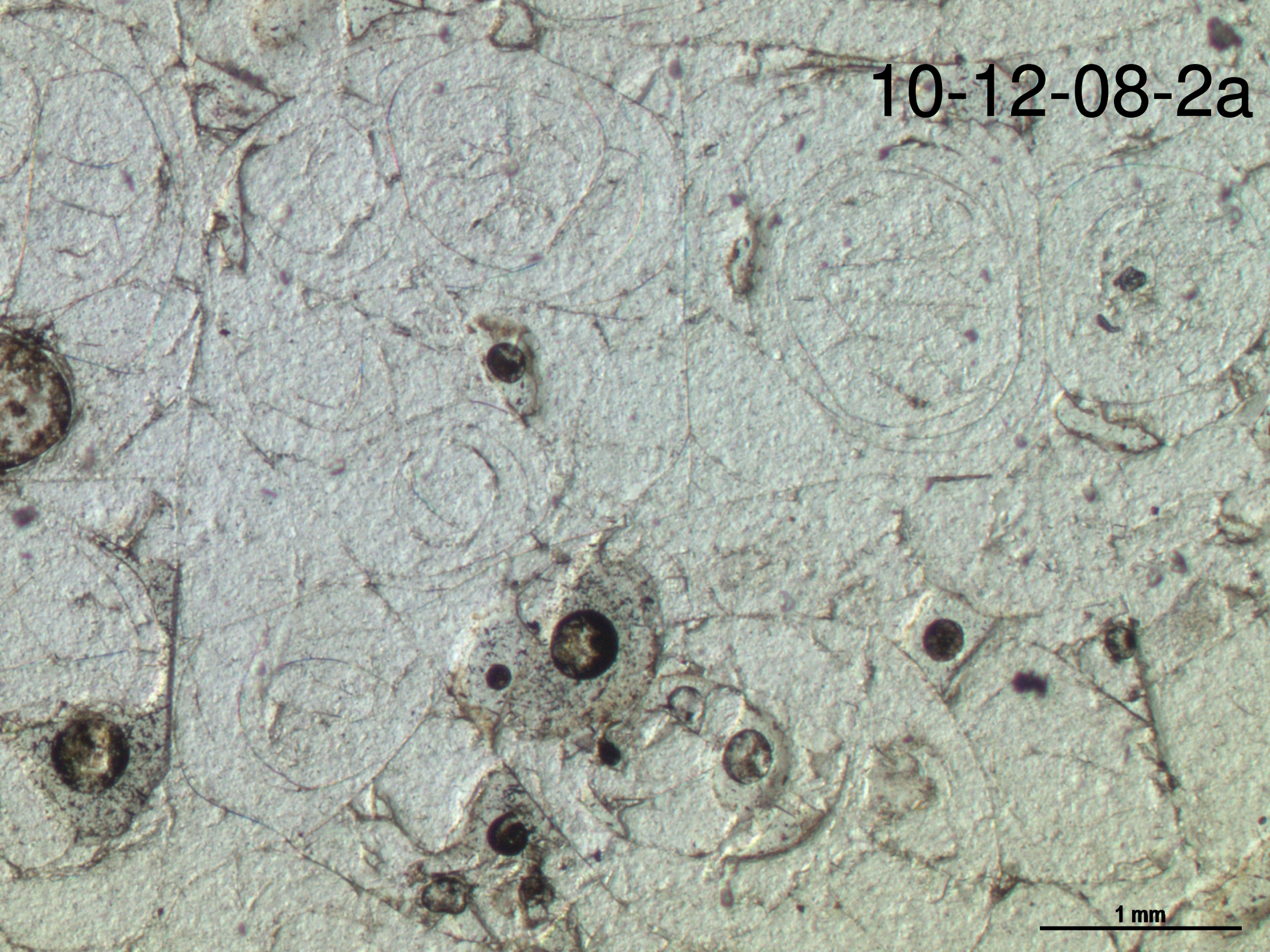
10-12-08-2a
1 mm

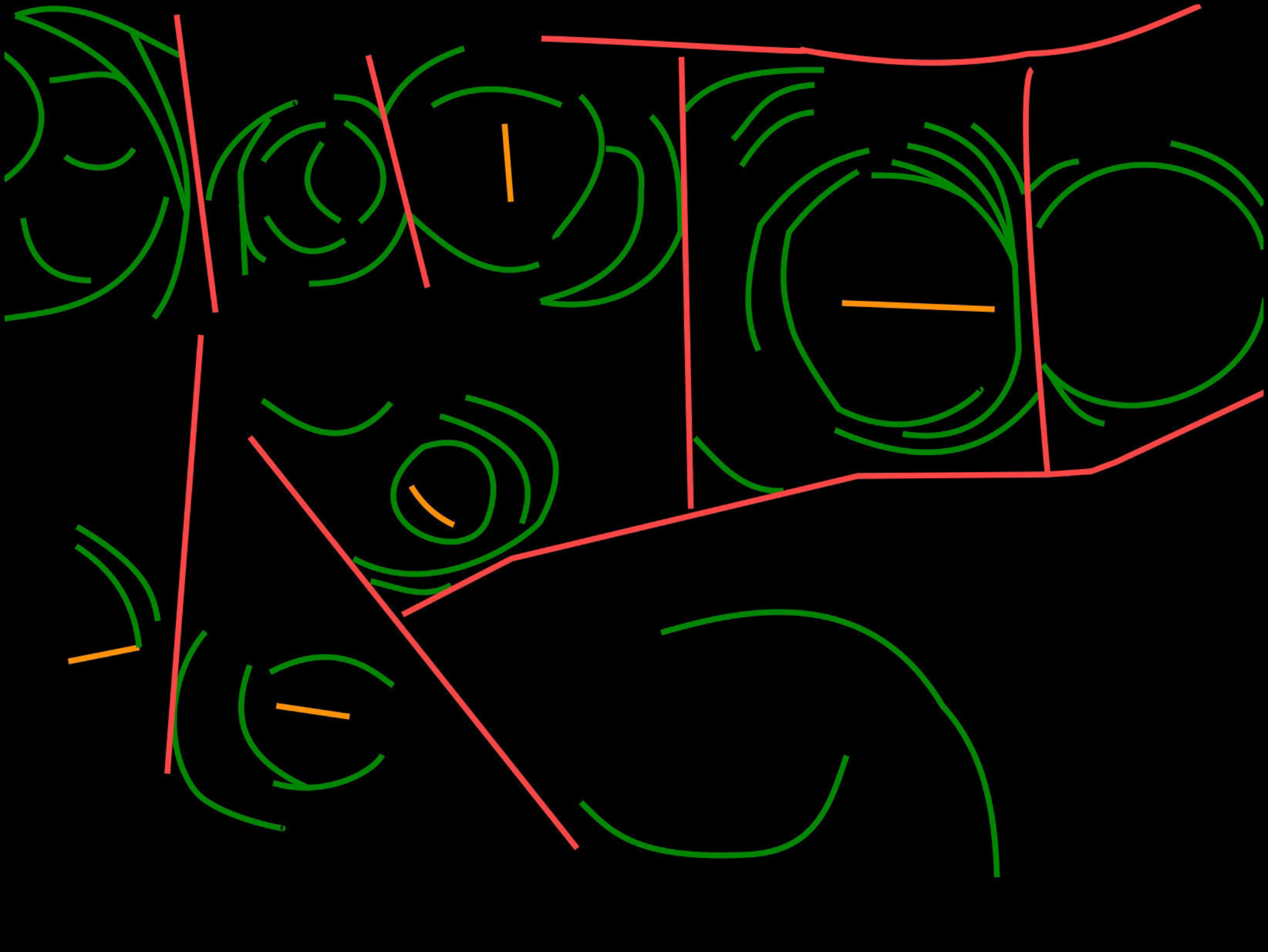

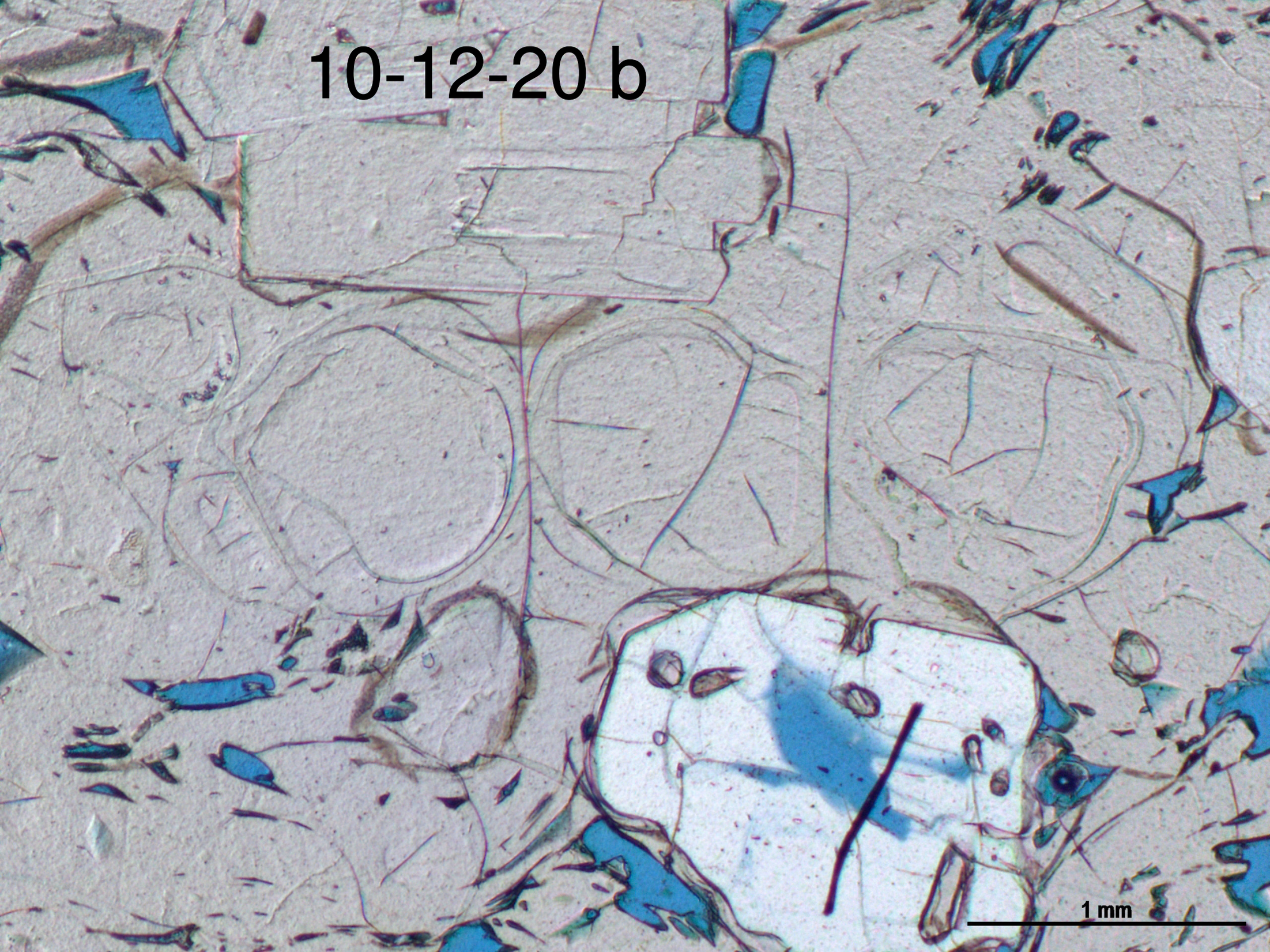
10-12-20 b
1 mm

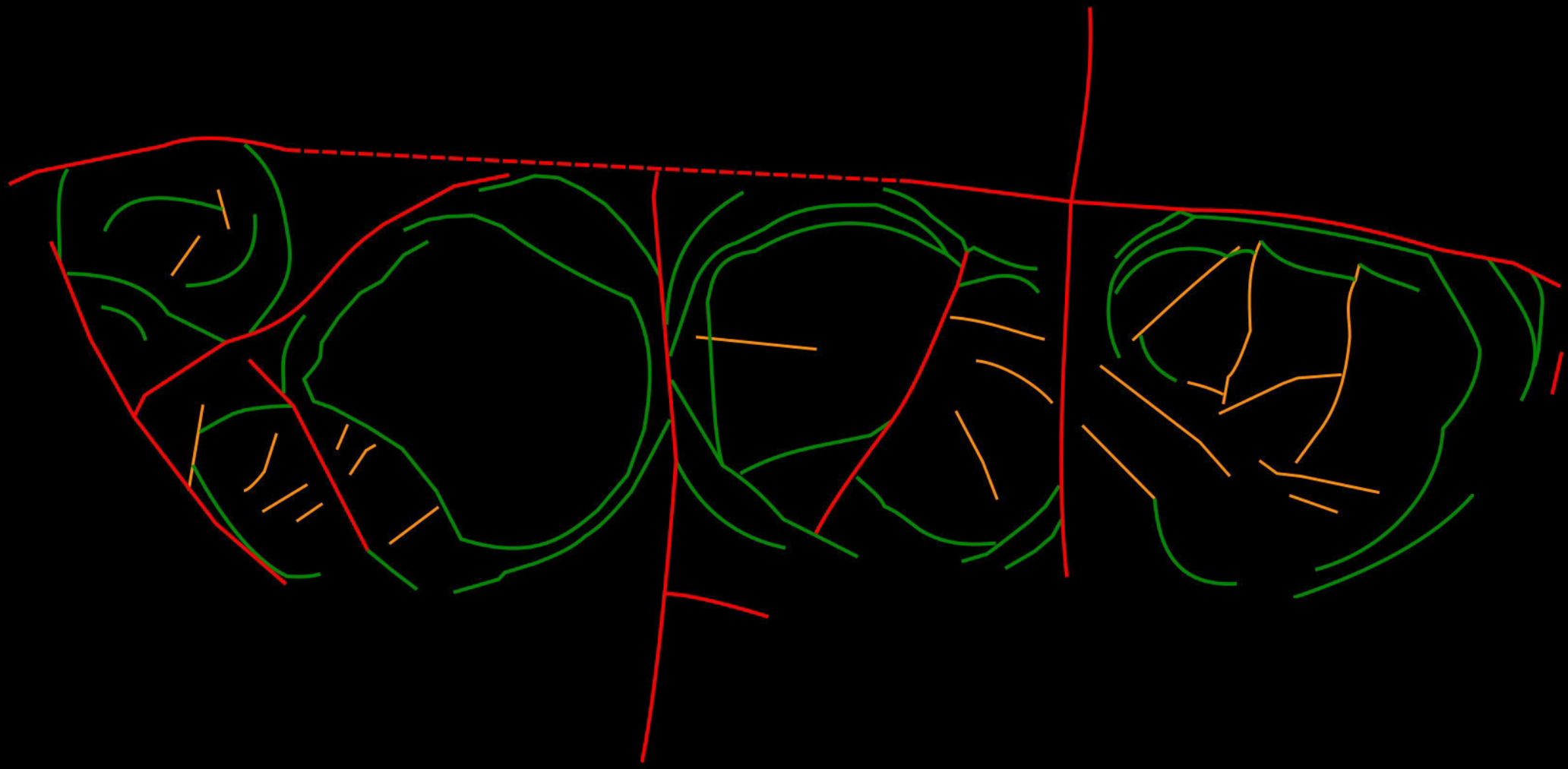

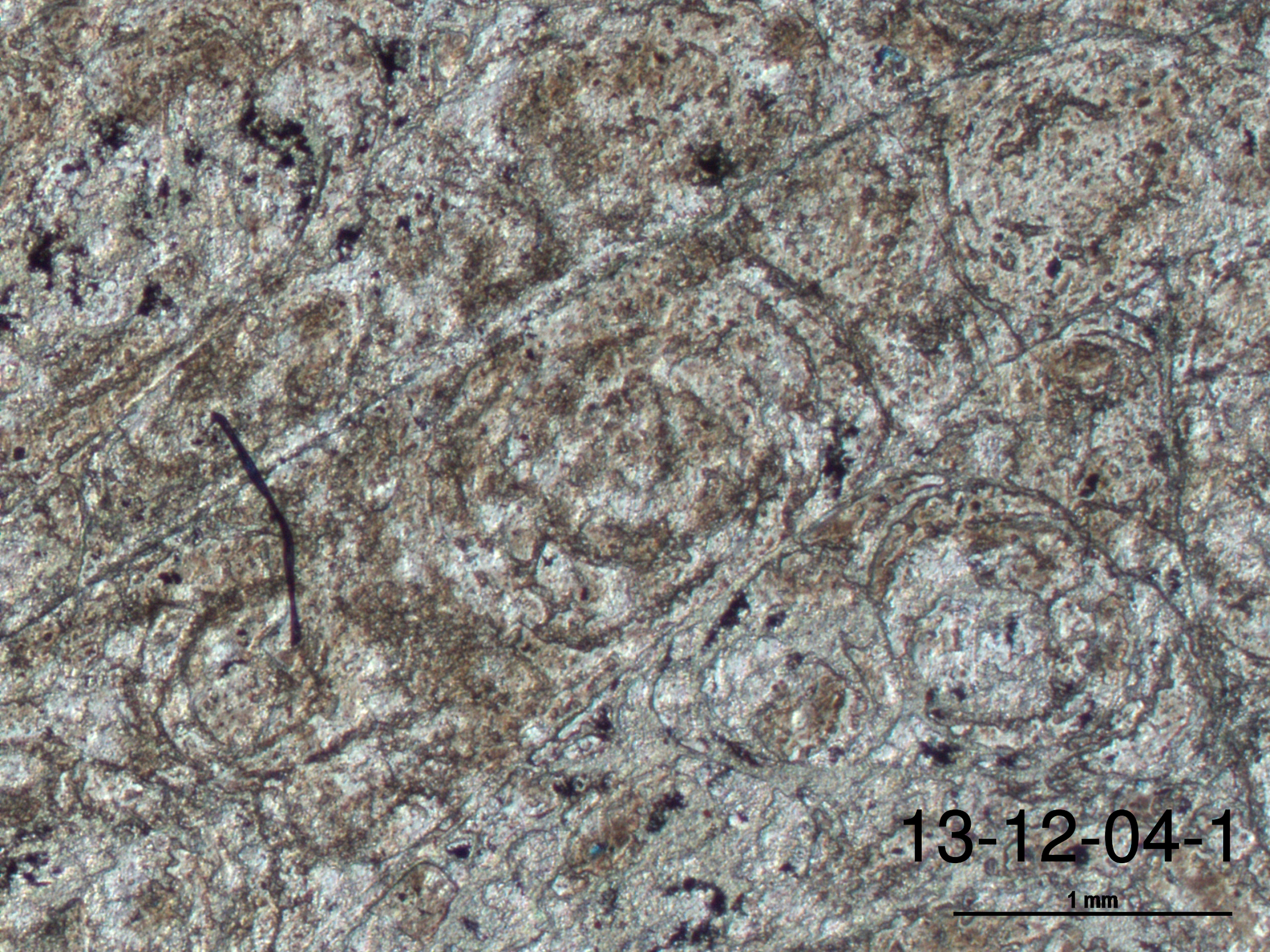
13-12-04-1
1 mm

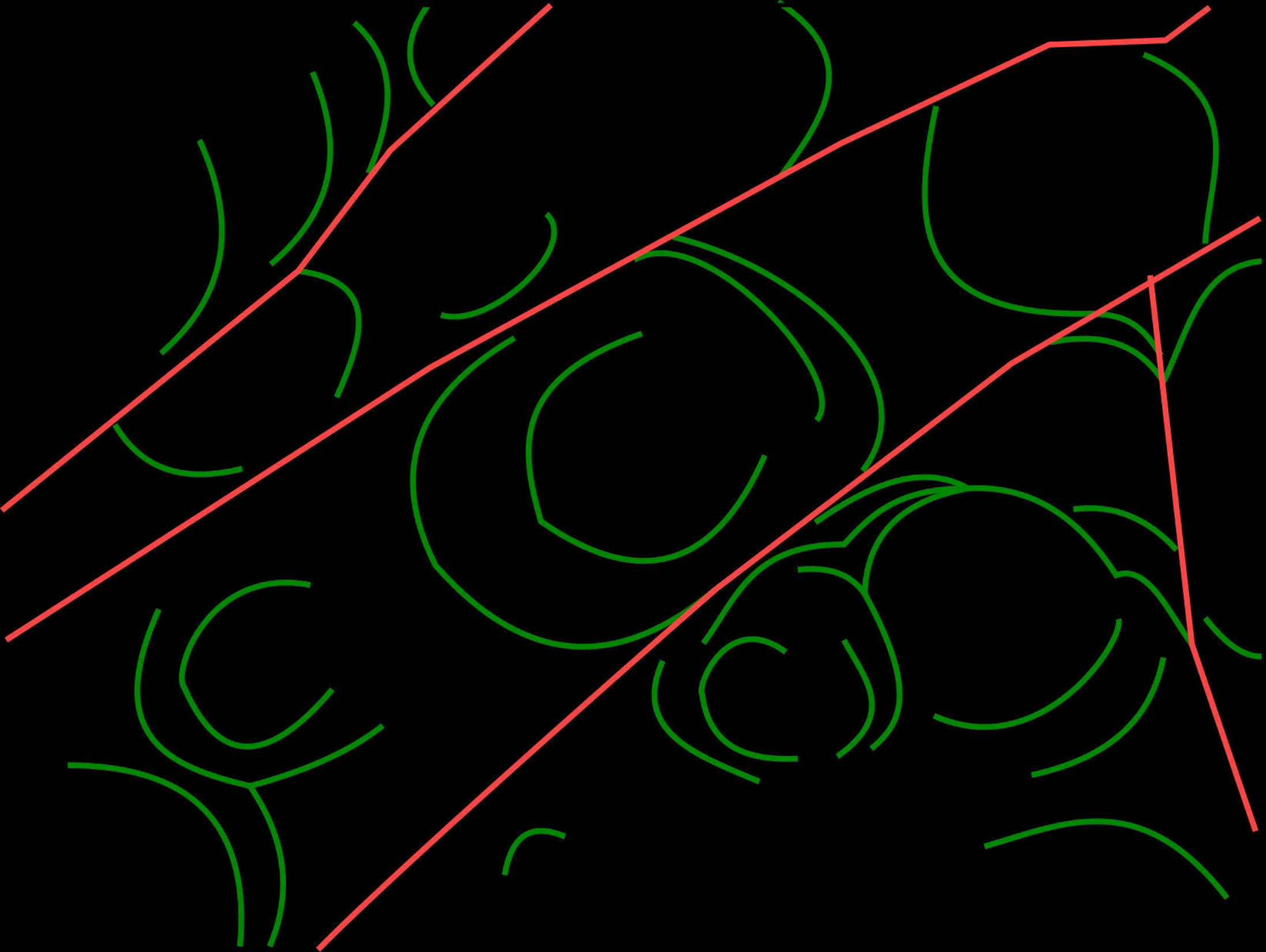

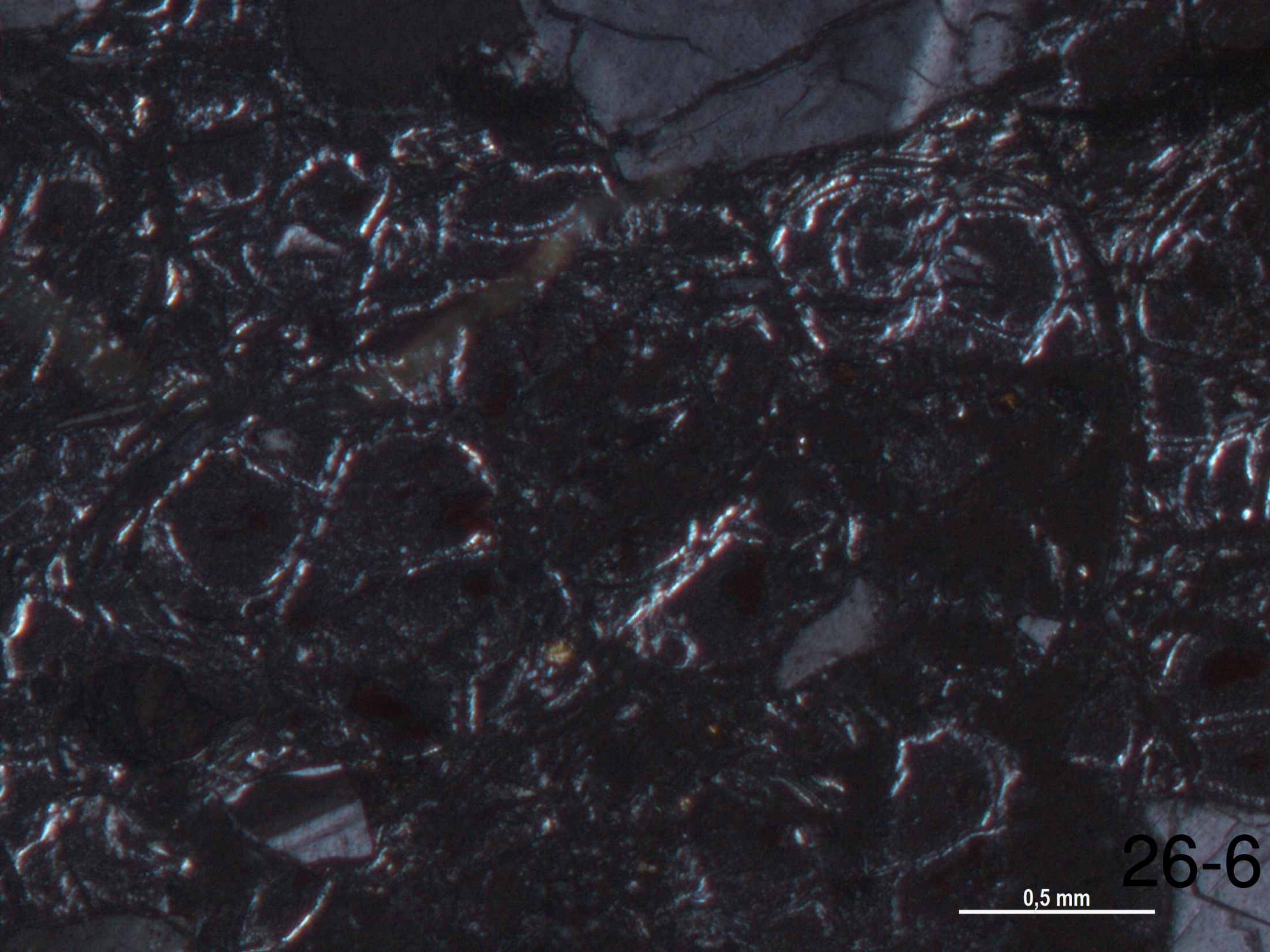
26-6
0,5 mm

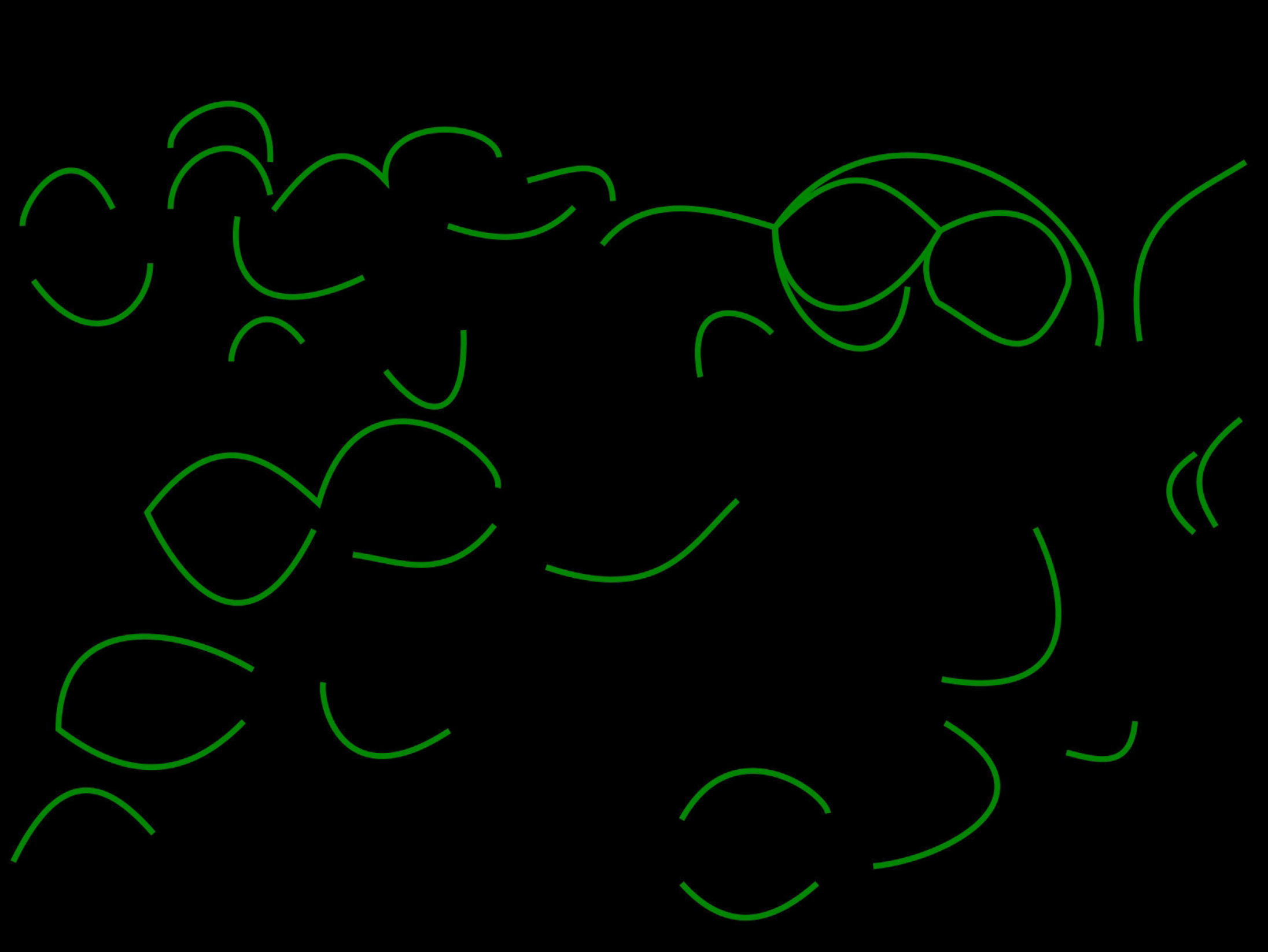

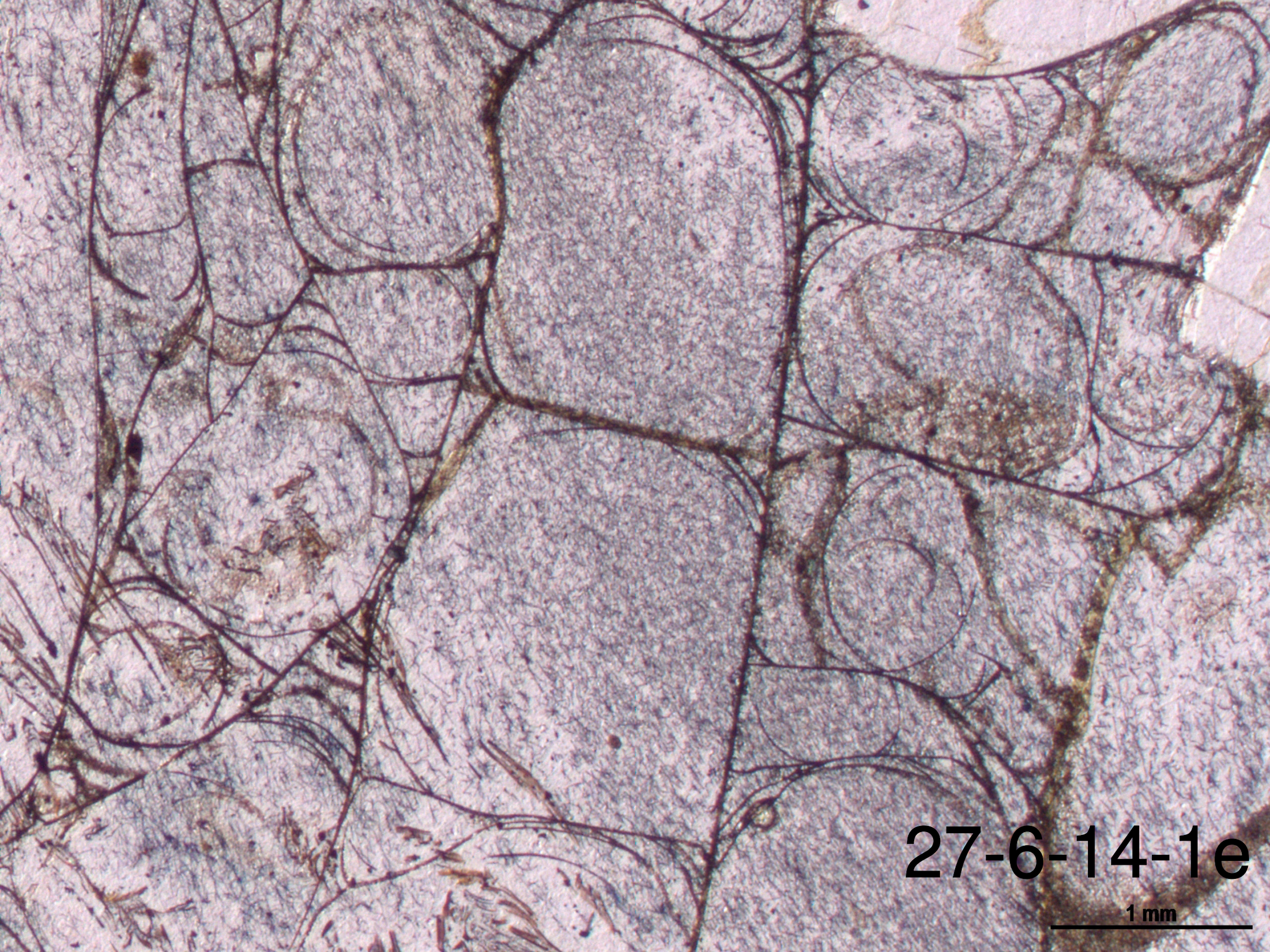
27-6-14-1e
1 mm

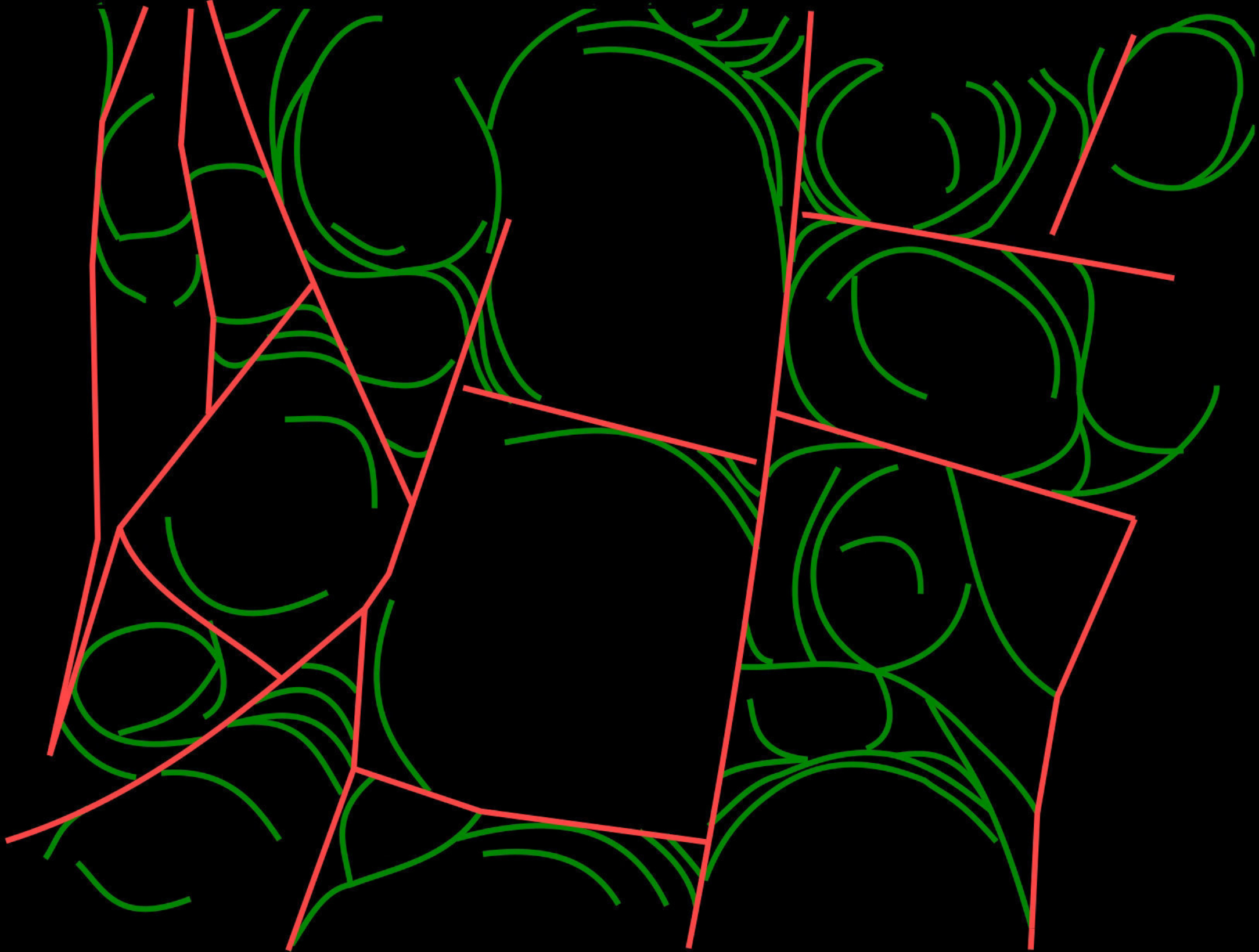

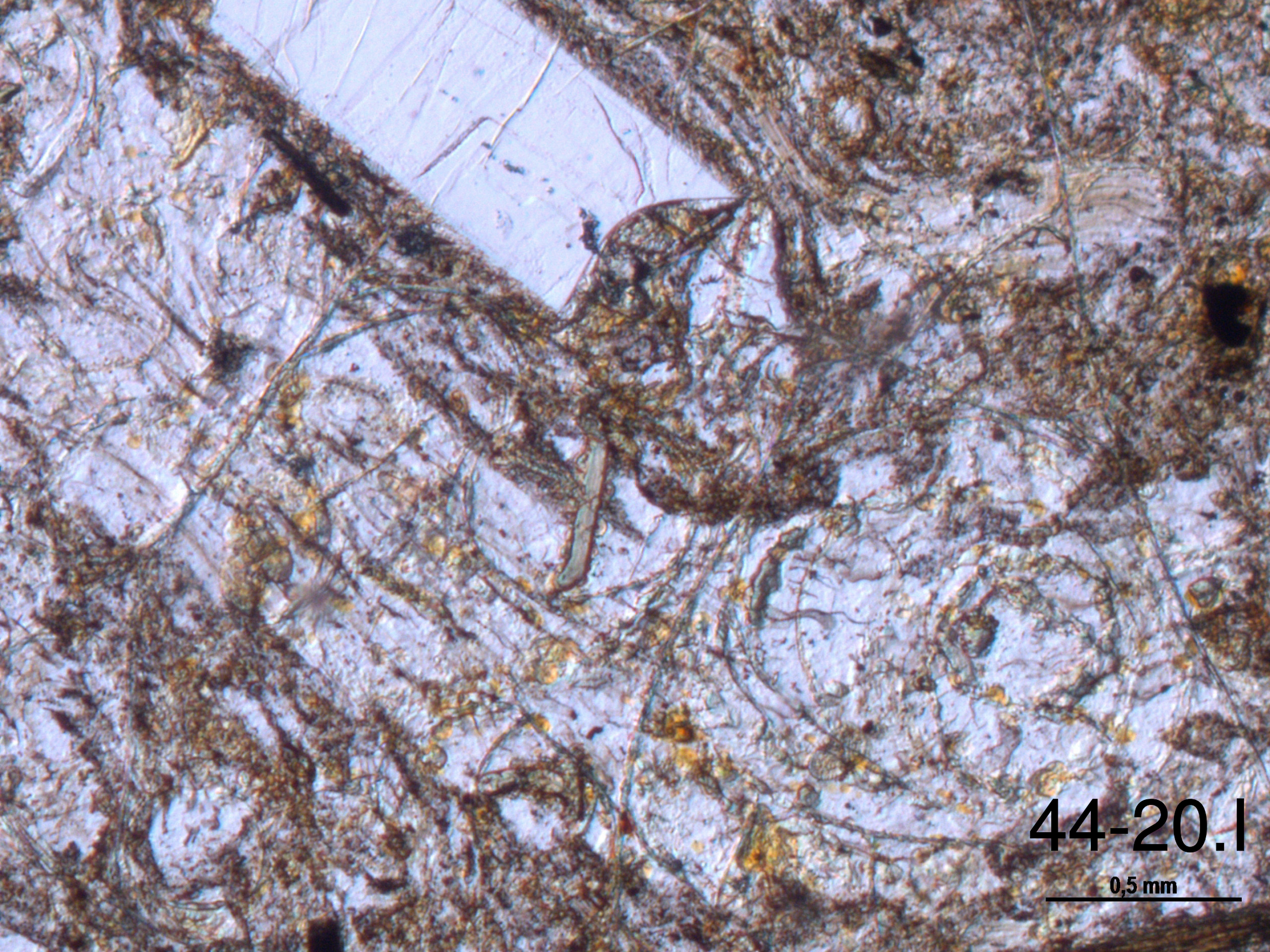
44-20.I
0,5 mm

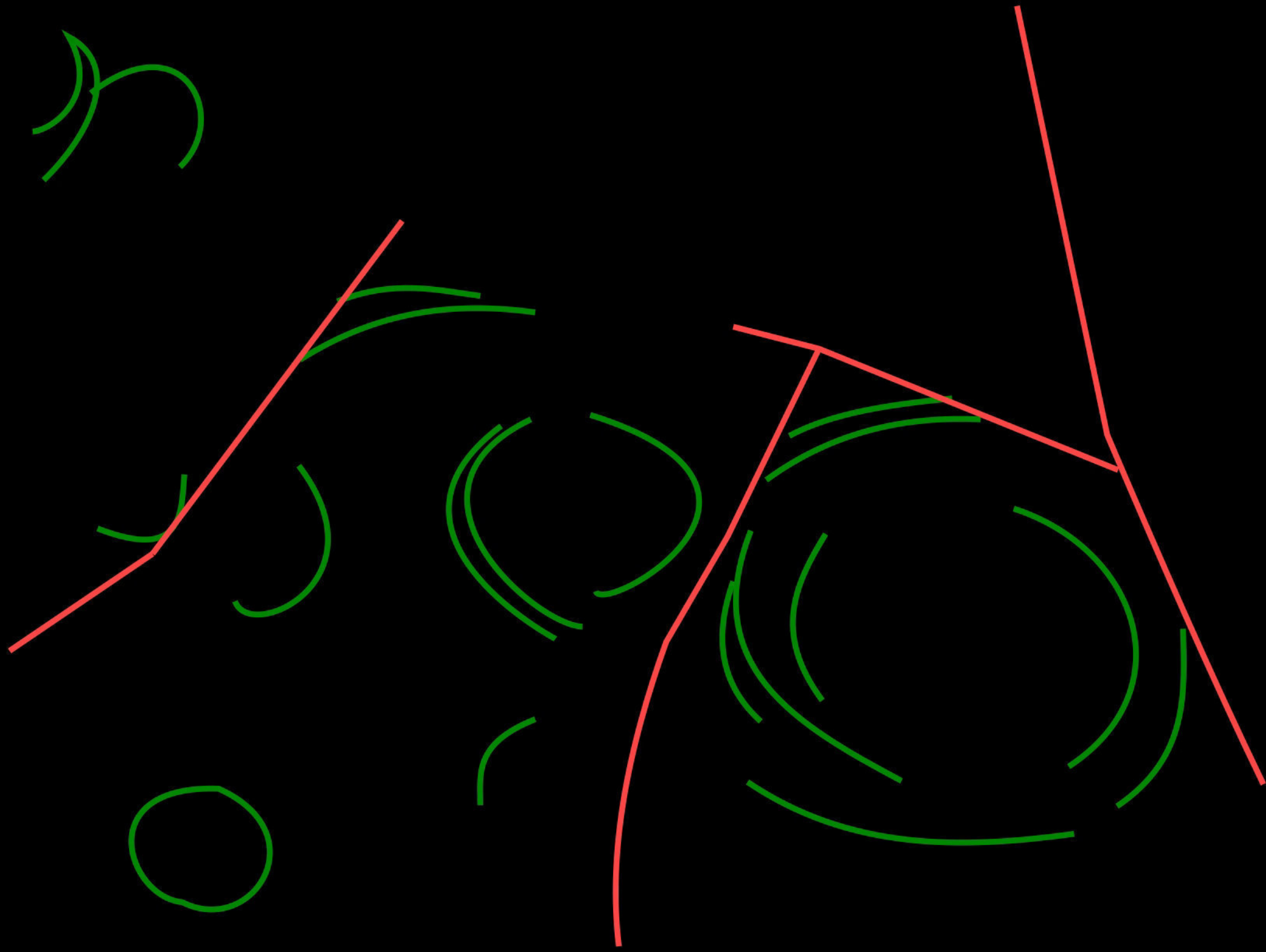

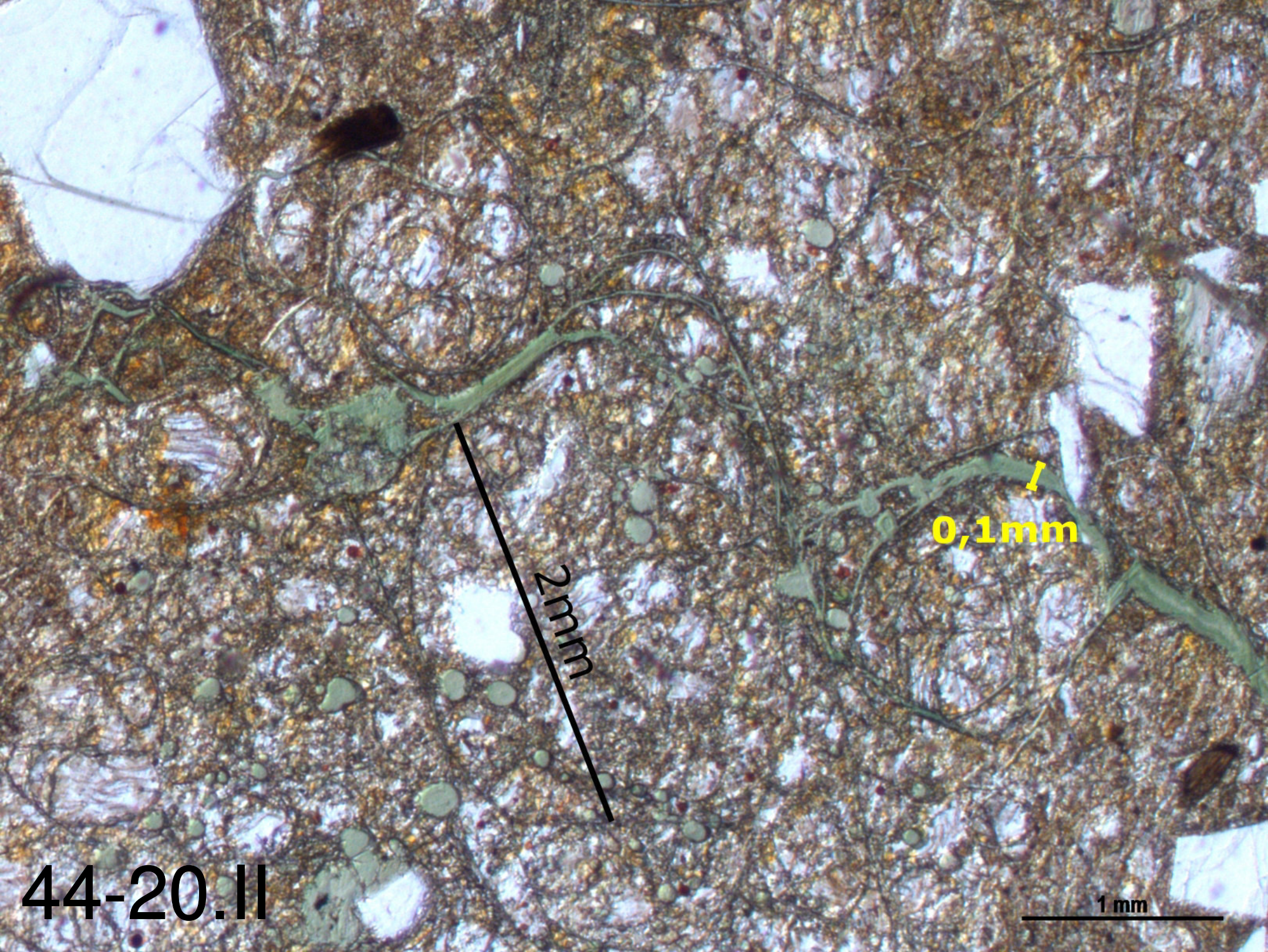
2mm
0,1mm
44-20.II
1 mm

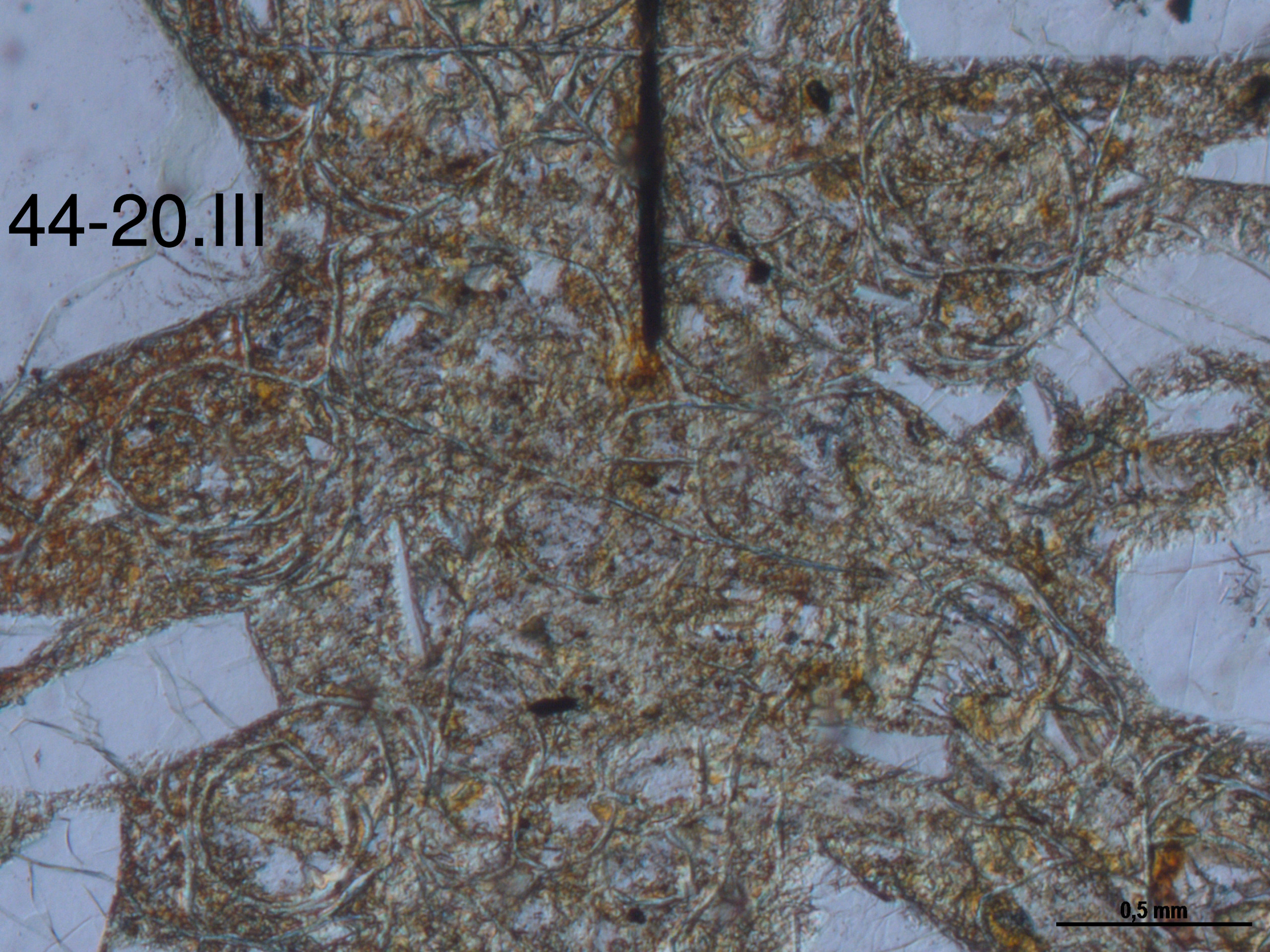
44-20.III
0,5 mm

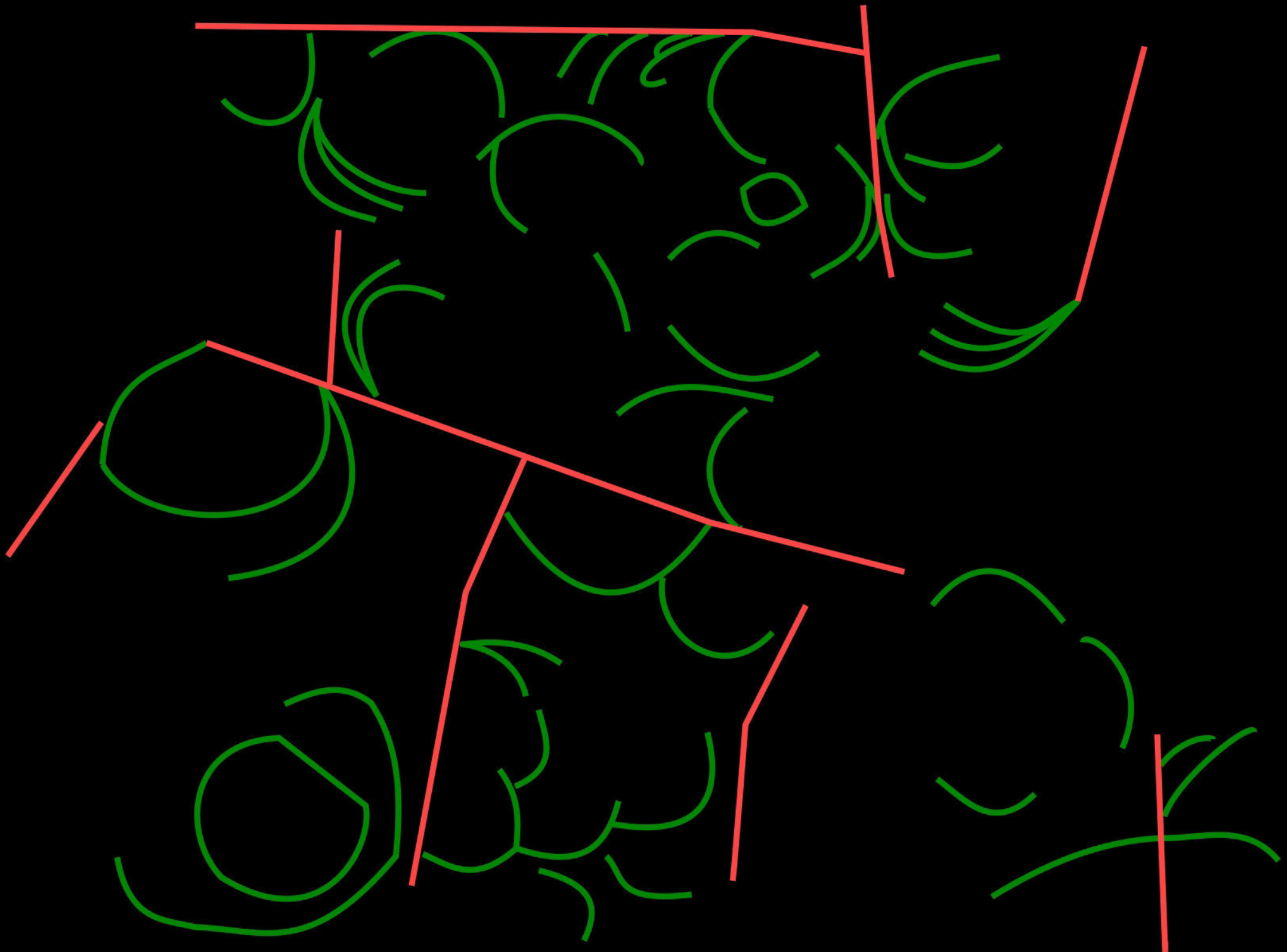

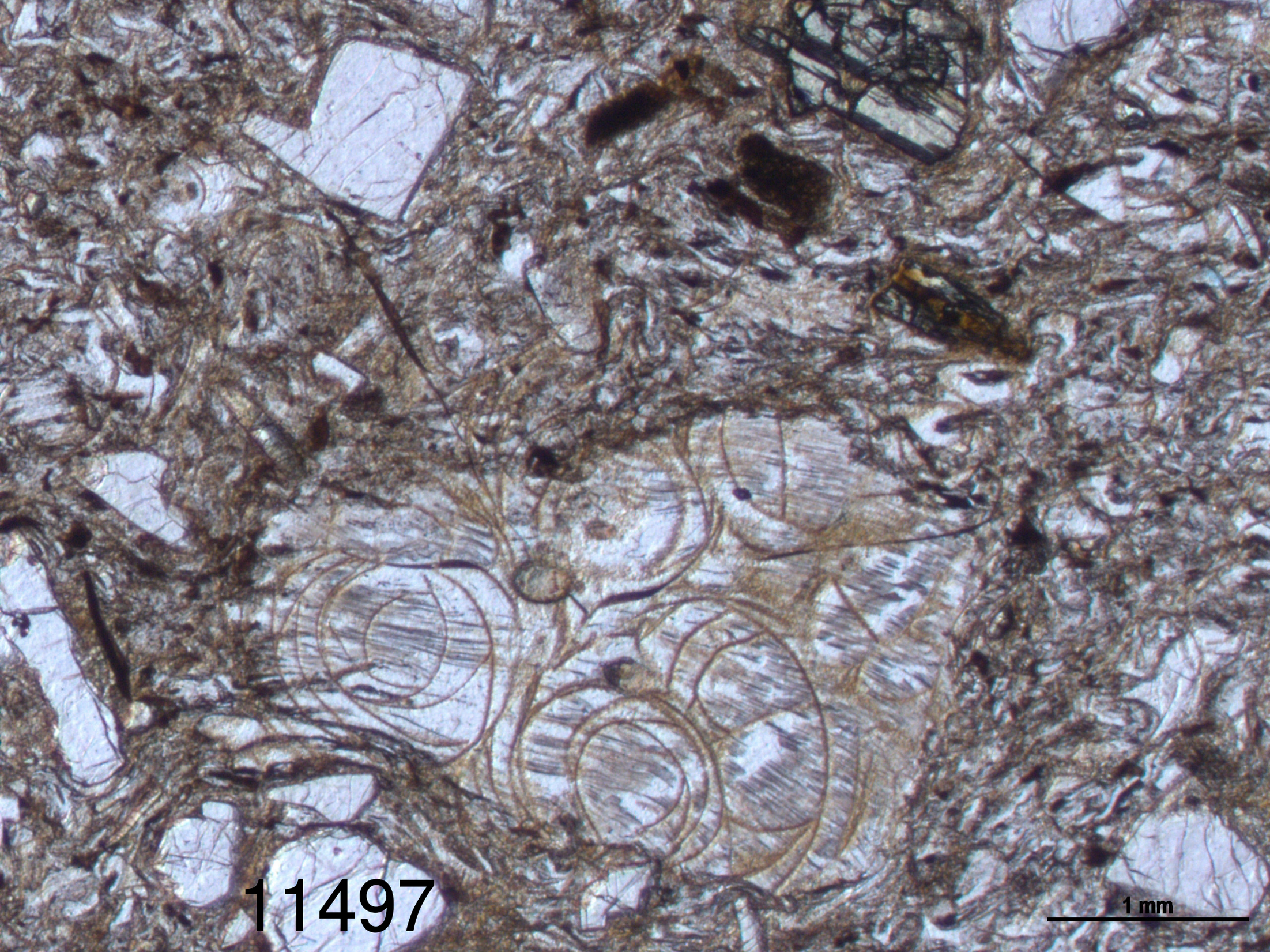
11497
1 mm

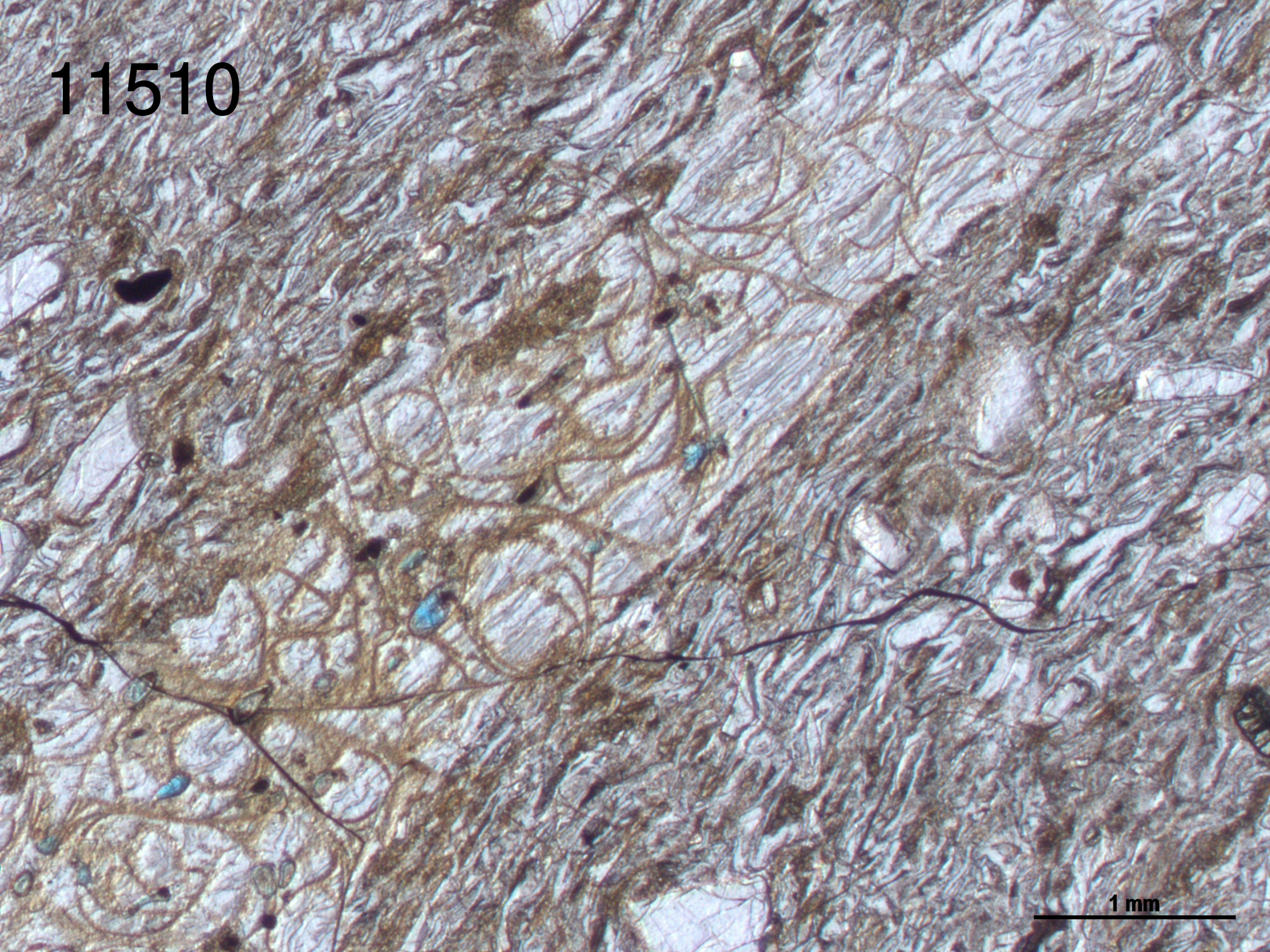
11510
1 mm

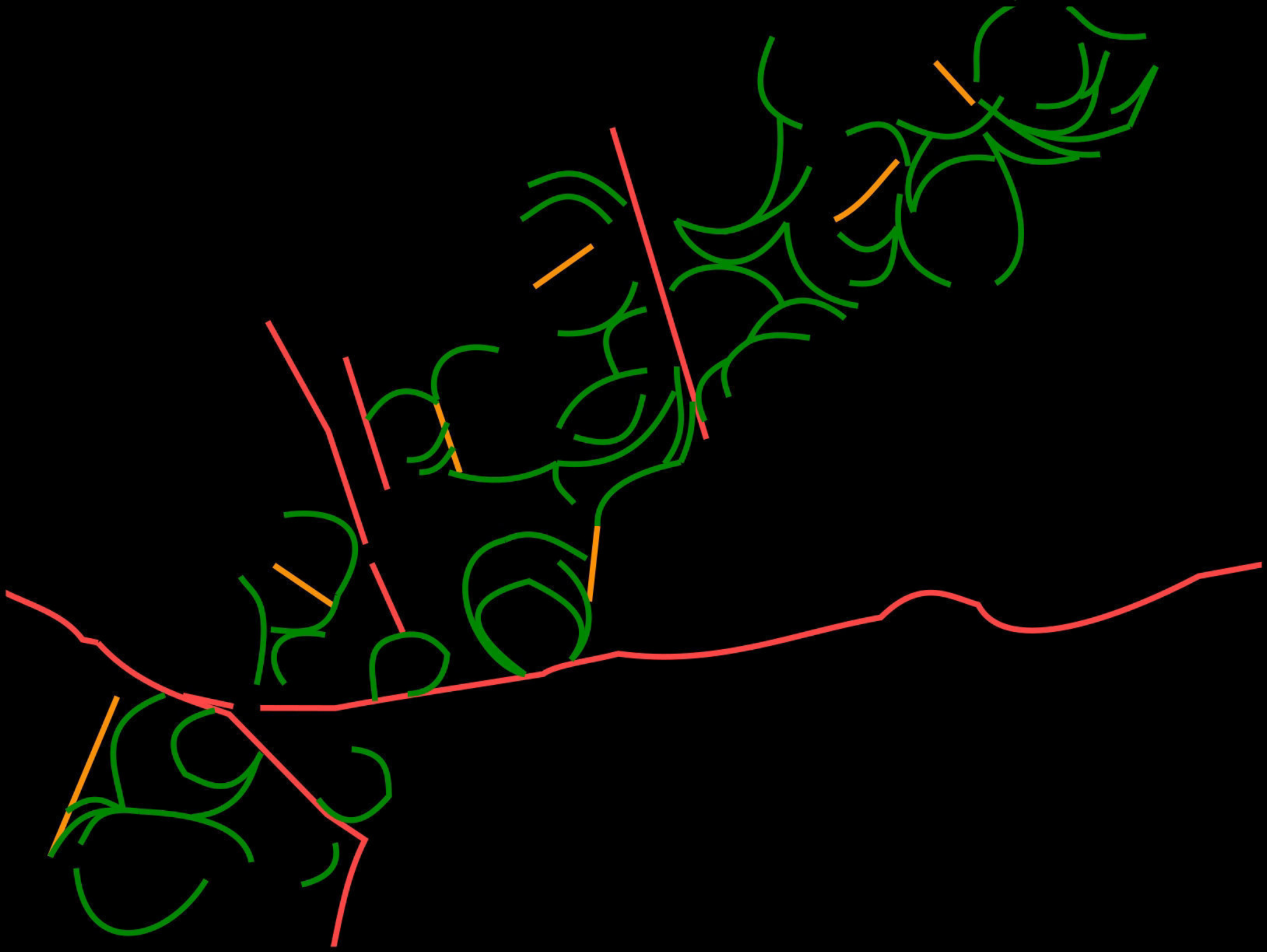

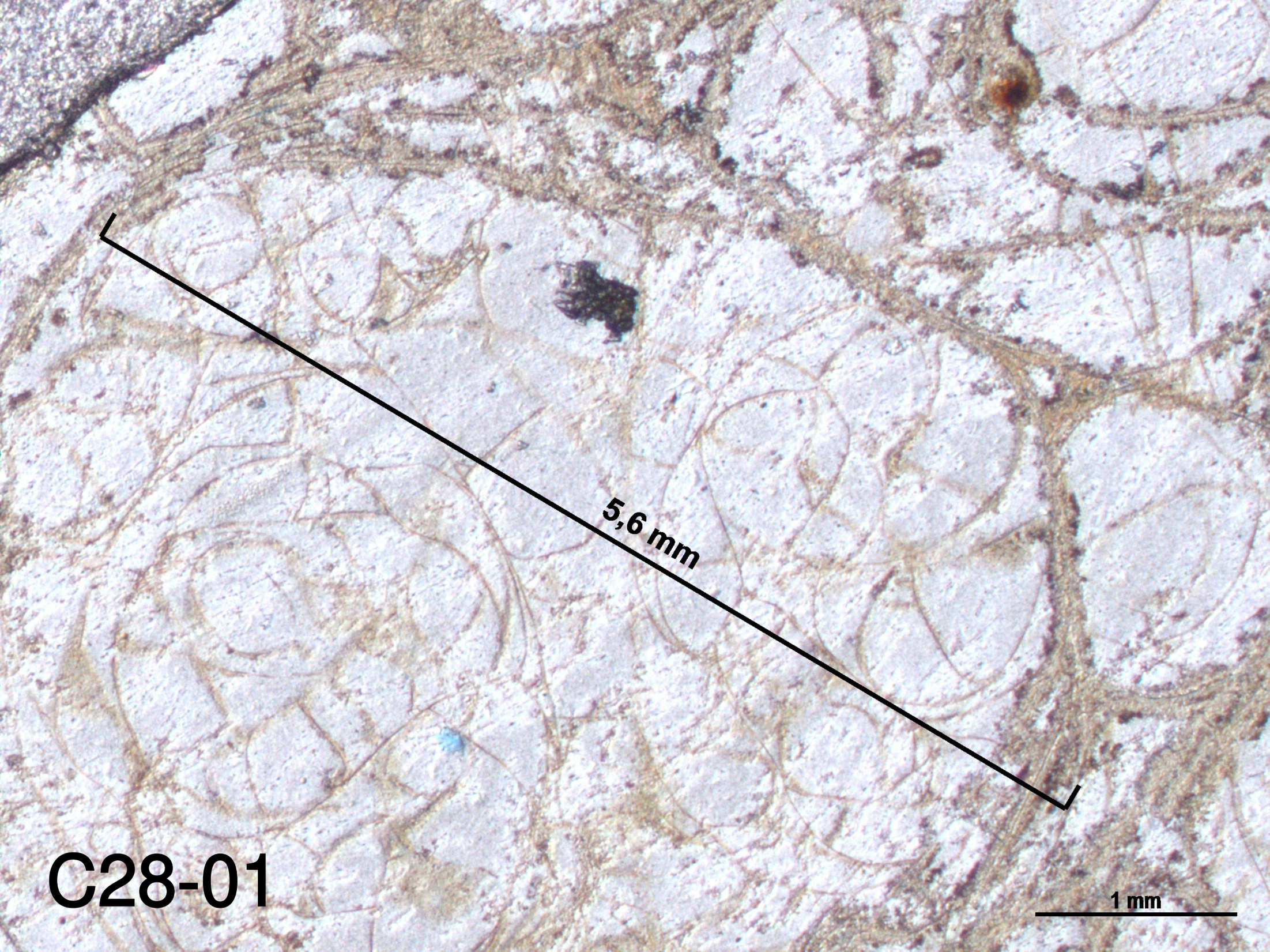
5,6 mm
C28-01
1 mm

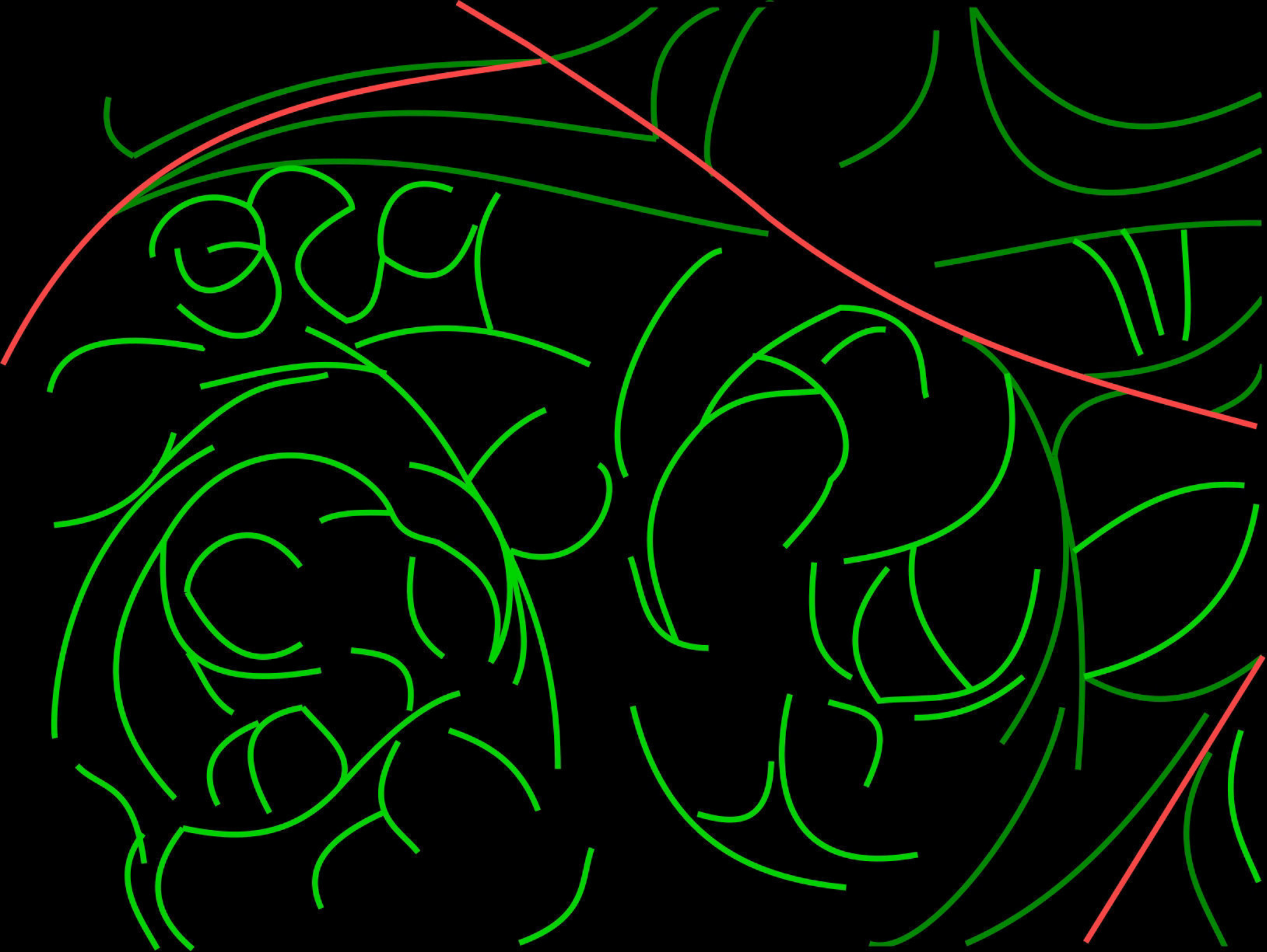

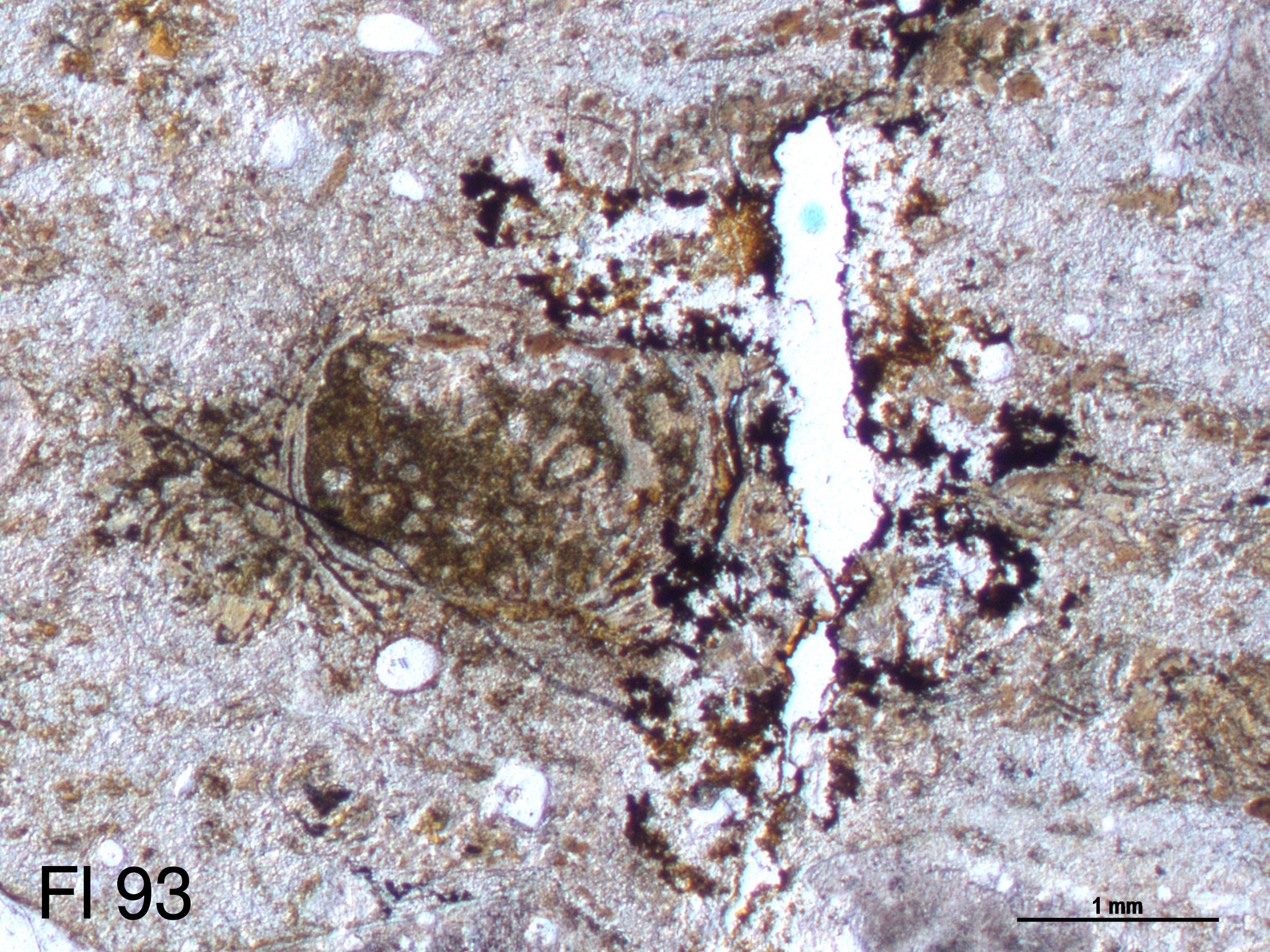
Fl 93
1 mm

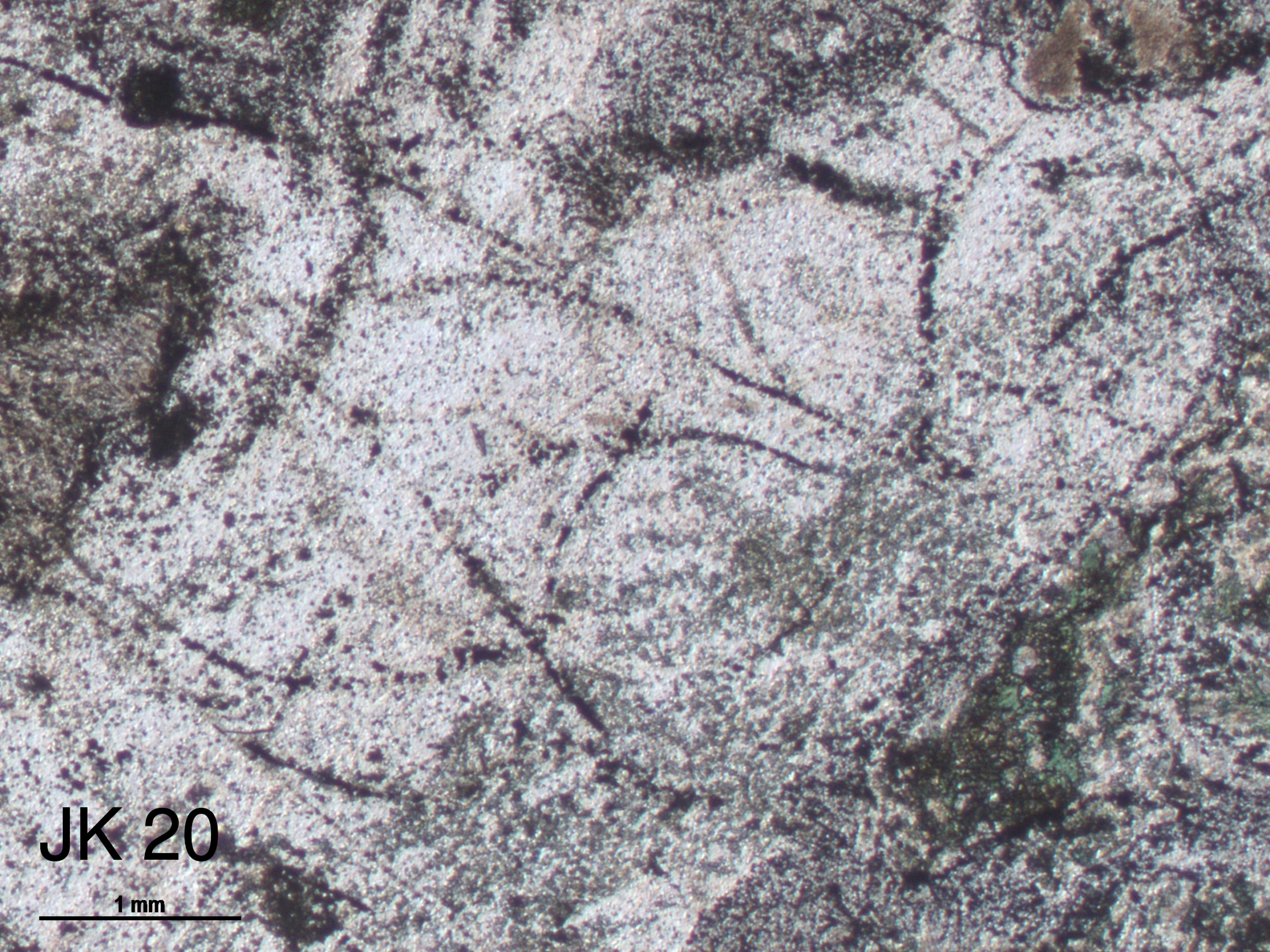
JK 20
1 mm

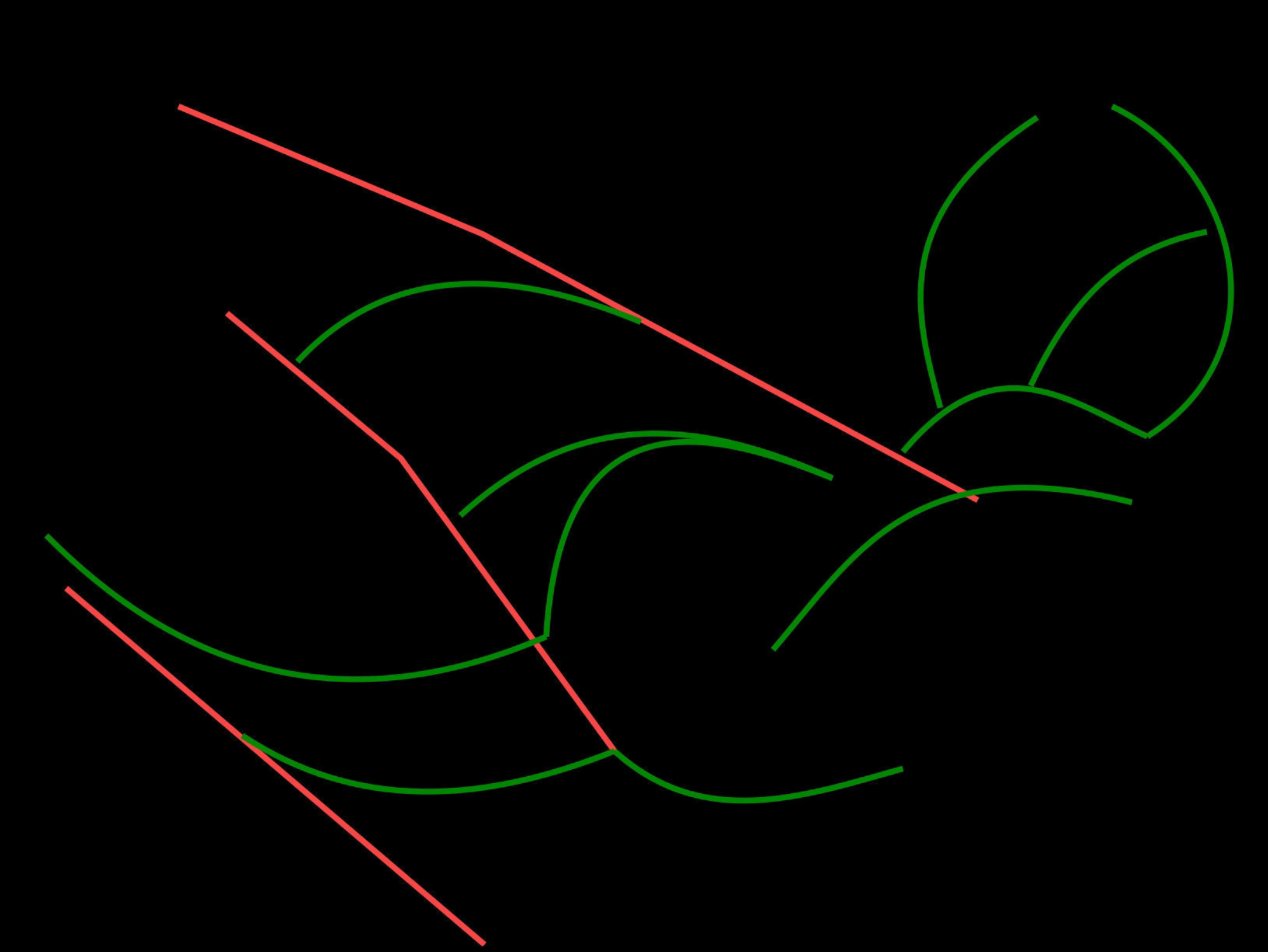

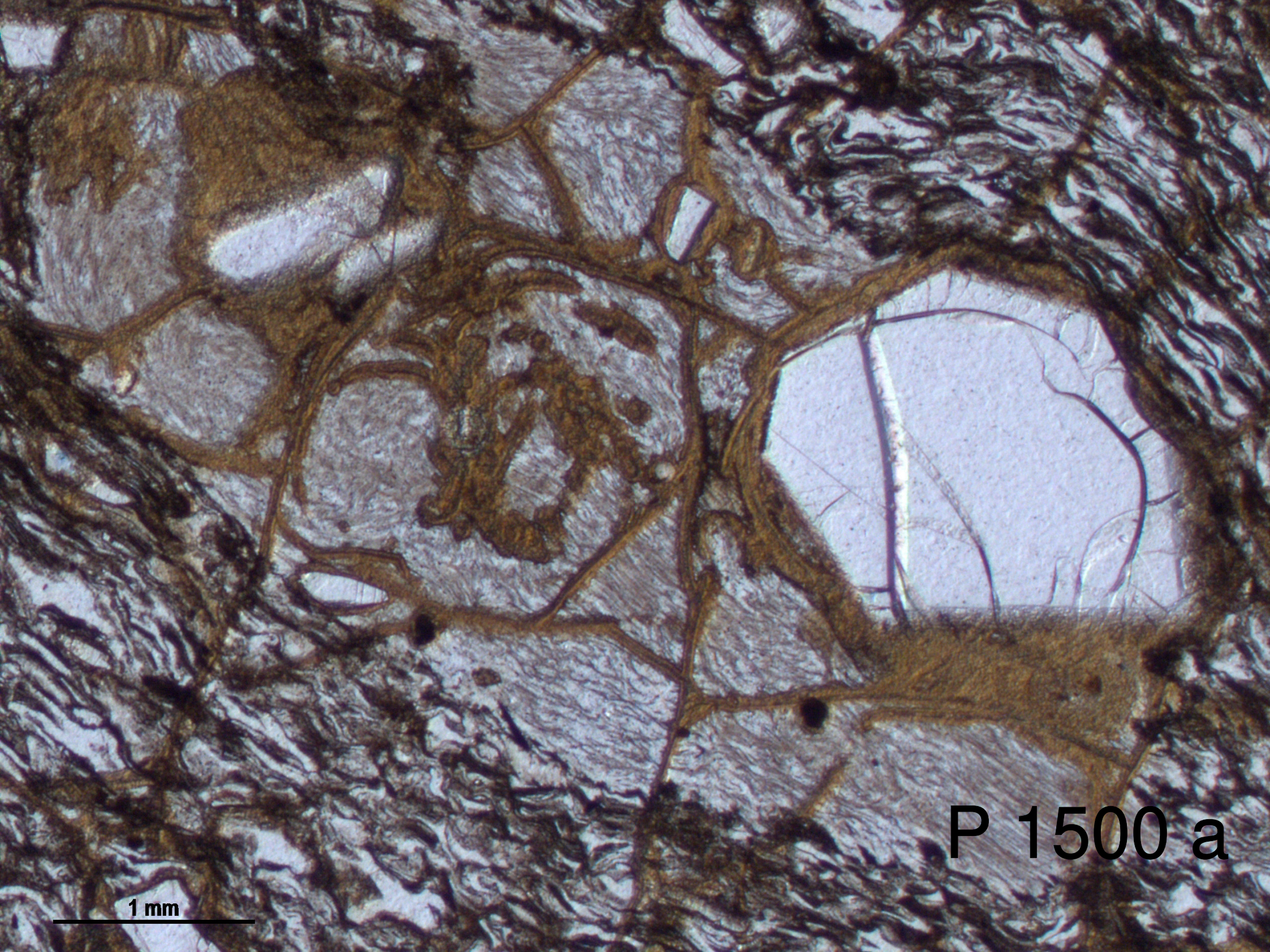
P 1500 a
1 mm

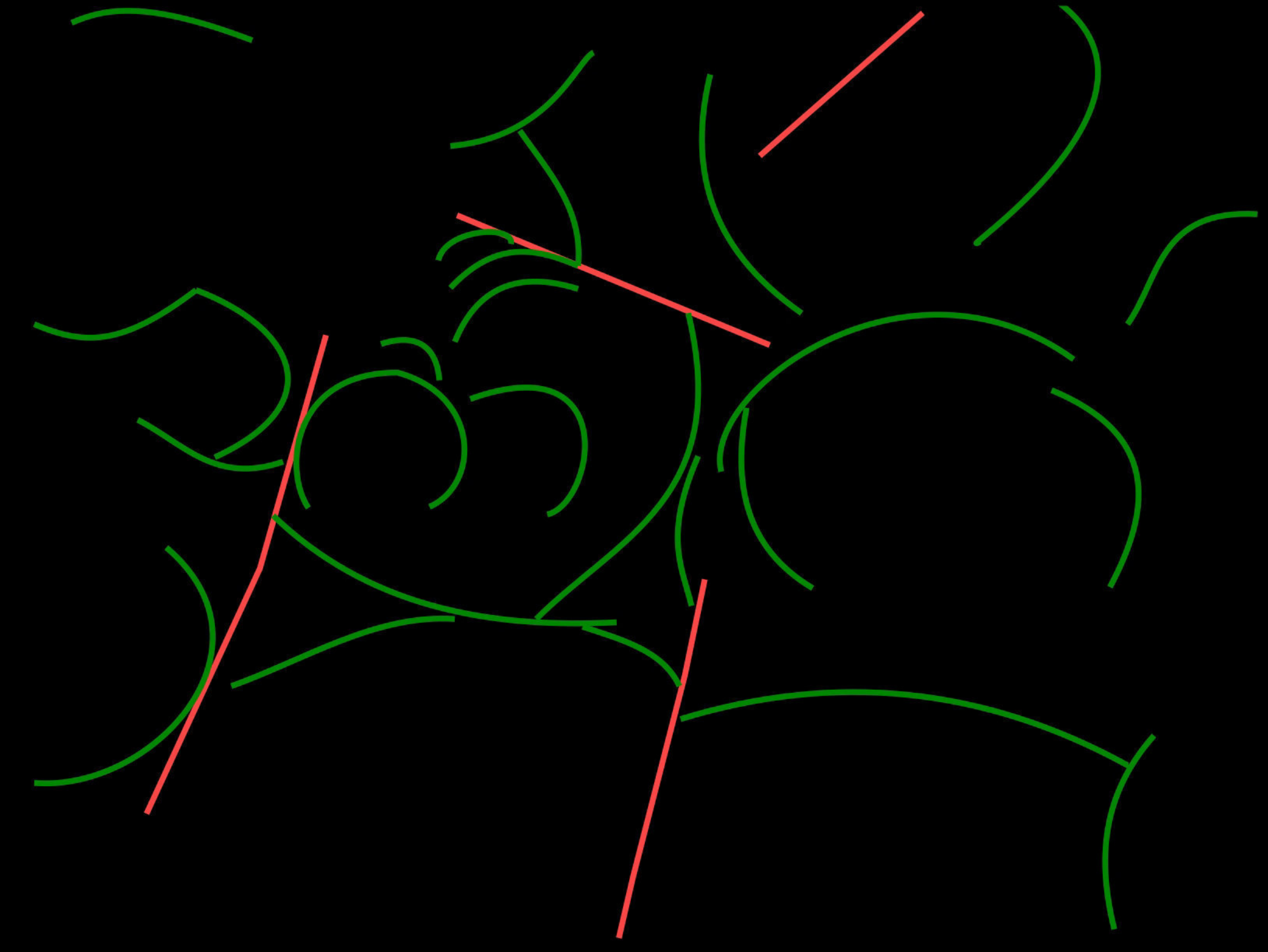

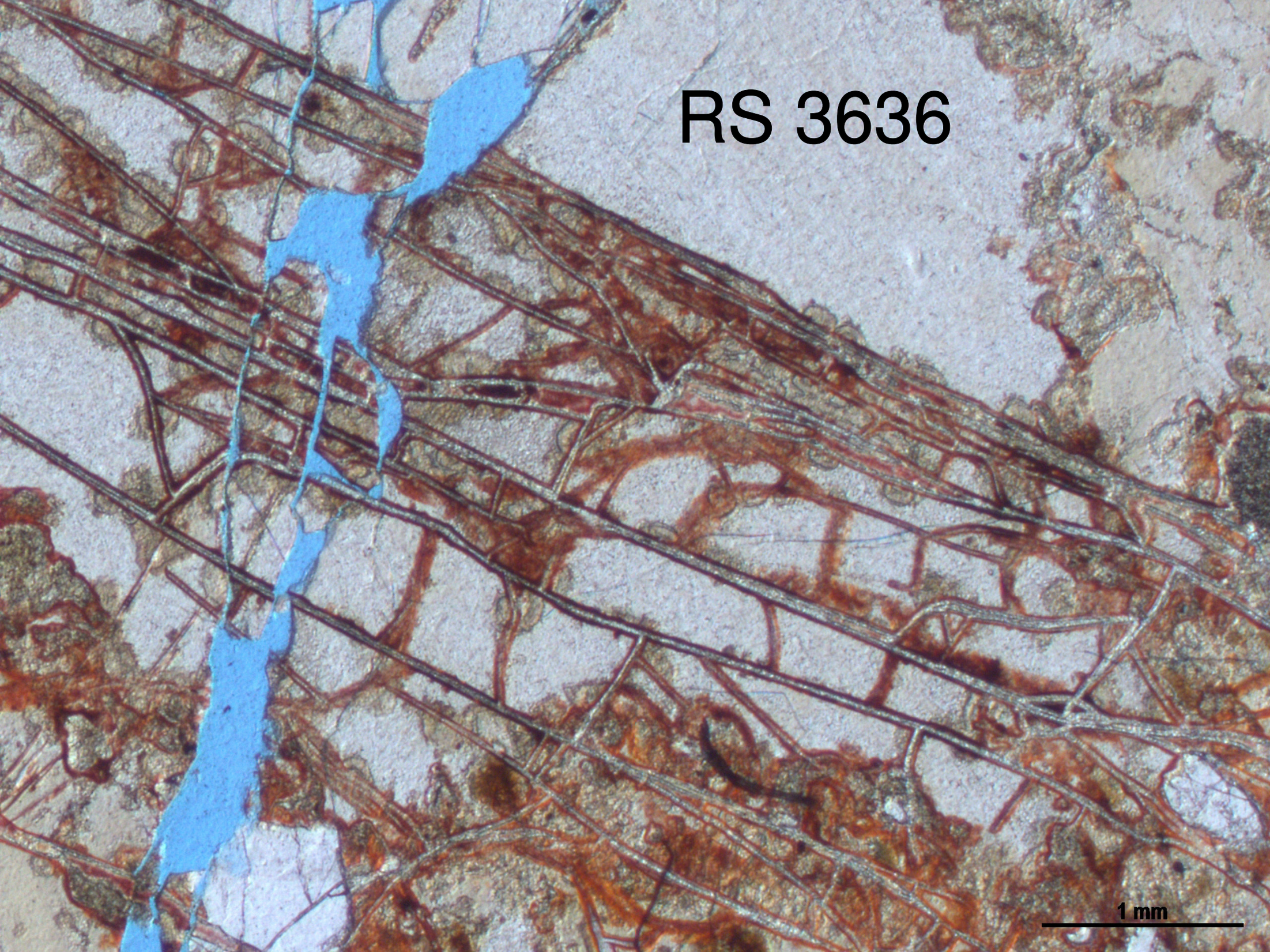
RS 3636
1 mm

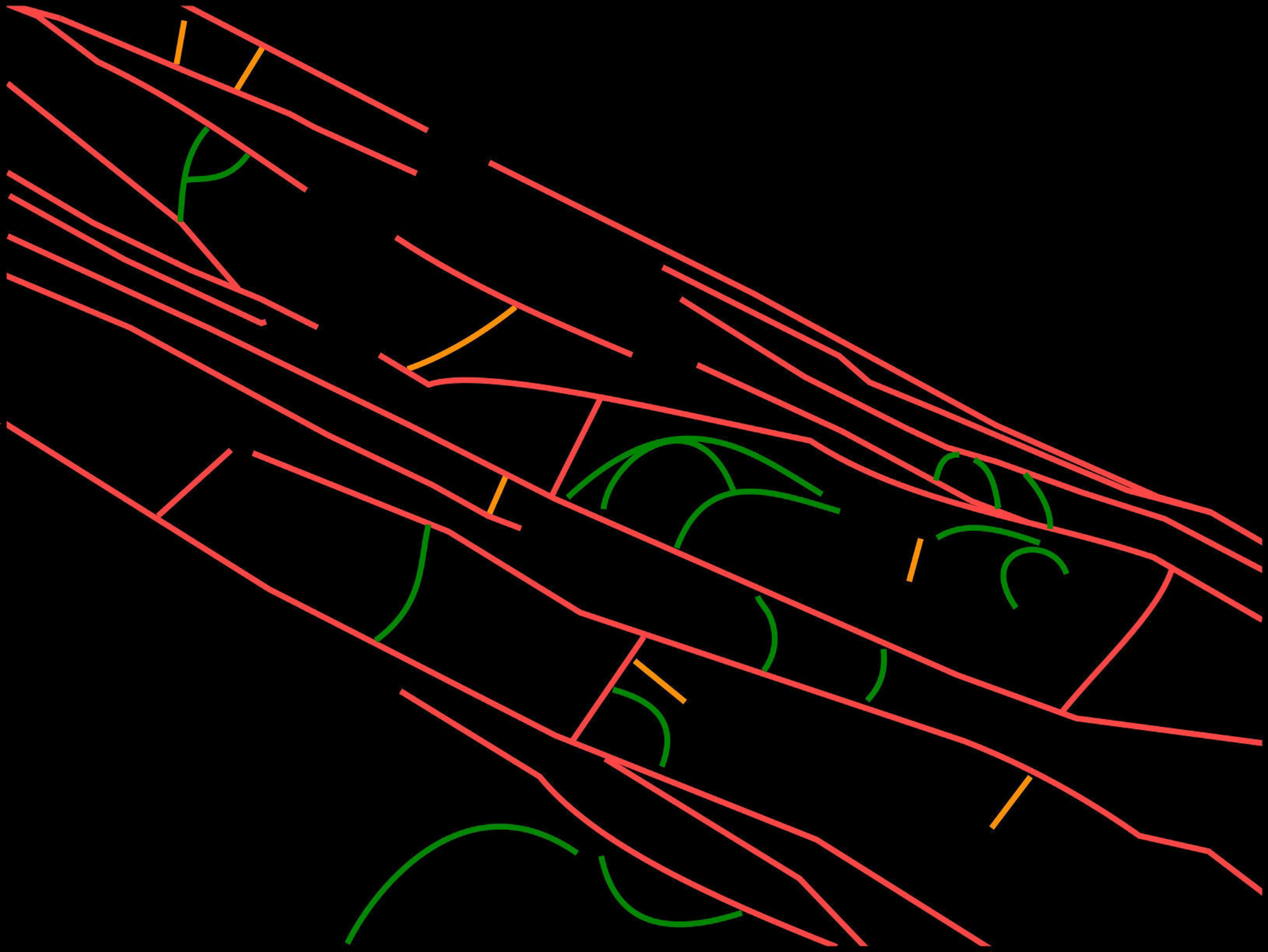

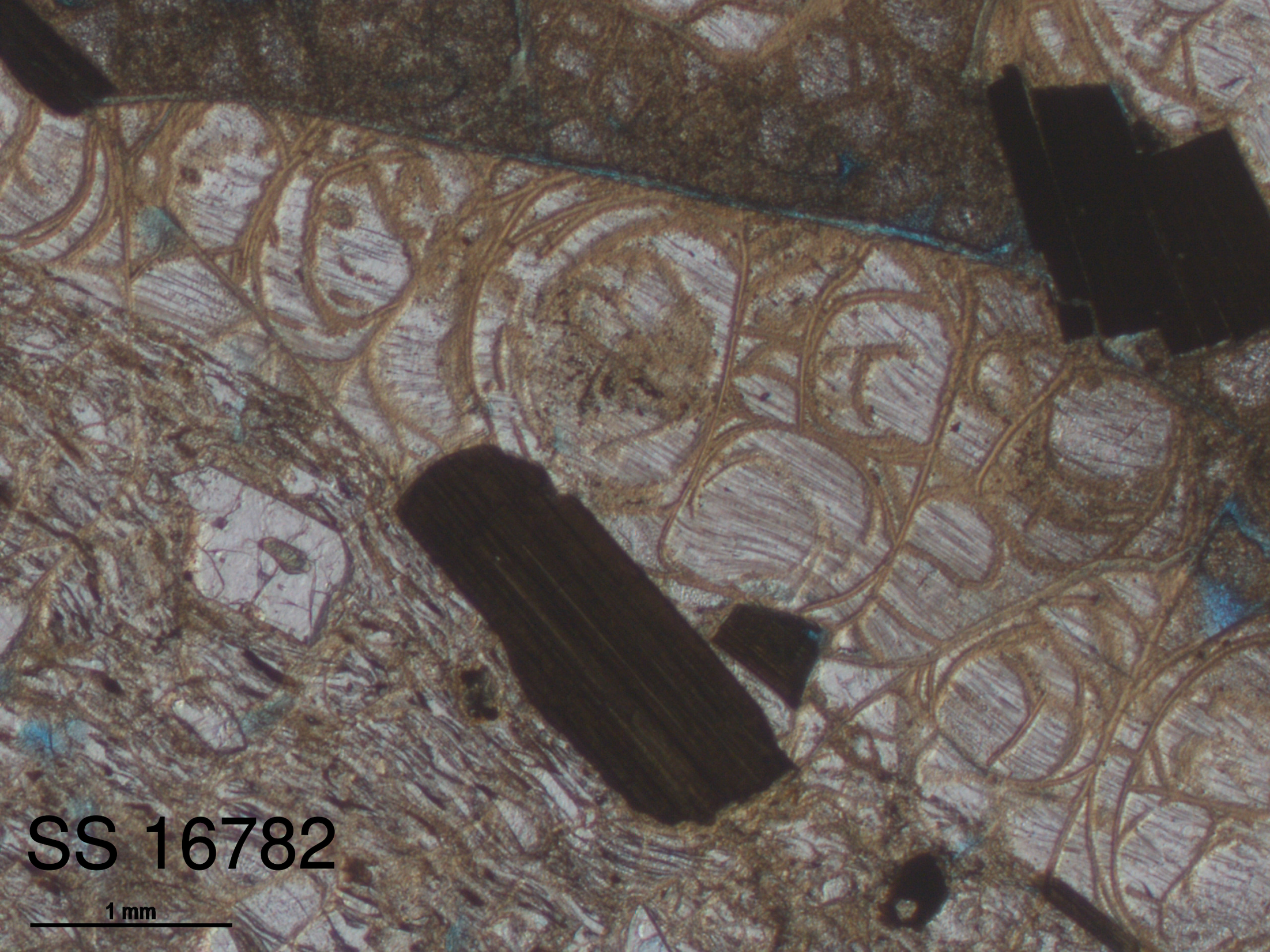
SS 16782
1 mm

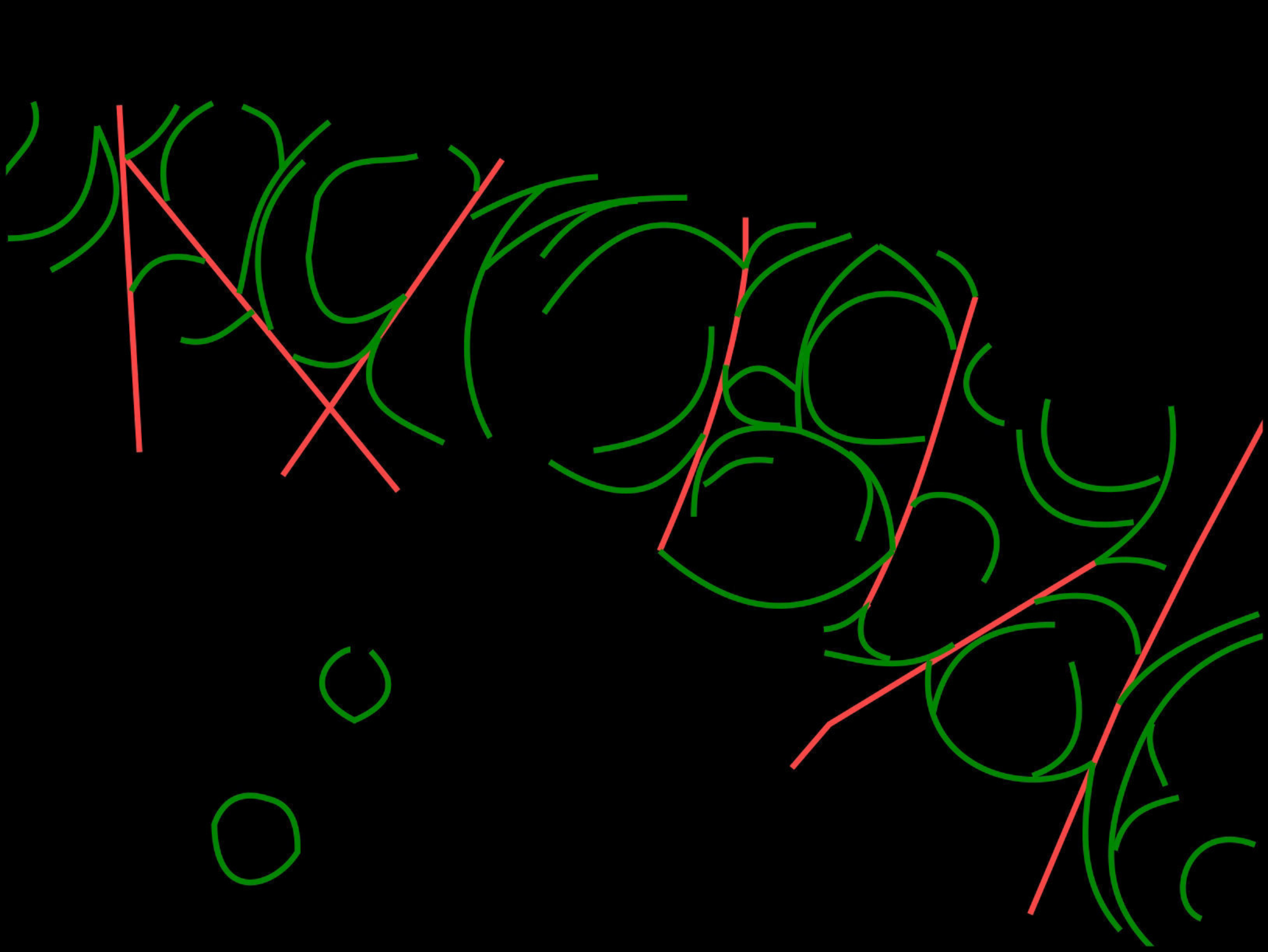


Tokai 24-1
1 mm

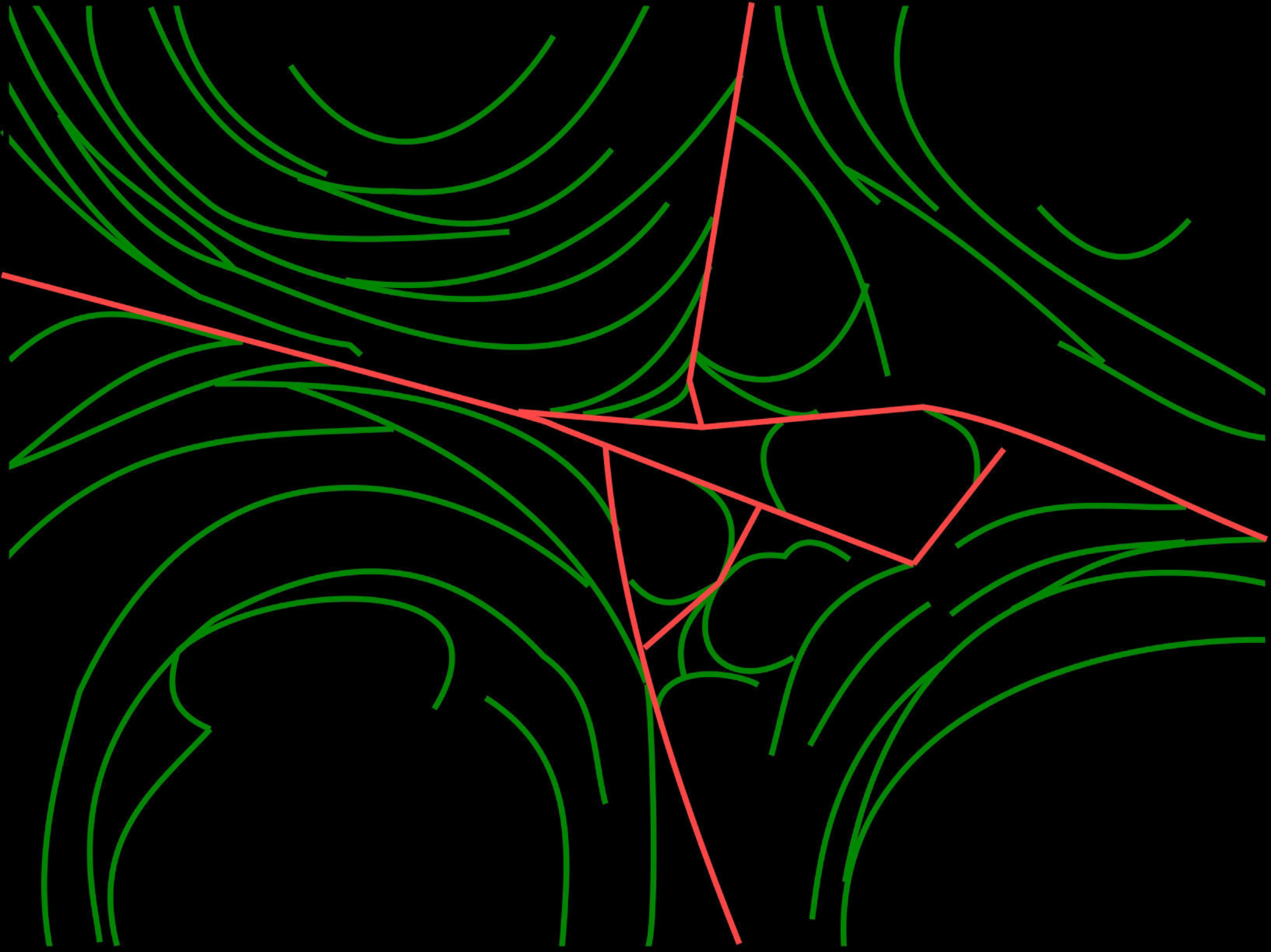

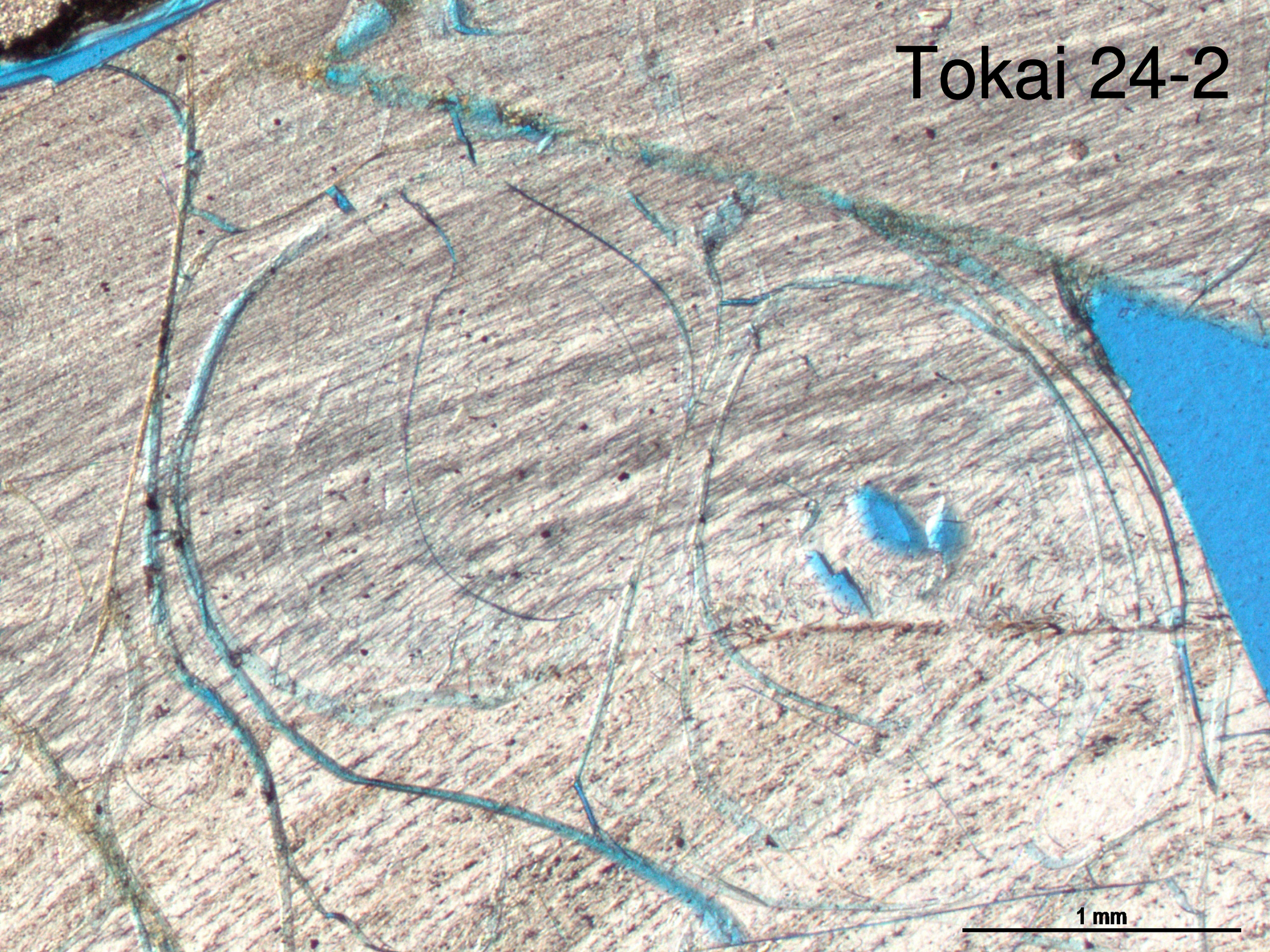
Tokai 24-2
1 mm

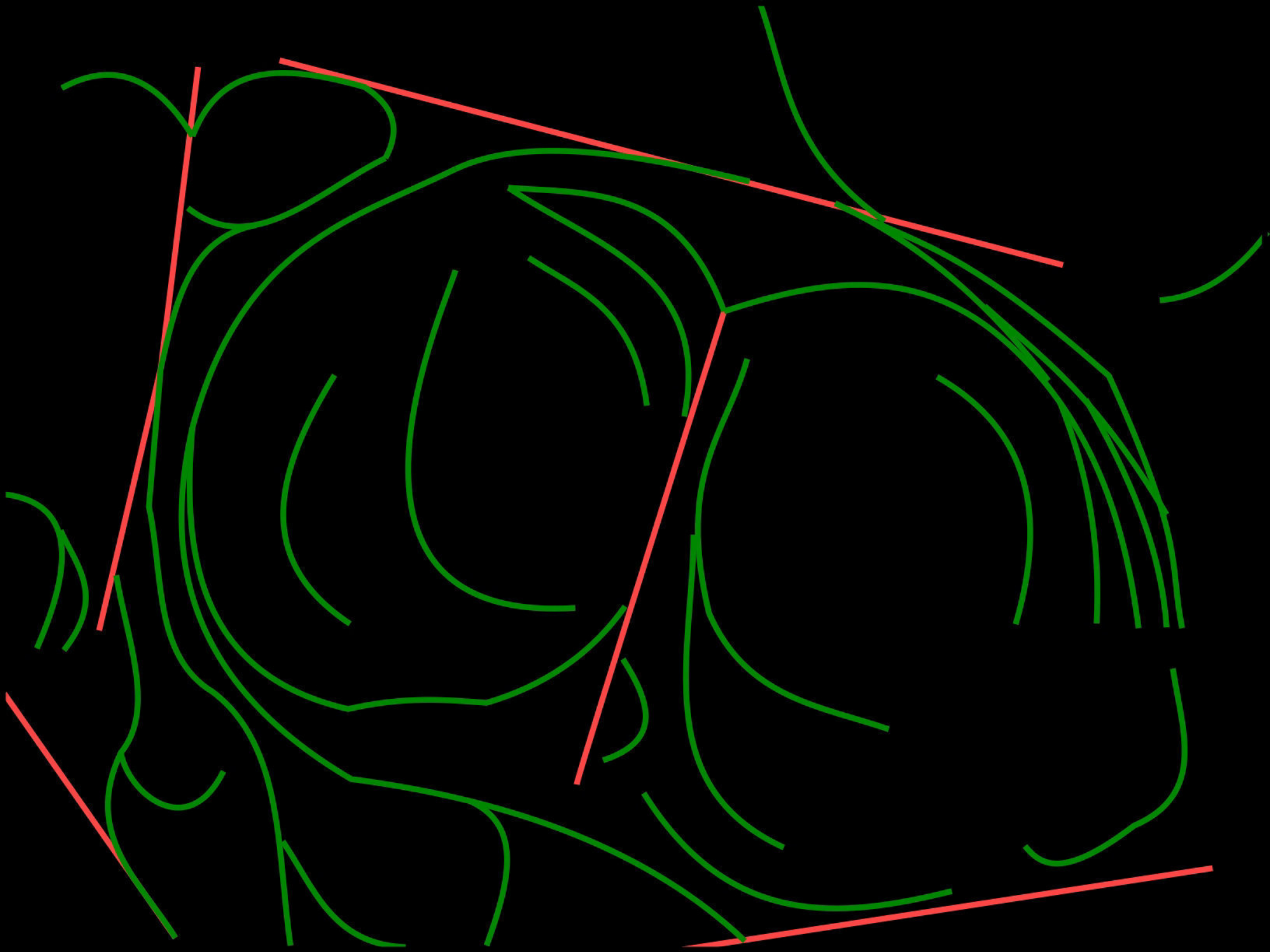

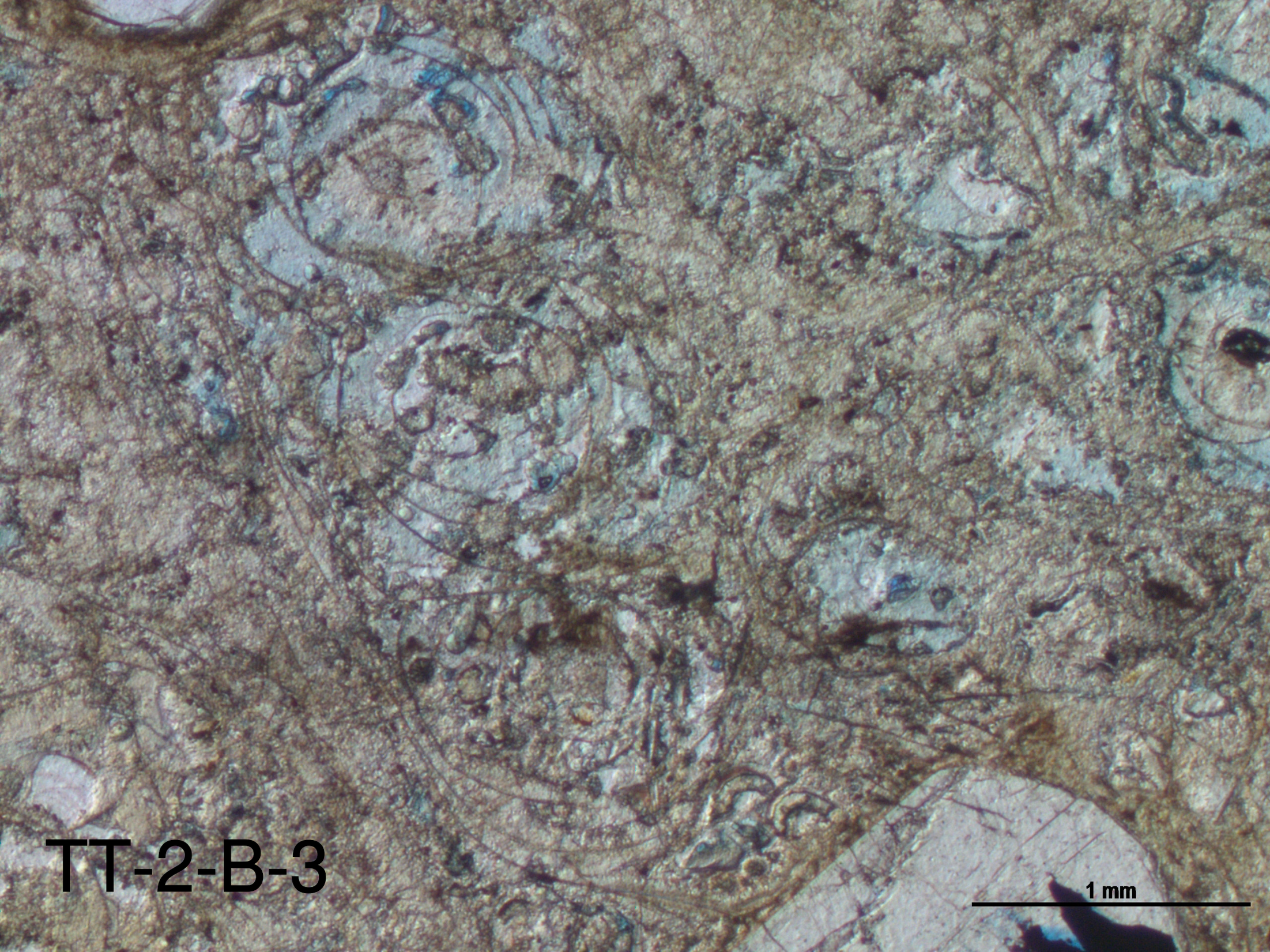
TT-2-B-3
1 mm

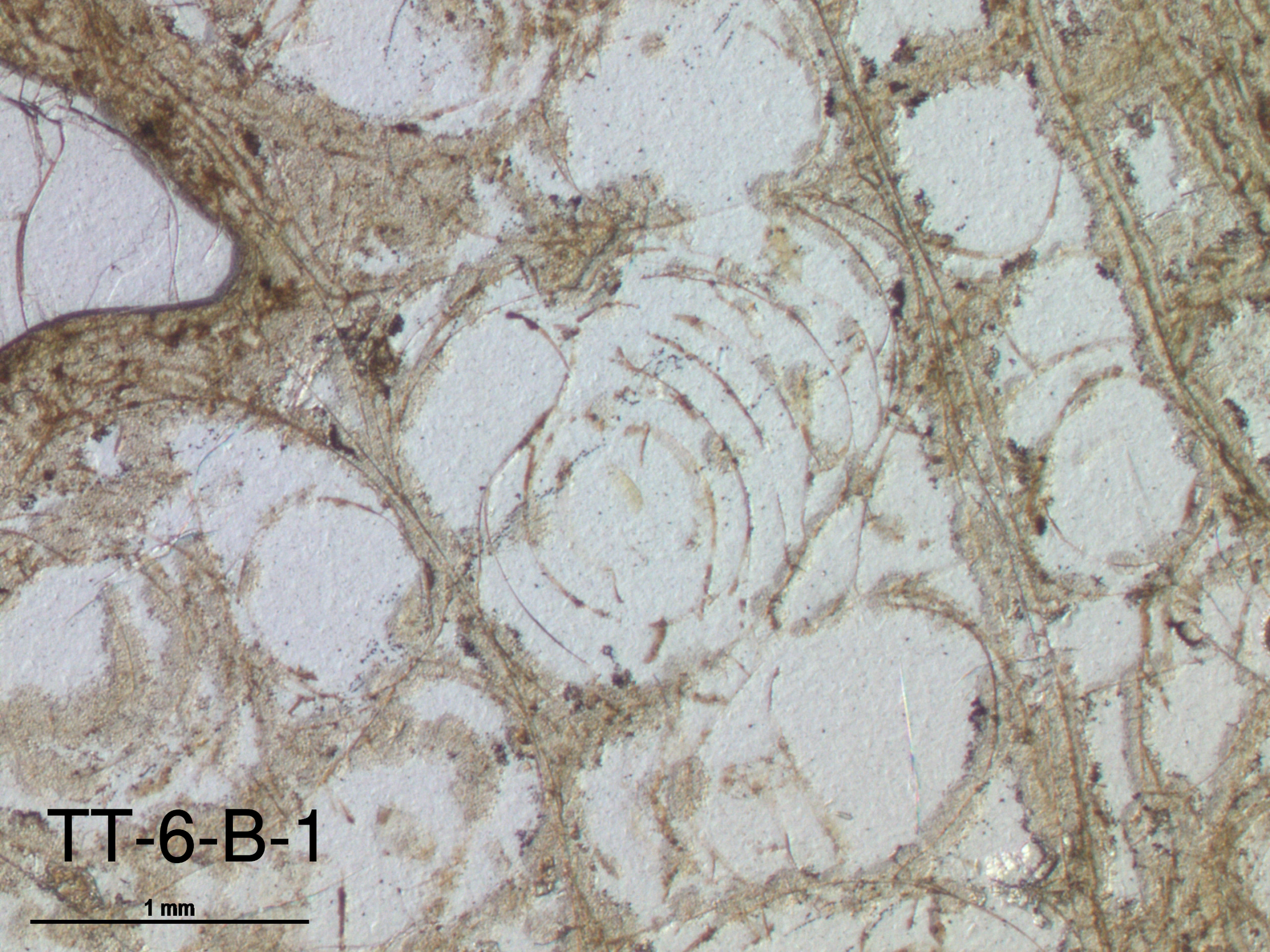
TT-6-B-1
1 mm

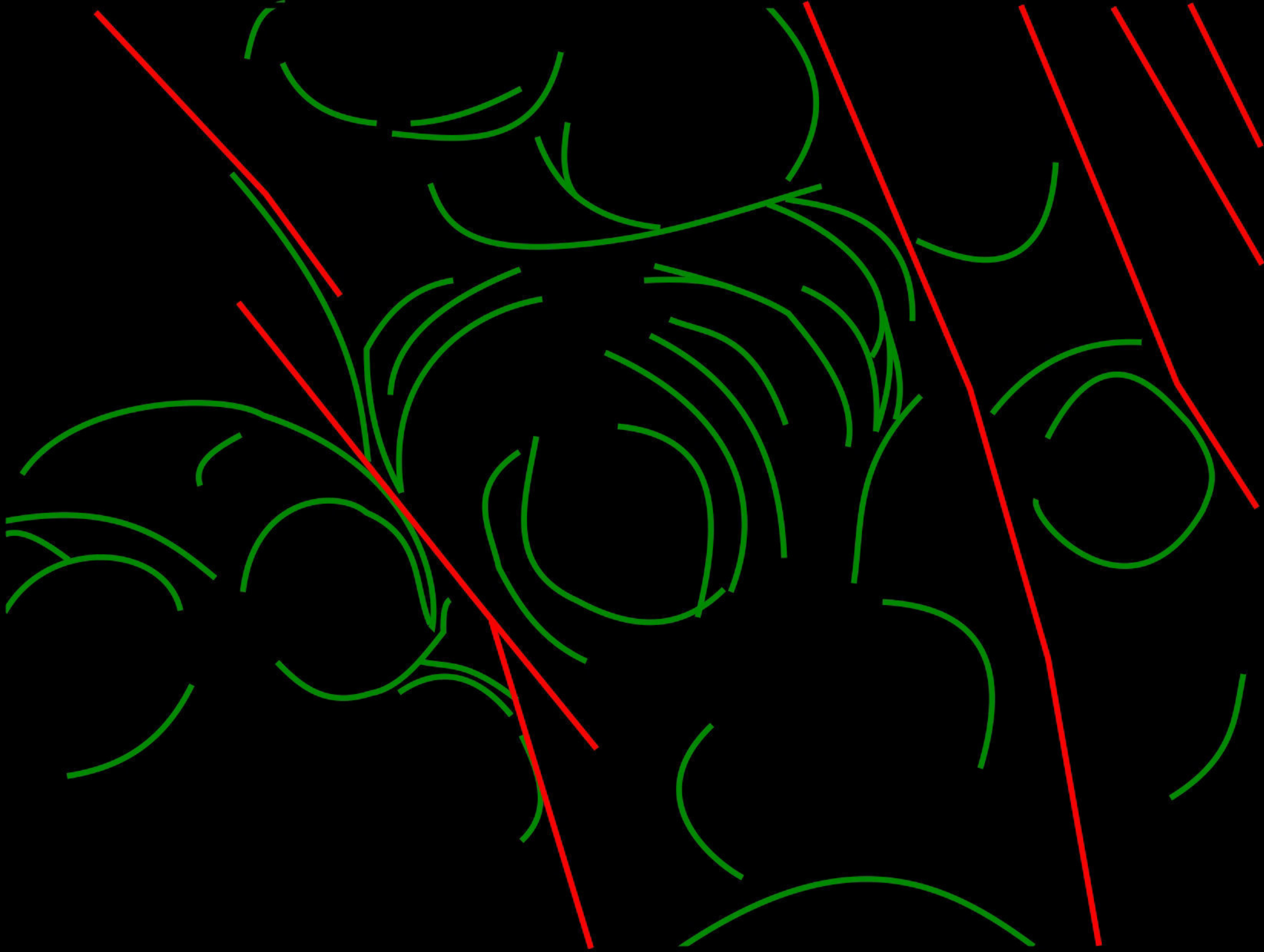

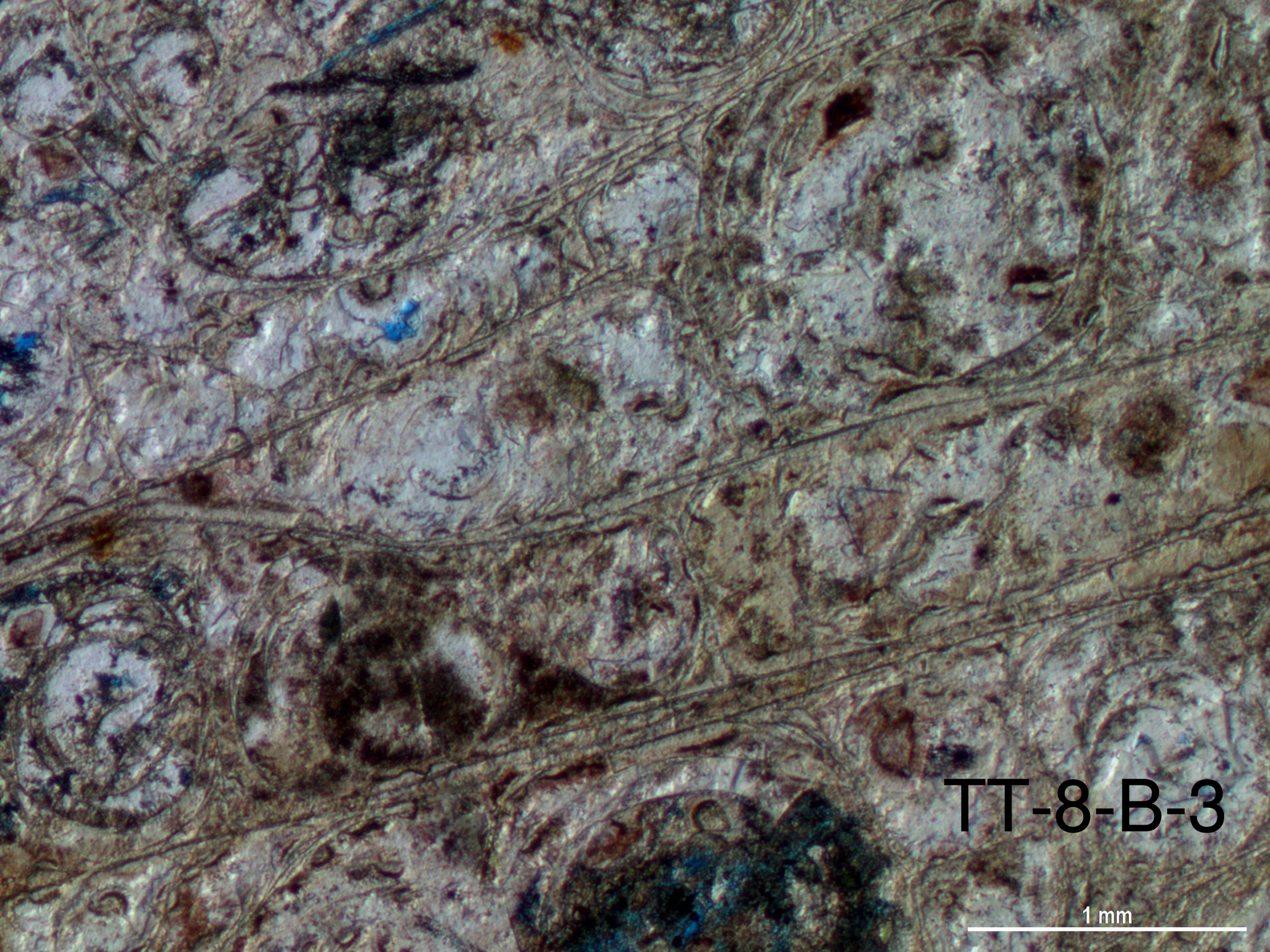
TT-8-B-3
1 mm

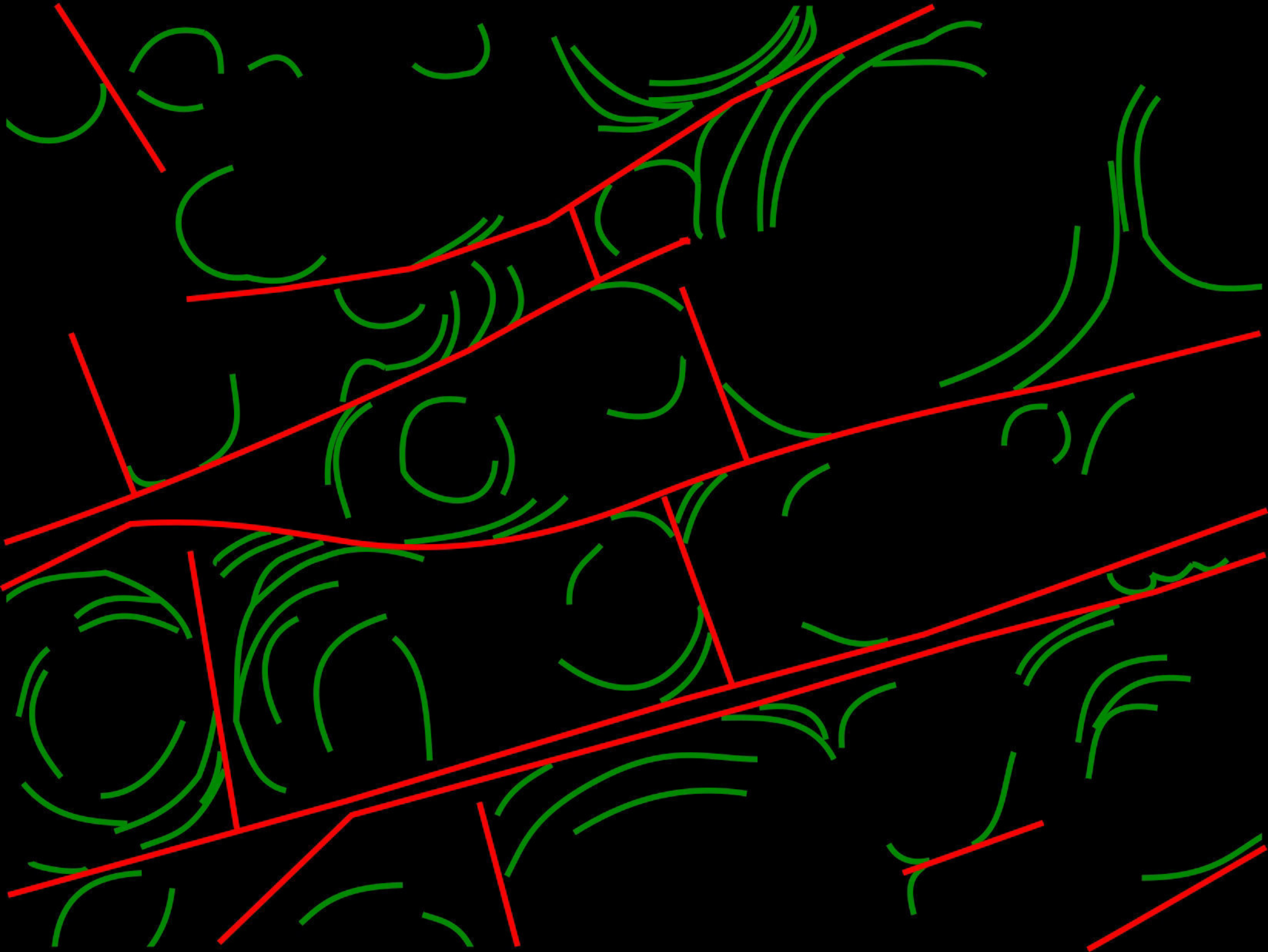

8.2. CT images

5-12-04-3

5-12-04-3

5-12-04-3

8.3. Thermal analysis

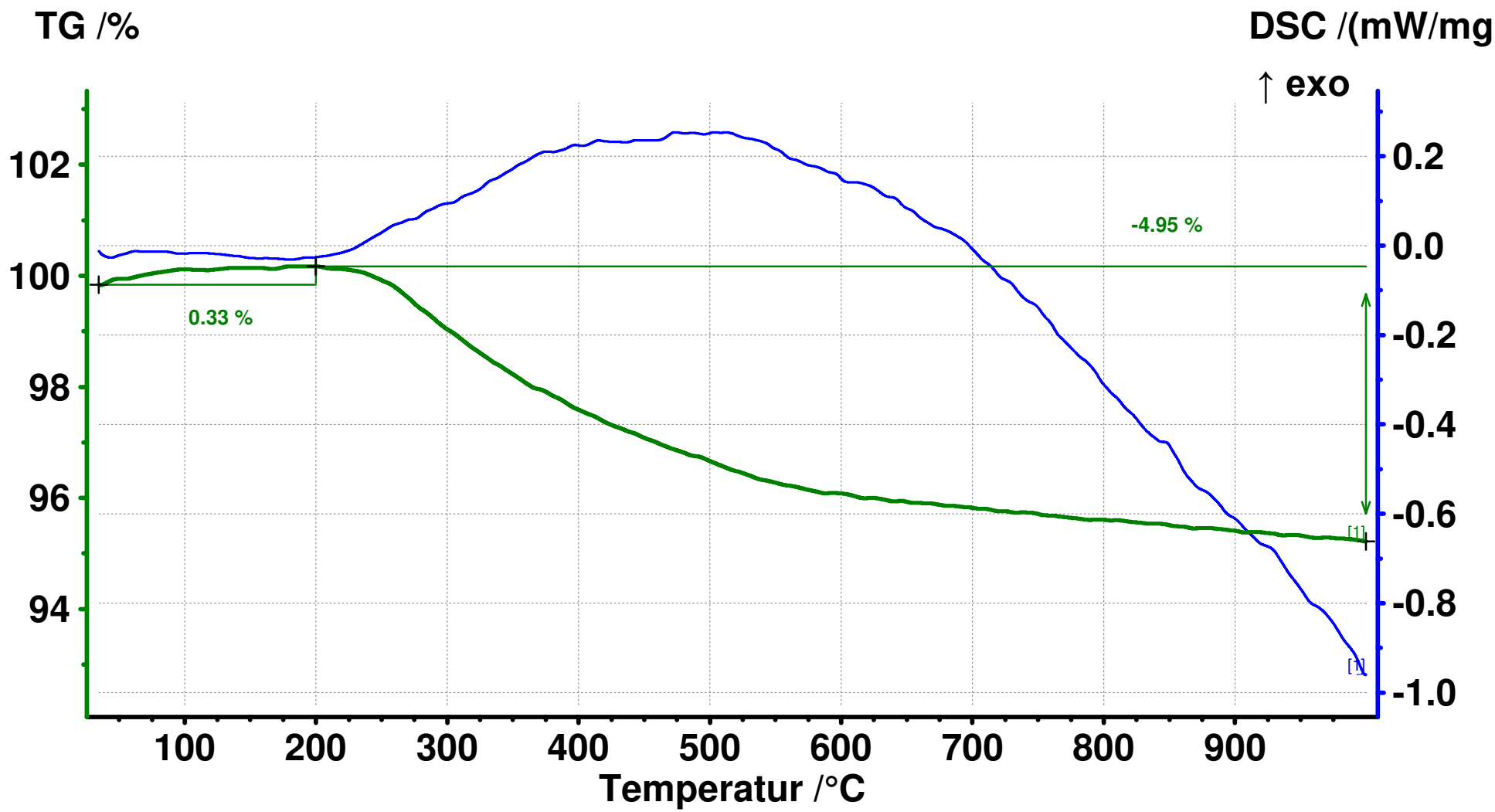

Hauptansicht 2021-04-29 10:31 Nutzer: User

Gerät :	NETZSCH STA 409 PC/PG		**Datei :** C:\NETZSCH\Proteus61\data\4477 3 8 97 1.ngb-dsv		
Projekt :	Messung	**Material :**	Obsidian	**Segmente :**	1/1
Proben-ID :	Prof. Breitkreuz	**Korrektur-Datei :**	4370 KK SL 10K Korund 2021.ngb-bsv	**Tiegel :**	DSC/TG pan Al2O3
Datum/Zeit :	29.04.2021 08:42:52	**Tempkal./Empf. Datei :**	cal Al2O3 2018 SL T.ngb-tsv / cal Al2O3 2018 SL E.ngb-esv	**Atmosphäre :**	AIR(80/20)/70 / <kein Gas>/--- / <kein Gas>/---
Labor :	F4 IKGB - Keramik	**Bereich :**	20°C/10.0(K/min)/1000°C	**TG Korr/Messber :**	820/30000 mg
Operator :	Ludewig	**Probentr./TC :**	DSC(/TG) HIGH RG 2 / S	**DSC Korr/Messber :**	820/5000 µV
Probe :	3 - 8 - 97 - 1, 20.280 mg	**Modus /Messtyp :**	DSC-TG / Probe + Korrektur		

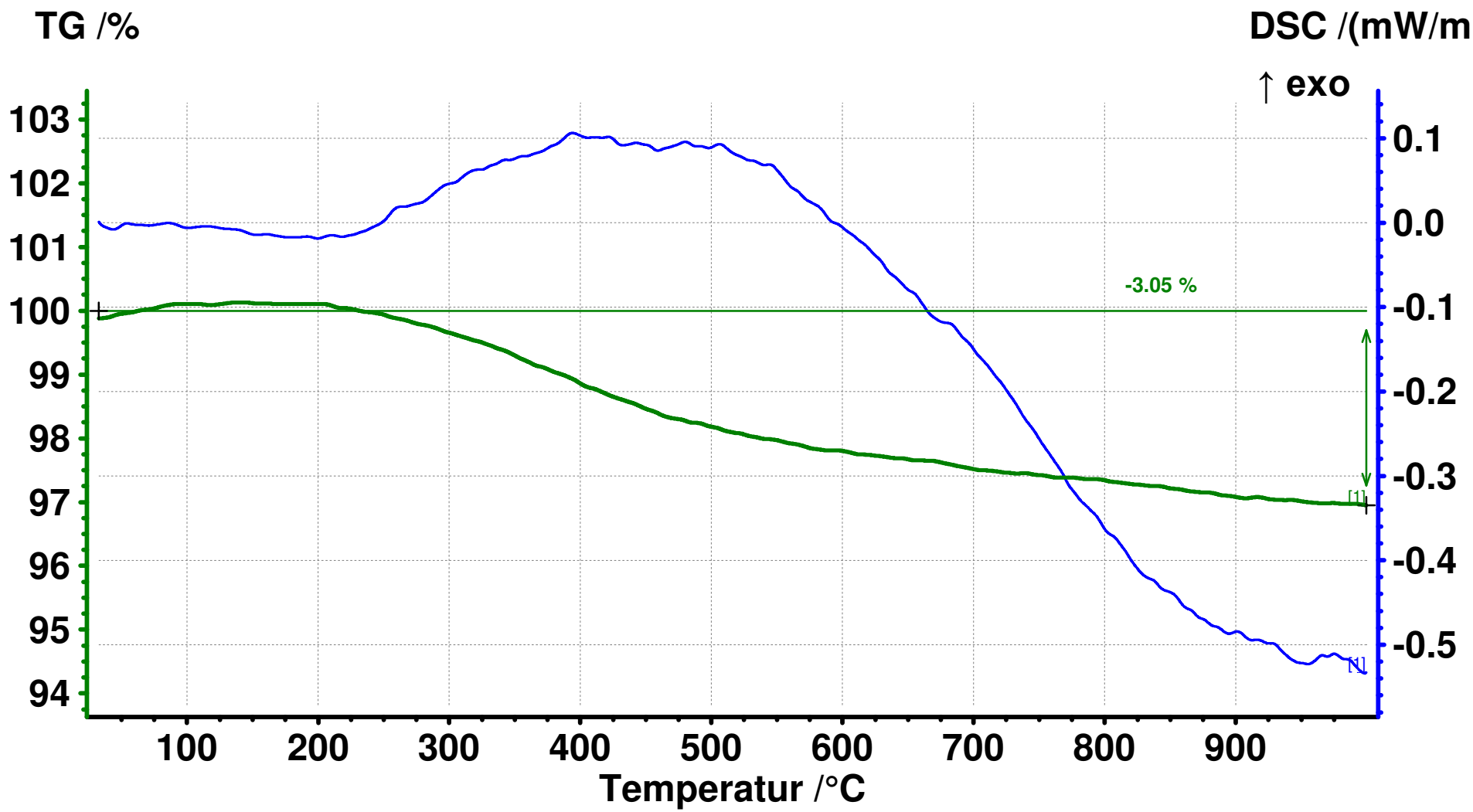

Hauptansicht 2021-05-17 09:15 Nutzer: User

Gerät :	NETZSCH STA 409 PC/PG		**Datei :** C:\NETZSCH\Proteus61\data\4483 10 12 20b.ngb-dsv		
Projekt :	Messung	**Material :**	Obsidian	**Segmente :**	1/1
Proben-ID :	Prof. Breitkreuz	**Korrektur-Datei :**	4370 KK SL 10K Korund 2021.ngb-bsv	**Tiegel :**	DSC/TG pan Al2O3
Datum/Zeit :	11.05.2021 13:32:24	**Tempkal./Empf. Datei :**	cal Al2O3 2018 SL T.ngb-tsv / cal Al2O3 2018 SL E.ngb-esv	**Atmosphäre :**	AIR(80/20)/70 / <kein Gas>/--- / <kein Gas>/---
Labor :	F4 IKGB - Keramik	**Bereich :**	20°C/10.0(K/min)/1000°C	**TG Korr/Messber :**	820/30000 mg
Operator :	Ludewig	**Probentr./TC :**	DSC(/TG) HIGH RG 2 / S	**DSC Korr/Messber :**	820/5000 µV
Probe :	10 12 20b, 23.290 mg	**Modus /Messtyp :**	DSC-TG / Probe + Korrektur		

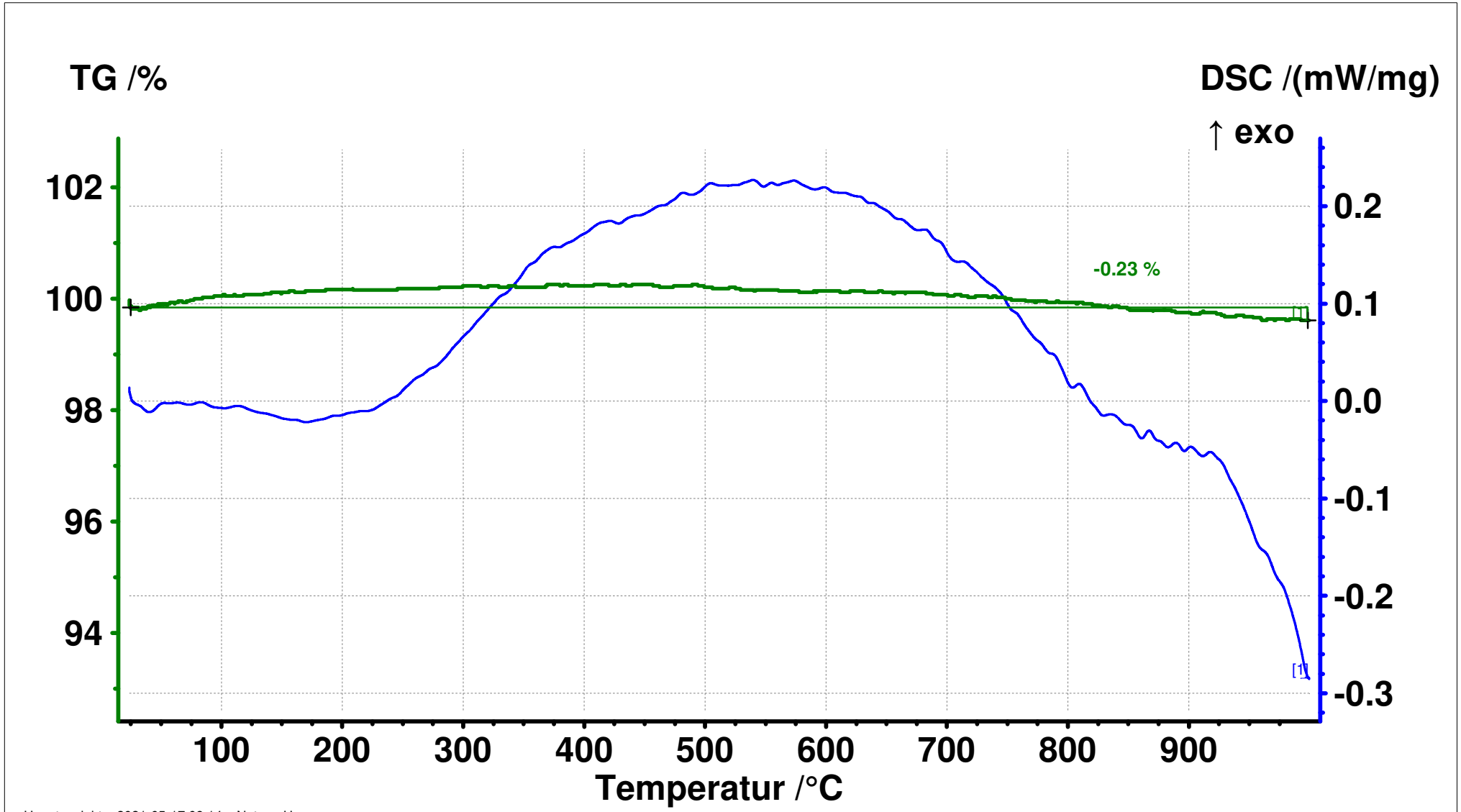

Hauptansicht 2021-05-17 09:14 Nutzer: User

Gerät : NETZSCH STA 409 PC/PG			**Datei :** C:\NETZSCH\Proteus61\data\4482 4 8 97 7.ngb-dsv		
Projekt :	Messung	**Material :**	Obsidian	**Segmente :**	1/1
Proben-ID :	Prof. Breitkreuz	**Korrektur-Datei :**	4370 KK SL 10K Korund 2021.ngb-bsv	**Tiegel :**	DSC/TG pan Al2O3
Datum/Zeit :	11.05.2021 10:48:24	**Tempkal./Empf. Datei :**	cal Al2O3 2018 SL T.ngb-tsv / cal Al2O3 2018 SL E.ngb-esv	**Atmosphäre :**	AIR(80/20)/70 / <kein Gas>/--- / <kein Gas>/---
Labor :	F4 IKGB - Keramik	**Bereich :**	20°C/10.0(K/min)/1000°C	**TG Korr/Messber :**	020/30000 mg
Operator :	Ludewig	**Probentr./TC :**	DSC(/TG) HIGH RG 2 / S	**DSC Korr/Messber :**	820/5000 µV
Probe :	4 8 97 7, 21.870 mg	**Modus /Messtyp :**	DSC-TG / Probe + Korrektur		

Erzeugt mit NETZSCH Proteus Software

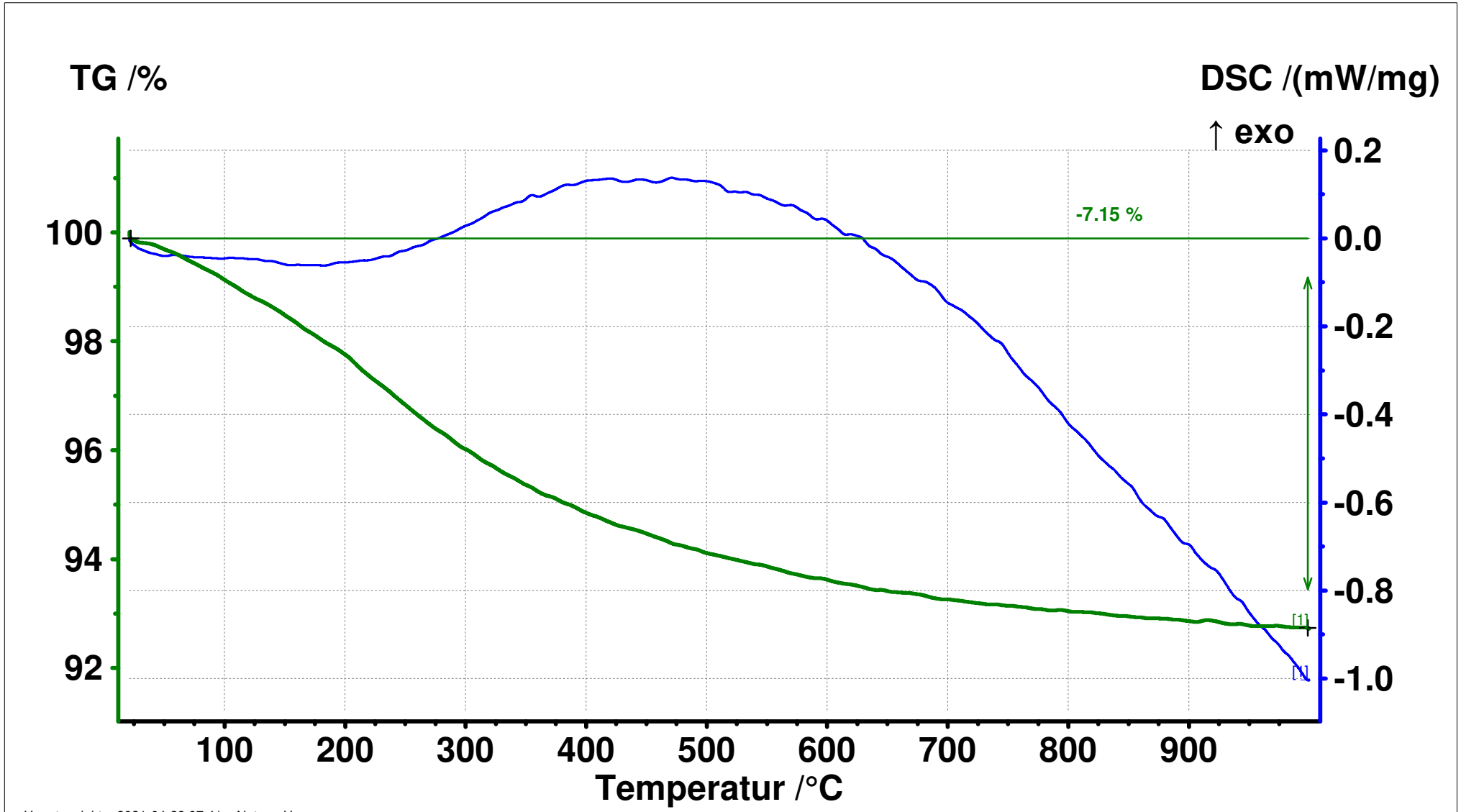

Hauptansicht 2021-04-29 07:41 Nutzer: User

Gerät : NETZSCH STA 409 PC/PG			**Datei :** C:\NETZSCH\Proteus61\data\4476 C 28 01.ngb-dsv		
Projekt :	Messung	**Material :**	Obsidian	**Segmente :**	1/1
Proben-ID :	Prof. Breitkreuz	**Korrektur-Datei :**	4370 KK SL 10K Korund 2021.ngb-bsv	**Tiegel :**	DSC/TG pan Al2O3
Datum/Zeit :	29.04.2021 06:01:20	**Tempkal./Empf. Datei :**	cal Al2O3 2018 SL T.ngb-tsv / cal Al2O3 2018 SL E.ngb-esv	**Atmosphäre :**	AIR(80/20)/70 / <kein Gas>/--- / <kein Gas>/---
Labor :	F4 IKGB - Keramik	**Bereich :**	20°C/10.0(K/min)/1000°C	**TG Korr/Messber :**	820/30000 mg
Operator :	Ludewig	**Probentr./TC :**	DSC(/TG) HIGH RG 2 / S	**DSC Korr/Messber :**	820/5000 µV
Probe :	C 28 / 01, 21.365 mg	**Modus /Messtyp :**	DSC-TG / Probe + Korrektur		

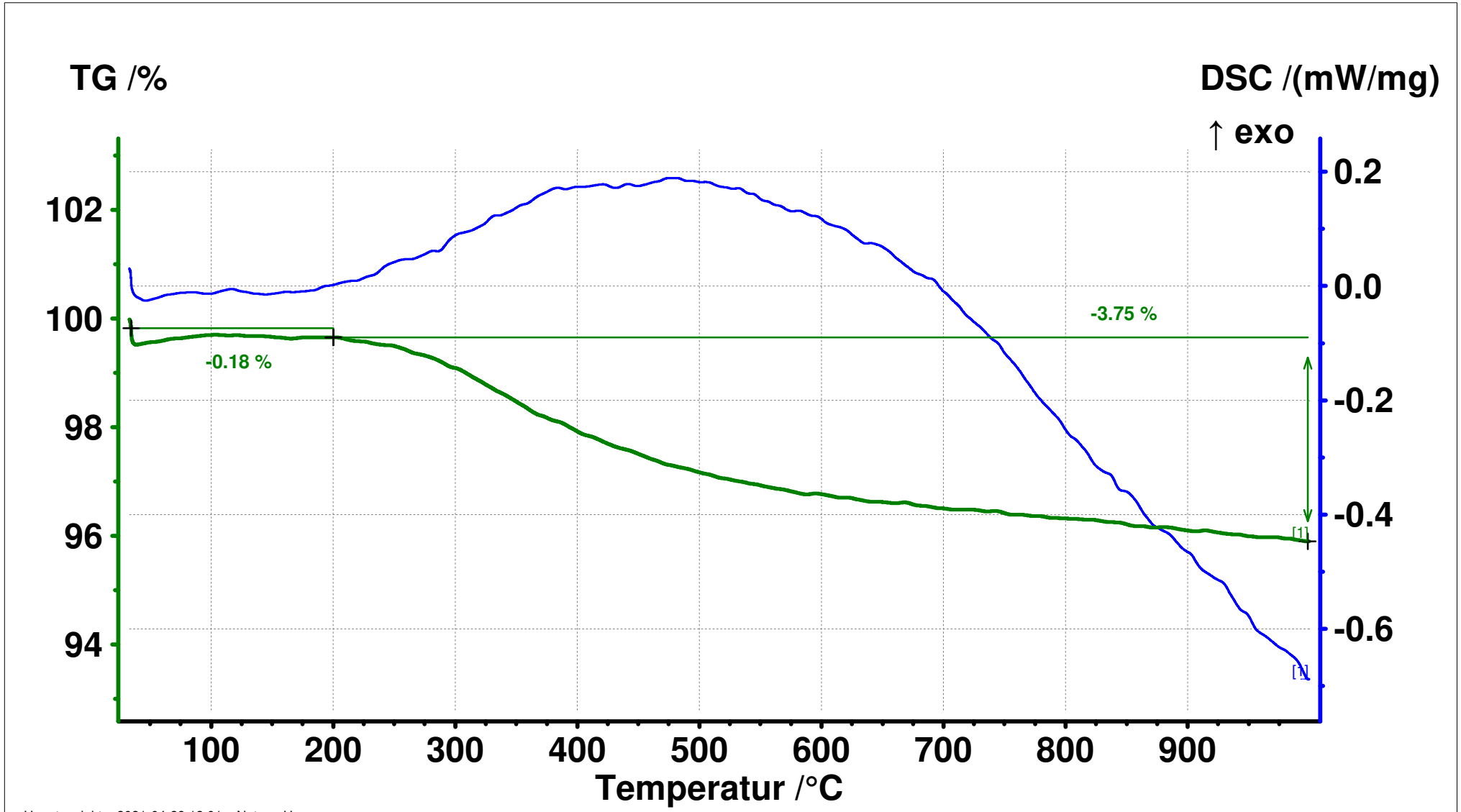

Hauptansicht 2021-04-29 13:01 Nutzer: User

Gerät :	NETZSCH STA 409 PC/PG		**Datei :** C:\NETZSCH\Proteus61\data\4478 27 6 14 le.ngb-dsv		
Projekt :	Messung	**Material :**	Obsidian	**Segmente :**	1/1
Proben-ID :	Prof. Breitkreuz	**Korrektur-Datei :**	4370 KK SL 10K Korund 2021.ngb-bsv	**Tiegel :**	DSC/TG pan Al2O3
Datum/Zeit :	29.04.2021 11:21:04	**Tempkal./Empf. Datei :**	cal Al2O3 2018 SL T.ngb-tsv / cal Al2O3 2018 SL E.ngb-esv	**Atmosphäre :**	AIR(80/20)/70 / <kein Gas>/--- / <kein Gas>/---
Labor :	F4 IKGB - Keramik	**Bereich :**	20°C/10.0(K/min)/1000°C	**TG Korr/Messber :**	820/30000 mg
Operator :	Ludewig	**Probentr./TC :**	DSC(/TG) HIGH RG 2 / S	**DSC Korr/Messber :**	820/5000 µV
Probe :	27 6 14 le, 21.325 mg	**Modus /Messtyp :**	DSC-TG / Probe + Korrektur		

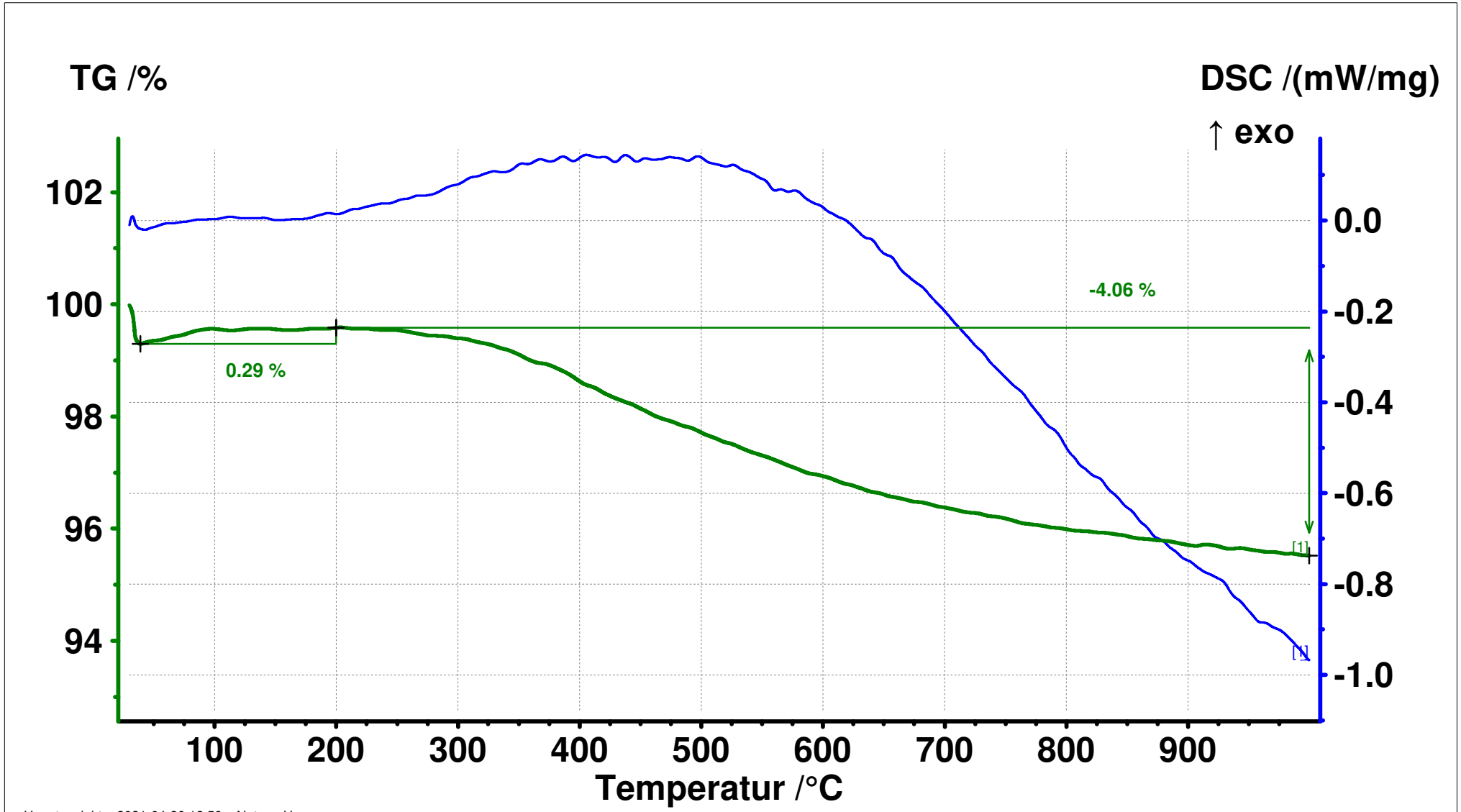

Hauptansicht 2021-04-30 12:50 Nutzer: User

Gerät :	NETZSCH STA 409 PC/PG		**Datei :** C:\NETZSCH\Proteus61\data\4481 5 11 07 3b.ngb-dsv		
Projekt :	Messung	**Material :**	Obsidian	**Segmente :**	1/1
Proben-ID :	Prof. Breitkreuz	**Korrektur-Datei :**	4370 KK SL 10K Korund 2021.ngb-bsv	**Tiegel :**	DSC/TG pan Al2O3
Datum/Zeit :	30.04.2021 10:57:45	**Tempkal./Empf. Datei :**	cal Al2O3 2018 SL T.ngb-tsv / cal Al2O3 2018 SL E.ngb-esv	**Atmosphäre :**	AIR(80/20)/70 / <kein Gas>/--- / <kein Gas>/---
Labor :	F4 IKGB - Keramik	**Bereich :**	20°C/10.0(K/min)/1000°C	**TG Korr/Messber :**	820/30000 mg
Operator :	Ludewig	**Probentr./TC :**	DSC(/TG) HIGH RG 2 / S	**DSC Korr/Messber :**	820/5000 µV
Probe :	5 11 07 3b, 21.995 mg	**Modus /Messtyp :**	DSC-TG / Probe + Korrektur		

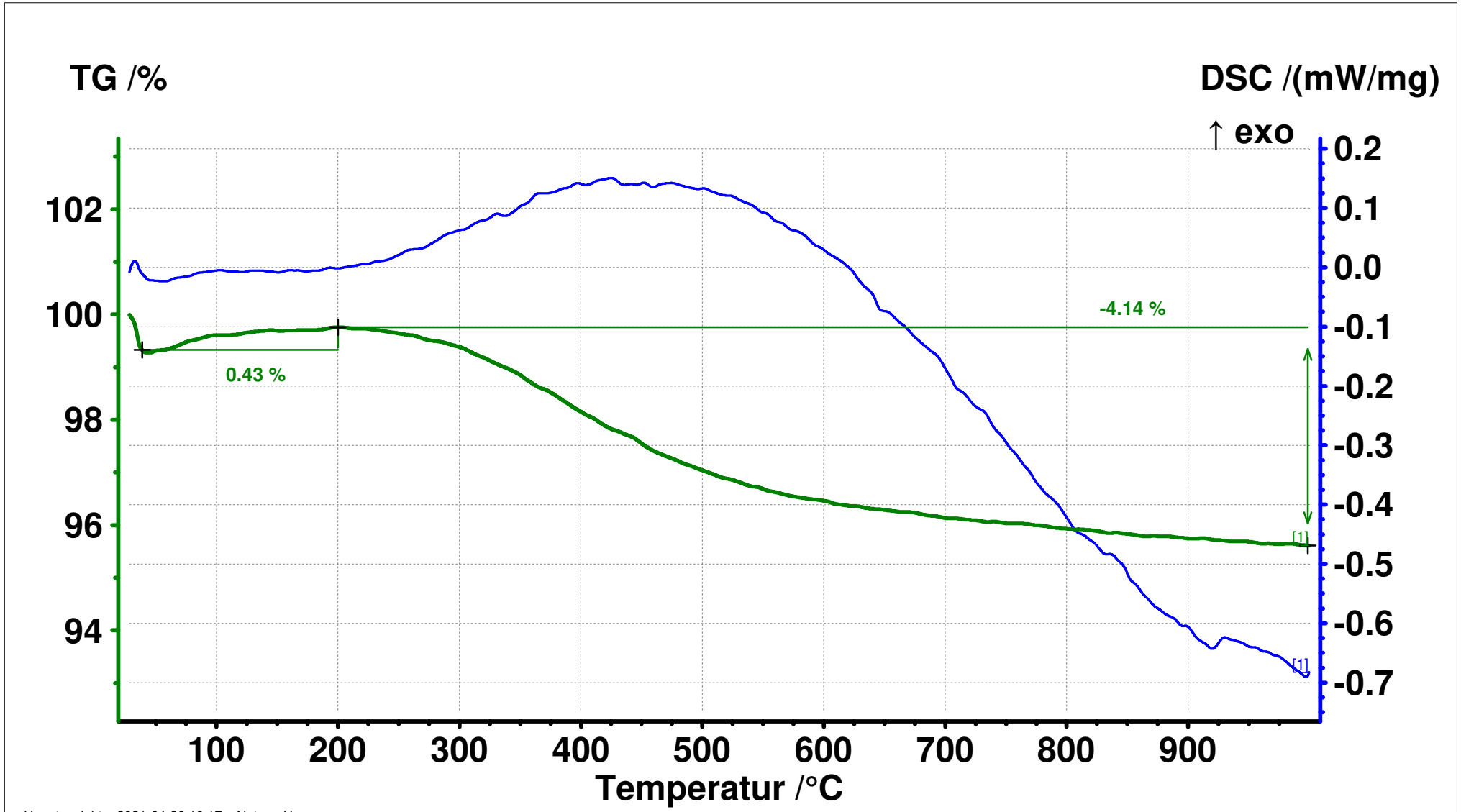

Hauptansicht 2021-04-30 10:17 Nutzer: User

Gerät :	NETZSCH STA 409 PC/PG		**Datei :** C:\NETZSCH\Proteus61\data\4480 5 12 04 3.ngb-dsv		
Projekt :	Messung	**Material :**	Obsidian	**Segmente :**	1/1
Proben-ID :	Prof. Breitkreuz	**Korrektur-Datei :**	4370 KK SL 10K Korund 2021.ngb-bsv	**Tiegel :**	DSC/TG pan Al2O3
Datum/Zeit :	30.04.2021 08:20:50	**Tempkal./Empf. Datei :**	cal Al2O3 2018 SL T.ngb-tsv / cal Al2O3 2018 SL E.ngb-esv	**Atmosphäre :**	AIR(80/20)/70 / <kein Gas>/--- / <kein Gas>/---
Labor :	F4 IKGB - Keramik	**Bereich :**	20°C/10.0(K/min)/1000°C	**TG Korr/Messber :**	820/30000 mg
Operator :	Ludewig	**Probentr./TC :**	DSC(/TG) HIGH RG 2 / S	**DSC Korr/Messber :**	820/5000 µV
Probe :	5 12 04 3, 20.655 mg	**Modus /Messtyp :**	DSC-TG / Probe + Korrektur		

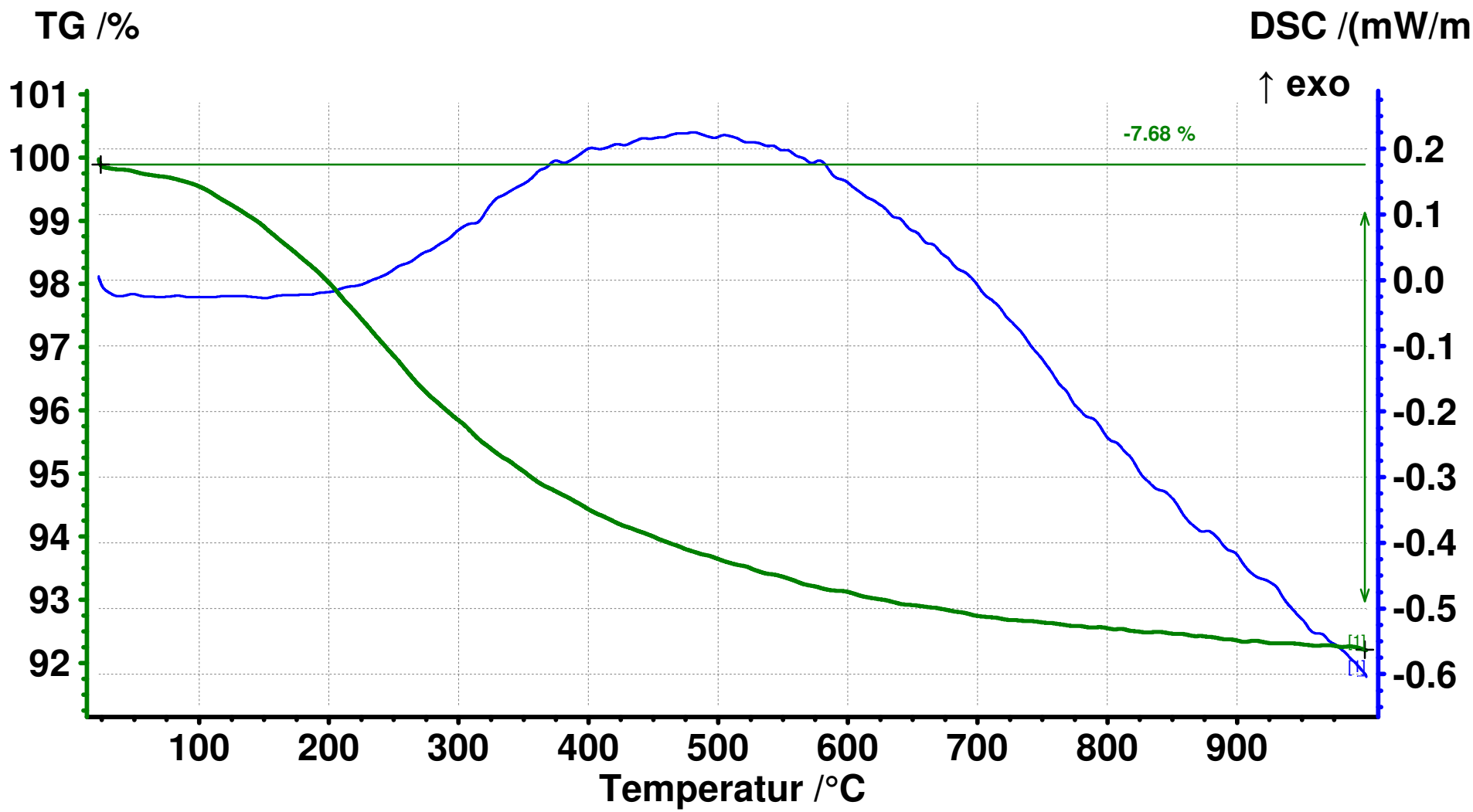

Hauptansicht 2021-04-30 07:25 Nutzer: User

Gerät :	NETZSCH STA 409 PC/PG			**Datei :**	C:\NETZSCH\Proteus61\data\4479 6 4 01 la.ngb-dsv
Projekt :	Messung	**Material :**	Obsidian	**Segmente :**	1/1
Proben-ID :	Prof. Breitkreuz	**Korrektur-Datei :**	4370 KK SL 10K Korund 2021.ngb-bsv	**Tiegel :**	DSC/TG pan Al2O3
Datum/Zeit :	30.04.2021 05:45:19	**Tempkal./Empf. Datei :**	cal Al2O3 2018 SL T.ngb-tsv / cal Al2O3 2018 SL E.ngb-esv	**Atmosphäre :**	AIR(80/20)/70 / <kein Gas>/--- / <kein Gas>/---
Labor :	F4 IKGB - Keramik	**Bereich :**	20°C/10.0(K/min)/1000°C	**TG Korr/Messber :**	820/30000 mg
Operator :	Ludewig	**Probentr./TC :**	DSC(/TG) HIGH RG 2 / S	**DSC Korr/Messber :**	820/5000 µV
Probe :	6 4 01 la, 23.085 mg	**Modus /Messtyp :**	DSC-TG / Probe + Korrektur		

8.4. EMP measurements

8.4.1. Thin section scans with profiles for EMP measurements

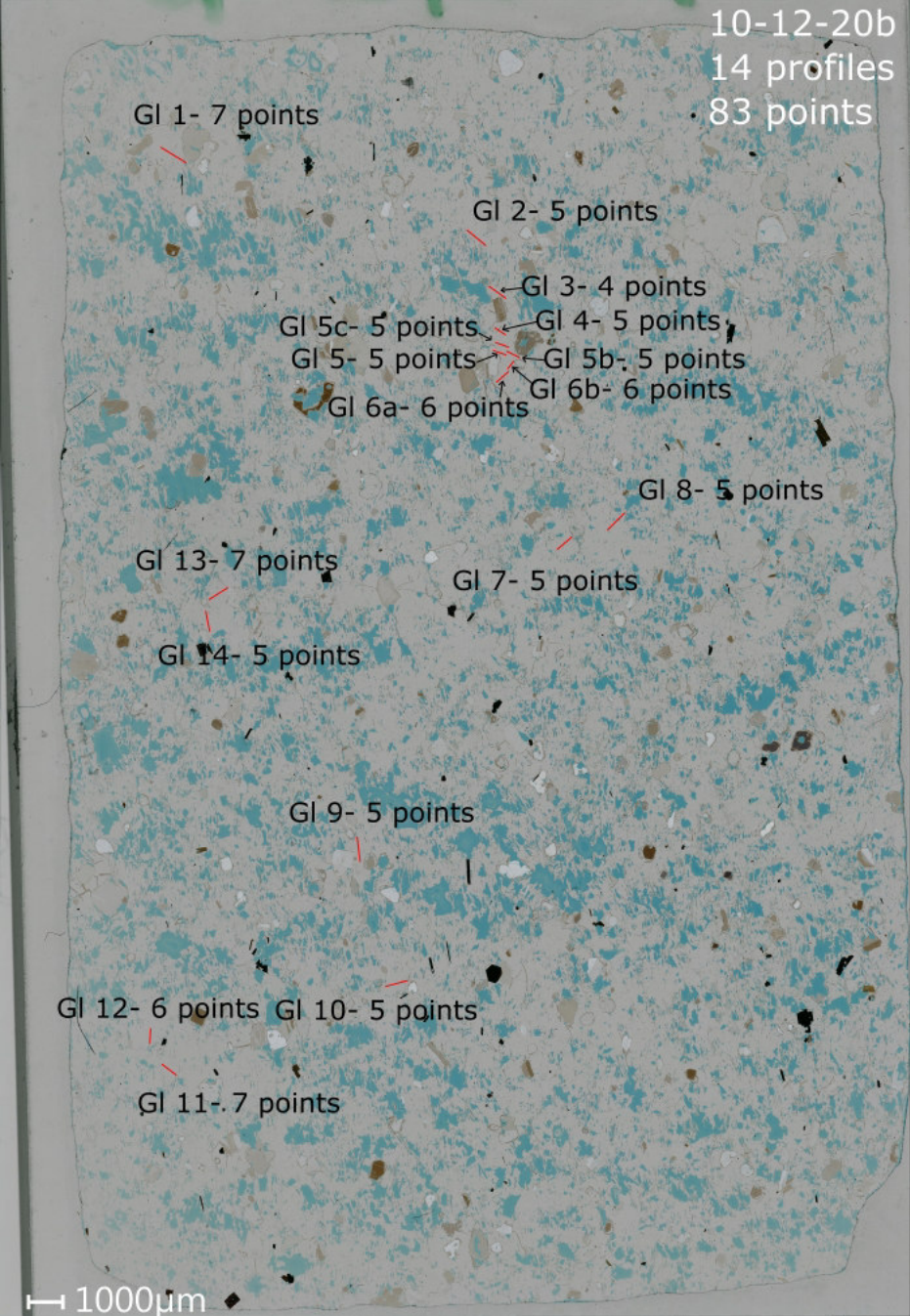
10-12-20b
14 profiles
83 points
Gl 1- 7 points
Gl 2- 5 points
Gl 3- 4 points
Gl 4- 5 points
Gl 5c- 5 points
Gl 5- 5 points
Gl 5b- 5 points
Gl 6b- 6 points
Gl 6a- 6 points
Gl 8- 5 points
Gl 13- 7 points
Gl 7- 5 points
Gl 14- 5 points
Gl 9- 5 points
Gl 12- 6 points
Gl 10- 5 points
Gl 11- 7 points
1000µm

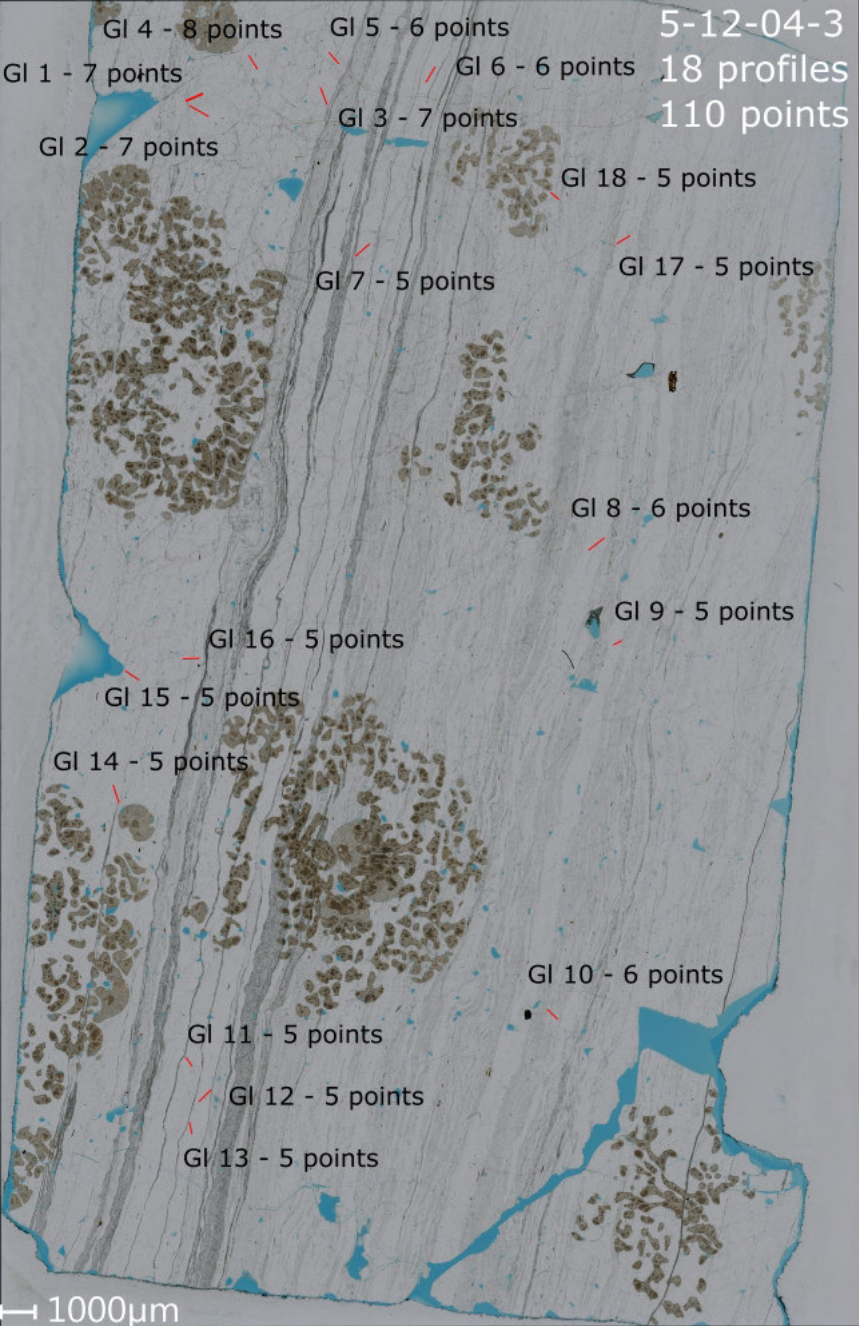
Gl 4 - 8 points
Gl 5 - 6 points
5-12-04-3
18 profiles
110 points
Gl 1 - 7 points
Gl 6 - 6 points
Gl 3 - 7 points
Gl 2 - 7 points
Gl 18 - 5 points
Gl 17 - 5 points
Gl 7 - 5 points
Gl 8 - 6 points
Gl 9 - 5 points
Gl 16 - 5 points
Gl 15 - 5 points
Gl 14 - 5 points
Gl 10 - 6 points
Gl 11 - 5 points
Gl 12 - 5 points
Gl 13 - 5 points
1000µm

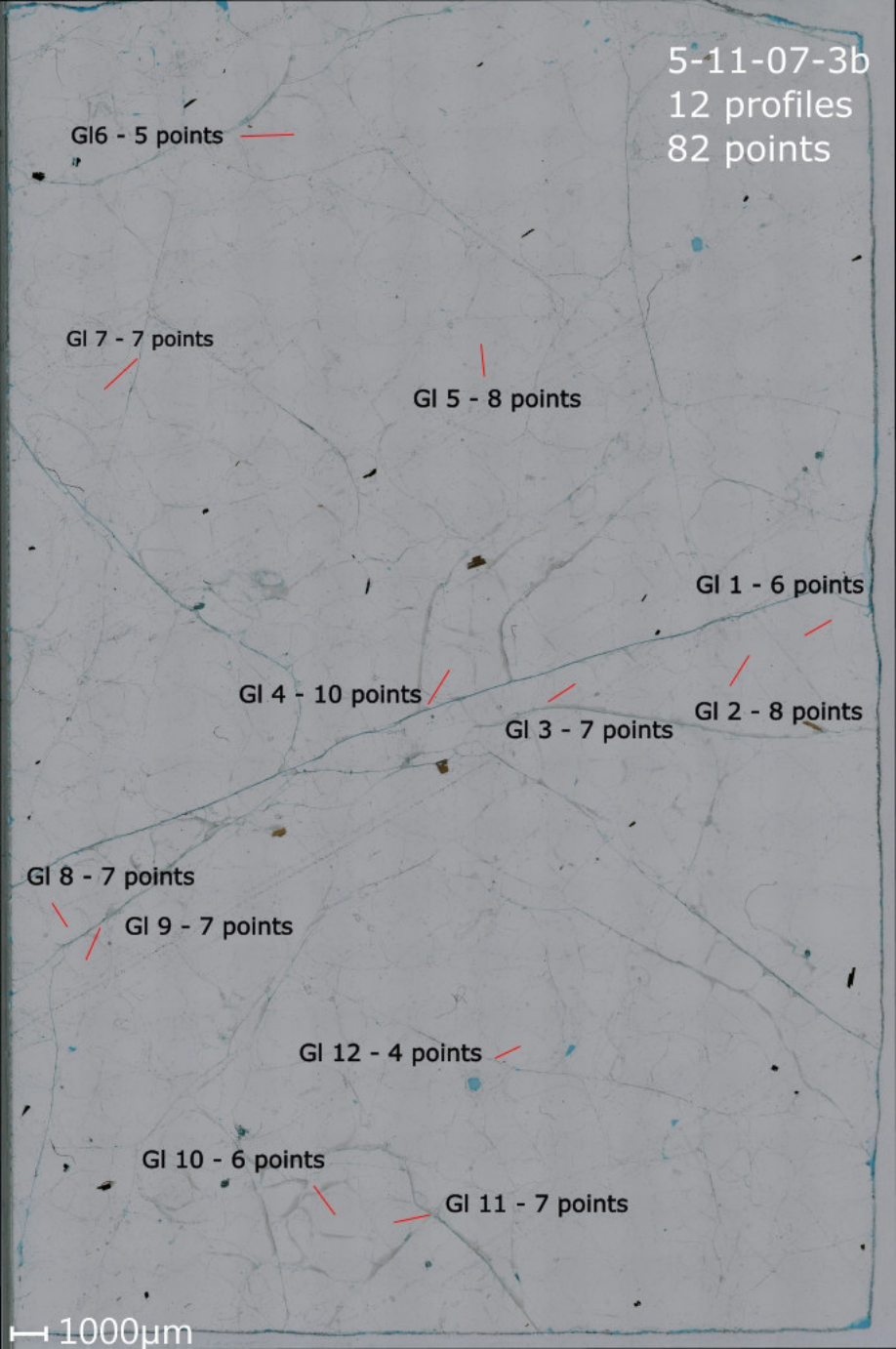
5-11-07-3b
12 profiles
82 points
Gl6 - 5 points
Gl 7 - 7 points
Gl 5 - 8 points
Gl 1 - 6 points
Gl 4 - 10 points
Gl 2 - 8 points
Gl 3 - 7 points
Gl 8 - 7 points
Gl 9 - 7 points
Gl 12 - 4 points
Gl 10 - 6 points
Gl 11 - 7 points
1000µm

8.4.2. Results & Calibration

Measurement condition

WDS elements

	Element	X-ray	Crystal	CH	Acc.v	Peak Pos.	(nm)	BG_L	BG_U	(mm)
1	K	Ka	PETJ	1	15	119.852	0.37414	2.415	0.915	
2	Si	Ka	PETJ	1	15	228.255	0.71254	4.187	4.771	
3	Ca	Ka	PETJ	1	15	107.589	0.33584	2.678	1.507	
4	Cl	Ka	PETH	2	15	151.426	0.47278	1.915	2.115	
5	Sn	La	PETH	2	15	115.209	0.35999	4.479	3.533	
6	Na	Ka	TAP	3	15	129.551	1.19101	3.201	5.039	
7	Mg	Ka	TAP	3	15	107.528	0.989	5.709	4.519	
8	Al	Ka	TAP	3	15	90.591	0.83393	6.11	5.071	
9	Ti	Ka	LIFH	4	15	191.089	0.27485	3.352	3.644	
10	Cr	Ka	LIFH	4	15	159.048	0.22897	3.834	6.548	
11	Fe	Ka	LIFL	5	15	134.606	0.1936	4.877	4.934	
12	Mn	Ka	LIFL	5	15	146.151	0.21018	3.692	5.269	
13	Ni	Ka	LIFL	5	15	115.243	0.16579	3.788	12.195	

	Element	Peak	Back	Pksk	Gain	High.V	Base.L	Window.W	Mode
1	K	20	10.0 (s)	0	4	1700	2	0 (V)	Int
2	Si	20	10.0 (s)	2	8	1698	2	0 (V)	Int
3	Ca	30	10.0 (s)	0	4	1696	2	0 (V)	Int
4	Cl	30	10.0 (s)	2	8	1671	1.8	0 (V)	Int
5	Sn	40	15.0 (s)	2	8	1654	1.8	0 (V)	Int
6	Na	20	10.0 (s)	0	8	1732	2	4.8 (V)	Dif
7	Mg	20	10.0 (s)	0	8	1719	2	4.8 (V)	Dif
8	Al	20	10.0 (s)	0	8	1710	2	4.8 (V)	Dif
9	Ti	30	10.0 (s)	0	16	1786	2	0 (V)	Int
10	Cr	30	10.0 (s)	2	16	1778	2	0 (V)	Int
11	Fe	30	10.0 (s)	0	16	1728	2	0 (V)	Int
12	Mn	30	10.0 (s)	0	16	1728	2	0 (V)	Int
13	Ni	30	10.0 (s)	2	16	1711	1.3	0 (V)	Int

Measurement order of WDS

Order	Channel 1	2	3	4	5
1	K1PKa_Am	Cl2PKa_A	Na3TKa_A	Ti4LKa_A	Fe5LKa_A
2	Si1PKa_A	Sn2PLa_A	Mg3TKa_A	Cr4LKa_A	Mn5LKa_A
3	Ca1PKa_A	0	Al3TKa_A	0	Ni5LKa_A
Calc.	Elements :	O	(Anion)		

Standard Data

	Element	Standard	Mass(%)	ZAF Fac.	Z	A	F
1	K2O	Sanidine_AST	12.11	1.0676	1.2031	0.8871	1.0003
2	SiO2	Diopside_AST	55.37	3.2145	4.3999	0.7299	1.0009
3	CaO	Diopside_AST	25.73	0.863	0.9345	0.9234	1.0001
4	Cl	Tugtupite_AST	7.58	1.617	1.9952	0.8104	1
5	SnO2	Sn_AST	126.9591	1.1788	1.3157	0.896	1
6	Na2O	Albite_AST	11.59	5.3768	10.7239	0.4995	1.0038
7	MgO	Diopside_AST	18.62	4.7033	7.8638	0.5952	1.0049
8	Al2O3	Plagioclase_AST	28.53	4.1586	5.853	0.7029	1.0109
9	TiO2	Rutile_AST	100	0.5913	0.606	0.9757	1
10	Cr2O3	Chromiumoxide_AST	100	0.3641	0.3706	0.9825	1
11	FeO	Hematite_AST	89.87	0.2176	0.2206	0.9866	1
12	MnO	Bustamite_AST	24.31	0.2624	0.2704	0.9705	1.0001
13	NiO	Nickel_Silicide_AST	102.6928	0.1223	0.1238	0.9877	1

Standard Intensity of WDS

	Element	Curr.(A)	Net(cps)	Bg-(cps)	Bg+(cps)	S.D.(%)	Date	
1	K	1.52E-08	947.6	8.3	10.9	0.52	44316	0.36525463
2	Si	1.511E-08	1911.7	3	3.1	0.36	44316	0.362939815
3	Ca	1.511E-08	1761.8	11.9	14.1	0.38	44316	0.362939815
4	Cl	1.509E-08	678.6	8.3	6.1	0.61	44316	0.387013889
5	Sn	1.506E-08	11901.6	118.9	90.8	0.17	44316	0.393923611
6	Na	1.512E-08	873.5	11.5	4.5	0.54	44316	0.367638889
7	Mg	1.511E-08	2221.1	14.5	10	0.34	44316	0.362939815

8	Al	1.51E-08	4416	25.7	16.8	0.24	44316	0.370127315
9	Ti	1.512E-08	4424.5	13.3	13.8	0.24	44316	0.372569444
10	Cr	1.512E-08	6595.1	26	20.2	0.2	44316	0.379791667
11	Fe	1.511E-08	5878.3	24.1	18	0.21	44316	0.374988426
12	Mn	1.51E-08	1293.3	11.2	9	0.44	44316	0.377314815
13	Ni	1.501E-08	7679.5	46	30.7	0.18	44316	0.384699074

No.	Name	K2O	SiO_2-Calc	CaO	Cl	SnO_2	Na_2O	MgO	Al_2O_3	TiO_2	Cr_2O_3	FeO	MnO	NiO	Total-Calc	100-Total
		[wt.%]	[wt.%]	[wt.%]	[wt.%]	[wt.%]	[wt.%]	[wt.%]	[wt.%]	[wt.%]	[wt.%]	[wt.%]	[wt.%]	[wt.%]	[wt.%]	[wt.%]
1	5-12-04-3-Gl1-1	5.74	73.62	0.74	0.13	0.00	1.89	0.06	11.94	0.14	0.00	0.48	0.02	0.01	94.76	5.24
2	5-12-04-3-Gl1-2	5.82	73.26	0.69	0.11	0.00	2.06	0.06	11.82	0.13	0.00	0.39	0.03	0.02	94.38	5.62
3	5-12-04-3-Gl1-3	5.68	73.86	0.71	0.12	0.00	2.31	0.06	11.78	0.17	0.00	0.48	0.04	0.00	95.23	4.77
4	5-12-04-3-Gl1-4	5.67	72.82	0.72	0.11	0.00	2.33	0.07	11.67	0.13	0.00	0.51	0.03	0.00	94.04	5.96
5	5-12-04-3-Gl1-5	5.40	72.20	0.72	0.15	0.00	1.61	0.07	12.34	0.14	0.01	0.59	0.04	0.00	93.26	6.74
6	5-12-04-3-Gl1-6	5.76	73.29	0.68	0.10	0.00	2.06	0.06	11.89	0.11	0.00	0.48	0.03	0.02	94.50	5.50
7	5-12-04-3-Gl1-7	5.63	73.27	0.70	0.12	0.00	2.12	0.06	11.82	0.12	0.00	0.47	0.04	0.00	94.34	5.66
8	5-12-04-3-Gl2-1	5.61	73.95	0.71	0.12	0.00	1.95	0.08	11.74	0.13	0.00	0.53	0.07	0.00	94.89	5.11
9	5-12-04-3-Gl2-2	5.63	73.49	0.72	0.12	0.00	2.13	0.07	11.82	0.14	0.00	0.54	0.03	0.00	94.69	5.31
10	5-12-04-3-Gl2-3	5.59	72.46	0.71	0.13	0.00	2.00	0.09	11.75	0.13	0.02	0.59	0.05	0.00	93.51	6.49
11	5-12-04-3-Gl2-4	5.49	72.57	0.68	0.11	0.00	1.85	0.07	11.84	0.16	0.00	0.63	0.05	0.00	93.46	6.54
12	5-12-04-3-Gl2-5	5.53	73.01	0.75	0.14	0.00	1.88	0.09	11.73	0.16	0.00	0.56	0.03	0.00	93.88	6.12
13	5-12-04-3-Gl2-6	5.48	72.68	0.69	0.12	0.00	1.99	0.08	11.72	0.13	0.00	0.56	0.05	0.00	93.50	6.50
14	5-12-04-3-Gl2-7	5.65	73.52	0.74	0.13	0.00	1.46	0.09	11.76	0.17	0.00	0.60	0.03	0.00	94.15	5.85
15	5-12-04-3-Gl3-1	5.47	73.08	0.71	0.10	0.00	1.88	0.09	11.78	0.11	0.00	0.57	0.03	0.00	93.81	6.19
16	5-12-04-3-Gl3-2	5.67	72.81	0.73	0.10	0.00	2.00	0.08	11.71	0.13	0.00	0.56	0.04	0.03	93.85	6.15
17	5-12-04-3-Gl3-3	5.59	72.70	0.72	0.11	0.00	1.72	0.09	11.73	0.11	0.00	0.52	0.04	0.00	93.32	6.68
18	5-12-04-3-Gl3-4	5.27	73.53	0.72	0.11	0.00	2.59	0.05	11.76	0.14	0.00	0.53	0.05	0.00	94.75	5.25
19	5-12-04-3-Gl3-5	5.27	72.95	0.72	0.13	0.00	2.59	0.06	11.82	0.14	0.00	0.48	0.04	0.00	94.19	5.81
20	5-12-04-3-Gl3-6	5.68	71.96	0.75	0.14	0.00	2.25	0.05	11.67	0.09	0.01	0.51	0.06	0.01	93.17	6.83
21	5-12-04-3-Gl3-7	5.51	72.20	0.69	0.13	0.00	2.51	0.06	11.78	0.13	0.01	0.53	0.03	0.01	93.58	6.42
22	5-12-04-3-Gl4-1	5.62	73.26	0.70	0.12	0.00	2.26	0.08	11.77	0.15	0.00	0.53	0.06	0.00	94.55	5.45
23	5-12-04-3-Gl4-2	5.45	72.64	0.72	0.12	0.00	1.74	0.09	12.02	0.11	0.00	0.61	0.04	0.01	93.54	6.46
24	5-12-04-3-Gl4-3	5.73	71.78	0.72	0.10	0.00	2.17	0.09	11.73	0.12	0.00	0.56	0.02	0.01	93.03	6.97
25	5-12-04-3-Gl4-4	5.55	73.60	0.70	0.14	0.00	2.34	0.06	11.80	0.14	0.00	0.56	0.08	0.00	94.95	5.05
26	5-12-04-3-Gl4-5	5.13	72.69	0.71	0.13	0.00	2.57	0.07	11.74	0.14	0.00	0.56	0.04	0.00	93.78	6.22
27	5-12-04-3-Gl4-6	5.12	72.21	0.72	0.13	0.00	2.62	0.09	11.82	0.12	0.00	0.56	0.06	0.00	93.44	6.56
28	5-12-04-3-Gl4-7	5.22	73.98	0.74	0.10	0.00	2.63	0.06	11.85	0.12	0.00	0.53	0.04	0.02	95.29	4.71

No.	Name	K2O [wt.%]	SiO_2-Calc [wt.%]	CaO [wt.%]	Cl [wt.%]	SnO_2 [wt.%]	Na_2O [wt.%]	MgO [wt.%]	Al_2O_3 [wt.%]	TiO_2 [wt.%]	Cr_2O_3 [wt.%]	FeO [wt.%]	MnO [wt.%]	NiO [wt.%]	Total-Calc [wt.%]	100-Total [wt.%]
29	5-12-04-3-Gl4-8	5.63	73.29	0.73	0.13	0.00	1.82	0.06	11.80	0.13	0.02	0.54	0.06	0.03	94.25	5.75
30	5-12-04-3-Gl5-1	5.66	72.73	0.72	0.12	0.00	1.94	0.07	11.64	0.14	0.03	0.55	0.04	0.00	93.62	6.38
31	5-12-04-3-Gl5-2	5.61	72.26	0.70	0.11	0.00	2.38	0.09	11.77	0.11	0.01	0.51	0.04	0.00	93.57	6.43
32	5-12-04-3-Gl5-3	4.99	68.38	0.69	0.14	0.00	1.38	0.10	12.67	0.15	0.00	0.69	0.03	0.01	89.23	10.77
33	5-12-04-3-Gl5-4	5.07	69.95	1.45	0.11	0.00	1.61	1.04	11.33	0.16	0.00	2.31	0.21	0.00	93.23	6.77
34	5-12-04-3-Gl5-5	5.42	72.24	0.71	0.11	0.00	2.29	0.06	11.72	0.11	0.00	0.51	0.06	0.00	93.22	6.78
35	5-12-04-3-Gl5-6	5.12	72.30	0.72	0.11	0.00	2.60	0.11	11.72	0.12	0.00	0.63	0.04	0.01	93.48	6.52
36	5-12-04-3-Gl6-1	5.57	72.64	0.69	0.12	0.00	2.45	0.07	11.87	0.13	0.00	0.42	0.04	0.00	93.98	6.02
37	5-12-04-3-Gl6-2	5.44	72.89	0.69	0.11	0.00	2.51	0.08	11.79	0.10	0.00	0.43	0.04	0.01	94.08	5.92
38	5-12-04-3-Gl6-3	5.39	72.18	0.71	0.10	0.00	2.50	0.05	11.76	0.16	0.00	0.98	0.02	0.01	93.85	6.15
39	5-12-04-3-Gl6-4	5.86	72.52	0.70	0.11	0.00	2.15	0.07	11.92	0.14	0.00	0.38	0.01	0.03	93.89	6.11
40	5-12-04-3-Gl6-5	5.69	73.11	0.69	0.11	0.00	1.79	0.06	11.80	0.14	0.00	0.43	0.05	0.00	93.86	6.14
41	5-12-04-3-Gl7-1	5.49	72.05	0.73	0.11	0.00	2.09	0.05	11.85	0.10	0.00	0.58	0.03	0.00	93.05	6.95
42	5-12-04-3-Gl7-2	5.59	71.40	0.74	0.13	0.00	2.03	0.06	11.66	0.12	0.00	0.43	0.05	0.00	92.20	7.80
43	5-12-04-3-Gl7-3	5.62	71.35	0.65	0.10	0.00	2.41	0.05	11.69	0.13	0.00	0.64	0.04	0.02	92.69	7.31
44	5-12-04-3-Gl7-4	5.70	72.31	0.69	0.10	0.00	2.45	0.05	11.79	0.12	0.00	0.46	0.04	0.00	93.72	6.28
45	5-12-04-3-Gl7-5	5.21	72.01	0.70	0.11	0.00	2.57	0.08	11.71	0.17	0.02	0.54	0.04	0.00	93.13	6.87
46	5-12-04-3-Gl8-1	5.48	71.30	0.71	0.11	0.00	1.41	0.10	11.66	0.12	0.00	0.64	0.05	0.00	91.57	8.43
47	5-12-04-3-Gl8-2	5.45	72.13	0.72	0.11	0.00	1.48	0.10	11.74	0.15	0.02	0.62	0.06	0.01	92.58	7.42
48	5-12-04-3-Gl8-3	5.37	70.94	0.75	0.11	0.00	2.36	0.09	11.55	0.12	0.03	0.61	0.06	0.00	91.99	8.01
49	5-12-04-3-Gl8-4	5.37	71.88	0.68	0.13	0.00	2.49	0.11	11.73	0.14	0.00	0.60	0.04	0.00	93.17	6.83
50	5-12-04-3-Gl8-5	5.07	71.97	0.73	0.10	0.00	2.52	0.10	11.80	0.11	0.00	0.64	0.04	0.00	93.09	6.91
51	5-12-04-3-Gl8-6	4.86	71.44	0.74	0.11	0.00	2.70	0.07	11.78	0.14	0.00	0.55	0.05	0.00	92.44	7.56
52	5-12-04-3-Gl9-1	5.62	71.40	0.90	0.08	0.00	1.63	0.28	11.51	0.12	0.00	0.85	0.07	0.02	92.46	7.54
53	5-12-04-3-Gl9-2	5.76	72.10	0.70	0.08	0.00	2.17	0.06	11.57	0.13	0.00	0.37	0.04	0.00	92.96	7.04
54	5-12-04-3-Gl9-3	5.67	71.79	0.70	0.11	0.00	2.13	0.05	11.77	0.16	0.00	0.39	0.07	0.00	92.83	7.17
55	5-12-04-3-Gl9-4	5.57	72.44	0.68	0.12	0.00	2.32	0.05	11.67	0.12	0.00	0.50	0.03	0.01	93.51	6.49
56	5-12-04-3-Gl9-5	4.82	71.25	0.68	0.12	0.00	2.69	0.09	11.75	0.14	0.00	0.53	0.05	0.04	92.16	7.84

No.	Name	K2O	SiO_2-Calc	CaO	Cl	SnO_2	Na_2O	MgO	Al_2O_3	TiO_2	Cr_2O_3	FeO	MnO	NiO	Total-Calc	100-Total
		[wt.%]	[wt.%]	[wt.%]	[wt.%]	[wt.%]	[wt.%]	[wt.%]	[wt.%]	[wt.%]	[wt.%]	[wt.%]	[wt.%]	[wt.%]	[wt.%]	[wt.%]
57	5-12-04-3-Gl10-1	5.49	71.09	0.79	0.11	0.00	2.32	0.22	11.63	0.12	0.00	0.64	0.07	0.00	92.49	7.51
58	5-12-04-3-Gl10-2	5.71	71.30	0.70	0.08	0.00	2.27	0.06	11.65	0.13	0.00	0.38	0.02	0.00	92.30	7.70
59	5-12-04-3-Gl10-3	5.65	70.96	0.65	0.09	0.00	2.24	0.05	11.67	0.15	0.00	0.38	0.04	0.00	91.88	8.12
60	5-12-04-3-Gl10-4	5.67	72.13	0.67	0.10	0.00	1.73	0.03	11.77	0.12	0.00	0.35	0.05	0.00	92.62	7.38
61	5-12-04-3-Gl10-5	5.54	71.57	0.71	0.12	0.00	2.35	0.05	11.76	0.15	0.00	0.37	0.04	0.00	92.65	7.35
62	5-12-04-3-Gl10-6	5.66	71.11	0.70	0.12	0.00	1.77	0.06	11.82	0.16	0.00	0.39	0.03	0.00	91.80	8.20
63	5-12-04-3-Gl11-1	5.46	72.36	0.69	0.11	0.00	2.49	0.06	11.82	0.12	0.02	0.49	0.03	0.00	93.63	6.37
64	5-12-04-3-Gl11-2	5.52	71.30	0.71	0.13	0.00	1.70	0.10	11.85	0.13	0.01	0.54	0.01	0.00	91.99	8.01
65	5-12-04-3-Gl11-3	5.62	71.79	0.75	0.11	0.00	2.39	0.07	11.83	0.12	0.02	0.49	0.01	0.00	93.19	6.81
66	5-12-04-3-Gl11-4	5.65	72.92	0.67	0.14	0.00	2.35	0.07	11.88	0.15	0.00	0.44	0.02	0.00	94.29	5.71
67	5-12-04-3-Gl11-5	5.41	71.15	0.70	0.13	0.00	2.47	0.06	11.81	0.12	0.02	0.43	0.01	0.00	92.29	7.71
68	5-12-04-3-Gl12-1	5.36	71.42	0.69	0.14	0.00	2.50	0.08	11.71	0.11	0.00	0.61	0.06	0.00	92.67	7.33
69	5-12-04-3-Gl12-2	5.49	70.72	0.66	0.11	0.00	1.60	0.07	11.76	0.12	0.00	0.54	0.05	0.00	91.12	8.88
70	5-12-04-3-Gl12-3	5.30	73.18	0.68	0.14	0.00	2.54	0.11	11.85	0.13	0.01	0.60	0.06	0.01	94.59	5.41
71	5-12-04-3-Gl12-4	5.42	71.38	0.74	0.14	0.00	2.31	0.10	11.77	0.14	0.00	0.60	0.05	0.01	92.65	7.35
72	5-12-04-3-Gl12-5	5.13	71.84	0.73	0.12	0.00	2.53	0.09	11.80	0.13	0.01	0.61	0.05	0.00	93.02	6.98
73	5-12-04-3-Gl13-1	5.63	72.65	0.70	0.10	0.00	1.91	0.06	11.83	0.15	0.00	0.49	0.03	0.02	93.55	6.45
74	5-12-04-3-Gl13-2	5.64	71.79	0.66	0.11	0.00	1.61	0.08	11.74	0.16	0.00	0.58	0.05	0.00	92.41	7.59
75	5-12-04-3-Gl13-3	5.53	71.35	0.68	0.11	0.00	1.87	0.05	11.82	0.14	0.00	0.51	0.05	0.01	92.14	7.86
76	5-12-04-3-Gl13-4	5.53	71.33	0.69	0.11	0.00	2.33	0.06	11.74	0.14	0.00	0.47	0.04	0.01	92.44	7.56
77	5-12-04-3-Gl13-5	5.78	71.97	0.70	0.12	0.00	1.64	0.06	11.70	0.15	0.00	0.39	0.03	0.00	92.55	7.45
78	5-12-04-3-Gl14-1	5.61	71.10	0.66	0.11	0.00	1.99	0.06	11.64	0.14	0.00	0.48	0.04	0.00	91.82	8.18
79	5-12-04-3-Gl14-2	5.58	71.15	0.67	0.11	0.00	1.67	0.06	11.71	0.10	0.00	0.44	0.05	0.02	91.56	8.44
80	5-12-04-3-Gl14-3	5.51	71.17	0.66	0.11	0.00	1.75	0.06	11.64	0.13	0.01	0.43	0.04	0.01	91.52	8.48
81	5-12-04-3-Gl14-4	5.57	72.52	0.68	0.11	0.00	1.83	0.05	11.86	0.13	0.00	0.45	0.03	0.04	93.26	6.74
82	5-12-04-3-Gl14-5	5.52	72.11	0.65	0.09	0.00	2.45	0.05	11.87	0.13	0.00	0.44	0.04	0.00	93.34	6.66
83	5-12-04-3-Gl15-1	5.00	68.16	0.73	0.12	0.00	1.25	0.23	12.30	0.12	0.02	0.88	0.02	0.00	88.83	11.17
84	5-12-04-3-Gl15-2	5.54	71.09	0.69	0.09	0.00	1.99	0.04	11.71	0.15	0.00	0.45	0.05	0.02	91.82	8.18

No.	Name	K2O	SiO_2-Calc	CaO	Cl	SnO_2	Na_2O	MgO	Al_2O_3	TiO_2	Cr_2O_3	FeO	MnO	NiO	Total-Calc	100-Total
		[wt.%]	[wt.%]	[wt.%]	[wt.%]	[wt.%]	[wt.%]	[wt.%]	[wt.%]	[wt.%]	[wt.%]	[wt.%]	[wt.%]	[wt.%]	[wt.%]	[wt.%]
85	5-12-04-3-Gl15-3	5.46	70.79	0.69	0.09	0.00	2.10	0.06	11.73	0.11	0.00	0.44	0.05	0.01	91.52	8.48
86	5-12-04-3-Gl15-4	5.23	70.75	0.69	0.10	0.00	2.54	0.07	11.71	0.12	0.00	0.46	0.07	0.01	91.73	8.27
87	5-12-04-3-Gl15-5	5.40	68.55	0.61	0.11	0.00	1.73	0.08	11.24	0.13	0.00	5.91	0.09	0.02	93.87	6.13
88	5-12-04-3-Gl16-1	5.62	71.06	0.68	0.12	0.00	1.55	0.07	11.64	0.13	0.00	0.51	0.07	0.03	91.46	8.54
89	5-12-04-3-Gl16-2	5.60	70.28	0.69	0.11	0.00	2.37	0.05	11.73	0.12	0.01	0.47	0.03	0.00	91.45	8.55
90	5-12-04-3-Gl16-3	5.18	70.17	0.73	0.12	0.00	2.57	0.05	11.77	0.09	0.00	0.50	0.02	0.01	91.20	8.80
91	5-12-04-3-Gl16-4	5.54	71.52	0.74	0.11	0.00	2.36	0.08	11.70	0.15	0.01	0.52	0.04	0.00	92.77	7.23
92	5-12-04-3-Gl16-5	5.09	71.59	0.72	0.12	0.00	2.63	0.07	11.78	0.12	0.00	0.53	0.04	0.01	92.70	7.30
93	5-12-04-3-Gl17-1	5.51	70.80	0.70	0.10	0.00	1.39	0.15	11.77	0.15	0.00	0.60	0.05	0.01	91.23	8.77
94	5-12-04-3-Gl17-2	5.66	71.78	0.68	0.08	0.00	2.11	0.06	11.83	0.13	0.00	0.42	0.03	0.00	92.77	7.23
95	5-12-04-3-Gl17-3	5.54	70.84	0.78	0.09	0.00	2.48	0.10	11.63	0.16	0.00	0.40	0.03	0.00	92.05	7.95
96	5-12-04-3-Gl17-4	5.66	70.74	0.72	0.10	0.00	1.86	0.10	11.63	0.12	0.01	0.39	0.04	0.00	91.36	8.64
97	5-12-04-3-Gl17-5	5.58	72.50	0.70	0.10	0.00	1.62	0.10	11.68	0.15	0.00	0.52	0.04	0.01	92.99	7.01
98	5-12-04-3-Gl18-1	5.57	71.33	0.64	0.11	0.00	1.90	0.04	11.64	0.12	0.02	0.43	0.05	0.00	91.85	8.15
99	5-12-04-3-Gl18-2	5.65	69.60	0.62	0.12	0.00	1.25	0.19	11.87	0.12	0.00	0.57	0.05	0.00	90.05	9.95
100	5-12-04-3-Gl18-3	5.70	71.90	0.61	0.11	0.00	2.38	0.05	11.65	0.12	0.01	0.48	0.05	0.00	93.06	6.94
101	5-12-04-3-Gl18-4	5.93	71.07	0.59	0.11	0.00	2.20	0.04	11.80	0.15	0.03	0.47	0.05	0.00	92.43	7.57
102	5-12-04-3-Gl18-5	5.59	71.52	0.63	0.12	0.00	2.31	0.10	11.65	0.15	0.00	0.52	0.04	0.00	92.63	7.37
103	5-11-07-3b-Gl1-1	5.64	68.44	0.37	0.10	0.00	2.38	0.10	13.29	0.06	0.00	0.64	0.07	0.00	91.09	8.91
104	5-11-07-3b-Gl1-2	5.16	68.90	0.37	0.09	0.00	2.69	0.09	13.31	0.07	0.01	0.64	0.07	0.00	91.40	8.60
105	5-11-07-3b-Gl1-3	5.00	69.51	0.36	0.10	0.00	2.81	0.09	13.26	0.08	0.02	0.64	0.04	0.00	91.92	8.08
106	5-11-07-3b-Gl1-4	4.50	69.64	0.37	0.11	0.00	3.25	0.10	13.47	0.07	0.00	0.63	0.07	0.01	92.21	7.79
107	5-11-07-3b-Gl1-5	4.48	69.09	0.39	0.12	0.00	3.32	0.08	13.41	0.08	0.00	0.63	0.07	0.01	91.70	8.30
108	5-11-07-3b-Gl1-6	5.39	69.06	0.39	0.10	0.00	2.55	0.07	13.23	0.08	0.01	0.63	0.05	0.00	91.57	8.43
109	5-11-07-3b-Gl2-1	5.54	68.77	0.35	0.09	0.00	2.37	0.09	13.25	0.09	0.01	0.62	0.07	0.00	91.25	8.75
110	5-11-07-3b-Gl2-2	4.58	69.04	0.33	0.09	0.00	3.12	0.09	13.37	0.10	0.00	0.67	0.08	0.00	91.47	8.53
111	5-11-07-3b-Gl2-3	5.71	68.90	0.33	0.09	0.00	1.94	0.12	13.24	0.08	0.00	0.70	0.05	0.00	91.16	8.84

No.	Name	K2O	SiO_2-Calc	CaO	Cl	SnO_2	Na_2O	MgO	Al_2O_3	TiO_2	Cr_2O_3	FeO	MnO	NiO	Total-Calc	100-Total
		[wt.%]	[wt.%]	[wt.%]	[wt.%]	[wt.%]	[wt.%]	[wt.%]	[wt.%]	[wt.%]	[wt.%]	[wt.%]	[wt.%]	[wt.%]	[wt.%]	[wt.%]
112	5-11-07-3b-Gl2-4	5.52	68.89	0.37	0.09	0.00	2.63	0.11	13.30	0.10	0.00	0.66	0.09	0.02	91.78	8.22
113	5-11-07-3b-Gl2-5	5.91	68.09	0.35	0.11	0.00	1.61	0.08	13.07	0.12	0.00	0.61	0.06	0.00	90.01	9.99
114	5-11-07-3b-Gl2-6	5.70	68.49	0.34	0.10	0.00	2.08	0.09	13.18	0.13	0.01	0.64	0.06	0.00	90.83	9.17
115	5-11-07-3b-Gl2-7	5.71	68.07	0.33	0.10	0.00	2.23	0.08	13.22	0.13	0.00	0.62	0.09	0.00	90.59	9.41
116	5-11-07-3b-Gl2-8	5.92	68.67	0.38	0.12	0.00	2.03	0.11	13.25	0.10	0.02	0.64	0.08	0.01	91.33	8.67
117	5-11-07-3b-Gl3-1	4.88	67.90	0.35	0.11	0.00	2.95	0.09	13.20	0.09	0.00	0.64	0.06	0.00	90.27	9.73
118	5-11-07-3b-Gl3-2	4.71	69.38	0.34	0.11	0.00	3.14	0.07	13.33	0.08	0.00	0.66	0.09	0.02	91.93	8.07
119	5-11-07-3b-Gl3-3	4.76	68.07	0.35	0.09	0.00	3.07	0.09	13.25	0.10	0.00	0.66	0.08	0.00	90.52	9.48
120	5-11-07-3b-Gl3-4	5.65	68.38	0.36	0.10	0.00	2.29	0.09	13.37	0.07	0.01	0.67	0.11	0.00	91.09	8.91
121	5-11-07-3b-Gl3-5	5.44	68.86	0.34	0.09	0.00	2.63	0.11	13.41	0.07	0.00	0.63	0.08	0.01	91.67	8.33
122	5-11-07-3b-Gl3-6	5.93	68.85	0.35	0.11	0.00	2.06	0.09	13.24	0.07	0.02	0.61	0.08	0.03	91.44	8.56
123	5-11-07-3b-Gl3-7	5.73	68.42	0.35	0.10	0.00	2.50	0.08	13.24	0.08	0.01	0.64	0.04	0.00	91.20	8.80
124	5-11-07-3b-Gl4-1	4.45	68.75	0.37	0.09	0.00	3.26	0.10	13.30	0.08	0.00	0.60	0.06	0.00	91.06	8.94
125	5-11-07-3b-Gl4-2	4.70	69.73	0.38	0.09	0.00	3.17	0.10	13.39	0.09	0.00	0.65	0.08	0.00	92.39	7.61
126	5-11-07-3b-Gl4-3	4.41	69.13	0.36	0.08	0.00	3.33	0.09	13.48	0.08	0.00	0.63	0.06	0.00	91.65	8.35
127	5-11-07-3b-Gl4-4	5.71	69.66	0.36	0.11	0.00	2.23	0.09	13.33	0.07	0.01	0.67	0.05	0.00	92.28	7.72
128	5-11-07-3b-Gl4-5	4.54	68.44	0.35	0.11	0.00	3.20	0.08	13.41	0.06	0.01	0.68	0.07	0.00	90.95	9.05
129	5-11-07-3b-Gl4-6	5.79	68.19	0.39	0.11	0.00	1.92	0.08	13.31	0.07	0.00	0.63	0.08	0.00	90.56	9.44
130	5-11-07-3b-Gl4-7	5.15	67.00	0.35	0.08	0.00	2.70	0.09	13.21	0.13	0.01	0.67	0.07	0.00	89.46	10.54
131	5-11-07-3b-Gl4-8	4.94	68.47	0.35	0.13	0.00	2.89	0.09	13.22	0.06	0.02	0.64	0.08	0.00	90.88	9.12
132	5-11-07-3b-Gl4-9	5.65	68.73	0.35	0.11	0.00	2.59	0.10	13.24	0.09	0.00	0.65	0.08	0.00	91.59	8.41
133	5-11-07-3b-Gl4-10	4.48	68.73	0.36	0.09	0.00	3.25	0.09	13.39	0.10	0.00	0.68	0.07	0.00	91.24	8.76
134	5-11-07-3b-Gl5-1	4.72	69.68	0.36	0.11	0.00	3.08	0.10	13.28	0.09	0.00	0.65	0.07	0.01	92.14	7.86
135	5-11-07-3b-Gl5-2	5.21	68.13	0.40	0.10	0.00	2.70	0.06	13.28	0.09	0.00	0.65	0.06	0.00	90.69	9.31
136	5-11-07-3b-Gl5-3	4.45	68.80	0.38	0.09	0.00	3.23	0.10	13.39	0.08	0.00	0.65	0.07	0.02	91.25	8.75
137	5-11-07-3b-Gl5-4	5.54	68.09	0.37	0.12	0.00	2.27	0.09	13.18	0.07	0.01	0.64	0.08	0.00	90.44	9.56
138	5-11-07-3b-Gl5-5	4.65	69.16	0.35	0.11	0.00	3.27	0.08	13.34	0.06	0.02	0.61	0.06	0.03	91.74	8.26
139	5-11-07-3b-Gl5-6	5.37	68.35	0.37	0.09	0.00	2.58	0.09	13.37	0.08	0.00	0.64	0.06	0.00	90.99	9.01

No.	Name	K2O	SiO_2-Calc	CaO	Cl	SnO_2	Na_2O	MgO	Al_2O_3	TiO_2	Cr_2O_3	FeO	MnO	NiO	Total-Calc	100-Total
		[wt.%]	[wt.%]	[wt.%]	[wt.%]	[wt.%]	[wt.%]	[wt.%]	[wt.%]	[wt.%]	[wt.%]	[wt.%]	[wt.%]	[wt.%]	[wt.%]	[wt.%]
140	5-11-07-3b-Gl5-7	5.71	69.29	0.37	0.11	0.00	2.08	0.11	13.04	0.09	0.00	0.63	0.06	0.00	91.48	8.52
141	5-11-07-3b-Gl5-8	5.90	69.06	0.37	0.09	0.00	1.71	0.10	13.06	0.07	0.02	0.64	0.07	0.00	91.06	8.94
142	5-11-07-3b-Gl6-1	5.69	68.08	0.38	0.10	0.00	1.89	0.09	12.99	0.06	0.01	0.63	0.04	0.02	89.96	10.04
143	5-11-07-3b-Gl6-2	5.13	68.72	0.37	0.11	0.00	2.70	0.07	13.34	0.09	0.00	0.62	0.10	0.00	91.24	8.76
144	5-11-07-3b-Gl6-3	4.85	69.11	0.33	0.10	0.00	2.84	0.08	13.22	0.09	0.00	0.64	0.07	0.00	91.33	8.67
145	5-11-07-3b-Gl6-4	4.41	69.69	0.36	0.10	0.00	3.25	0.10	13.49	0.07	0.02	0.65	0.05	0.00	92.18	7.82
146	5-11-07-3b-Gl6-5	5.93	67.87	0.36	0.10	0.00	1.90	0.10	13.19	0.08	0.00	0.59	0.08	0.01	90.19	9.81
147	5-11-07-3b-Gl7-1	4.50	69.23	0.36	0.11	0.00	3.24	0.09	13.40	0.08	0.01	0.65	0.08	0.00	91.75	8.25
148	5-11-07-3b-Gl7-2	4.44	69.57	0.37	0.11	0.00	3.30	0.09	13.49	0.09	0.00	0.65	0.07	0.00	92.19	7.81
149	5-11-07-3b-Gl7-3	5.38	68.47	0.36	0.11	0.00	2.46	0.09	13.32	0.04	0.03	0.66	0.07	0.00	90.99	9.01
150	5-11-07-3b-Gl7-4	4.74	70.36	0.35	0.13	0.00	3.12	0.08	13.37	0.07	0.01	0.67	0.07	0.00	92.98	7.02
151	5-11-07-3b-Gl7-5	5.31	68.50	0.36	0.10	0.00	2.61	0.09	13.23	0.10	0.02	0.63	0.04	0.01	90.99	9.01
152	5-11-07-3b-Gl7-6	4.53	69.03	0.36	0.09	0.00	3.26	0.10	13.27	0.11	0.00	0.69	0.05	0.00	91.49	8.51
153	5-11-07-3b-Gl7-7	5.76	68.30	0.38	0.12	0.00	1.94	0.08	13.11	0.08	0.00	0.63	0.07	0.00	90.46	9.54
154	5-11-07-3b-Gl8-1	5.33	69.01	0.37	0.10	0.00	2.76	0.08	13.32	0.07	0.00	0.62	0.09	0.01	91.75	8.25
155	5-11-07-3b-Gl8-2	5.65	68.87	0.37	0.10	0.00	2.06	0.10	13.20	0.07	0.02	0.68	0.09	0.01	91.19	8.81
156	5-11-07-3b-Gl8-3	4.70	68.24	0.38	0.11	0.00	3.07	0.10	13.37	0.08	0.02	0.68	0.09	0.00	90.84	9.16
157	5-11-07-3b-Gl8-4	4.68	68.85	0.34	0.11	0.00	3.09	0.09	13.31	0.07	0.00	0.62	0.07	0.00	91.21	8.79
158	5-11-07-3b-Gl8-5	5.91	68.01	0.33	0.10	0.00	1.84	0.08	13.20	0.09	0.00	0.67	0.06	0.00	90.29	9.71
159	5-11-07-3b-Gl8-6	5.51	68.69	0.37	0.09	0.00	2.41	0.09	13.18	0.08	0.00	0.67	0.07	0.00	91.16	8.84
160	5-11-07-3b-Gl8-7	4.70	68.27	0.34	0.10	0.00	3.14	0.08	13.43	0.08	0.01	0.66	0.11	0.00	90.93	9.07
161	5-11-07-3b-Gl9-1	5.29	69.13	0.35	0.10	0.00	2.49	0.09	13.33	0.08	0.01	0.64	0.08	0.02	91.60	8.40
162	5-11-07-3b-Gl9-2	5.56	66.87	0.38	0.12	0.00	2.01	0.10	13.18	0.07	0.00	0.72	0.06	0.00	89.07	10.93
163	5-11-07-3b-Gl9-3	4.99	69.00	0.37	0.10	0.00	2.86	0.08	13.22	0.11	0.00	0.67	0.08	0.00	91.48	8.52
164	5-11-07-3b-Gl9-4	4.81	69.51	0.35	0.10	0.00	3.06	0.10	13.33	0.08	0.00	0.64	0.07	0.01	92.05	7.95
165	5-11-07-3b-Gl9-5	4.68	69.42	0.35	0.11	0.00	3.14	0.10	13.33	0.07	0.03	0.63	0.06	0.00	91.92	8.08
166	5-11-07-3b-Gl9-6	5.74	69.18	0.35	0.11	0.00	2.36	0.08	13.37	0.10	0.02	0.62	0.06	0.01	92.00	8.00
167	5-11-07-3b-Gl9-7	4.87	69.27	0.39	0.10	0.00	2.90	0.09	13.22	0.09	0.02	0.63	0.07	0.00	91.64	8.36

No.	Name	K2O	SiO_2-Calc	CaO	Cl	SnO_2	Na_2O	MgO	Al_2O_3	TiO_2	Cr_2O_3	FeO	MnO	NiO	Total-Calc	100-Total
		[wt.%]	[wt.%]	[wt.%]	[wt.%]	[wt.%]	[wt.%]	[wt.%]	[wt.%]	[wt.%]	[wt.%]	[wt.%]	[wt.%]	[wt.%]	[wt.%]	[wt.%]
168	5-11-07-3b-Gl10-1	5.17	69.51	0.35	0.10	0.00	2.74	0.08	13.34	0.07	0.02	0.63	0.07	0.00	92.09	7.91
169	5-11-07-3b-Gl10-2	4.58	70.48	0.35	0.11	0.00	3.09	0.09	13.39	0.08	0.00	0.61	0.07	0.01	92.87	7.13
170	5-11-07-3b-Gl10-3	4.51	69.59	0.36	0.09	0.00	3.14	0.09	13.37	0.09	0.02	0.67	0.10	0.03	92.06	7.94
171	5-11-07-3b-Gl10-4	4.60	71.04	0.37	0.10	0.00	3.25	0.10	13.40	0.08	0.00	0.63	0.08	0.02	93.66	6.34
172	5-11-07-3b-Gl10-5	4.36	68.95	0.40	0.10	0.00	3.28	0.08	13.32	0.08	0.01	0.62	0.07	0.01	91.27	8.73
173	5-11-07-3b-Gl10-6	4.44	69.20	0.36	0.10	0.00	3.29	0.10	13.34	0.06	0.02	0.62	0.08	0.00	91.61	8.39
174	5-11-07-3b-Gl11-1	4.74	70.83	0.35	0.11	0.00	3.10	0.10	13.38	0.09	0.02	0.65	0.08	0.00	93.43	6.57
175	5-11-07-3b-Gl11-2	4.54	68.80	0.35	0.10	0.00	3.12	0.07	13.41	0.09	0.00	0.63	0.07	0.01	91.19	8.81
176	5-11-07-3b-Gl11-3	5.36	69.42	0.37	0.10	0.00	2.51	0.07	13.26	0.11	0.01	0.65	0.09	0.01	91.95	8.05
177	5-11-07-3b-Gl11-4	5.02	69.93	0.37	0.11	0.00	3.00	0.09	13.38	0.09	0.00	0.66	0.06	0.00	92.70	7.30
178	5-11-07-3b-Gl11-5	4.50	69.28	0.35	0.11	0.00	3.31	0.08	13.30	0.09	0.00	0.67	0.10	0.00	91.79	8.21
179	5-11-07-3b-Gl11-6	4.53	69.00	0.34	0.09	0.00	3.17	0.09	13.43	0.10	0.00	0.71	0.06	0.00	91.50	8.50
180	5-11-07-3b-Gl11-7	5.86	69.56	0.35	0.11	0.00	1.79	0.09	13.12	0.12	0.00	0.63	0.09	0.01	91.73	8.27
181	5-11-07-3b-Gl12-1	5.14	68.80	0.37	0.10	0.00	2.72	0.09	13.31	0.07	0.00	0.60	0.08	0.03	91.31	8.69
182	5-11-07-3b-Gl12-2	5.46	68.79	0.37	0.10	0.00	2.71	0.07	13.31	0.09	0.01	0.63	0.07	0.01	91.63	8.37
183	5-11-07-3b-Gl12-3	4.85	70.25	0.40	0.10	0.00	3.05	0.08	13.33	0.09	0.00	0.62	0.09	0.00	92.87	7.13
184	5-11-07-3b-Gl12-4	4.50	69.66	0.38	0.10	0.00	3.18	0.10	13.39	0.12	0.00	0.65	0.08	0.02	92.18	7.82
185	10-12-20b-Gl1-1	4.81	74.27	0.61	0.11	0.00	2.97	0.06	11.95	0.06	0.01	0.54	0.09	0.01	95.50	4.50
186	10-12-20b-Gl1-2	4.94	75.65	0.61	0.13	0.00	3.27	0.05	12.16	0.07	0.00	0.58	0.07	0.00	97.52	2.48
187	10-12-20b-Gl1-3	4.93	75.87	0.60	0.13	0.00	3.30	0.05	12.13	0.08	0.00	0.58	0.09	0.00	97.76	2.24
188	10-12-20b-Gl1-4	5.05	76.23	0.59	0.13	0.00	3.31	0.05	12.15	0.06	0.00	0.60	0.08	0.00	98.26	1.74
189	10-12-20b-Gl1-5	4.88	75.33	0.60	0.14	0.00	3.31	0.05	12.24	0.04	0.00	0.59	0.08	0.01	97.29	2.71
190	10-12-20b-Gl1-6	4.85	75.64	0.61	0.12	0.00	3.35	0.05	12.22	0.07	0.00	0.60	0.09	0.02	97.62	2.38
191	10-12-20b-Gl1-7	4.92	76.31	0.55	0.12	0.00	3.29	0.04	12.29	0.06	0.02	0.56	0.08	0.01	98.24	1.76
192	10-12-20b-Gl2-1	4.95	74.28	0.61	0.14	0.00	2.97	0.04	11.92	0.10	0.00	0.54	0.10	0.00	95.62	4.38
193	10-12-20b-Gl2-2	4.69	73.40	0.60	0.13	0.00	3.03	0.04	11.91	0.07	0.00	0.56	0.07	0.00	94.51	5.49
194	10-12-20b-Gl2-3	4.74	73.39	0.61	0.13	0.00	3.08	0.06	11.98	0.07	0.00	0.52	0.08	0.00	94.67	5.33

No.	Name	K2O	SiO_2-Calc	CaO	Cl	SnO_2	Na_2O	MgO	Al_2O_3	TiO_2	Cr_2O_3	FeO	MnO	NiO	Total-Calc	100-Total
		[wt.%]	[wt.%]	[wt.%]	[wt.%]	[wt.%]	[wt.%]	[wt.%]	[wt.%]	[wt.%]	[wt.%]	[wt.%]	[wt.%]	[wt.%]	[wt.%]	[wt.%]
195	10-12-20b-Gl2-4	5.01	74.11	0.62	0.13	0.00	3.04	0.04	11.89	0.06	0.02	0.55	0.09	0.00	95.56	4.44
196	10-12-20b-Gl2-5	4.83	72.60	0.56	0.12	0.00	3.04	0.04	11.92	0.06	0.00	0.48	0.08	0.00	93.73	6.27
197	10-12-20b-Gl3-1	2.69	70.67	1.61	0.05	0.00	5.76	0.03	15.11	0.05	0.00	0.36	0.04	0.00	96.36	3.64
198	10-12-20b-Gl3-2	4.60	73.86	0.59	0.12	0.00	3.18	0.05	12.05	0.05	0.00	0.44	0.08	0.00	95.02	4.98
199	10-12-20b-Gl3-3	4.86	74.28	0.57	0.14	0.00	3.31	0.04	12.26	0.04	0.00	0.54	0.08	0.00	96.12	3.88
200	10-12-20b-Gl3-4	5.04	74.52	0.61	0.12	0.00	3.30	0.04	12.21	0.05	0.00	0.55	0.06	0.02	96.51	3.49
201	10-12-20b-Gl3-5	4.74	72.67	0.61	0.12	0.00	3.16	0.06	11.69	0.04	0.00	0.57	0.10	0.00	93.75	6.25
202	10-12-20b-Gl4-1	4.62	73.36	0.56	0.11	0.00	3.03	0.05	11.97	0.05	0.01	0.53	0.10	0.00	94.40	5.60
203	10-12-20b-Gl4-2	4.77	72.44	0.58	0.13	0.00	3.07	0.05	11.78	0.06	0.00	0.57	0.09	0.00	93.53	6.47
204	10-12-20b-Gl4-3	4.93	76.09	0.60	0.12	0.00	3.35	0.05	12.32	0.05	0.02	0.60	0.08	0.01	98.22	1.78
205	10-12-20b-Gl4-4	4.82	75.32	0.60	0.13	0.00	3.29	0.04	12.20	0.06	0.03	0.61	0.08	0.03	97.21	2.79
206	10-12-20b-Gl4-5	4.78	74.83	0.59	0.14	0.00	3.21	0.05	12.08	0.06	0.01	0.60	0.09	0.00	96.44	3.56
207	10-12-20b-Gl5-1	4.84	74.43	0.59	0.12	0.00	3.22	0.06	12.03	0.03	0.01	0.58	0.05	0.01	95.95	4.05
208	10-12-20b-Gl5-2	4.75	73.93	0.57	0.12	0.00	3.08	0.06	11.98	0.05	0.00	0.58	0.12	0.00	95.23	4.77
209	10-12-20b-Gl5-3	4.86	74.66	0.55	0.14	0.00	3.29	0.05	12.27	0.05	0.01	0.56	0.08	0.00	96.53	3.47
210	10-12-20b-Gl5-4	4.89	74.21	0.61	0.11	0.00	3.35	0.05	12.20	0.09	0.01	0.58	0.08	0.00	96.18	3.82
211	10-12-20b-Gl5-5	4.94	74.55	0.59	0.15	0.00	3.27	0.05	12.17	0.06	0.01	0.60	0.10	0.00	96.49	3.51
212	10-12-20b-Gl5b-1	4.88	71.92	0.53	0.12	0.00	2.95	0.06	11.76	0.03	0.00	0.56	0.09	0.00	92.88	7.12
213	10-12-20b-Gl5b-2	4.90	74.27	0.56	0.10	0.00	3.27	0.03	12.09	0.05	0.01	0.58	0.08	0.00	95.92	4.08
214	10-12-20b-Gl5b-3	4.98	76.11	0.57	0.13	0.00	3.30	0.05	12.14	0.05	0.00	0.56	0.07	0.01	97.97	2.03
215	10-12-20b-Gl5b-4	4.95	76.27	0.58	0.13	0.00	3.18	0.05	12.22	0.06	0.01	0.53	0.10	0.00	98.08	1.92
216	10-12-20b-Gl5b-5	4.94	74.59	0.58	0.12	0.00	3.37	0.05	12.28	0.04	0.01	0.59	0.07	0.00	96.64	3.36
217	10-12-20b-Gl5c-1	4.75	72.86	0.58	0.11	0.00	3.03	0.05	11.94	0.07	0.00	0.57	0.08	0.00	94.04	5.96
218	10-12-20b-Gl5c-2	4.76	74.89	0.57	0.12	0.00	3.15	0.05	12.14	0.05	0.00	0.52	0.08	0.00	96.33	3.67
219	10-12-20b-Gl5c-3	4.84	76.22	0.58	0.12	0.00	3.22	0.05	12.20	0.05	0.00	0.54	0.08	0.03	97.92	2.08
220	10-12-20b-Gl5c-4	4.88	73.83	0.58	0.13	0.00	3.19	0.05	12.10	0.07	0.01	0.58	0.08	0.00	95.49	4.51
221	10-12-20b-Gl5c-5	4.96	75.77	0.58	0.13	0.00	3.38	0.06	12.25	0.06	0.02	0.59	0.08	0.00	97.86	2.14
222	10-12-20b-Gl6a-1	4.69	72.61	0.56	0.11	0.00	3.11	0.06	11.89	0.07	0.00	0.48	0.09	0.02	93.67	6.33

No.	Name	K2O	SiO_2-Calc	CaO	Cl	SnO_2	Na_2O	MgO	Al_2O_3	TiO_2	Cr_2O_3	FeO	MnO	NiO	Total-Calc	100-Total
		[wt.%]	[wt.%]	[wt.%]	[wt.%]	[wt.%]	[wt.%]	[wt.%]	[wt.%]	[wt.%]	[wt.%]	[wt.%]	[wt.%]	[wt.%]	[wt.%]	[wt.%]
223	10-12-20b-Gl6a-2	4.67	72.97	0.59	0.12	0.00	3.12	0.05	11.92	0.04	0.00	0.48	0.08	0.00	94.03	5.97
224	10-12-20b-Gl6a-3	4.77	74.53	0.59	0.13	0.00	3.18	0.05	12.07	0.06	0.00	0.57	0.10	0.00	96.05	3.95
225	10-12-20b-Gl6a-4	4.84	74.05	0.56	0.12	0.00	3.28	0.05	12.09	0.08	0.00	0.57	0.05	0.00	95.70	4.30
226	10-12-20b-Gl6a-5	4.98	74.37	0.60	0.14	0.00	3.30	0.05	12.24	0.05	0.02	0.57	0.08	0.00	96.37	3.63
227	10-12-20b-Gl6a-6	4.90	75.52	0.57	0.13	0.00	3.35	0.05	12.22	0.08	0.00	0.57	0.09	0.00	97.48	2.52
228	10-12-20b-Gl6b-1	4.70	72.95	0.54	0.10	0.00	3.14	0.04	11.90	0.05	0.00	0.46	0.05	0.00	93.93	6.08
229	10-12-20b-Gl6b-2	4.78	73.36	0.58	0.13	0.00	3.06	0.07	11.83	0.07	0.01	0.59	0.06	0.02	94.54	5.46
230	10-12-20b-Gl6b-3	4.82	74.33	0.52	0.11	0.00	3.13	0.05	11.98	0.06	0.00	0.49	0.10	0.00	95.61	4.39
231	10-12-20b-Gl6b-4	4.93	74.75	0.56	0.11	0.00	3.28	0.04	12.27	0.07	0.00	0.54	0.09	0.00	96.63	3.37
232	10-12-20b-Gl6b-5	4.94	74.70	0.56	0.13	0.00	3.28	0.04	12.23	0.06	0.00	0.57	0.07	0.00	96.57	3.43
233	10-12-20b-Gl6b-6	4.89	75.73	0.55	0.13	0.00	3.27	0.05	12.21	0.06	0.00	0.54	0.09	0.00	97.53	2.47
234	10-12-20b-Gl7-1	4.72	74.86	0.57	0.11	0.00	3.12	0.06	11.83	0.06	0.00	0.50	0.08	0.00	95.90	4.10
235	10-12-20b-Gl7-2	4.74	73.78	0.54	0.12	0.00	3.05	0.05	11.84	0.06	0.00	0.53	0.07	0.00	94.77	5.23
236	10-12-20b-Gl7-3	4.82	74.96	0.59	0.11	0.00	3.13	0.03	12.09	0.03	0.00	0.55	0.07	0.02	96.40	3.60
237	10-12-20b-Gl7-4	4.95	75.71	0.59	0.16	0.00	3.34	0.05	12.30	0.04	0.00	0.59	0.08	0.00	97.82	2.18
238	10-12-20b-Gl7-5	5.04	75.67	0.61	0.13	0.00	3.35	0.06	12.17	0.06	0.00	0.61	0.08	0.02	97.78	2.22
239	10-12-20b-Gl8-1	5.24	72.65	0.54	0.13	0.00	2.78	0.04	11.80	0.08	0.01	0.54	0.10	0.00	93.90	6.10
240	10-12-20b-Gl8-2	5.09	72.70	0.58	0.15	0.00	2.89	0.07	11.77	0.06	0.01	0.55	0.10	0.00	93.95	6.05
241	10-12-20b-Gl8-3	4.88	74.85	0.59	0.12	0.00	3.00	0.05	12.02	0.06	0.00	0.48	0.08	0.00	96.12	3.88
242	10-12-20b-Gl8-4	4.79	73.88	0.56	0.14	0.00	3.07	0.06	11.91	0.05	0.00	0.54	0.07	0.02	95.09	4.91
243	10-12-20b-Gl8-5	4.79	74.57	0.59	0.12	0.00	3.08	0.06	12.04	0.04	0.00	0.53	0.08	0.00	95.90	4.10
244	10-12-20b-Gl9-1	4.79	73.21	0.59	0.11	0.00	3.03	0.04	11.92	0.05	0.00	0.52	0.06	0.00	94.32	5.68
245	10-12-20b-Gl9-2	4.79	74.45	0.58	0.13	0.00	3.03	0.06	11.99	0.03	0.00	0.49	0.06	0.00	95.60	4.40
246	10-12-20b-Gl9-3	4.91	76.05	0.62	0.12	0.00	3.25	0.05	12.24	0.06	0.03	0.59	0.11	0.01	98.03	1.97
247	10-12-20b-Gl9-4	4.86	75.53	0.61	0.11	0.00	3.34	0.06	12.25	0.04	0.00	0.56	0.07	0.01	97.44	2.56
248	10-12-20b-Gl9-5	4.98	74.67	0.61	0.11	0.00	3.31	0.05	12.24	0.05	0.00	0.57	0.07	0.01	96.67	3.33
249	10-12-20b-Gl10-1	4.83	72.25	0.55	0.12	0.00	3.03	0.05	11.97	0.06	0.01	0.39	0.07	0.00	93.31	6.69
250	10-12-20b-Gl10-2	4.67	71.41	0.58	0.13	0.00	3.04	0.04	11.88	0.07	0.03	0.54	0.05	0.02	92.47	7.53

No.	Name	K2O	SiO_2-Calc	CaO	Cl	SnO_2	Na_2O	MgO	Al_2O_3	TiO_2	Cr_2O_3	FeO	MnO	NiO	Total-Calc	100-Total
		[wt.%]	[wt.%]	[wt.%]	[wt.%]	[wt.%]	[wt.%]	[wt.%]	[wt.%]	[wt.%]	[wt.%]	[wt.%]	[wt.%]	[wt.%]	[wt.%]	[wt.%]
251	10-12-20b-Gl10-3	4.74	72.03	0.62	0.14	0.00	3.24	0.03	11.86	0.06	0.01	0.57	0.10	0.03	93.43	6.57
252	10-12-20b-Gl10-4	4.87	73.97	0.56	0.12	0.00	3.21	0.05	12.19	0.04	0.00	0.61	0.07	0.00	95.70	4.30
253	10-12-20b-Gl10-5	4.82	73.51	0.59	0.11	0.00	3.16	0.05	11.97	0.02	0.02	0.57	0.06	0.01	94.90	5.10
254	10-12-20b-Gl11-1	5.15	73.79	0.53	0.06	0.00	2.82	0.05	11.81	0.07	0.01	0.33	0.08	0.04	94.73	5.27
255	10-12-20b-Gl11-2	5.14	71.49	0.59	0.09	0.00	2.87	0.05	11.94	0.07	0.00	0.51	0.07	0.01	92.82	7.18
256	10-12-20b-Gl11-3	4.86	72.00	0.61	0.07	0.00	3.04	0.04	11.91	0.04	0.00	0.47	0.08	0.00	93.13	6.87
257	10-12-20b-Gl11-4	4.77	73.06	0.62	0.11	0.00	3.07	0.05	11.98	0.03	0.00	0.58	0.09	0.00	94.35	5.65
258	10-12-20b-Gl11-5	4.84	71.98	0.59	0.15	0.00	3.26	0.05	11.83	0.04	0.00	0.61	0.10	0.00	93.44	6.56
259	10-12-20b-Gl11-6	4.89	74.11	0.61	0.11	0.00	3.29	0.05	12.15	0.08	0.00	0.55	0.10	0.00	95.94	4.06
260	10-12-20b-Gl11-7	4.78	73.45	0.62	0.11	0.00	3.24	0.04	12.05	0.03	0.00	0.55	0.09	0.00	94.97	5.03
261	10-12-20b-Gl12-1	4.63	72.98	0.58	0.12	0.00	3.10	0.05	11.92	0.06	0.02	0.61	0.06	0.00	94.11	5.89
262	10-12-20b-Gl12-2	4.96	70.85	0.59	0.14	0.00	2.80	0.05	11.70	0.04	0.00	0.57	0.07	0.00	91.76	8.24
263	10-12-20b-Gl12-3	4.86	72.54	0.58	0.13	0.00	2.99	0.06	12.02	0.03	0.01	0.60	0.07	0.00	93.89	6.11
264	10-12-20b-Gl12-4	4.88	74.23	0.58	0.12	0.00	3.09	0.05	12.03	0.06	0.03	0.56	0.09	0.01	95.73	4.27
265	10-12-20b-Gl12-5	4.77	73.76	0.58	0.14	0.00	3.05	0.06	12.07	0.07	0.00	0.55	0.09	0.00	95.11	4.89
266	10-12-20b-Gl12-6	4.78	73.40	0.62	0.12	0.00	3.25	0.05	11.98	0.06	0.00	0.50	0.08	0.02	94.85	5.15
267	10-12-20b-Gl13-1	4.72	72.69	0.57	0.11	0.00	3.18	0.05	11.82	0.06	0.00	0.55	0.07	0.00	93.81	6.19
268	10-12-20b-Gl13-2	4.73	71.33	0.59	0.11	0.00	2.99	0.05	11.97	0.06	0.01	0.56	0.07	0.01	92.48	7.52
269	10-12-20b-Gl13-3	4.74	72.72	0.60	0.12	0.00	3.10	0.06	11.95	0.05	0.02	0.54	0.07	0.00	93.95	6.05
270	10-12-20b-Gl13-4	4.87	75.11	0.59	0.13	0.00	3.33	0.06	12.29	0.07	0.01	0.60	0.07	0.01	97.12	2.88
271	10-12-20b-Gl13-5	4.61	72.10	0.58	0.13	0.00	3.03	0.04	11.64	0.07	0.00	0.51	0.10	0.00	92.80	7.20
272	10-12-20b-Gl13-6	4.86	73.51	0.61	0.13	0.00	3.35	0.06	12.34	0.04	0.01	0.56	0.10	0.01	95.59	4.41
273	10-12-20b-Gl13-7	4.93	74.48	0.61	0.13	0.00	3.35	0.04	12.23	0.06	0.00	0.55	0.08	0.00	96.46	3.54
274	10-12-20b-Gl14-1	4.76	73.02	0.59	0.12	0.00	2.97	0.04	11.87	0.10	0.01	0.60	0.09	0.00	94.17	5.83
275	10-12-20b-Gl14-2	4.74	72.63	0.58	0.12	0.00	3.08	0.05	12.03	0.04	0.01	0.55	0.09	0.00	93.93	6.07
276	10-12-20b-Gl14-3	4.77	74.30	0.58	0.11	0.00	3.25	0.05	12.01	0.07	0.00	0.54	0.08	0.00	95.76	4.24
277	10-12-20b-Gl14-4	4.92	74.44	0.56	0.13	0.00	3.31	0.04	12.19	0.07	0.00	0.56	0.07	0.03	96.31	3.69

No.	Name	K2O [wt.%]	SiO_2-Calc [wt.%]	CaO [wt.%]	Cl [wt.%]	SnO_2 [wt.%]	Na_2O [wt.%]	MgO [wt.%]	Al_2O_3 [wt.%]	TiO_2 [wt.%]	Cr_2O_3 [wt.%]	FeO [wt.%]	MnO [wt.%]	NiO [wt.%]	Total-Calc [wt.%]	100-Total [wt.%]
278	10-12-20b-Gl14-5	4.91	74.01	0.59	0.13	0.00	3.30	0.06	12.24	0.08	0.03	0.58	0.10	0.01	96.04	3.96
all	mean	5.16	71.73	0.57	0.11	0.00	2.66	0.07	12.32	0.09	0.01	0.59	0.06	0.01	93.38	93.38
5-12-04-3	mean	5.50	71.91	0.71	0.11	0.00	2.11	0.09	11.76	0.13	0.00	0.59	0.04	0.01	92.97	92.97
5-11-07-3b	mean	5.10	68.94	0.36	0.10	0.00	2.72	0.09	13.30	0.08	0.01	0.64	0.07	0.01	91.43	91.43
10-12-20b	mean	4.83	73.96	0.59	0.12	0.00	3.19	0.05	12.08	0.06	0.01	0.55	0.08	0.01	95.51	95.51

8.5. Stochastic image analysis

	LAp	SVp	LAs	SVs	LAu	SVu	LAt	SVges	LAt_ber	ratio p	ratio s	ratio u
5_12_04	0.76	0.97	2.61	3.32	0.00	0.00	3.26	4.15	3.37	0.23	0.80	0.00
1_8_97_1	0.38	0.48	1.04	1.32	0.02	0.03	1.41	1.80	1.44	0.27	0.74	0.01
1_8_97_3b	0.37	0.47	1.39	1.77	0.00	0.00	1.82	2.32	1.76	0.20	0.76	0.00
10_12_20_b	1.11	1.41	1.27	1.62	0.37	0.47	2.66	3.39	2.75	0.42	0.48	0.14
1_8_97_7b	0.34	0.43	1.28	1.63	0.02	0.03	1.60	2.04	1.64	0.21	0.80	0.01
3_8_97_1	0.44	0.56	1.53	1.95	0.00	0.00	1.92	2.44	1.97	0.23	0.80	0.00
5_11_07_3b	0.37	0.47	1.14	1.45	0.00	0.00	1.49	1.90	1.51	0.25	0.77	0.00
6_4_01_1a	0.60	0.76	1.08	1.38	0.02	0.03	1.67	2.13	1.70	0.36	0.65	0.01
8 Ta PS	0.27	0.34	0.38	0.48	0.00	0.00	0.62	0.79	0.65	0.44	0.61	0.00
9_9_01	0.05	0.06	0.75	0.95	0.00	0.00	0.80	1.02	0.80	0.06	0.94	0.00
10_12_08	0.68	0.87	1.39	1.77	0.18	0.23	2.19	2.79	2.25	0.31	0.63	0.08
26_6	0.00	0.00	1.90	2.42	0.00	0.00	1.90	2.42	1.90	0.00	1.00	0.00
27_6_14_1e	0.66	0.84	2.07	2.64	0.00	0.00	2.60	3.31	2.73	0.25	0.80	0.00
44,20,I	0.65	0.83	1.84	2.34	0.05	0.06	2.49	3.17	2.54	0.26	0.74	0.02
44,20,II	0.34	0.43	1.08	1.38	0.03	0.04	1.42	1.81	1.45	0.24	0.76	0.02
44,20,III	0.80	1.02	2.26	2.88	0.00	0.00	2.97	3.78	3.06	0.27	0.76	0.00
11497.00	0.14	0.18	1.02	1.30	0.00	0.00	1.14	1.45	1.16	0.12	0.89	0.00
11510.00	0.16	0.20	1.08	1.38	0.07	0.09	1.29	1.64	1.31	0.12	0.84	0.05
C28_01	0.45	0.57	2.11	2.69	0.00	0.00	2.50	3.18	2.56	0.18	0.84	0.00
Fl_93	0.16	0.20	0.55	0.70	0.00	0.00	0.69	0.88	0.71	0.23	0.80	0.00
JK_20	0.11	0.14	0.57	0.73	0.00	0.00	0.68	0.87	0.68	0.16	0.84	0.00
P_1500a	0.27	0.34	0.68	0.87	0.00	0.00	0.93	1.18	0.95	0.29	0.73	0.00
RS_3636	1.14	1.45	0.65	0.83	0.06	0.08	1.81	2.30	1.85	0.63	0.36	0.03
SS_16782	0.26	0.33	1.24	1.58	0.14	0.18	1.58	2.01	1.64	0.16	0.78	0.09
Tokai_24_1	0.76	0.97	2.31	2.94	0.00	0.00	2.94	3.74	3.07	0.26	0.79	0.00
Tokai_24_2	0.53	0.67	2.00	2.55	0.00	0.00	2.41	3.07	2.53	0.22	0.83	0.00
TT-2-B-3	0.44	0.56	1.91	2.43	0.00	0.00	2.29	2.92	2.35	0.19	0.83	0.00
TT-6-B-1	0.76	0.97	2.01	2.56	0.00	0.00	2.73	3.48	2.77	0.28	0.74	0.00
TT-8-B-3	0.84	1.07	2.49	3.17	0.00	0.00	3.30	4.20	3.33	0.25	0.75	0.00
13_12_04_1	0.49	0.62	2.33	2.97	0.00	0.00	2.79	3.55	2.82	0.18	0.84	0.00
mean	0.48	0.61	1.47	1.87	0.03	0.04	1.93	2.46	1.98	0.24	0.76	0.02
max	1.14	1.45	2.61	3.32	0.37	0.47	3.30	4.20	3.37	0.63	1.00	0.14
min	0.00	0.00	0.38	0.48	0.00	0.00	0.62	0.79	0.65	0.00	0.36	0.00

MODIFIED	LAp	SVp	LAs	SVs	LAu	SVu	LAt	SVges	LAt_ber		ratio p	ratio s	ratio u
5_12_04	0.76	0.97	2.61	3.32			3.26	4.15	3.37		0.23	0.80	
1_8_97_1	0.38	0.48	1.04	1.32	0.02	0.03	1.41	1.80	1.44		0.27	0.74	0.01
1_8_97_3b	0.37	0.47	1.39	1.77			1.82	2.32	1.76		0.20	0.76	
10_12_20_b	1.11	1.41	1.27	1.62	0.37	0.47	2.66	3.39	2.75		0.42	0.48	0.14
1_8_97_7b	0.34	0.43	1.28	1.63	0.02	0.03	1.60	2.04	1.64		0.21	0.80	0.01
3_8_97_1	0.44	0.56	1.53	1.95			1.92	2.44	1.97		0.23	0.80	
5_11_07_3b	0.37	0.47	1.14	1.45			1.49	1.90	1.51		0.25	0.77	
6_4_01_1a	0.60	0.76	1.08	1.38	0.02	0.03	1.67	2.13	1.70		0.36	0.65	0.01
8 Ta PS	0.27	0.34	0.38	0.48			0.62	0.79	0.65		0.44	0.61	
9_9_01	0.05	0.06	0.75	0.95			0.80	1.02	0.80		0.06	0.94	
10_12_08	0.68	0.87	1.39	1.77	0.18	0.23	2.19	2.79	2.25		0.31	0.63	0.08
26_6			1.90	2.42			1.90	2.42	1.90				
27_6_14_1e	0.66	0.84	2.07	2.64			2.60	3.31	2.73		0.25	0.80	
44,20,I	0.65	0.83	1.84	2.34	0.05	0.06	2.49	3.17	2.54		0.26	0.74	0.02
44,20,II	0.34	0.43	1.08	1.38	0.03	0.04	1.42	1.81	1.45		0.24	0.76	0.02
44,20,III	0.80	1.02	2.26	2.88			2.97	3.78	3.06		0.27	0.76	
11497.00	0.14	0.18	1.02	1.30			1.14	1.45	1.16		0.12	0.89	
11510.00	0.16	0.20	1.08	1.38	0.07	0.09	1.29	1.64	1.31		0.12	0.84	0.05
C28_01	0.45	0.57	2.11	2.69			2.50	3.18	2.56		0.18	0.84	
Fl_93	0.16	0.20	0.55	0.70			0.69	0.88	0.71		0.23	0.80	
JK_20	0.11	0.14	0.57	0.73			0.68	0.87	0.68		0.16	0.84	
P_1500a	0.27	0.34	0.68	0.87			0.93	1.18	0.95		0.29	0.73	
RS_3636	1.14	1.45	0.65	0.83	0.06	0.08	1.81	2.30	1.85		0.63	0.36	0.03
SS_16782	0.26	0.33	1.24	1.58	0.14	0.18	1.58	2.01	1.64		0.16	0.78	0.09
Tokai_24_1	0.76	0.97	2.31	2.94			2.94	3.74	3.07		0.26	0.79	
Tokai_24_2	0.53	0.67	2.00	2.55			2.41	3.07	2.53		0.22	0.83	
TT-2-B-3	0.44	0.56	1.91	2.43			2.29	2.92	2.35		0.19	0.83	
TT-6-B-1	0.76	0.97	2.01	2.56			2.73	3.48	2.77		0.28	0.74	
TT-8-B-3	0.84	1.07	2.49	3.17			3.30	4.20	3.33		0.25	0.75	
13_12_04_1	0.49	0.62	2.33	2.97			2.79	3.55	2.82		0.18	0.84	
mean	0.49	0.63	1.47	1.87	0.10	0.12	1.93	2.46	1.98		0.25	0.75	0.05
max	1.14	1.45	2.61	3.32	0.37	0.47	3.30	4.20	3.37	0.00	0.63	0.94	0.14
min	0.05	0.06	0.38	0.48	0.02	0.03	0.62	0.79	0.65	0.00	0.06	0.36	0.01

	Anzahl Zellen N(W)	Anzahl Berührpunkte mit Rand Ne(W)	Anzahl Knoten k	Dünnschliffläche A	Knoten pro Fläche λ0	Anzahl Zelle pro Flächeneinheit λ2	mittlere Fläche einer Zelle a
5-12-04-3_1	8.00	6.00	8.00	30.72	0.26	0.13	7.68
5-12-04-3_3	7.00	7.00	5.00	30.72	0.16	0.08	12.29
5-12-04-3_4	7.00	7.00	5.00	30.72	0.16	0.08	12.29
5-12-04-3_5	7.00	7.00	4.00	15.64	0.26	0.16	6.26
5-12-04-3_6	8.00	5.00	9.00	15.64	0.58	0.29	3.48
5-12-04-3_7	8.00	5.00	10.00	15.64	0.64	0.29	3.48
5-12-04-3_8	15.00	11.00	16.00	15.64	1.02	0.54	1.84
5-12-04-3_9	7.00	8.00	5.00	15.64	0.32	0.13	7.82
5-12-04-3_10	10.00	9.00	9.00	15.64	0.58	0.29	3.48
5-12-04-3_11	9.00	7.00	9.00	15.64	0.58	0.29	3.48
						mean	6.21

8.6. Porosity & Permeability measurements

TRIPLE WEIGHT

	m dry			average	m sat			average	m sus.			average	Vpore	Vbulk	phi	phi, %
13-12-04-1	22.791	22.790	22.791	22.791	22.926	22.924	22.917	22.922	14.341	14.350	14.346	14.346	0.132	8.577	0.015	1.54
10-12-20b	39.452	39.446	39.444	39.447	42.156	42.197	42.212	42.188	22.681	22.683	22.797	22.720	2.741	19.468	0.141	14.08
Fl 93	27.851	27.851	27.850	27.851	28.269	28.266	28.265	28.267	17.211	17.219	17.213	17.214	0.416	11.052	0.038	3.76
9-9-01-Lentia	40.862	40.860	40.860	40.861	41.896	41.893	41.891	41.893	24.388	24.390	24.383	24.387	1.033	17.506	0.059	5.90
6-4-01-1a	28.646	28.645	28.646	28.646	28.715	28.710	28.709	28.711	16.193	16.189	16.193	16.192	0.066	12.520	0.005	0.52
C28-01	44.006	44.005	44.008	44.006	44.358	44.359	44.357	44.358	24.903	24.913	24.909	24.908	0.352	19.450	0.018	1.81
27-6-14-1e	43.592	43.592	43.592	43.592	43.833	43.815	43.809	43.819	25.510	25.512	25.508	25.510	0.227	18.309	0.012	1.24
Tokai 24-1	23.623	23.620	23.620	23.621	23.926	23.930	23.884	23.913	13.561	13.560	13.562	13.561	0.292	10.352	0.028	2.82
Tokai 24-1	32.998	32.996	32.997	32.997	33.380	33.387	33.393	33.387	19.022	10.020	19.009	16.017	0.390	17.370	0.022	2.24
5-12-04-3	33.208	33.209	33.208	33.208	33.363	33.359	33.356	33.359	19.168	19.156	19.158	19.161	0.151	14.199	0.011	1.06
5-11-07-3b	22.937	22.937	22.938	22.937	22.994	22.991	22.988	22.991	13.253	13.249	13.280	13.261	0.054	9.730	0.006	0.55
1-8-97-3b	23.544	23.541	23.542	23.542	24.026	24.019	24.020	24.022	13.795	13.789	13.795	13.793	0.479	10.229	0.047	4.69

HE PYCNOMETER

sample 1-8-97-3b mass: 23.54

length:	21.88			**diameter:**	24.73		
	21.79				24.69		
	21.73				24.73		
average:	21.80	mm			24.72	mm	
	2.18	cm			2.47	cm	

run	Volume	Density
1	9.6519	2.4391
2	9.6472	2.4403
3	9.6449	2.4409
average	9.6480	2.4401

Volume V	10.46	cc
rho(bulk)	2.25	
phi	0.07762284	7.76 %

PERMEABILITY

1	2	3	4	5	6	7	8	9	10	11
Sample N°	**Sample Name**	**Length** (cm)	**Dia** (cm)	**Atm. Press.** (psi)	**Screen Height** (cm) (tranverse K)	**Screen Width** (cm) (tranverse K only)	**Confining Pressure Radial** (psig)	**Confining Pressure Axial** (psig)	**Date Time of test**	**PT01** (psig)
1	1_8_97	2.18	2.47	14.73			125	0	8.2.21 10:31 AM	1.66
	1_8_97	2.18	2.47	14.73			125	0	8.2.21 10:41 AM	3.96
	1_8_97	2.18	2.47	14.73			125	0	8.2.21 10:52 AM	4.76
	1_8_97	2.18	2.47	14.73			125	0	8.2.21 11:01 AM	5.27
	1_8_97	2.18	2.47	14.73			125	0	8.2.21 11:09 AM	5.90

Min K (mD)	Max K (mD)	Max DP (psi/inch)
0.0	0.1	1.8
0.1	1.0	3.9
1	10	4
10	100	3
100	1.000	1.2
1.000	10.000	0.5
10.000	100.000	0.11

12	13	14	15	16	17	18	19	20	21	22
Optionnal DPT01 (psid)	**Optionnal TE01** (°C)	**FQT01** (Ncc/min)	**Optionnal FQT02** (Ncc/min)	**FQT03** (Ncc/min)	**Ka (mD)**	$K_{Klinkenberg}$ (mD) *applicable only in backward mode*	$K_{Klinkenberg}$ **Factor b** (Atm) *applicable only in backward mode*	K_K Correl factor R2	**Darcy conditions granted**	**Measured at stabilisation**
0.003	24.8	0.565		-0.2	0.691				**OK**	OK
0.003	25.2	3.487		-0.2	1.669				**OK**	OK
0.003	25.5	4.529		-0.3	1.764	**10.956**	**-0.983**	-0.966	**OK**	OK
0.003	25.8	5.226		-0.3	1.816				**OK**	OK
0.003	25.9	6.132		-0.3	1.870				**OK**	OK

average:	1.817